



**Rigidizable Inflatable Get-Away-Special Experiment (RIGEX)
Post Flight Analysis, Ground Testing, Modeling,
and Future Applications**

THESIS

Brett J. Cooper, Captain, USAF
AFIT/GA/ENY/09-M02

**DEPARTMENT OF THE AIR FORCE
AIR UNIVERSITY**

AIR FORCE INSTITUTE OF TECHNOLOGY

Wright-Patterson Air Force Base, Ohio

APPROVED FOR PUBLIC RELEASE; DISTRIBUTION UNLIMITED.

The views expressed in this thesis are those of the author and do not reflect the official policy or position of the United States Air Force, Department of Defense, or the United States Government.

RIGIDIZABLE INFLATABLE GET-AWAY-SPECIAL EXPERIMENT (RIGEX)
POST FLIGHT ANALYSIS, GROUND TESTING, MODELING,
AND FUTURE APPLICATIONS

THESIS

Presented to the Faculty
Department of Aeronautics & Astronautics
Graduate School of Engineering and Management
Air Force Institute of Technology
Air University
Air Education and Training Command
In Partial Fulfillment of the Requirements for the
Degree of Master of Science in Aerospace Engineering

Brett J. Cooper, BS

Captain, USAF

March 2009

APPROVED FOR PUBLIC RELEASE; DISTRIBUTION UNLIMITED.

RIGIDIZABLE INFLATABLE GET-AWAY-SPECIAL EXPERIMENT (RIGEX)
POST FLIGHT ANALYSIS, GROUND TESTING, MODELING,
AND FUTURE APPLICATIONS

Brett J. Cooper, BS
Captain, USAF

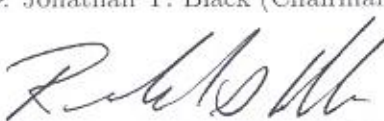
Approved:



Dr. Jonathan T. Black (Chairman)

18 MAR 09

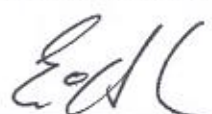
Date



Dr. Richard G. Cobb (Member)

13 MAR 09

Date



Lt Col Eric D. Swenson, PhD (Member)

13 Mar 09

Date

Abstract

The Rigidizable Inflatable Get-Away-Special EXperiment (RIGEX) Space Shuttle experiment was run successfully onboard STS-123 (*Endeavour*) in March 2008. The objective of this thesis is to analyze the space flight and post space flight test data, correlate the data to previous ground tests, and update finite element models. In turn, this research will help demonstrate the feasibility of using lightweight and low stowage volume (high packaging ratio) inflatable/rigidizable space structures in remote sensing applications.

RIGEX was an Air Force Institute of Technology graduate-student-built Space Shuttle cargo bay experiment intended to heat and inflate three 20-inch long carbon fiber tubes in a microgravity environment. Designed to measure the individual tubes' structural characteristics and deployed configuration, pressure, temperature, vibration response, and physical alignment data were all collected successfully on-orbit and are presented in comparison to pre- and post flight ground test data. Using the space and ground test results, previously developed finite element models of the tubes are updated and models of mission oriented structures are created for trade study purposes. Finally, tube and truss deployment processes are examined, and suggestions for future experiments and applications are provided.

RIGEX successfully accomplished its mission statement by validating the heating and inflation methods of the inflatable/rigidizable tubes, and successfully met all other primary and secondary research objectives.

Acknowledgements

I'd like to thank Dr. Black for his excellent direction through the thesis process and continual problem solving help, Dr. Cobb for his guidance in all things RIGEX, and Lt Col Swenson for his help with Finite Element Modeling. In addition, I'd like to thank my Reverend for his steady influence and all of my friends and fellow students. AFIT challenged us and made us better engineers.

I'd be remiss if I failed to mention the 13 master's students and summer interns who poured their heart and soul into developing and preparing RIGEX for flight. The success of RIGEX on-orbit is testament to your tenacity and commitment to excellence.

Above all, none of this would have been possible without the support of my loving wife; she is the rock on which I stand while reaching for the stars.

Brett J. Cooper

Table of Contents

	Page
Abstract	iv
Acknowledgements	v
List of Figures	ix
List of Tables	xii
List of Abbreviations	xiii
I. Introduction	1
1.1 Why RIGEX? Motivation for the Warfighter	1
1.2 RIGEX Objectives	5
1.3 Research Objectives	5
1.4 Thesis Overview	6
II. Background Information	8
2.1 Literature Review	8
2.1.1 Inflatable and Rigidizable Space Structures	9
2.1.2 Previous RIGEX Efforts	18
2.2 RIGEX Overview	26
2.2.1 L’Garde, Inc. Inflatable Rigidizable Tubes	26
2.2.2 Final RIGEX Configuration	27
2.3 Theory Review	28
2.3.1 Vibration Response and Modal Analysis	28
2.3.2 Finite Element Modeling	33
III. Test Methodology	36
3.1 Space Flight Testing	36
3.1.1 Temperature	36
3.1.2 Pressure	39
3.1.3 Accelerometer Based Testing	41
3.1.4 Imaging	43
3.2 Post Space Flight Vibration Testing	43
3.2.1 Flight Computer Testing	44
3.2.2 dSpace Testing	44
3.3 Ground Testing	45
3.3.1 Validation of Previous Ground Testing	46
3.3.2 Single Axis Laser Vibrometer Testing	46

	Page
3.3.3 Triaxial Scanning Laser Vibrometer Testing	47
3.3.4 Displacement Measurements	49
3.4 Finite Element Modeling	51
3.4.1 Individual Tube Models	51
3.4.2 Mission Oriented Structure Models	51
IV. Results and Discussion	52
4.1 Space Flight Test Results	52
4.1.1 Temperature Results	53
4.1.2 Pressure Results	58
4.1.3 Accelerometer Results	62
4.1.4 Image Results	80
4.2 Post Space Flight Test Results	85
4.2.1 Changes from Space Flight Configuration	86
4.2.2 Flight Computer Test Results	86
4.2.3 dSpace Test Results	87
4.3 Ground Test Results	100
4.3.1 Validation of Previous Ground Testing Results	100
4.3.2 Single Axis Laser Vibrometer Testing	104
4.3.3 Triaxial Laser Vibrometer Test Results	104
4.3.4 Displacement Measurement Results	121
4.4 Finite Element Modeling Results	123
4.4.1 Fundamental Frequency and Young's Modulus	124
4.4.2 Individual Tube Model Results	125
4.4.3 Mission Oriented Structures Model Results	129
4.5 Conclusions	131
4.5.1 Space Flight Test Results	131
4.5.2 Post Space Flight Test Results	134
4.5.3 Ground Test Results	135
4.5.4 Finite Element Models	136
V. Correlation with Previous Testing	137
5.1 Comparison of Temperature Data	138
5.2 Comparison of Pressure Data	140
5.3 Comparison of Vibration Testing Results	141
5.3.1 Space Flight and Preflight Results	142
5.3.2 Space Flight and Post Space Flight Testing	143
5.3.3 Preflight and Post Space Flight Testing	143
5.4 Comparison of Finite Element Models	144
5.5 Deployment Processes	147
5.6 Technology Readiness Level Review	148
5.7 Conclusions	149

	Page
VI. Conclusions and Recommendations	151
6.1 Conclusions	151
6.2 Recommendations	153
6.2.1 Lessons Learned	153
6.2.2 The Future and Legacy of RIGEX	153
Appendix A. RIGEX Post Flight Examination and Condition	155
A.1 Inoperable Components	155
A.1.1 Initial Anomalies	155
A.1.2 Anomaly Determination	155
A.1.3 Anomaly Resolution	156
A.1.4 Probable Cause	156
A.2 Contaminant in Connections	157
A.3 Oven Conditions	158
A.4 Shipping Environment	158
Appendix B. Matlab Scripts	160
Appendix C. RIGEX Flight Code	186
Bibliography	226
Vita	229

List of Figures

Figure	Page
1.1. RIGEX in <i>Endeavour</i> Cargo Bay on Orbit	2
1.2. Inflatable Antennas	3
1.3. Inflatable Antenna Experiment	4
2.1. Truss Structural Efficiency	12
2.2. L’Garde, Inc. Inflatable Decoys	14
2.3. Bigelow Aerospace Inflatables	15
2.4. Inflatable/Rigidizable Sunshades	16
2.5. Inflatable/Rigidizable Solar Arrays	17
2.6. RIGEX Student Involvement	19
2.7. Quarter Structure	21
2.8. Example Battery Stack	23
2.9. Cutaway of RIGEX Inside the CAPE	25
2.10. Example Tubes	27
2.11. RIGEX Configuration	28
2.12. Spring Mass Damper System	29
2.13. Example Finite Element Mesh	34
3.1. RIGEX Test Hierarchy	37
3.2. Space Flight Testing Timeline	38
3.3. Thermocouple Locations and Z-Fold Flight Tubes	39
3.4. PZTs Mounted to Tubes	42
3.5. Modal Response Testing Schematic	44
3.6. Ometron Single Axis Laser Vibrometer Test Setup	47
3.7. Polytec Triaxial Scanning Laser Vibrometer Test Setup	48
3.8. Scan Grid Overlayed on Tube 3	49
3.9. Platinum FaroArm	50
4.1. Standard Switch Panel 2	53
4.2. RIGEX Temperature Data	54
4.3. RIGEX Structure Temperature	55
4.4. Shuttle Attachment Stations	56
4.5. Shuttle Cargo Bay Temperatures	57
4.6. Inflation Pressure vs. Time	60

	Page	
4.7.	Inflation Acceleration vs. Time	63
4.8.	Accelerometer and Tube Coordinate Systems	65
4.9.	Ambient and Excited Acceleration Time Histories	66
4.10.	Chirp Input Signal	68
4.11.	Tube 1 Space Flight FRF Drift	71
4.12.	Tube 2 Space Flight FRF Drift	72
4.13.	Tube 3 Space Flight FRF Drift	73
4.14.	Tube 1 Space Flight X-Axis FRF	75
4.15.	Tube 2 Space Flight X-Axis FRF	75
4.16.	Tube 3 Space Flight X-Axis FRF	76
4.17.	Tube 1 Three Axis Averaged Space Flight FRF	77
4.18.	Tube 2 Three Axis Averaged Space Flight FRF	78
4.19.	Tube 3 Three Axis Averaged Space Flight FRF	79
4.20.	Tube 1 Deployment Images	81
4.21.	Tube 2 Deployment Images	82
4.22.	Tube 3 Deployment Images	83
4.23.	Change Detection Analysis	85
4.24.	SimuLink Simulation Model	87
4.25.	Tube 1 dSpace FRF and Coherence Plot	89
4.26.	Tube 2 dSpace FRF and Coherence Plot	90
4.27.	Tube 3 dSpace FRF and Coherence Plot	91
4.28.	Tube 1 SignalCalc FRF and Coherence Plot	94
4.29.	Tube 2 SignalCalc FRF and Coherence Plot	95
4.30.	Tube 3 SignalCalc FRF and Coherence Plot	96
4.31.	Tube 1 SignalCalc High Resolution FRF and Coherence Plot	97
4.32.	Tube 2 SignalCalc High Resolution FRF and Coherence Plot	98
4.33.	Tube 3 SignalCalc High Resolution FRF and Coherence Plot	99
4.34.	Old Tube 1 FRF and Coherence Plot	101
4.35.	Old Tube 2 FRF and Coherence Plot	102
4.36.	Old Tube 3 FRF and Coherence Plot	103
4.37.	Tube 1 Scanned Surface	106
4.38.	Tube 1 X-Axis 0 – 500Hz	108
4.39.	Tube 1 Y-Axis 0 – 5000Hz	109
4.40.	Tube 1 Operational Deflection Shapes	110

	Page
4.41. Tube 2 Scanned Surface	112
4.42. Tube 2 X-Axis 0 – 500Hz	113
4.43. Tube 2 Y-Axis 0 – 5000Hz	114
4.44. Tube 2 Operational Deflection Shapes	115
4.45. Tube 3 Scanned Surface	117
4.46. Tube 3 X-Axis 0 – 500Hz	118
4.47. Tube 3 Y-Axis 0 – 5000Hz	119
4.48. Tube 3 Operational Deflection Shapes	120
4.49. Actual vs. Straight Displacements	122
4.50. Finely Meshed FE model Mode Shapes	129
4.51. Coarsely Meshed FE model Mode Shapes	129
4.52. Mission Oriented Structures	130
4.53. Deformed Triangular Cross Section Truss	132
4.54. Deformed Flat Panel Model	133
5.1. Space Flight and Preflight Temperature Correlation (A)	139
5.2. Space Flight and Preflight Temperature Correlation (B)	139
5.3. Space Flight and Preflight Inflation Pressure Correlation	141
5.4. Moeller's Pressure and Temperature Results	142
5.5. Technology Readiness Scale	149
A.1. Stake Contaminant on the Accelerometer Connections	158
A.2. Pre- and Post flight Oven Photographs	159
A.3. Tripped shock damage detectors	159

List of Tables

Table		Page
2.1.	Comparison of Deployable Antenna Types	11
2.2.	Single's Short Tube Natural Frequencies	20
2.3.	Philley's Tube Natural Frequencies	20
2.4.	Tube Physical Properties	26
4.1.	On-Orbit Instantaneous Pressure Census Readings	62
4.2.	Space Flight Natural Frequencies	74
4.3.	Change Detection Analysis Results	84
4.4.	dSpace Vibration Response Test SignalCalc Settings	88
4.5.	Three Tube dSpace Natural Frequencies	93
4.6.	Increased Resolution SignalCalc Settings	93
4.7.	Polytec Settings	105
4.8.	Tube 1 Polytec Results	106
4.9.	Tube 2 Polytec Results	111
4.10.	Tube 3 Polytec Results	116
4.11.	Deployed Tube Deviations (Ground)	122
4.12.	Deployed Tube Deviations (Space)	122
4.13.	Flight Tube Fundamental Frequencies	124
4.14.	Flight Tube Young's modulus Estimate for FE model	125
4.15.	Fine Model Results	127
4.16.	Coarse Model Results	128
4.17.	Mission Oriented Structures Model Results	131
5.1.	Space Flight and Preflight Temperature Correlation	138
5.2.	RIGEX and Aluminum Tube and Truss Comparison	145
5.3.	Technology Readiness Level 7 Assessment	150
A.1.	Component Functional Test Results	157

List of Abbreviations

Abbreviation		Page
RIGEX	Rigidizable Inflatable Get-Away-Special Experiment	iv
AFIT	Air Force Institute of Technology	1
CAPE	Canister for All Payload Ejections	1
NASA	National Aeronautics and Space Administration	1
DoD	Department of Defense	2
SAR	Synthetic Aperture Radar	2
IAE	Inflatable Antenna Experiment	4
DARPA	Defense Advanced Research Projects Agency	5
GAS	Get-Away-Special	5
FE	Finite Element	6
FEA	Finite Element Analysis	6
ICBM	Intercontinental Ballistic Missile	8
T_g	Glass Transition	10
PZT	Piezoelectric Transducer	19
STP	Space Test Program	20
DAC	Digital to Analog Converter	22
FRF	Frequency Response Function	29
FEMAP	Finite Element Model Analysis Program	34
ADC	Analog to Digital Converter	41
CAD	Computer Aided Design	50
SSP2	Standard Switch Panel 2	52
TRL	Technology Readiness Level	137
LEDs	Light Emitting Diodes	155

RIGIDIZABLE INFLATABLE GET-AWAY-SPECIAL EXPERIMENT

(RIGEX)

POST FLIGHT ANALYSIS, GROUND TESTING, MODELING,

AND FUTURE APPLICATIONS

I. Introduction

THE Rigidizable Inflatable Get-Away-Special EXperiment (RIGEX) is an Air Force Institute of Technology (AFIT) graduate-student-built Space Shuttle Canister for All Payload Ejections (CAPE) experiment designed to heat, inflate, and rigidize three carbon fiber tubes in the microgravity space environment. RIGEX ran successfully onboard the *Endeavour* (STS-123) in March 2008. Pressure, temperature, vibration response, and physical alignment data for the 20-inch long tubes were all collected successfully on-orbit. Figure 1.1 (a) and (b) are National Aeronautics and Space Administration (NASA) images of the *Endeavour* with cargo bay doors open, taken from the International Space Station. RIGEX is inside the CAPE marked with red arrows overlayed on the pictures.

1.1 *Why RIGEX? Motivation for the Warfighter*

Air Force Basic Doctrine, as developed in Air Force Doctrine Document 1, provides the basic Principles of War and Tenets of Air and Space Power [1]. Inflatable/Rigidizable technology utilized in RIGEX fundamentally supports the tenets of Flexibility and Versatility, Synergistic Effects, and Persistence. The seventeen Key Operational Functions are subject to the Tenets of Air and Space Power, and RIGEX technology supports five of seventeen: Counterspace, Information Operations, Spacelift, Surveillance and Reconnaissance, and finally, Command and Control. Finally, this technology supports Air and Space Superiority and Information Superiority, two of the six the basic Air Force areas of expertise known as Air Force Distinctive Capabilities.

How do carbon fiber tubes support these capabilities, functions, and tenets? Elaborated upon in greater detail in Chapter II, the ability to create space structures orders

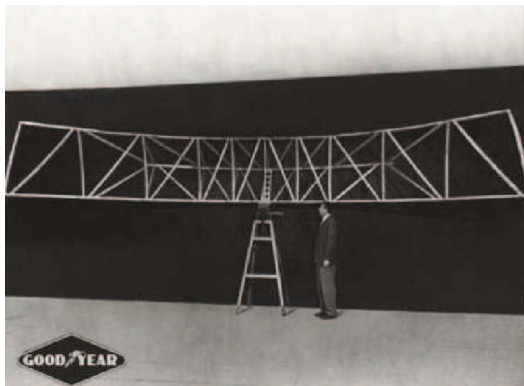


Figure 1.1: (a) International Space Station photo of approaching *Endeavour* with cargo bay open. RIGEX is visible, mounted aft of the cargo in the back left corner. Photo Courtesy of NASA.

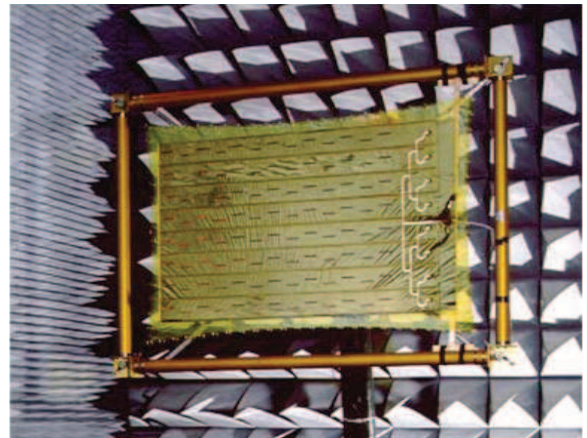
(b) International Space Station photo of docked *Endeavour*'s cargo bay. RIGEX is clearly visible, attached to the rear left cargo bay sill. This photo was taken after the *Kibo* logistics module had been removed from the cargo bay. Photo Courtesy of NASA.

of magnitude larger and lighter than those currently in operation, with little deployment complexity and therefore increased system reliability, is the primary advantage in the inflatable/rigidizable technology demonstrated in RIGEX [18]. Inflatable space structures enjoy the advantage of weighing 50-75% less than mechanical alternatives and can be packaged in 25% of the volume [3]. Immediate examples of future Air Force space missions which can make use of these larger and lighter space structures include imagery, signals collection, communications, decoys, radar, and reflector arrays. Indeed, this technology's ability to produce larger intelligence sensors with greater spatial resolution and increased ground coverage footprint, combined with the synergistic effects of larger communications arrays able to transmit more data are the primary capabilities of inflatable/rigidizable technologies which support most of the Distinctive Capabilities, Key Operational Functions, and Tenets of Air and Space Power mentioned above.

Figure 1.2 helps develop a sense of perspective of how this technology could benefit the warfighter. As far back as the 1950's, NASA, the Department of Defense (DoD), and the aerospace industry have tried to tackle the problems associated with deploying large antennas on-orbit (Figure 1.2 (a)). In particular, a considerable amount of effort has been applied towards an inflatable Synthetic Aperture Radar (SAR). Traditional



(a)



(b)

Figure 1.2: (a) A Goodyear inflatable/rigidizable 3 X 10 meter parabolic search radar structure developed in the late 1950's to early 1960's [10].

(b) A 2 X 1.1 meter L'Garde inflatable/rigidizable SAR antenna developed in 2002. The antenna is rolled up to save space and uses RIGEX technology for support [21].

SAR antennas are made of solid panels that are stowed for launch by being folded into smaller sections and are then deployed by mechanical devices, which link heavy support structures necessary to maintain the antenna shape. The limiting factor for aperture size of SAR antennas is the size of the launch vehicle's aerodynamic fairing. A balance must be struck between fitting the stowed panels within the aerodynamic fairing and deployment complexity, which increases with every fold. Thus, large apertures necessary for high resolution require either larger, more expensive launch vehicles or highly complex (and thus more prone to failure) deployment processes [18]. Recent efforts by NASA, ILC Dover, Inc., and L'Garde, Inc. (Figure 1.2 (b)) have dramatically increased the packaging efficiency of SAR antennas by rolling up inflatable/rigidizable antennas. Dramatically reducing the dimensions of a satellite stowed for launch, these rolled-up SAR antenna missions could fit into much smaller aerodynamic fairings. Combining the smaller launch fairing and the projected order of magnitude mass savings, inflatable SAR missions could use smaller, cheaper launch vehicles than currently possible. Finally, RIGEX technology can be used to completely remove the heavy support structure necessary to maintain antenna shape [21], and the deployment process is generally more reliable than traditional methods, perhaps the most important benefit of RIGEX technology (see Table 2.1) [3].



Figure 1.3: (a) The 14 X 18 meter IAE after deployment, viewed from the *Endeavour* (STS-77). The entire reflector was stowed inside of a container the size of an office desk, demonstrating the incredible packaging efficiency of inflatables [9].
 (b) An AFIT concept of a very large aperture using membrane optics supported by an inflated torus and inflatable/rigidizable structures connecting the optics to the focal sensors [36].

Perhaps even more ambitious than the radar antenna work are the efforts to create extremely large aperture observatories using light weight membrane optics and inflatable/rigidizable structures. Figure 1.3 (a) shows the Inflatable Antenna Experiment (IAE), a \$1 million 14 X 18 meter reflector array that was packaged into a container the size of an office desk; it was successfully deployed in 1996 from the *Endeavour* [9]. Using the IAE as a stepping stone, NASA has ambitions for very large space observatories capable of characterizing planets in orbit around nearby stars using clustered 20-40 meter diameter optical collectors [18]. From an Air Force perspective of earth observation, a 14 meter mirror orbiting at 1000 kilometers altitude would yield imagery with greater than 0.1 meter resolution over a much larger ground footprint than currently available. This high resolution with large coverage area would clearly allow simultaneous surveillance and reconnaissance over the whole battlespace.

1.2 RIGEX Objectives

DiSebastion [7] was the first of fourteen students to work on the RIGEX project. Working with the Defense Advanced Research Projects Agency (DARPA) and other national cosponsors, he developed the overall RIGEX mission statement:

To verify and validate ground testing of inflation and rigidization methods for inflatable space structures against a zero gravity space environment.

In support of the mission statement, DiSebastion also developed the primary and secondary objectives, which set results expectations for RIGEX:

Primary Objective:

- Design a Get-Away-Special (GAS) experiment to collect data on space-rigidized structures for validation of ground testing methods.

Secondary Objectives:

- Return inflated/rigidized structures to laboratory for additional testing.
- Enable application of rigidized structures to operational space systems.
- Implement systems engineering principles into the experiment's design.

Expanding upon DiSebastion's objectives, Goodwin [11] developed additional primary objectives based on the lack of an onboard telemetry system:

Additional Primary Objectives

- Recover the RIGEX Payload
- Post-process the experiment's flight data at AFIT

For completeness, Goodwin also revised DiSebastion's primary objective, removing 'Get-Away-Special' and inserting 'Canister for All Payload Ejections'. GAS canisters were no longer being flown on shuttle missions, they had been replaced with the CAPE.

1.3 Research Objectives

Given the RIGEX mission statement, objectives, and the on-orbit success, the primary research objectives for this thesis are to:

- Present results and analysis of the space and post space flight data.
- Correlate and compare the space flight data to previous ground testing.

- Update the tube finite element (FE) model using ground test data.

In addition, several secondary research objectives were set to help develop the follow-on efforts to apply the information provided by the primary research objectives:

- Analyze tube and truss deployment process.
- Develop suggestions for future experiments and applications.
- Create FE models of large space structures based on RIGEX tubes.

Finally, the experiment results will be discussed relative to the previously-established mission statement and primary/secondary objectives. Based on these results, the objectives will be qualified as accomplished or unaccomplished.

1.4 Thesis Overview

This thesis will overview the attempt to meet the research objectives listed in Section 1.3, and provide the footing for the next step forward. An outline with brief synopsis for each chapter is presented here:

- **Chapter I:** Provide a RIGEX introduction, develop motivation for the Warfighter, and spell out the research objectives.
- **Chapter II:** Review literature regarding past, present, and future inflatable space structures, and review both modal analysis and finite element analysis (FEA) theory.
- **Chapter III:** Develop the test methodology used for space flight, post space flight and ground testing, as well as the FEA modeling set up.
- **Chapter IV:** Present and discusses the test and model results.
- **Chapter V:** Compare space flight test data to pre- and post flight test data, compare model results, and compile any remaining analysis.
- **Chapter VI:** Wrap up with conclusions from the test and model data and state recommendations for future work.
- **Appendix A:** Examine the post flight condition of RIGEX.

- **Appendix B:** Example MATLAB Scripts used to analyze the data and develop the results.
- **Appendix C:** Provides the “As Flown” C++ Flight Code.

II. Background Information

THIS chapter presents a literature review of previous RIGEX work and relevant inflatable space structures, setting the stage for the high level overview of the final RIGEX design that follows. The overview provides physical characteristics of the inflatable/rigidizable tubes and the experiment itself. A theory review concludes the chapter, covering finite element modeling and vibration response testing with modal analysis.

2.1 Literature Review

Investigation in inflatable deployable space structures began in the 1950's [10]. Early space lift vehicles, which were converted Intercontinental Ballistic Missiles (ICBM), had very limited payload weight and volume capacity. NASA recognized inflatables, humanity's oldest flight technology, exhibited the right mix of low weight and small stowed volume necessary to reach orbit onboard the contemporary launch vehicles. The rapid increase in launch vehicle volume and weight capacity of the 1960's allowed designers to return to heavier, though more familiar, mechanical deployment methods which led to waning interest in inflatables during the 1960's and 1970's [3]. Other reasons for the decline included concerns with long-term environmental effects potentially causing material degradation, exaggerated fears of meteoroid flux causing punctures and thus deflation, and finally, perceived risks created by a lack analytical tools and experience. These concerns led spacecraft designers to build mechanical structures based on established aerospace technology [41].

Interest in inflatable structures has returned, however, spurred on by ever increasing launch costs and increasingly challenging requirements placed on mission payloads. As mission requirements demand greater performance, mission payload complexity increases, which in turn increases payload weight and volume. The mission payload is almost always the spacecraft configuration design driver [43], and traditionally accounts for 17-50% of the spacecraft dry weight, with an average around 30%. The spacecraft must be large enough to accommodate payload dimensions and/or be able to manipulate the payload if necessary, and the spacecraft must generate the power necessary for mission payload

operation plus the spacecraft bus allowance and battery recharging. Given this relation between mission payload and spacecraft size, if the space system exceeds the current launch capability - no matter how necessary or revolutionary a mission payload may be - the spacecraft cannot be launched [33].

In such an environment, low mass, cost, and packaged volume can factor prominently in both the satellite design process and program feasibility [20]. In Section 1.1, an optical system with an aperture 20-40m in diameter is discussed. The only practical way to achieve such a large system given current launch capacity is to utilize the superior packaging efficiency of inflatable/rigidizable structures. Consider the Hubble Space Telescope - aperture diameter of 2.4m, overall spacecraft dimensions are 4.2m diameter and 13.1m length - this effectively fills the Space Shuttle cargo bay, dimensioned 4.6m diameter by 18.1m length. The obvious conclusion is current technology combined with current space lift technology cannot meet the order of magnitude growth NASA is looking for. With no substantial increase in launch capability for the foreseeable future, deployable inflatable/rigidizable structures are the only viable solution.

Broadening the discussion from mission payloads to include habitats, aero brakes, decoys, solar sails, sunshades, solar arrays, rovers, and much more, the horizon is bright for space structures utilizing inflatable/rigidizable materials.

2.1.1 Inflatable and Rigidizable Space Structures. An inflatable/rigidizable space structure is defined as a structure that prior to inflation is highly flexible and enables efficient packaging and reliable deployment. Upon inflation, an inflatable/- rigidizable space structure is rigidized to obtain a high degree of structural stiffness and strength. After rigidization, the inflation gas is diffusely vented to ambient. This rigidization is what separates inflatable space structures from inflatable/rigidizable structures. Inflatables require continuous internal pressure to maintain shape, whereas once an inflatable/rigidizable structure is rigidized, it no longer requires internal pressure for structural integrity.

The structural stiffness of inflatable and inflatable/rigidizable space structures is often favorably comparable to traditional mechanically deployed structures which are 3-4

times heavier [12]. An excellent example demonstrating this characteristic is the Atlas missile [42]. The skin and interior structures of the Atlas were made as thin as possible to increase payload capacity. The tradeoff of thin structures for payload weight resulted in insufficient structural stiffness, which led to buckling under dynamic flight loads. The buckling problem was negated by pressurizing (inflating) the internal structure with fuel, which rigidized the missile's skin and increased buckling resistance dramatically.

In addition to stiffness, there are other favorable attributes of inflatable/rigidizable structures. A high degree of surface accuracy is possible through accurate design and construction of the structure along with accurate control of the inflation pressure. Also, inflatable/rigidizable structures exhibit highly repeatable deployments that are extremely reliable. In fact, if designed correctly, inflatable/rigidizable structures only have one single point of failure - the inflation system [3]. One drawback to inflatable/rigidizable space structures is the weight penalty of the inflation system, typically a significant percentage of the inflatable structures mass. A poorly designed configuration could conceivably approach 25% of the entire inflatable structure's mass [18].

There are many types of inflation (deployment) and rigidization methods which are coupled with an extensive library of materials associated with inflatable/rigidizable structures. This multitude of inflation and rigidization methods provides designers a large degree of flexibility. Inflatable structures can be divided into three categories: continuously inflated, single inflation rigidized, and single inflation non-rigidized. These structures have three types of inflation systems to choose from: tanked-gas systems, phase-change systems, and chemical gas-generation systems. Tanked-gas systems are ideal for small gas volume requirements and can be used for all three inflation systems. Phase-change systems can be used for the three inflation systems, but uncertainty in the sublimation process can lead to over or under inflation. Chemical gas-generation systems are ideal for continuously inflated missions because of the ability to regulate pressure. In addition to the choices for inflation systems, there are similarly a variety of methods with which to conduct the rigidization process, including pressure-rigidized aluminum foil, sub-glass transition temperature (T_g) rigidizable composites, Hydrogel rigidization,

and Ultra Violet radiation rigidization [12]. RIGEX uses the tanked-gas inflation system and the sub- T_g composite rigidization method, discussed in greater detail in Section 3.1.

Figure 2.1 is a graph created in 1978 by NASA engineers that clearly shows the advantage of inflatable/rigidizable truss structures over mechanical methods. The chart plots the structural efficiency function $(\frac{Mass}{Length})^{\frac{5}{3}}$ against axial loading for coilable longerons, mechanically deployable trusses, and inflatable trusses. The three red lines indicate various Young's modulus values for inflatable trusses. This figure clearly demonstrates the strength to weight advantage inflatable/rigidizable truss structure enjoy over traditional truss structures.

Table 2.1 presents another tangible manner in which inflatable/rigidizable structures stand out from traditional mechanically deployed structures. Relative scaling for several pertinent antenna design factors is provided, comparing inflatable, mesh, and panel radar antenna.

2.1.1.1 Current and Previous Inflatable and Rigidizable Space Structures.

In the short history of space exploration, there are many examples of inflatable and inflatable/rigidizable space structures. The first space inflatable to reach orbit was NASA's *Echo 1a*, launched in 1960 [6]. Designed as the first passive communication satellite, it reflected two frequencies suitable for transmission of telephone and television signals. Weighing 136 pounds, it was stowed within a spherical container 26 inches in diameter. Upon inflation, however, *Echo 1a* measured an astounding 100 feet in diameter - 46 times larger than its stowed dimensions. A suborbital experiment using a smaller model of the Echo 1a used small amounts of gas trapped inside of the folds for inflation, but this design was changed as the trapped gas caused rapid expansion which ripped the

Table 2.1: Mass, reliability, packing efficiency, and cost comparison of three types of deployable radar antennas. [18]

Design Factor	Inflatable	Mesh	Panel
Mass	Low	Low	High
Reliability	High	Low	Medium
Packing Efficiency	High	Medium	Medium
Cost	Low	High	Medium

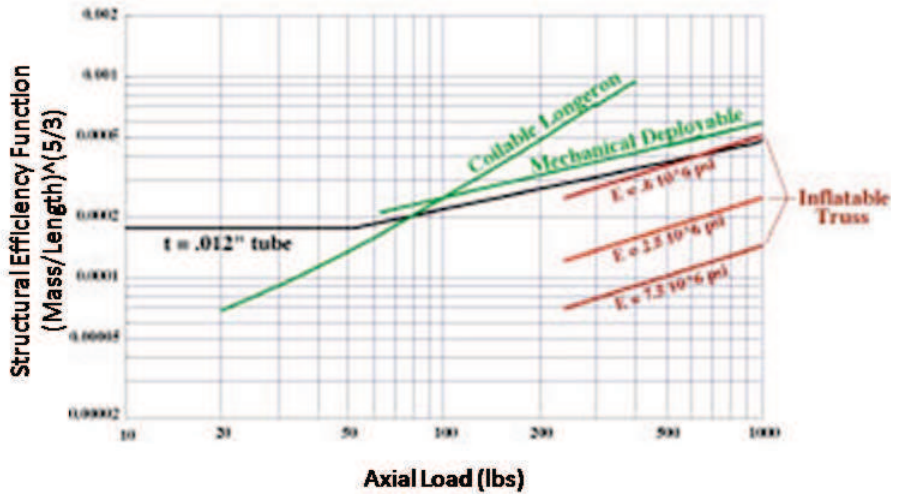


Figure 2.1: Structural Efficiency vs. Axial Loads for deployable trusses. Inflatable/-Rigidizable trusses become increasingly attractive as the Young’s modulus values increase, leading researchers to search for rigidization methods which produce exceptionally stiff structures [26].

fragile fabric. *Echo 1a* flew with a phase-change gas sublimation system; 10 pounds of powdered benzoic acid and 20 pounds of powdered anthraquinone were mixed and resulted in a chemical reaction which generated gas slowly for inflation. After launch, many trans- and intercontinental telephone signals were successfully passed, and a portrait of President Eisenhower became the first “outer space wire photo”, or facsimile. *Echo 1a*’s size made it easily observable with the human eye, and a target for micrometeorites. After having flown through a meteoroid shower, it was punctured multiple times, but it still maintained enough functional shape to allow television signals to be relayed off of the surface, a first for satellites. This demonstrated the fact that very little pressure is needed to maintain an inflatable space structure’s shape - calculations have shown only 0.0001 atmospheres would be required to keep wrinkles out of a 14 meter inflated antenna [41]. Solar pressure eventually degraded *Echo 1a*’s orbit and *Echo 1a* reentered in 1968.

Concern about the micrometeroid flux environment (early estimates were three orders of magnitude too high [41]) led to intensive research to eliminate inflation pressure weak link via rigidization methods. *Echo II*, the second inflatable space structure, was actually the first inflatable/rigidizable space structure. Using the pressure rigidized alu-

minum foil technique, inflation strain hardened the aluminum coating of *Echo* II into a spherical shape and the internal pressure was released via built in vents. After the pressure was released, *Echo* II retained its spherical shape. Launched in 1964, *Echo* II provided the first quantitative measurements of solar pressure, and deorbited in 1969 [6].

Explorer IX, XIX, and *PAGEOS* I are further examples of early NASA inflatable missions and carried on the legacy of the Echo missions. As scientific interest waned for inflatables in the 1970's, they developed an important role in the ICBM community. Low weight, small stowed volume, reliability, and the ability to withstand nuclear blasts led to the use of inflatables as decoys [41]. Rigidization was not necessary as the flight time was minimal along the ballistic trajectory. The design flexibility of the inflatable decoys allowed for creation of a credible optical-radar replica of a Mark-12 Reentry Vehicle [19]. L'garde, Inc. produced these decoys from the 1970's through the mid 1980's [10]. Figure 2.2 (a) is a picture of a decoy deployed in a space test, and (b) is a close up look of a deployed decoy.

No topic on inflatable structures would be complete without mentioning the Inflatable Antenna Experiment, discussed in Section 1.1 and depicted in Figure 1.3. Flown in May 1996, the wildly successful IAE reopened the eyes of the space community to the potential of inflatable and inflatable/rigidizable space structures.

While NASA and the DoD corner a large part of the inflatable space structure market, commercial companies are using inflatable technology for projects designed for profit making in the growing private space economy. Bigelow Aerospace is the preeminent example. Building on NASA's unused TransHab design, Bigelow is working on plans for a space hotel assembled from several inflated modules [34]. Critical aspects of the TransHab program are rolled into Bigelow's designs, and relevant to the ECHO discussion above, micrometeroid and debris protection technology is one such aspect. Bigelow and Johnson Space Center engineers have developed a protection scheme that utilizes alternating layers of a ceramic fabric and thick foam, which offers as much micrometeroid protection as any spacecraft NASA has ever flown [34]. When pressurized to 10psi, the outer skin (composed of a material called Vectran) is harder than steel. When debris hits the skin,



Figure 2.2: (a) The Lightweight Replica in space [19].
 (b) A photo of the Inflatable Exoatmospheric Object, a credible optical-radar replica of a Mark 12 [19].

it disintegrates into smaller pieces that continue to break up and exhaust themselves before they penetrate the shell [23].

Bigelow Aerospace has successfully launched and deployed two inflatable space habitats, *Genesis* I and II. Launched in July 2006 and June 2007, the two habitats continue to operate and provide engineers data on the inflatable habitats' interactions with the space environment. The *Genesis* vehicles are similar in appearance, but *Genesis* II has additional avionics, cameras, and attitude control devices [2]. Both vehicles measure 4.4m in length and the stowed diameter was 1.6m, which allowed for launch on a converted Russian ICBM; when inflated the diameter measures 4.4m, which would just barely fit into the space shuttle cargo bay. This is yet another demonstration of the packaging efficiency of inflatables. Bigelow's next step is the *Sundancer*, a much larger habitat designed to be the focal point of future space hotels. Though specific stowed dimensions are not available, the *Sundancer* is manifested on a SpaceX Falcon 9, which has a fairing with an inner maximum usable diameter of 4.6m [39]; the deployed dimensions of *Sundancer* measure 8.7m length by 6.3m in diameter, yielding 180m³ of living space [5]. Finally, building on the *Sundancer* is the BA 330, a 330m³ habitat which can house 6 people and remarkably boasts 2.75 times the livable volume of most International Space Station Modules. The BA 330 would be the backbone of the orbiting space hotel. Figure



Figure 2.3: (a) Relative sizes of the Bigelow Aerospace habitat modules [2].
(b) A photo of *Genesis* II deployed on-orbit [2].

2.3 (a) shows the relative sizes of the various deployed space habitats, and (b) shows *Genesis* II deployed on-orbit, with solar panels extended and external cameras visible.

Turning to inflatable/rigidizable space structures, interest has shifted from rigidizing whole space structures similar to *Echo* II to only rigidizing subsets of the spacecraft. Structures supporting SAR antennas and optical sensors have already been discussed, but consider rigidized sunshades and solar arrays. Sunshades are used to block external stray light sources that would generally limit sensitivity of optical payloads, and also attenuate heat transfer from external sources (the sun) to the spacecraft [18]. The Webb Space Telescope (formerly known as the Next Generation Space Telescope) design requires a large sunshade to enable passive cooling of the spacecraft, and inflatable/rigidizable technology was investigated but not chosen. The design utilized a planar “party favor” roll out method and rigid crucifix supports. Figure 2.4 (a) shows a $\frac{1}{2}$ scale of the Webb Space Telescope inflatable/rigidizable roll out technology demonstrator, and (b) shows a functional scale model inflatable/rigidizable support structure for a sub-millimeter telescope.

Another application of inflatable/rigidizable technology that has been making progress in the last decade are inflatable/rigidizable solar arrays. Designs and working prototypes



(a)



(b)

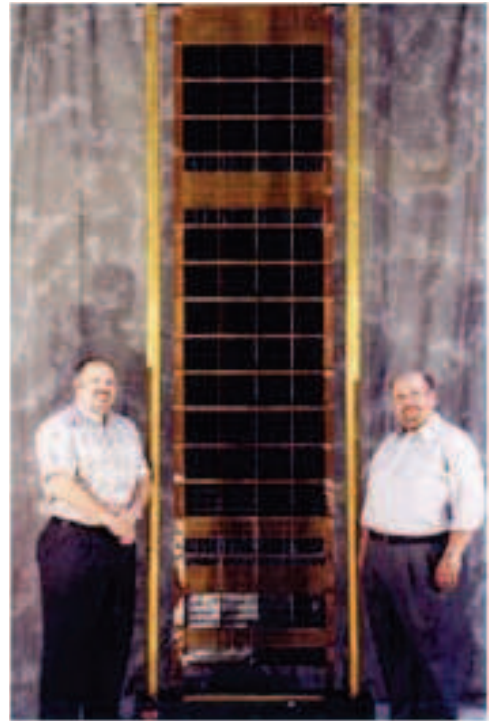
Figure 2.4: (a) NGST roll out sunshade technology demonstrator, with thermoset rigidizable crucifix supports [16].
 (b) Inflatable/Rigidizable sunshade support structure [10].

exist for both large and small solar arrays. L’Garde, Inc. has developed a 500W array, shown in Figure 2.5 (b), that boasts a stowed volume of 0.04m^3 and a power density of $109 \frac{\text{W}}{\text{kg}}$ [20]. ILC Dover has developed a $3 \times 10\text{m}$ 6000W array, but packaging information is not readily available. Rough scaling from the Figure 2.5 (a) seems to indicate it collapses into a box approximately $3\text{m} \times 0.3\text{m} \times 0.3\text{m}$, or 0.27m^3 . The L’Garde array is ideal for smaller satellites, and the ILC Dover array was designed for a constellation of low earth orbiting communications satellites.

2.1.1.2 Future Applications of Inflatable Rigidizable Structures. NASA, the DoD, and the aerospace industry have set their sights on future inflatable/rigidizable space structures. Larger aperture optics assemblies, inflatable/rigidizable SAR antennas, and components to a space hotel have all already been mentioned. Solar sails, communication systems, planetary exploratory rovers, and solar concentrators are also being researched.



(a)



(b)

Figure 2.5: (a) ILC Dover, Inc. roll out solar array technology demonstrator for the Teledesic communications satellite program [16].

(b) L’Garde, Inc. inflatable/Rigidizable solar array for small satellites [19].

Inflatable space reflector antennas show promise for improving all aspects of performance. The lightweight and low stowed volume characteristics of inflatables would allow larger reflector arrays, which would in turn increase data rates and reception sensitivity. This technology would be well suited to small satellites (along with the L’Garde solar arrays); engineers envision a 1-3m inflatable radio frequency reflector with a conventional feed horn [35]. Such a system could weigh less than 3kg and be stowed in a 0.1m X 0.1m box. Growing this data transmission system an order of magnitude would allow a deep space mission a high data rate antenna that synergistically doubled as a solar concentrator. This would allow for solar-powered deep space missions, alleviating public concern over the perceived danger of launching the nuclear power sources deep space missions typically require.

Solar sails have long been recognized as one of the most efficient space propulsion methods. Propulsion is provided by solar protons impacting the deployable sail and

transferring momentum to the spacecraft. The sail eliminates needs for onboard propulsion mechanisms and the associated fuel, saving room for mission payloads. A large enough solar sail could significantly shorten the interplanetary travel times via small but continuous acceleration. Solar sail technology development is highly analogous to the solar shade and large solar concentrator efforts [18].

Thus far, the predominant role for inflatables in planetary exploration has been impact attenuation systems, such as giant airbags surrounding planetary landers. NASA's Jet Propulsion Laboratory has created a planetary rover that rides on large, inflated spherical wheels. Capable of driving tens of kilometers a day, this rover could traverse over small to medium rocks, rather than around them. The increased ground contact surface area would make steep hills and large rocks easier to negotiate, and would provide increased wind storm protection. In a terrestrial application, this technology is also being looked at as a means to clear active land mines.

2.1.2 Previous RIGEX Efforts. For 8 years, 13 students and 2 summer interns designed, built, and space qualified RIGEX. Given only a set of deployed and stowed tubes, these students successfully tackled a technology demonstration experiment as an educational project. Figure 2.6 presents a student timeline with associated research summaries, but does not include the summer interns Maddux and Ponziani.

The following sections break the timeline up into three phases: Early Years, Refining the Design, and Assembly, Integration, and Space Qualification. The work done by each of the students is summarized in the appropriate phase. This thesis picks up at the conclusion of the Assembly, Integration, and Space Qualification phase.

2.1.2.1 The Early Years. RIGEX begins with John D. DiSebastion III [7], a systems engineering master's student. DiSebastion first reviewed the multitude of system engineering processes utilized in spacecraft design, and settled on NASA's system engineering process. NASA's process was chosen because it provided the most applicable framework, and because the experiment was slated to fly on the space shuttle. He developed the mission statement, as well as the primary and secondary objectives, and continued by selecting components and integrating them into a preliminary design

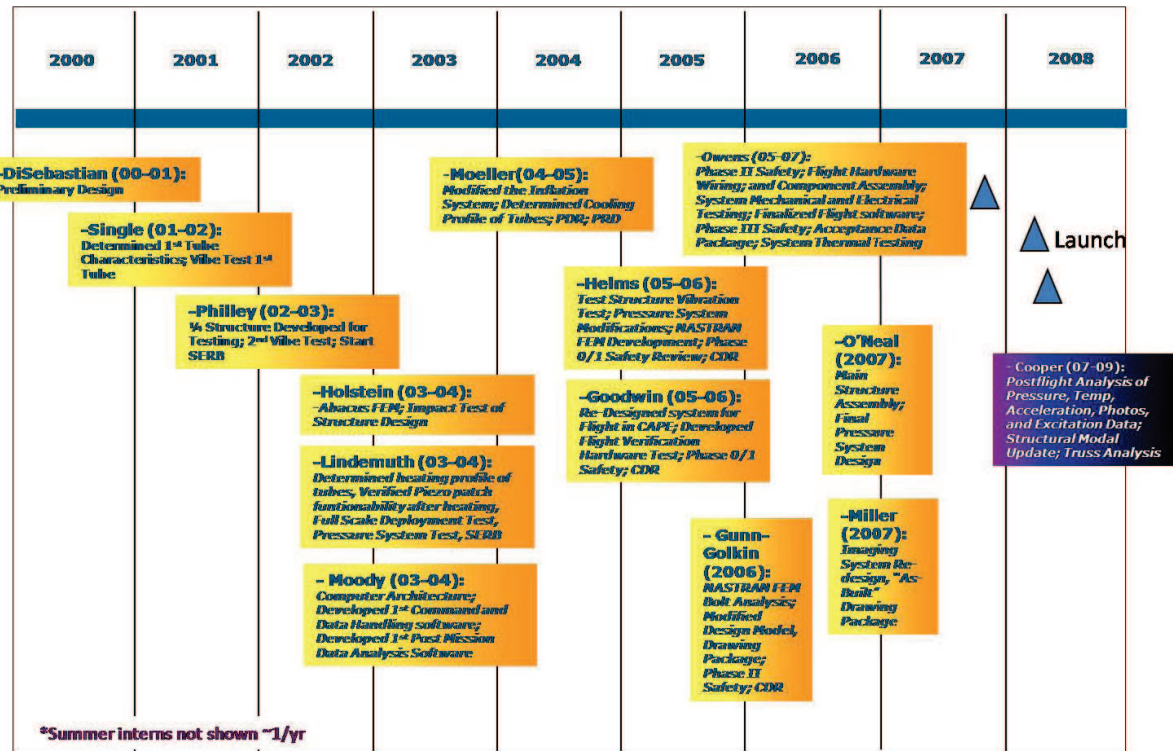


Figure 2.6: RIGEX timeline showing student activities.

layout. Using the selected components, DiSebastion created a weight and cost estimate and concluded by developing an operations concept and main event calendar.

Thomas G. Single [37] was the second student to contribute to RIGEX. An astronautical engineering master's student, he conducted modal response analysis testing on the first sample tubes provided to AFIT. Using 20-inch (similar to the flight articles) and 50-inch tubes, Single split his vibration response testing and modal analysis into three domains: ambient condition testing with shaker table inputs, ambient condition testing with Piezoelectric Transducers (PZT) inputs, and vacuum chamber testing with PZT inputs. Using both accelerometers and laser vibrometers, Single arrived at fairly consistent results for the ambient testing for deployed tubes (Table 2.2) and determined that while increased tube temperature shifted natural frequency to slightly lower frequencies as expected, internal pressure did little to change the natural frequencies.

Thomas L. Philly [33], another astronautical engineering master's student, was the third RIGEX student. Philly concentrated on developing a RIGEX prototype, conducting vibration response and modal analysis on the second delivery of tubes, and beginning

Table 2.2: Single's results for the first three natural frequencies of a 20 inch tube. [37]

Mode	Ambient PZT Driving (Hz)	Ambient Shaker Driving (Hz)
1st Bending	32	33
1st Torsional	63	63
2nd Bending	229	231

coordination with the DoD Space Test Program (STP). The vacuum chamber's limited size forced Philly to build a prototype which consisted of only one bay (the original design called for four bays and a center column for batteries and the inflation system), which was referred to as the "quarter section" and is shown in Figure 2.7. Philly conducted tube deployment tests using Kapton-covered tubes and the prototype oven and inflation system. These tests validated the heating and inflation systems and indicated the tube deployment process was relatively insensitive to inflation pressure. Philley's modal analysis results are presented in Table 2.3. The second batch of tubes demonstrated higher natural frequencies, attributed to the increased manufacturing quality.

The next three students worked simultaneously on RIGEX, wrapping up this phase of RIGEX development. The first student discussed is Raymond G. Holstein [15], the third astronautical engineering master's student to work on RIGEX. Holstein focused on conducting FEA on the rigidized tubes and the design of the RIGEX support structure. Using Philley's vibration response and modal analysis results and the results of his own vibration response testing (via ping testing) of a tube and the quarter structure, Holstein tuned models of a tube and the quarter structure to determine the Finite Element software's capability to match experimental data. Once confident in the results from the tube and quarter structure model, Holstein conducted an eigenvalue and stress analysis of the then current configuration of the RIGEX support structure to verify the structure

Table 2.3: Philley's modal response analysis results for the second set of tubes. [33]

Mode	Ambient Quarter Structure (Hz)	Vacuum Quarter Structure (Hz)
1st Bending	62.75	60.625
1st Torsional	236.5	235.9375
2nd Bending	654.0	651.25



Figure 2.7: Photo of the quarter section. The prototype of the final pressurization system and oven latch design are shown.

met NASA's ultimate strength requirements. When analyzing the 20g loading case, he found unacceptable stress concentrations which led to the removal of a computer access hole and increasing the thickness of the top plate.

Steven N. Lindemuth [22] was a space systems master's student, and focused on refining the initial heating and inflation system designs. Lindemuth first conducted a heating profile test on a flight-representative Kapton covered tube. Using multiple thermocouples at various locations (see Section 3.1.1 and Figure 3.3 for more detail), he was able to determine the ideal thermocouple locations and an approximate time required for a tube to reach T_g . Next, Lindemuth verified the ability of the flight model PZT and bonding material to survive the heating process. He did this by heating a tube with a PZT attached to 170°C (20°C margin of safety) and then verifying the PZT functionality after the tube had cooled. Finally, Lindemuth conducted a long term pressure retention test on the then current inflation system configuration. His results

indicated that the inflation system would maintain enough pressure to sustain a 90 day launch delay. These results also led to suggestions for inflation system improvements, which were later incorporated.

David C. Moody [29] was the final student of the first phase. An electrical engineering master's student, he made great strides in designing the computer system and developing flight software. First, he split the original computer configuration into two PC-104 computers, one for data acquisition and the other for the imaging system. To prevent data aliasing, Moody placed an eighth-order Butterworth filter after the digital chirp input passed through a Digital to Analog Converter (DAC), discussed further in Sections 3.1.3.3 and 4.1.3.3. Having completed development of the computer configuration, he developed a complete wiring diagram. He then turned his energy to the flight and the analysis codes. While developing the flight code, Moody altered the timeline to conduct the experiment one tube at a time. With the conclusion of Moody's work, the design was ready to move to flight hardware.

2.1.2.2 Refining the Design. At this point, it is important to note NASA's decision to disband the GAS canister and move to the CAPE. This was a significant event, and while it led to a significant amount of redesign, RIGEX benefited from the CAPE's increased weight and volume allowance - the CAPE allowed 75% more weight and double the volume. Even better, the CAPE canisters offered experiments the flexibility to use power from the Space Shuttle. For RIGEX, this translated to the elimination of 80 pounds of batteries that were previously required to power the experiment (and freed up valuable internal space). Figure 2.8 shows one of the eight battery stacks that RIGEX had required when shuttle power had not been an option.

Chad R. Moeller [28] begins the second phase of the timeline. An astronautical engineering master's student, Moeller was the first student to contend with the CAPE transition. Moeller tackled the inflation system and picked up where Lindemuth had left off. With the switch to the CAPE, the batteries no longer filled the center cavity, and Moeller moved the inflation system to fill the center cavity. The increased volume allocations allowed a switch from one small high pressure tank to three larger low pres-

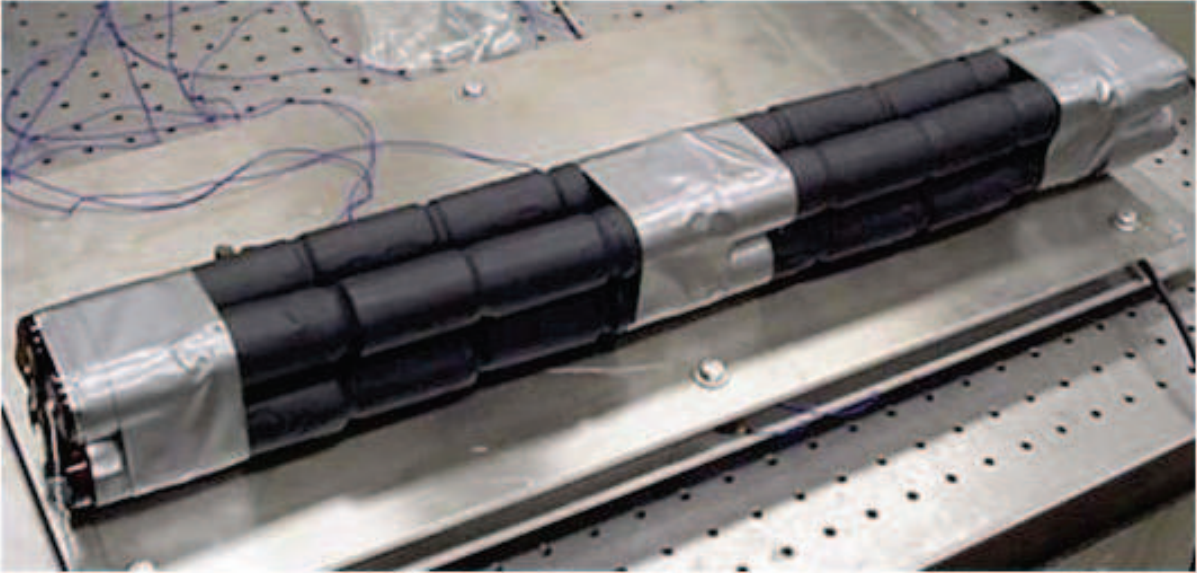


Figure 2.8: One of the eight battery stacks RIGEX required before the CAPE transition. The weight and volume required for these battery packs had previously been a major risk item [28].

sure tanks, which dramatically increased the reliability of the inflation system. Moeller essentially eliminated the potential for leaks by eliminating the need for a pressure regulator and pressure relief valve by pressurizing the large tanks to ambient. RIGEX could now sit for years on the launch pad and still maintain the pressure necessary to inflate the tubes. Moeller concluded his work by studying the cooling profile of the tubes. This was necessary to understand the time required for the tubes to rigidize before venting the inflation pressure.

Sarah K. Helms [14], the fifth astronautical engineering master's student to work on RIGEX, focused her efforts on three main tasks: the Space Shuttle integration process, vibration testing of an oven assembly, and development and application of the RIGEX structural model. Helms (and Goodwin) successfully completed the first milestones of the RIGEX launch integration process – the RIGEX Preliminary Design Review and Phase 0 & I Safety Review. Next, she attempted to verify structural integrity of the RIGEX oven assemblies and support structure through random vibration testing of a prototype oven and the RIGEX engineering model. Structural verification for the prototype ovens was achieved, but the engineering model failed due to seven bolts shearing. Moving on to the RIGEX structural flight model, she tested vibration response and created and

validated a FE model of the flight model. Initial analysis of the validated model began the process of structural verification necessary to meet NASA launch requirements.

Jeremy S. Goodwin [11], another astronautical engineering master's student, developed the first complete detailed RIGEX design drawings. His efforts included resizing the structure to better fit CAPE requirements, including implementing structural changes suggested by Helms and Holstein and adding a containment shroud. The containment shroud was a result of a containment analysis using methods developed by NASA. Goodwin moved RIGEX from battery to Space Shuttle power and updated Moody's electrical architecture. Finally, he worked on the tube vibration response testing and modal analysis. Goodwin changed the accelerometers from the large accelerometers used by Moody to the KXPA4 (see Section 3.1.3), increased the excitation amplitude by a power of 3, and updated the analysis code to use the recorded input signal as opposed to the mathematical idealized signal.

Anna E. Gunn-Golkin [13], the seventh RIGEX astronautical engineering master's student, wraps up the second phase of RIGEX development. Gunn-Golkin updated Goodwin's RIGEX detailed design by incorporating further changes and then conducted a comprehensive detailed FEA (based on her most recent detailed design) on RIGEX and the fasteners. Her FEA results indicated the first natural frequency was 185Hz. Continuing on to a static stress analysis, she developed an acceptable bolt pattern and bolt torque tolerances. Having met the NASA structural requirements, the protoflight unit could be constructed based on Gunn-Golkin's final detailed design drawings. Figure 2.9 shows RIGEX installed into the CAPE, one of Gunn-Golkin's detailed drawings.

2.1.2.3 Assembly, Integration, and Space Qualification. Brady O'Neal [30], a Navy aeronautical engineering master's student, begins the final phase of the timeline. O'Neal identified the necessary NASA documentation within the NASA documentation tree required for space worthiness validation, and how RIGEX would fulfill those requirements. He then details the mechanical construction of the protoflight unit and problems encountered during the iterative process. Finally, he details the plans necessary to finish space qualification through vacuum chamber and vibration testing.

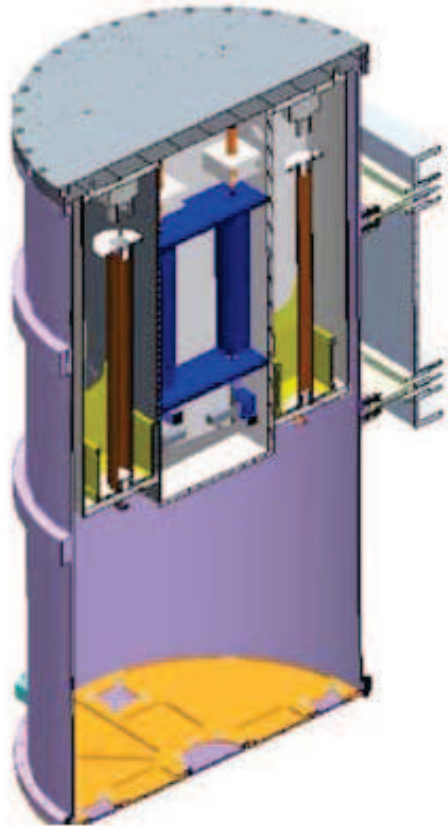


Figure 2.9: Cutaway drawing of RIGEX installed into the CAPE. Note Bay 1 and Bay 3 symmetry, and the center volume filled with large, low pressure tanks [13].

Zachery R. Miller [27], another Navy aeronautical engineering master's student, worked simultaneously with O'Neal and Jeremy Owens. Miller helped with construction procedures, handling instructions, and completed the final "as built" detailed drawings. Focusing on the inflation system, he wrote the procedures for testing the system and charging the pressure tanks. He then turned to reworking the obsolete imaging system by updating to smaller cameras that could handle the space environment. The cameras were programmable - when provided with a power source, the stand alone cameras took pictures at an assigned rate.

Jeremy J. Owens [31] an astronautical engineering master's student, concludes this final phase of RIGEX development. The culmination of Owens' work was all of the documentation necessary to turn RIGEX over to NASA for integration into the *Endeavour's* payload bay. He attacked the herculean task of completing all of the assembly, testing, verification, and qualification tasks, and finished the final integration. Beginning with

component level integration, he tested the operability and survivability of the heating system, imaging system, and solid state relays. After conducting the runaway heater test he moved on to system level testing, verifying the inflation system met over-pressure and leak requirements. He then conducted a flight representative tube deployment test using the flight hardware and the thermal vacuum. The next step was integration with the CAPE for certification Electro-Magnetic Interference, Vibration, and Weight and Balance testing. Owens' end product was an experiment ready for a ride to space.

2.2 RIGEX Overview

This section provides a high level overview of RIGEX, including the physical characteristics of the inflatable/rigidizable tubes and an overview of the experiment itself. For more detailed information regarding the final RIGEX configuration, the reader is encouraged to review Owens [31] and Miller [27].

2.2.1 L’Garde, Inc. Inflatable Rigidizable Tubes. L’Garde, Inc. manufactured several sets of tubes for RIGEX. Designed with a specific T_g temperature of 125°C, the tubes were manufactured from a proprietary material and resin; therefore only physically measurable properties are known. Table 2.4 provides measured physical properties of the tubes.

Section 4.4.1 provides the moment of inertia calculations and also calculations for rough estimates of Young’s modulus, using the fundamental frequency equation. Figure

Table 2.4: Physical properties and dimensions of the tubes. [37]

Property Description	Value
Aluminum Base Flange Mass	0.074kg
Aluminum Tip Flange Mass	0.0746kg
Aluminum Flange Outer Diameter	3 inches, 0.0762m
Beam Material Thickness	0.015 inches, 0.000381m
Beam Total Mass	0.24kg
Beam Material Density	$8.64 \times 10^2 \frac{\text{kg}}{\text{m}^3}$
Beam Outer Diameter	1.5 inches, 0.0381m
Beam Moment of Inertia	$8.030 \times 10^{-9} \text{m}^4$
Beam Length	20 inches, 0.508m



Figure 2.10: (a) Example tubes in z-fold and deployed configuration [31].
 (b) Coordinate system used to analyze tube characteristics.

2.10 (a) first shows two example tubes collapsed in a z-fold configuration, and then an example deployed tube. The tubes are covered in Kapton tape to protect the carbon fibers and resin from the space environment. Figure 2.10 (b) shows the tube centered coordinate system.

2.2.2 Final RIGEX Configuration. RIGEX consists of a cylinder based structure divided into four bays and a center volume. Three of the bays contain the inflatable/rigidizable experiments, and the fourth bay contains the computer, power input, and solid state relays. The center volume contains the three large, low pressure tanks used to store the inflation gas. The top plate mounts to the top of the CAPE canister, as seen in Figure 2.9. The bottom plate provides the mounting platform for the tubes, ovens, and the computer. The inflation system piping runs down from the storage tanks, through the bottom plate, and then over to the tube mounting location. Though not the final configuration, Figure 2.11 is a very descriptive visual overview of RIGEX.

On orbit, RIGEX operation begins with boot-up and a functional verification phase, tests each bay individually, and then powers down after clearing the memory of unnecessary data. Each bay follows the same process for testing: heater activation followed by

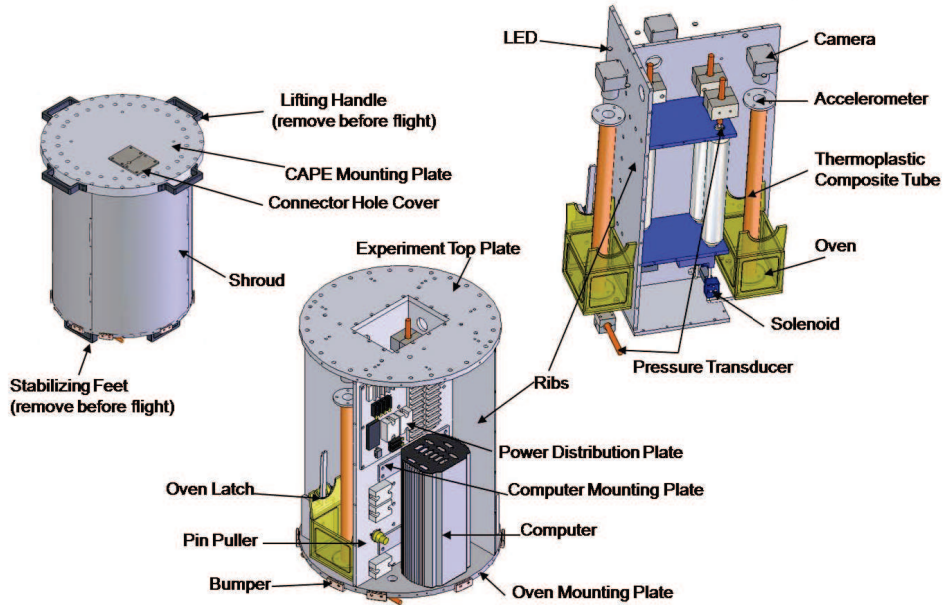


Figure 2.11: Gunn-Golkin’s notional drawing of the complete RIGEX configuration [13].

the tube deployment process and vibration testing. This process is discussed in greater detail in Section 3.1 and a timeline is presented visually in Figure 3.2.

2.3 Theory Review

This section presents a modal response analysis and finite element modeling theory review. These two topics were chosen as they represent the background behind the majority of the analysis effort. The primary references for the theory development below are class notes from Cobb [4] and Swenson [40]. Beyond the review conducted in this thesis, Single [37] and Goodwin [11] both present vibration and modal testing theory, and Holstein [15] and Helms [14] present FEA theory.

2.3.1 Vibration Response and Modal Analysis. The majority of testing associated with RIGEX is vibration testing. The purpose of this testing is to develop an understanding of a structure’s response as it is subjected to a variety of inputs. The modal properties of structures are often performance limitations, thus the vibration response for large space structures needs to be understood and controlled. This is particularly true for missions which require precise and accurate pointing and shape control.

Modal analysis is defined as the study of the dynamic characteristics of a mechanical structure. These dynamic characteristics consist of mode shapes, damping, and structural natural frequencies [17]. Structural natural frequencies are the frequencies at which structures exhibit amplified response (resonance) to harmonic inputs. Mode shapes are shapes that describe the motion of a structure at specific structural natural frequencies, and are mathematically represented by orthogonal vectors. There are two goals of the vibration response testing and modal analysis: generate frequency response functions (FRF), which represent the steady-state response over input for a range of frequencies, and to extract the natural frequencies and accompanying mode shapes from the FRFs.

Although all real systems are continuous, it is common to model their behavior discretely. Figure 2.12 presents a spring mass damper model with which the theory derivation starts. The equation of motion for a single degree of freedom system is given by Equation 2.1:

$$m\ddot{x}(t) + c\dot{x}(t) + kx(t) = F(t) \quad (2.1)$$

where

m = Mass

c = Damping Coefficient

k = Spring Constant

$F(t)$ = Forcing Function

$x(t)$ = Displacement Response

$\dot{x}(t)$ = Velocity Response

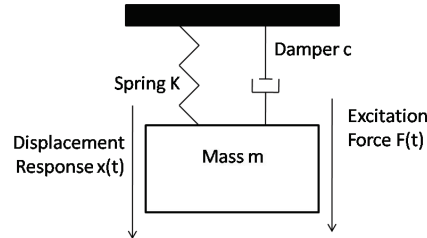


Figure 2.12: Discrete system consisting of a mass, spring, and damper.

$$\ddot{x}(t) = \text{Acceleration Response}$$

If one assumes $F(t)$ is a harmonic driving function, the solution can be written as:

$$x(t) = A\sin(\omega_n t - \phi) \quad (2.2)$$

where ω_n is the natural frequency, with units of $\frac{\text{rad}}{\text{s}}$. Natural frequency in Hertz is f_n . The natural frequency is a function of the spring constant k , and mass m :

$$\omega_n = \sqrt{\frac{k}{m}} = 2\pi f_n \quad (2.3)$$

The next step is transform this time domain equation into a frequency domain equation using the Laplace Transform of Equation 2.1, resulting in Equation 2.4:

$$(ms^2 + cs + k)X(s) = F(s) \quad (2.4)$$

where $X(s)$ is the Laplace Transform of the displacement measurement, or the frequency domain output, and $F(s)$ is the Laplace Transform of the harmonic driving function, or the frequency domain input. The Laplace Transform variable, s , is a complex number, and maps time domain functions into the complex frequency domain through $s = \sigma + j\omega$, where σ is the damping component, ω is the radian frequency and j is defined as:

$$j = \sqrt{-1} \quad (2.5)$$

Rearranging Equation 2.4 yields an equation that relates output and input, known as the transfer function, $H(s)$:

$$H(s) = \frac{X(s)}{F(s)} = \frac{1}{(ms^2 + cs + k)} \quad (2.6)$$

This transfer function allows easy computation of the steady-state system response magnitude and phase for a given input frequency, the definition of the FRF. Peaks in an FRF magnitude plot indicate increased steady-state response to oscillating inputs; the

location of these peaks in terms of frequency are the natural frequencies of the system under test.

Unfortunately, the underlying differential equations for real systems are often unknown and thus an alternate method is necessary to find the FRF; vibration testing is one such method [4]. As Equation 2.6 shows, FRFs can be measured by dividing the output (response) by the input. There are two approaches to vibration testing - time domain and frequency domain. If done correctly, both methods can yield acceptable data. RIGEX used the frequency domain method for vibration testing and modal analysis, and thus further review of the theory is necessary.

The discussion on frequency domain testing begins with a broad frequency band input, such as a chirp signal or white noise. The measured output time history is recorded at a given sample rate. The sample rate should be at least twice the highest frequency of interest to ensure all data is collected. Most spectral analyzers include a filter just prior to the data sampler to combat aliasing, a phenomena of digital sampling which can misrepresent frequency content of a given signal. As an aside, data aliasing drove Moody [29] to include an eight-order Butterworth filter in the data acquisition architecture, though Moody placed the filter after the digital output generator, after the D/A converter, as opposed to before the A/D converter on the sampling side.

The next step of the frequency domain technique is to take the discrete Fourier Transform of both the output signal (response) and the input signal (excitation) time history. The Fourier Transform of an assumed periodic output signal time history is defined as:

$$X_k = \frac{1}{T} \sum_{r=0}^{N-1} x_r e^{-j \frac{2\pi k}{N} r \Delta} \quad (2.7)$$

where

$$k = k^{\text{th}} \text{ harmonic of sampling frequency}$$

$$T = \text{Period of data block}$$

$$r = r^{\text{th}} \text{ sample of data block}$$

$$N = \text{Block size of data}$$

$$x_r = r^{\text{th}} \text{ sampled time history value } (x(t))$$

Δ = Sampling period

X_k = Fourier Transform of time history (k^{th} element)

Y_k , the Fourier Transform of the input signal time history, is similarly derived. Note that the notation has now changed; $x(t)$ now represents the input and $y(t)$ represents the output. The auto power spectral density is defined as the multiplication of a signal's discrete Fourier Transform and its complex conjugate; the cross power spectral density is defined as the multiplication of a signal's discrete Fourier Transform and another signal's discrete Fourier Transform. If the signals are completely unrelated, the cross power spectral density will be zero, and if a signal is purely real, its auto spectral density will be one. The auto and cross spectral densities are given by:

$$S_{xx}(\omega_k) = X_k * \text{conj}(X_k) \quad (2.8)$$

$$S_{yy}(\omega_k) = Y_k * \text{conj}(Y_k) \quad (2.9)$$

$$S_{xy}(\omega_k) = X_k * \text{conj}(Y_k) \quad (2.10)$$

where

$S_{xx}(\omega_k)$ = Input Auto Power Spectral Density

$S_{yy}(\omega_k)$ = Output Auto Power Spectral Density

$S_{xy}(\omega_k)$ = Input/Output Cross Power Spectral Density

The transfer functions, or steady state relationship of output over input, are related through the following equations:

$$H_1 = \frac{S_{xy_k}(\omega)}{S_{xx_k}(\omega)} \quad (2.11)$$

$$H_2 = \frac{S_{yy_k}(\omega)}{S_{yx_k}(\omega)} \quad (2.12)$$

H_1 and H_2 are the two kinds of FRFs. H_1 is sensitive to input noise and insensitive to output noise, and it provides the lower magnitude bound. H_2 is sensitive to output noise and insensitive to input noise, and it provides the upper magnitude. Either transfer function is acceptable when presenting data, however they are both used to calculate the

coherence, $\gamma^2(\omega)$ from the averaged values of $S_{xx}(\omega_k)$, $S_{yy}(\omega_k)$, and $S_{xy}(\omega_k)$. Coherence is a measure of how the output is linearly related to the output; it is essentially a data “goodness” function. Coherence is given by Equation 2.13

$$\gamma^2(\omega) = \frac{H_1(\omega)}{H_2(\omega)} \quad (2.13)$$

Coherence values range from 0 to 1; values below 0.8 (with the exception of natural frequencies) indicate suspect data. There are several reasons for low coherence values: nonlinear structures, digital filter leakage, time delays on the signals, and uncorrelated noise. Typically, coherence will present as phase data presents; noisy phase data indicates poor coherence [4].

The research presented in this thesis uses space and post space flight vibration testing to develop FRFs for each tube. These FRFs are developed through the methods described above and the test procedures developed in Chapter 3.

2.3.2 Finite Element Modeling. The finite element method is a numerical approach for simulating real structures [40]. The FE method is used to solve for dynamic characteristics analytically by combining and solving the equations of motion (Equation 2.14) for a structure broken up into many finite elements. A finite element can be thought of as a small piece of a structure that has simple spatial variation and is connected to other finite elements through nodes. The arrangement of the elements is called the mesh, and an example mesh is shown in Figure 2.13. Each element can be thought of as an approximation of a spring mass damper system, similar to that shown in Figure 2.12. The unknown field quantities are solved by the equations of motion at the nodes for each element. For the results presented, the nodes represent displacement in the three translational degrees of freedom. While classical techniques can solve simple geometry vibration response problems, the FE method is used on models with complex geometry. FEA works by breaking down a complex problem into many smaller, easier problems, and then using a computer to solve all of the smaller problems simultaneously.

A FE model can be as simple as one element with two nodes, but often are much more complicated. The accuracy of the solution is dependent on the validity of as-

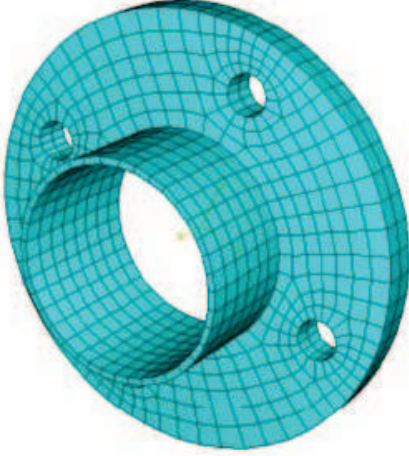


Figure 2.13: Example Finite Element mesh over a tube base flange [15].

sumptions and on the modeling characteristics such as type of elements used and the mesh density. FEA begins with the equations of motion for each element, which can be likened to Equation 2.1 (without the damper), and then “stacking” the equations of motion by aligning the nodes for each element and then removing the degrees of freedom that are constrained by boundary conditions. This will yield an equation of motion for each degree of freedom at each node with stiffness and mass matrices associated with displacement $\{x\}$ and acceleration $\{\ddot{x}\}$ vectors:

$$[M]\{\ddot{x}\} + [K]\{x\} = \{0\} \quad (2.14)$$

where $[M]$ and $[K]$ are the mass and stiffness matrices. After creating these matrices, the FEA software solves the following eigenvalue problem to determine natural frequencies (ω_n^2 , eigenvalues) and mode shapes ($\{\phi\}$, eigenvectors):

$$[[K] - \omega_n^2[M]]\{\phi\} = 0 \quad (2.15)$$

The research presented in this thesis will use Nastran and the Finite Element Model Analysis Program (FEMAP) to update existing tube FE models and perform the eigenvalue analysis. The FE models will then be tuned to match observed vibration behavior

and then applied in large space structures to quantify the advantage of using inflatable/- rigidizable tubes over the current mechanical technology.

III. Test Methodology

THIS chapter describes the testing methodology used on-orbit, on the ground, and in finite element models. Space flight testing was comprised of temperature, pressure, displacement, and vibration response tests. On the ground, testing was split into 2 phases: post space flight testing and ground testing. Post space flight testing centered on repeating the space flight vibration response tests and conducting modal analysis for comparison to the space flight test results. Ground testing first focused on repeating the vibration response testing with higher fidelity equipment and commercial modal analysis software, and then developing a 3-D spatial model of the deployed tubes using a precision contact measurement device. The chapter ends by discussing the modeling techniques used in updating a finely meshed tube FE model, creating a coarse tube FE model, and constructing large structures using the coarse FE models. This test hierarchy is shown in Figure 3.1.

3.1 Space Flight Testing

Designed as a space flight experiment from the beginning, RIGEX was built to meet objectives set by DiSebastion [7] and then expanded on by Goodwin [11] laid out in Section 1.2. In short, RIGEX was designed to verify and validate ground testing of inflation and rigidization methods (for inflatable space structures) in a space environment. To do this, RIGEX was built as a CAPE experiment which allowed tube deployment and vibration testing in the space environment onboard the *Endeavour* in March 2008.

The flight computer autonomously conducted the testing necessary to gather the data which meets these objectives. The specific space flight testing and data collection can be broken into four primary categories: temperature, pressure, modal, and imaging. Figure 3.2 shows the overall timeline for space flight testing as conducted by the final flight code version found in Appendix C. Each file recorded by the flight computer is saved in a **.dat* file.

3.1.1 Temperature. For sub- T_g inflatable/rigidizable tubes, the deployment process can be split into two steps. The first step is to heat a stowed tube beyond the

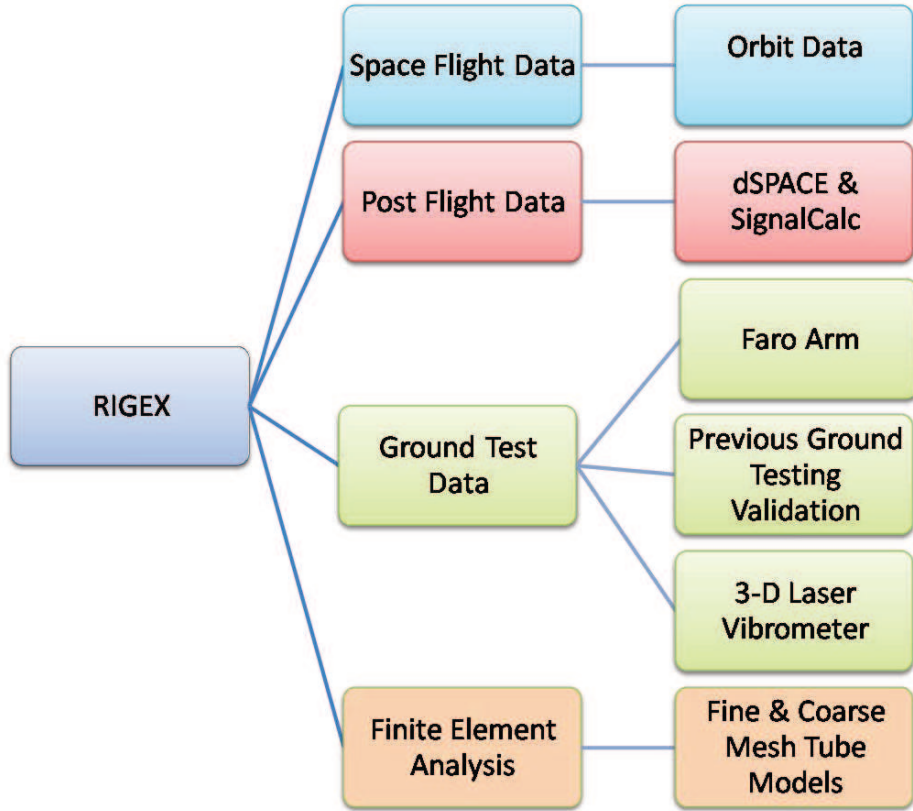


Figure 3.1: RIGEX hierarchy for test methodology.

glass transition temperature (T_g is a variable set in the manufacturing process, but for RIGEX, T_g was set at 125°C). After warming beyond T_g the tube becomes pliable and can then be inflated by pressurized gas. The tube temperature is extremely important during the heating process - incomplete deployment and performance degradation are very real prospects if the inflation process begins before the entire tube is warmed beyond T_g .

From the tube perspective, inflation of a partially flexible tube would deploy asymmetrically at best; at worst the tube would not deploy at all. From an experiment perspective, if the ovens don't shut down after the tube reaches its transition temperature it could lead to electrical damage to the rest of the experiment or a fire - either result is unacceptable. Consider a future system designed to deploy multiple tubes through the same ovens – overheating wastes valuable energy and could lead to oven degradation.

For RIGEX, temperature data was routed through the eight channel MSI-P440 thermocouple board in the flight computer stack. Each flight tube had two thermocou-

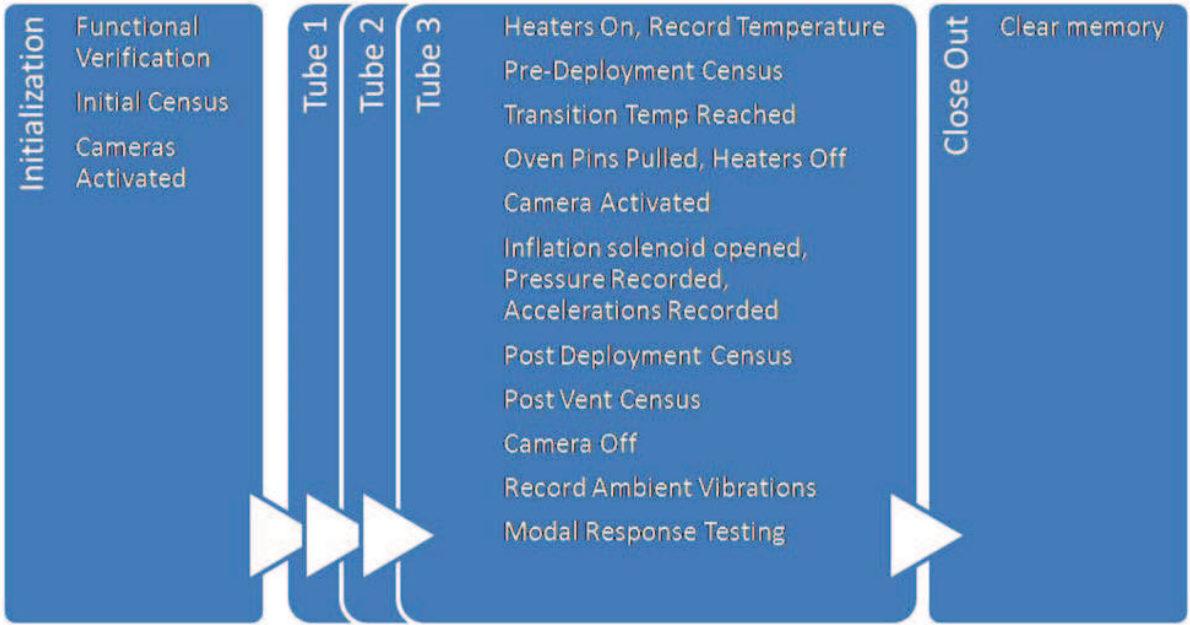


Figure 3.2: Overall space flight testing timeline.

ples, these thermocouples accounted for six of the eight channels on the board. The structural thermocouple accounted for the seventh, and the last channel which monitors the flight computer stack temperature was jumpered into itself to monitor computer stack temperature and provide self calibration.

3.1.1.1 Tube Thermocouples. Lindemuth [22] conducted tube heating profile tests to determine the best placement for the tube thermocouples. Figure 3.3 (a) shows the test locations; he argues location #2 is the most appropriate for thermocouple placement as it is partially protected from the top and side heaters by the top flange and location #4 (respectively) and therefore requires the longest time to heat. This argument is supported by his ambient and vacuum heating profile tests - location #2 consistently required more time to reach T_g than the other locations. One can therefore assume if location #2 has reached T_g , the rest of the tube has reached T_g as well and the tube is then ready for deployment.

In practice, only flight tube 2 (leftmost tube in Figure 3.3 (b)) had a thermocouple installed in location #2. As Figure 3.3 (b) shows, the folding of the flight tubes are not all identical. Flight tube 2's z-fold pattern, inflation cap, and end caps match Linde-

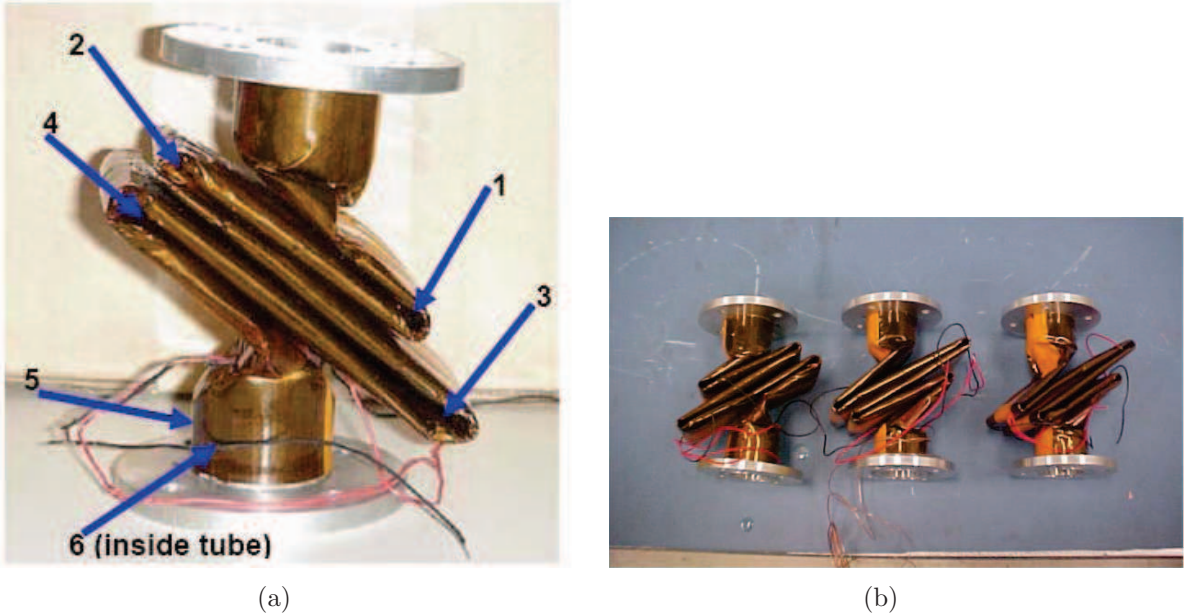


Figure 3.3: (a) Lindemuth's tube heating profile thermocouple locations [22]. (b) Flight tubes in z-fold configuration prior to installation in RIGEX. Note the leftmost tube's folds are 180° opposed to the other tubes. This tube is flight tube 2.

muth's tube used to test heating profiles. The other two tubes are flipped, a result of manufacturing the flight tubes by hand. While the bottom thermocouples are approximately in the same position on all three flight tubes, flight tube 2's top thermocouple is located approximately two inches below the other two tubes top thermocouple.

3.1.1.2 Structural and Thermocouple Board Temperature. The experiment structure and the flight computer temperature data was also collected. The structural temperature was collected by a thermocouple mounted in the computer bay attached to the bottom plate. This thermocouple provides the best representation possible of ambient conditions within the experiment. The computer stack temperature was monitored via the final thermocouple channel.

3.1.2 Pressure. Inflation is the second step in deploying the inflatable, rigidizable tubes, and can only be accomplished after the tubes have transitioned beyond T_g and become sufficiently pliable. The inflation system is just as critical to the successful deployment of the inflatable/rigidizable tubes as the temperature monitoring process. Without inflation pressure, there would simply be no deployment. DiSebastion [7], Phil-

ley [33], Lindemuth [22], Moeller [28], Helms [14], and O’Neal [30] all contributed to the inflation system design. In the end, the pressure system design utilized large nitrogen (N_2) reservoirs pressurized to ground ambient ($\sim 14\text{psi}$).

There were two types of pressure measurements during the course of on-orbit operation. The first was an instantaneous pressure census of the three reservoir and three tube pressure transducers; the second was monitoring the tube internal pressure for 5 seconds while the inflation solenoid was commanded open.

3.1.2.1 Instantaneous Pressure Census. The flight computer samples the six pressure transducer (three tube transducers, three reservoir transducers) readouts a total of ten times; once during the boot-up functional verification test at the beginning of the experiment and three times during each tube’s deployment and testing process. The first of the three pressure censuses occurs immediately after the heaters and LEDs are activated for each tube. For the particular tube being heated, this marks the last snapshot of the inflation reservoirs pressure before the inflation valve is opened. The next census occurs 300 seconds after the inflation solenoid has closed (Lindemuth’s [22] cooling profile tests indicated this would be ample time for the tube to rigidize in vacuum). This readout should indicate the tube and reservoir have approximately equalized pressure. Immediately following this census, the tube is vented to ambient through the inflation port. The final census occurs five seconds later, and should indicate a vacuum inside of the tube. Refer to Figure 3.2 for census occurrences.

3.1.2.2 Inflation pressure. When the flight computer establishes that both tube thermocouples are reading above 135°C or one of the tube thermocouple reads above 150°C , the flight computer commands the pin puller to pull the pin, unlocking the oven box. The flight code commands a one second pause, during which the tube begins to unfold – a manifestation of internal strain energy stored during the folding process. Next, the inflation solenoid is commanded open and the tube pressure transducer begins to record the inflation pressure. The computer records 5 seconds of pressure data at a 1000Hz sample rate. Ground inflation testing had demonstrated 5 seconds would be

ample time for complete deployment, and the 1000Hz sample rate help alleviate memory allocation limitations.

3.1.3 Accelerometer Based Testing. Accelerometer data collection begins with the deployment phase of the experiment. Each tube has an accelerometer mounted to the flange of the tube's top endcap, and the accelerometer is monitored three times:

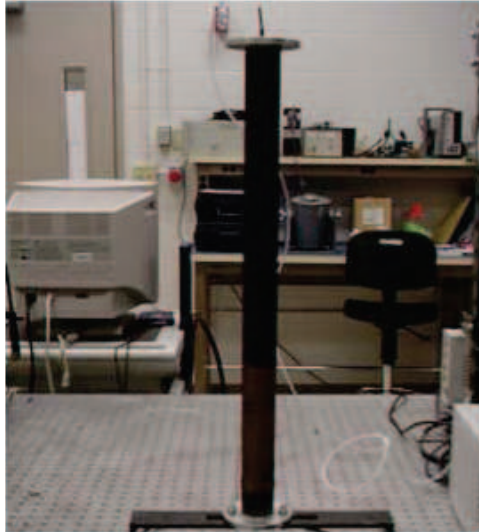
- During deployment, to track tube tip motion
- During an ambient data collection, to check both proper accelerometer function, ambient vibration environment, and the noise level
- During the vibration testing, to measure vibration response to the PZT input.

As discussed in Goodwin [11], the accelerometers are 5 volt Kionix KXPA4 triaxial accelerometers with a range of $\pm 2g$. The accelerometer's output voltage is passed through the Analog to Digital Converter (ADC) and the digital signal is recorded by the flight computer (PC-104) at 5000Hz, with the exception of the deployment data, which is sampled at 1000Hz.

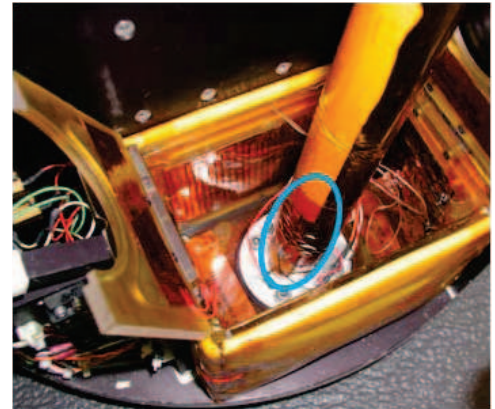
3.1.3.1 Deployment. When the tubes have reached T_g and the inflation solenoid is opened, the flight computer begins recording the endcap's accelerations during deployment for five seconds. The acceleration levels provide indication of how violent the deployment process was – one of the key lessons learned from the IAE was deployment must be controlled or the vehicle could depart from a controllable attitude. In addition, this data can (ideally) then be integrated twice to produce the precise route the tube endcap followed during deployment, similar to Moody's [29] efforts.

3.1.3.2 Ambient Accelerometer Measurements. Following the tube deployment and cooling/rigidizing period, the flight computer records five ambient accelerometer measurements one second in duration. These measurements were used to monitor the ambient environment and establish the noise level.

3.1.3.3 Vibration Testing. The vibration test wraps up the space flight testing for each tube. Beginning approximately 330 seconds after deployment, the testing



(a)



(b)

Figure 3.4: (a) A PZT (brown) mounted on an early tube (black) for Philley's vibration testing [33]. This PZT is larger than the PZTs mounted to flight tubes.
 (b) Flight tube with PZT (within the blue oval) mounted under Kapton. The red and black wires route the voltage to the PZT

consisted of 25 repetitions of a one second test. Developed by Moody [29] and Goodwin [11], the input was a 0 – 2000Hz chirp signal that is represented by Equation 3.1:

$$y(t) = \cos(2\pi(5 + (1000 - 5)t)t) \quad (3.1)$$

where $y(t)$ is the input voltage, and t is time. The chirp signal was digitally sampled at the flight computer's 5000Hz clock speed and passed through the DAC, the eighth order Butterworth filter, and a transformer which boosted the PZT input voltage to $\pm 5V$. For each one-second input, the flight computer recorded the X, Y, and Z accelerations reported by the accelerometer via the ADC. The flight computer saved the 5000 data points (one second of data sampled at 5000Hz) to *.dat file, opened a new file, and repeated the process. After 25 iterations had been completed, the flight computer advanced to the next tube. When all three tubes completed their testing, the on-orbit testing was complete. Figure 3.4 (a) shows an early PZT and tube setup and (b) shows a flight tube PZT.

3.1.4 Imaging. Each bay had a camera installed almost directly above the stowed tube. These cameras were programmed to begin autonomously taking photos when voltage was applied. Power was supplied at specific times throughout the experiment. During the initial functional verification, all three cameras were successively powered on and took an image. During the experiment, when a tube met the temperature criteria and the flight computer commanded the pin puller to activate, the camera was powered on and took images at 0.9 second intervals (the fastest rate) of the tube as it deployed. These “action photos” give a visual history of the manner in which the tubes deployed in the microgravity environment. Each tube was also imaged after the vibration testing was complete; this final on-orbit image provides a reference to the final deployed tube position.

On the ground, the cameras were powered on during post space flight testing to take pictures. These post space flight images provide an updated position reference of each tube following return to AFIT. This updated reference is necessary to conduct change detection analysis. Precise position and deployment error data of the deployed tube (on-orbit) can be determined by combining the flight images, post flight images, and the FaroArm testing discussed in Section 3.3.4. This process will help determine any tube position changes between space and ground – critical for future development of experiments or space structures which require joining multiple independently deployed tube truss structures.

3.2 Post Space Flight Vibration Testing

Post space flight test activities repeated the space flight vibration tests on the ground using the flight accelerometers, the RIGEX flight computer, the dSpace system as a flight computer surrogate, or the spectrum analyzer SignalCalc. These tests were conducted to determine the repeatability of the space flight vibration testing and begin the modal analysis effort. Figure 3.5 is an overview schematic showing the basic setup for the accelerometer-based post space flight vibration testing. The accelerometers and PZTs could use the flight computer or the dSpace and SignalCalc platform to generate the input.

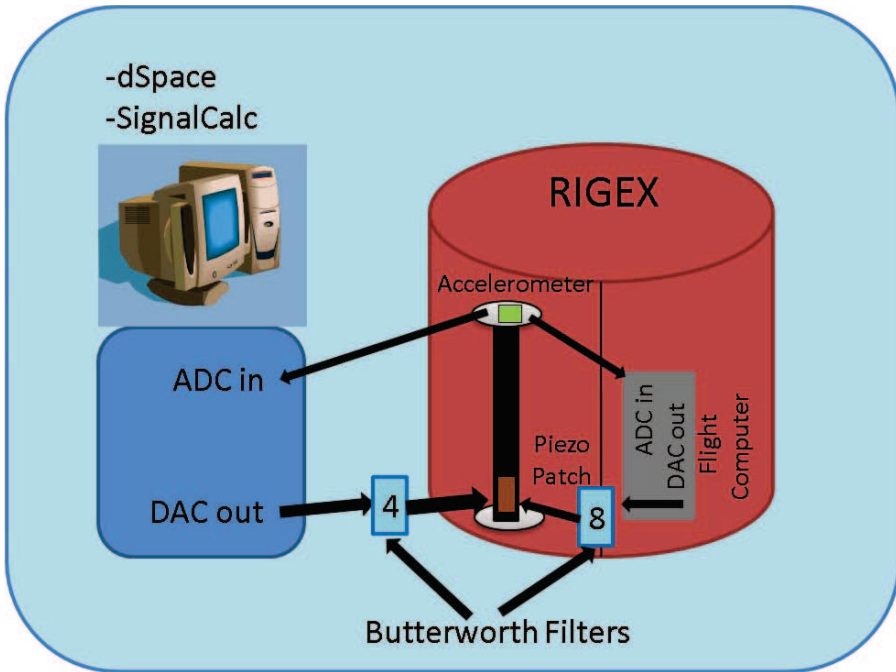


Figure 3.5: Schematic showing the basic test setup for the post flight vibration testing.

3.2.1 Flight Computer Testing. The objective of the flight computer post flight test was to determine the repeatability of the space flight vibration testing using the space flight hardware. Other than switching from shuttle power to the shuttle power emulator on the ground, this test used the exact flight configuration discussed above in Section 3.1.3.3.

3.2.2 dSpace Testing. The objective of the dSpace post space flight test was to determine the accuracy of the modal response data collected by the flight computer during both the space and post space flight tests, using dSpace as a surrogate flight computer. dSpace is a data acquisition hardware system which compiles MATLAB SimuLink *.mdl files and processes them at designated clock speeds. Moody [29] and Goodwin [11] utilized dSpace when designing the data acquisition computer system. Input signals and filters can be modeled in the SimuLink file, compiled, and then tested through dSpace rather than physically building the components and testing them. For the post space flight testing, dSpace was utilized because of the variable sample rate, which is set through the SimuLink model. The sampling rate was set to 5000Hz for direct comparison to the flight computer modal response tests.

SimuLink was used to generate the 0 – 2000Hz chirp output signal used in the space flight vibration response test and three inputs to record the triaxial accelerometer output. The output signal was routed through a DAC and then run through an external eighth order Butterworth filter, which output the filtered signal through a specially-created tube connector interface cable to excite the PZTs. A specially-created accelerometer interface cable connected the accelerometers through an ADC to dSpace, and the specially-created cable also connected to a power supply to provide voltage to the accelerometers. The cables plugged directly into the RIGEX’s existing 15 pin architecture, allowing dSpace to act as the surrogate flight computer.

After each test, the data is saved in a *.mat format for analysis in MATLAB.

3.2.2.1 SignalCalc Testing. SignalCalc was used simultaneously with the dSpace post space flight testing. This was done by splitting the PZT input signal and the accelerometer output signals and routing these signals into SignalCalc. The purpose for this redundant data collection is two-fold. First, this simultaneous data collect allows for the utilization of SignalCalc’s spectrum analyzer, which automatically processes the data and creates FRFs and coherence plots. Second, SignalCalc processes the data received through each channel’s ADC much faster than dSpace’s prescribed 5000Hz. This data is then exported to MATLAB for side by side comparison with the 5000Hz dSpace and Flight Computer data.

3.3 *Ground Testing*

Ground testing used more sophisticated testing hardware and methodology to develop the “truth” which could then be used for comparison purposes. Laser vibrometers are the primary measurement tool used in ground testing. Laser vibrometers are a non-contact instrument, and measure surface vibration velocity (in the direction of the laser beam only) through doppler shift. A laser vibrometer’s primary benefit is non-contact measurement. This avoids the undesirable mass-loading effects of traditional accelerometers and their associated cables, which can appreciably affect dynamic response due to added mass, stiffness, and damping [32].

3.3.1 Validation of Previous Ground Testing. Single [37], Holstein [15], Philley [33], Moody [29], and Goodwin [11] all completed some form of vibration testing and modal analysis on deployed tubes. Their pre-space flight testing defined the envelope for the space flight vibration tests and formed the underlying basis for all of the comparison analysis. Functionally, the pre-space flight testing verified the capability of the system (PC-104 computer, Butterworth filter, DAC, PZTs, ADC, and the Kionix Accelerometers) to conduct the vibration response tests. Tubes tested in pre-flight vibration testing were retested for two reasons:

- To validate the previous students' findings
- To verify the connection of the new ground cables to ground test equipment does not alter test results

Here, three previously deployed (early samples) tubes with PZTs attached were retested. Two tubes were similar in nature to the preflight ground test setup pictures shown in Single [37], Philley [33], and Goodwin [11], and the third tube was covered in Kapton in the same fashion as the flight articles.

The test article tubes were bolted to an adapter and then the adapter was bolted to an optical table. The SignalCalc output channel was linked through the spare flight transformer to the PZT for each tube. An accelerometer was attached to the top of the tube, oriented such that the X-axis was aligned with the attached PZT. This accelerometer was then linked through a RIGEX accelerometer cable to the Signal Calc input channels. The 1-D Laser Vibrometer was aligned with the X-axis (PZT, in fold; reference Figure 2.10), and then connected to another Signal Calc input channel. The same 1 – 2000Hz chirp input discussed in 3.2 was used. The test utilized both accelerometers and the laser vibrometer for direct comparison to previous findings and flight tube analysis. Ideally, the tests will line up with Goodwin's results; all of the prior tests used the old heavy accelerometers.

3.3.2 Single Axis Laser Vibrometer Testing. The Ometron VH300 single axis laser vibrometer was used in correlation with accelerometer testing for validation of the accelerometer results. The laser and accelerometer were aligned with the tube X-axis

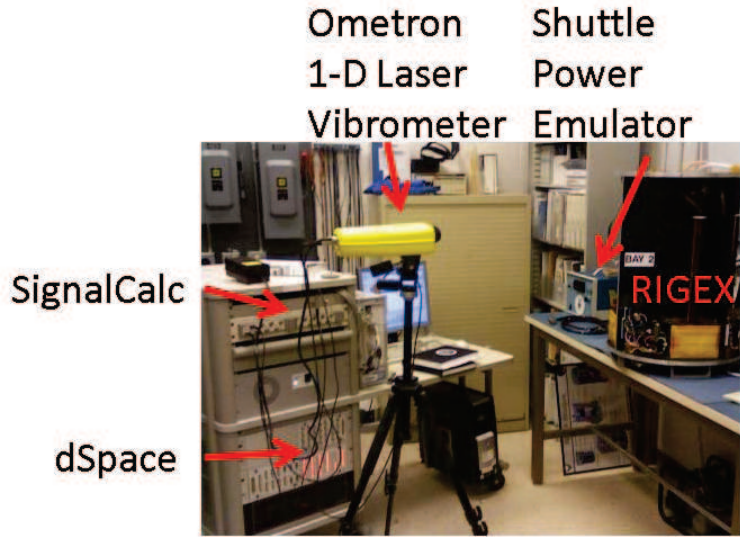


Figure 3.6: Ometron single axis laser vibrometer test setup with dSpace and Signal Calc computers and their interfaces are in the background.

and both were linked into SignalCalc. SignalCalc was used to drive PZTs using the input chirp signal. After taking X-axis data, the laser was repositioned and then Y-axis data taken for correlation with the accelerometer Y-axis. Refer to Figure 2.10 for a visual presentation of a tube coordinate system.

3.3.3 Triaxial Scanning Laser Vibrometer Testing. The Polytec PSV-400-3D, a set of three scanning laser vibrometers, was also used to measure the vibration response. The primary benefit to using a triaxial laser setup is the ability to observe the vibration response in three dimensions simultaneously. In addition, the Polytec PSV-400 scans over a user designated grid; this allows observation of the modal response over the entire viewable surface. The Polytec software allows the user to set a grid scan pattern and start the automatic scan process, at which point the software autonomously conducts the test. If provided the input signal, the Polytec software will calculate the desired FRFs and operating deflection shapes.

Figure 3.7 is shows the test setup used in the 3-D laser vibrometer testing. The Polytec system, shown mounted to a mast on the left side of the photo, is essentially three single-axis laser vibrometers with steerable mirrors that allow the beam to be moved along a grid scan pattern. Combining each scan point's responses from all three

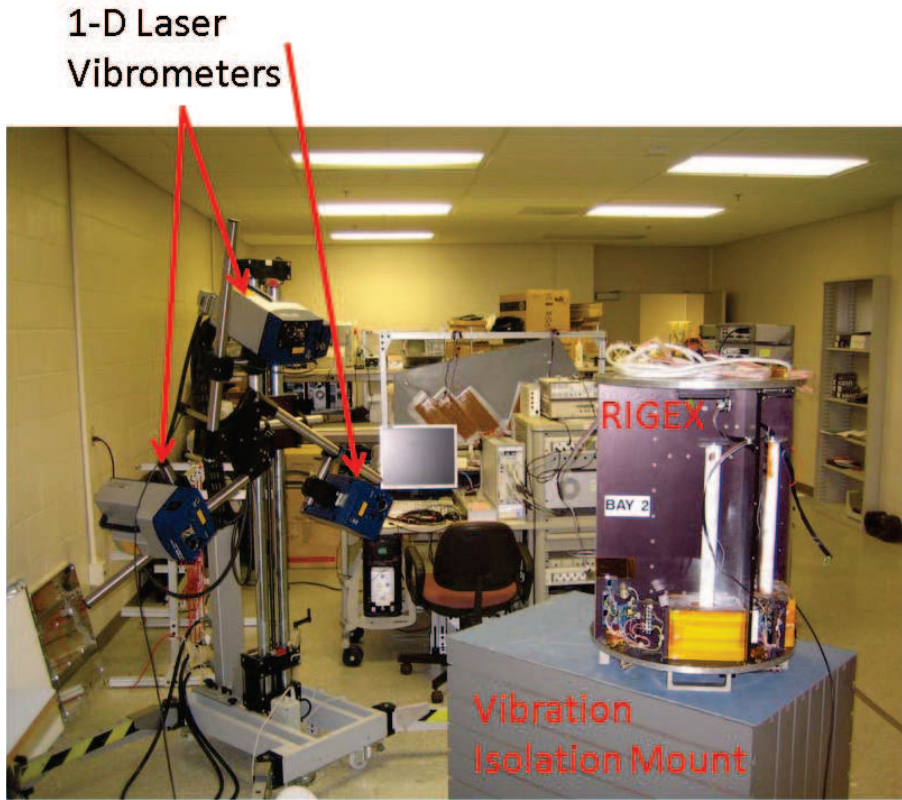


Figure 3.7: Polytec PSV-400-3D triaxial scanning laser vibrometer test setup with RIGEX on the vibration isolation mount. Note the tubes have been covered in Spot Check, an aerosol spray that increases surface reflectivity.

vibrometers allows the software to create and visually display the operating deflection shapes.

For this test, RIGEX was placed on vibration isolation mount to minimize external vibrations interacting with the testing. The Polytec system was configured such that the two lower lasers were slightly higher than the ovens, the lower limit of the scannable area on the tube. The two lower lasers effectively straddled the tube being tested, with the top laser approximately lining up with the tube. After aligning the top laser with a particular tube, a two and three dimensional calibration was conducted with the camera mounted to the top laser. A scan grid was overlayed over the target after the calibration, shown in Figure 3.8. The scan grid was limited to a narrow swath along the center length of the tube because the tube has a high curvature. For example, if a grid point was too far to one side, the grid point would be out of sight from the opposite side lower laser. This effect is similar to ships disappearing over the horizon.

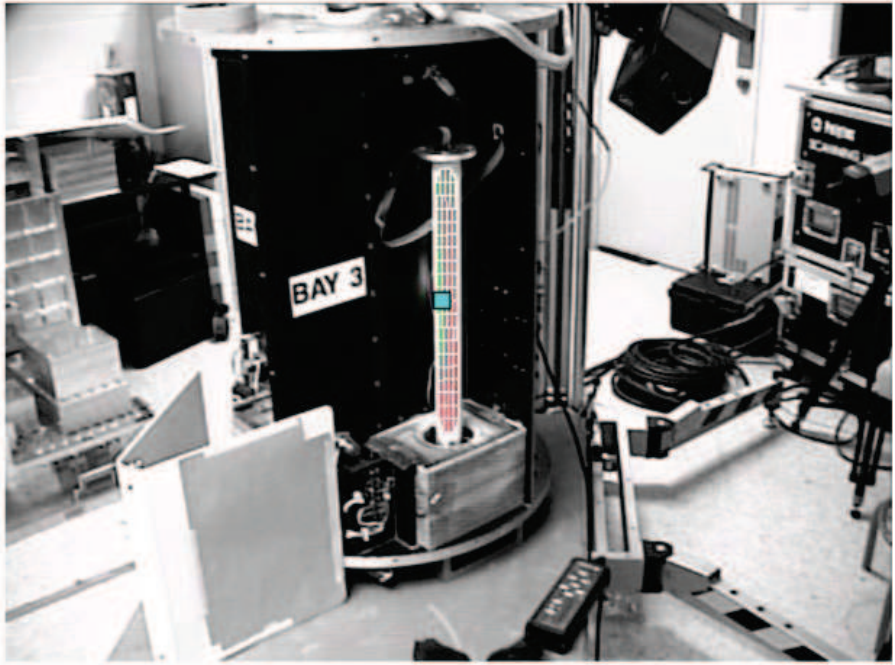


Figure 3.8: Top laser perspective of scan pattern overlayed on tube 3.

Once the grid was overlayed, a quick test run was attempted to determine if the lower lasers could “see” the outer grid points. If the lasers collected good data over the outer limits of the grid, the grid was validated. Four sets of tests were run for each tube – a 0 – 500Hz and 0 – 5000Hz chirp input tests for a tube with the accelerometer cable connected and disconnected from the accelerometer. For the 0 – 500Hz tests, an amplifier was added to the input line to increase the PZT driving power.

3.3.4 Displacement Measurements. A precise 3-D physical alignment measurement was the first (chronologically) ground test. The measurement was conducted with a Platinum FaroArm. AFIT’s Platinum FaroArm is a seven axis, six-foot-long arm with a hard contact probe type, and is used for contact measurements of objects with complex geometry. According to FARO’s website, the Platinum FaroArm is typically used for “alignment, calibration, inspection, reverse engineering and as-built documentation”, and measures with a spatial resolution accuracy of ± 0.0010 inches [8]. Figure 3.9 shows AFIT’s Platinum FaroArm with an example geometric object on the measurement table. The resulting 3-D model is shown on the attached computer.

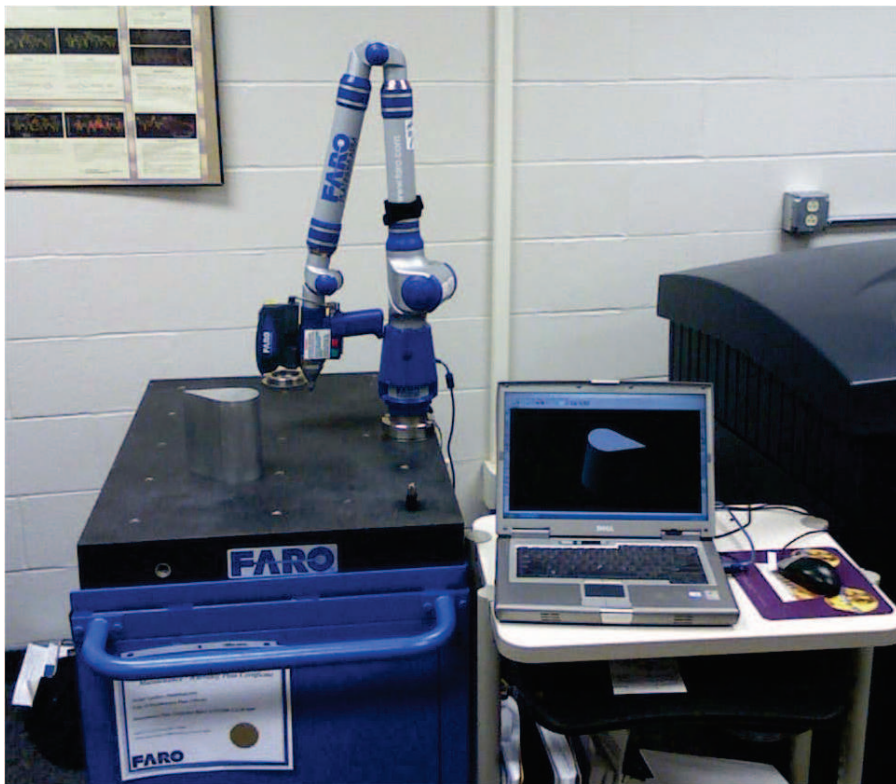


Figure 3.9: Platinum FaroArm with example object measured and modeled in a CAD program.

The Platinum FaroArm measures point clouds which are imported by the attached computer's Computer Aided Design (CAD) program. The CAD program prompts the user to select a geometric shape to fit the point cloud through, and thus creates a geometric model of the object being measured. To measure the deployed tubes, the test setup simply required RIGEX to be placed on the Platinum FaroArm's adjoining measurement table, and creation of point clouds for the bay walls, camera, tube top flange, and the tube itself.

As discussed in 3.1.4, a high resolution geometric model of the deployed tubes on the ground will allow determination of the deployed tubes position in space. Knowledge of deployment accuracy is critical when considering large, complex structures that must connect to other large complex structures in space.

3.4 Finite Element Modeling

This section reviews the process necessary to create finely and coarsely meshed FE models of individual tubes, as well as developing the procedure to create space structures to test with the coarse model.

3.4.1 Individual Tube Models. Two separate types of tube models will be developed. The first, an update to Holstein's model, was finely meshed to match actual tube characteristics as closely as possible. The second model was very coarsely meshed, consisting of only a few elements.

3.4.1.1 Update to Holstein's Tube Fine Mesh Model. Holstein [15] used Abaqus, an FEA program used often in industry. For the purposes of this thesis, FEMAP will be utilized; as such Holstein's Abaqus model needed to be ported into FEMAP for analysis and updating. Once the model file was exported to FEMAP, Young's modulus and the shear modulus were tuned to bring the model inline with the flight tube vibration response. The initial guess for Young's modulus is developed in Section 4.4.1. The objective is to match the first two structural natural frequencies.

3.4.1.2 Simple Coarse Mesh Model. This model was created from a clean slate. For the purposes of developing large models, a coarsely-meshed tube model with as few elements as possible is very desirable. The more elements per tube, the greater the analysis computation time per tube; on models with many tubes the higher fidelity becomes unwieldy, and often unnecessary. The first structural natural frequency (referred to as the fundamental frequency) dominates modal response of most structures, therefore the goal of this effort is to match the coarse model to the fundamental frequency behavior only.

3.4.2 Mission Oriented Structure Models. RIGEX was a large step in the direction of successful future inflatable and rigidizable space structures, both trusses and frame type structures. Using the 20-inch coarse mesh tube model discussed in 3.4.1.2, models of space structures are to be created and a comparison analysis conducted.

IV. Results and Discussion

THIS chapter provides the results of the testing proscribed in Chapter III. The chapter flow models Chapter III for ease in reference to the detailed test setup and test objective description. Space flight, post flight, and ground test data results are shown here individually, and the FE model results are included as well. The results are discussed, and relevant observations such as testing difficulties, data analysis, repeatability, applications to future missions, and regrets are included. Comparisons between the previous ground tests, space flight tests, post space flight tests, ground tests results, and finite element models are the topic of Chapter V.

RIGEX was a successful space flight test. All three tubes deployed, and temperature, pressure, vibration, and image data were successfully collected on-orbit. The post space flight testing and ground testing was accomplished, along with the image change detection analysis (except tube 2 – see 4.1.4), displacement measurements and finally, the FE model.

The return of the RIGEX for additional study is a unique characteristic among space flight experiments. Appendix A discusses the condition of RIGEX upon return to AFIT; Appendix B provides sample MATLAB scripts used to analyze the data, and the as-flown version of the flight code is provided in Appendix C.

4.1 *Space Flight Test Results*

Shortly before 0300 Eastern Standard Time on Flight Day 14 of STS-123 (24 March 2008), Mission Specialist Takao Doi activated RIGEX by flipping a single toggle switch on Standard Switch Panel 2 (SSP2) which provided current to the experiment. The toggle indicator display indicated nominal talkback functions; confirmation of both experiment activation and event sequencing was observed on the ground by monitoring the bus current telemetry. In particular, telemetry indicated three current draw increases (approximately $5A$ for 18 ± 2 minutes) corresponding to the heating cycle for each tube. After approximately 2 hours, RIGEX concluded testing during the astronaut sleep cycle and entered a standby mode. At the end of the crew sleep cycle, the DS-13 display indicator on SSP2 correctly indicated experiment completion, and RIGEX was powered



Figure 4.1: (a) Standard Switch Panel 2. The DS-13 toggle switch and display indicator are highlighted by the red oval in the center of the panel. This switch was the only interaction the astronauts had with RIGEX.

(b) Mission Patch for STS-123.

down by toggling the DS-13 switch. The data was successfully downloaded when RIGEX was removed from the *Endeavour*'s cargo bay, and post processing began when RIGEX returned to AFIT. SSP2 is shown in Figure 4.1 (a), with the toggle switch and indicator display located in the center of the panel and highlighted by the red oval. The STS-123 mission patch is shown in (b).

4.1.1 Temperature Results. Upon return to AFIT, RIGEX temperature data was the first space flight data processed. Overall, the RIGEX temperature data trended within expectations. Temperature data for the left and right cargo bay sill was mined from *Endeavour*'s telemetry data. RIGEX was mounted to the right cargo bay sill (shown in Figure 1.1), and thus the right cargo bay sill temperature data allows understanding of the boundary conditions RIGEX was subject to during operation. See Appendix A for the post flight oven inspections.

4.1.1.1 RIGEX Temperature Data. All of the temperature data was downloaded and processed successfully and is displayed in Figure 4.2. The tube heating profiles are clearly observable. Tubes 1 and 3 are in family, while tube 2 took 200 seconds longer to warm to deployment temperature. The change in temperature with respect to time is similar for all three tubes, but tube 2 takes longer to reach the initial

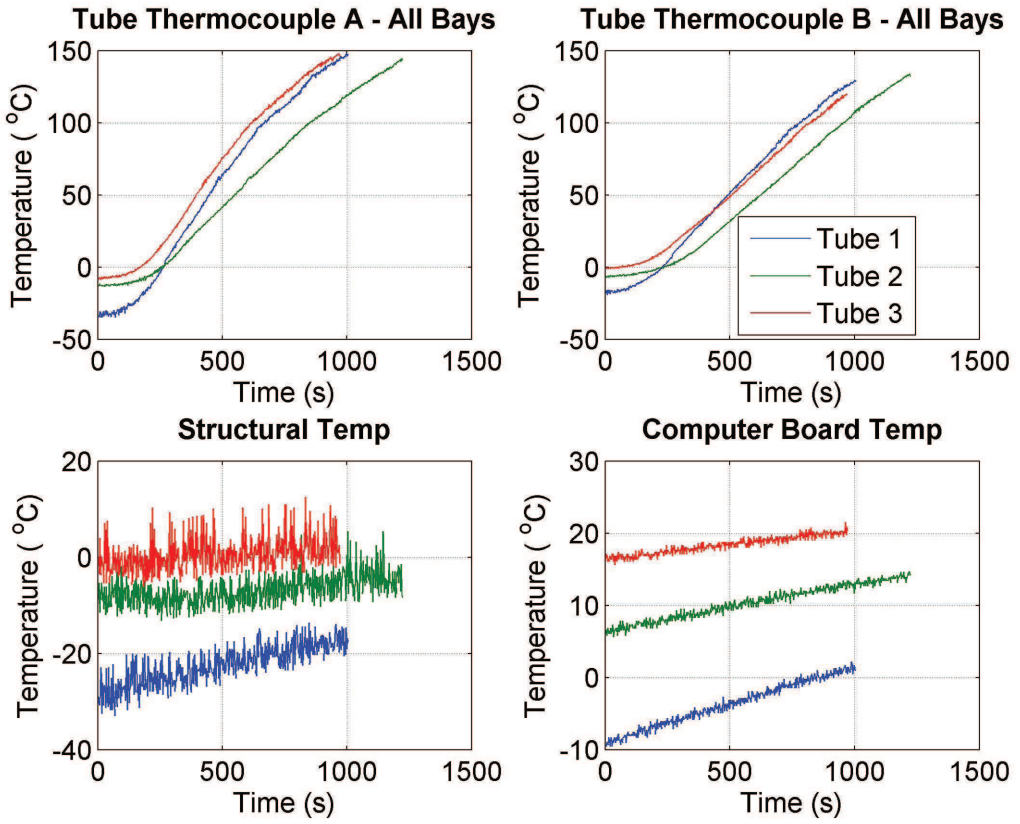


Figure 4.2: RIGEX recorded thermocouple temperature measurements during experiment activation.

“pull-up” curve (the change from relative steady temperature to steady temperature increase). Tube 2’s different thermocouple locations, discussed in Section 3.1.1.1, is the most likely explanation for its tardiness. Note that tube 1 thermocouple A recorded an initial temperature of -35°C , the lowest temperature reading for the entire experiment.

The computer bay and structural temperature temperatures were recorded during the heating of each tube. Their respective plots trend similarly, with the largest and smallest relative temperature increases occurring during the heating of tube 1 and tube 3, respectively. This phenomenon was expected; the heating of tube 1 began after a considerable cold soak (14 days in space) and the heating of tube 3 began as the structural temperature had almost reached equilibrium. This observation has important applications for future sub- T_g truss deployment systems – a balance must be struck when managing the external thermal radiation and conduction from the ovens. Warming the system up from ambient to an optimal temperature is the benefit of the ovens’ external

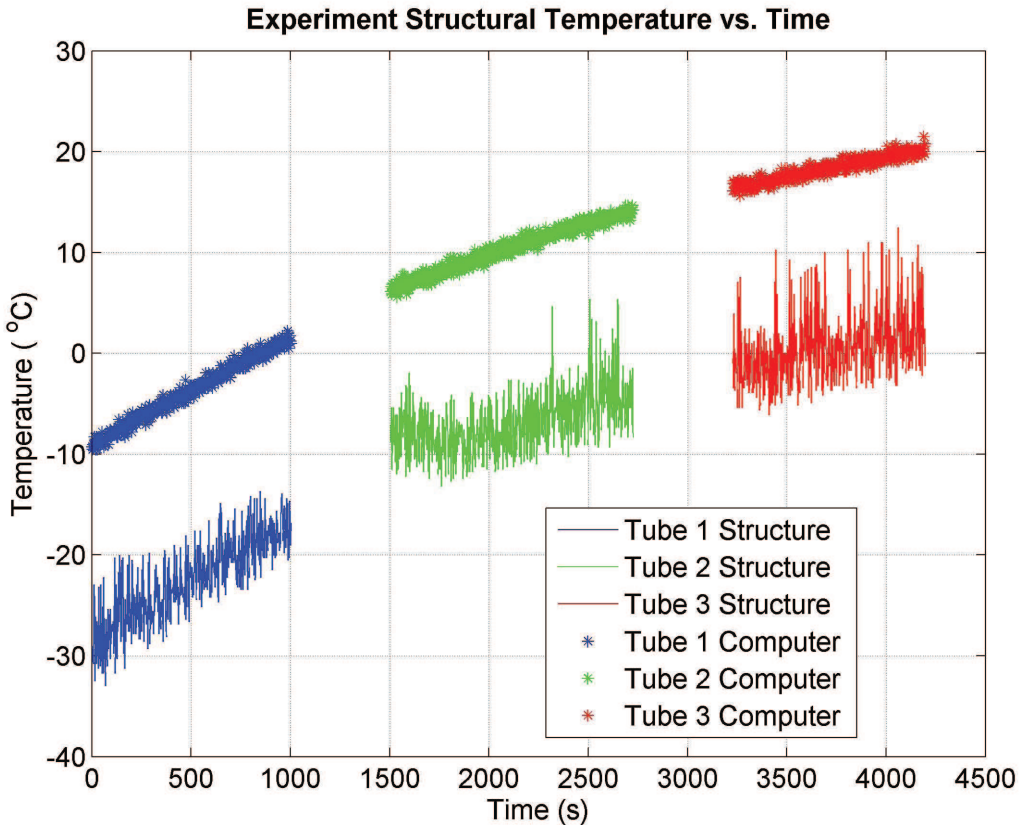


Figure 4.3: RIGEX structure temperature during experiment activation.

thermal radiation, but at optimal temperature the thermal loading must be managed to prevent overheating.

The structural and computer temperature were still trending higher, though at a decreased rate. The structure had considerable margin before it reached overheat temperatures and consists of relatively large surfaces which can radiate waste heat, whereas the computer was stacked inside of a tight housing with minimal surface area to radiate heat, and could conceivably overheat. Future missions need to consider the computer thermal environment carefully.

Given this discussion, observation of the structural temperature data in a timeline sense is also relevant. It is interesting to observe how the general temperature of RIGEX changed from initialization through the completion of tube 3's deployment. Figure 4.3 plots the structural and computer thermocouple data along the experiment timeline. The graph indicates the RIGEX was headed for an equilibrium computer and structural

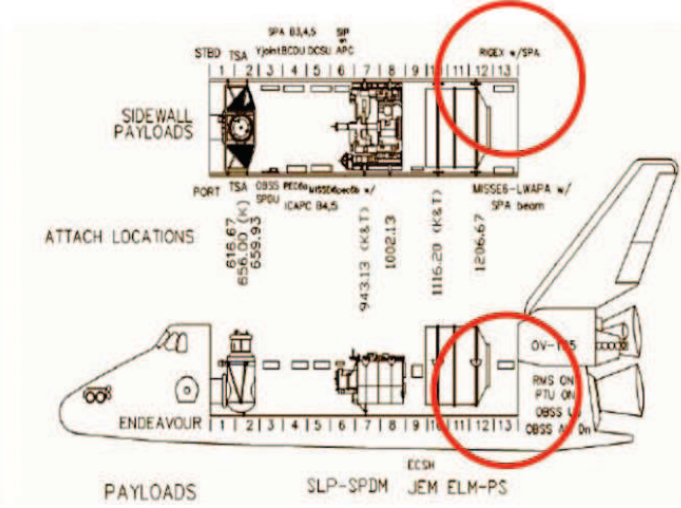


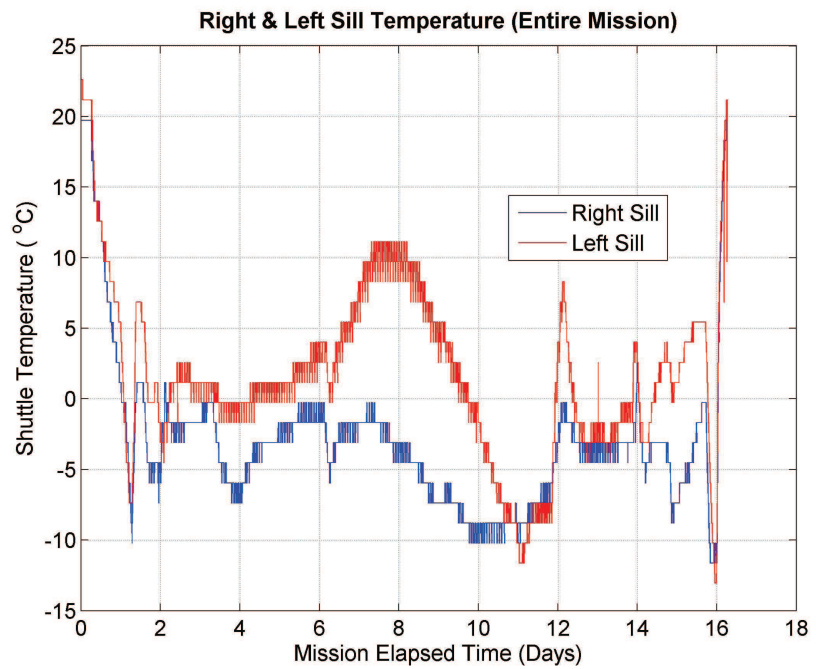
Figure 4.4: Attachment stations for *Endeavour*'s cargo bay. RIGEX was located at station 13 on the right cargo bay sill.

temperature. Structural thermal equilibrium will not only be dependent on internal thermal energy, but external as well. Thus it is appropriate to discuss RIGEX's thermal boundary conditions.

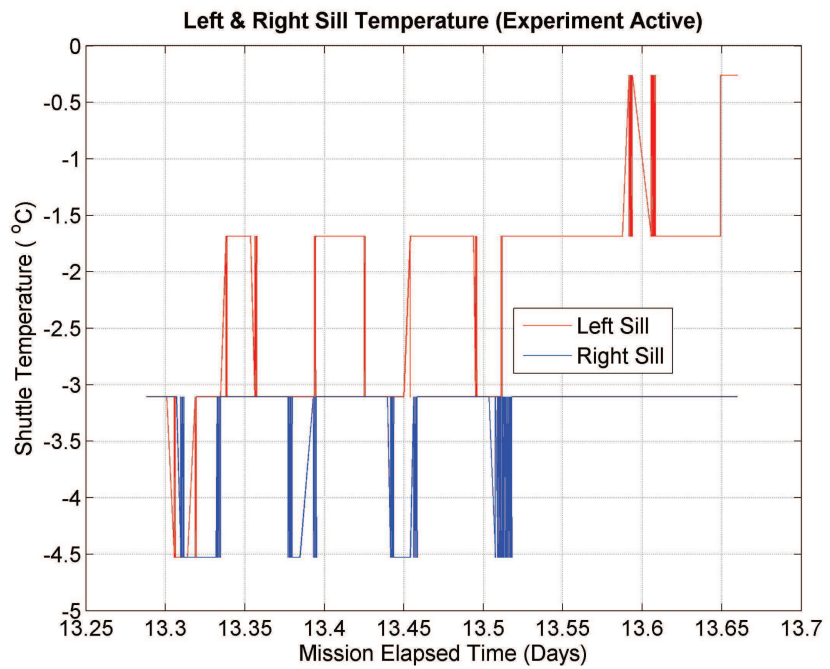
The computer thermocouple data is considerably less noisy than the structural thermocouple data in Figure 4.3. The structural thermocouple and tube thermocouple data have increased noise levels as a result of multiple wiring connections. The multiple wiring connections were instituted as design, construction, and troubleshooting aides, and the noise level increase was deemed acceptable.

4.1.1.2 Endeavour Cargo Bay Sill Temperature Data. AFIT was provided all of the temperature telemetry data for the left and right cargo bay sill (station 12) from STS-123. RIGEX was mounted to station 13 (Figure 4.4), so station 12 is an acceptable approximation of RIGEX's boundary conditions.

Cargo bay station 12 temperature data for the entire mission is shown in Figure 4.5 (a). Aside from the peaks at the beginning and end of the mission (associated with launch from and reentry to Earth ambient), station 12's temperature remained bounded between $\pm 10^{\circ}\text{C}$. Note the left sill was typically warmer than the right sill – this is probably a result of shading of the right sill by either the cargo bay doors or the International Space Station.



(a)



(b)

Figure 4.5: (a) Mission duration *Endeavour* cargo bay sill temperature data.
 (b) RIGEX operation *Endeavour* cargo bay sill temperature data.

Figure 4.5 (b) provides the cargo bay sill temperature for station 12 during RIGEX operation. The temperature data remains within -3 to -4.5°C (one telemetry bit) during RIGEX operation. Averaged out, this indicates RIGEX’s thermal boundary conditions were a constant 3.75°C during experiment activation. Therefore the shuttle cargo bay sill boundary conditions were benign and constant during experiment activation, and thus all of the measured internal temperature increases were a direct result of the heat produced by experiment.

4.1.2 Pressure Results. The next data set analyzed was the pressure data. The inflation pressure data is presented first, followed by the on-orbit pressure census data. Note that the sub- T_g structural configuration tested here has two single points of failure: the thermal and inflation systems. RIGEX sailed through the thermal process with flying colors, but encountered problems trying to inflate tube 1, which lends credence to the Section 2.1.1 statement that inflation systems are a single point of failure for these particular inflatable structures.

4.1.2.1 Inflation pressure. The inflation pressure data yielded a surprising result: tube 1 didn’t inflate while the tube pressure transducer was recording internal pressure – yet the post-deployment instantaneous pressure census showed equalized pressure in the tube and the reservoir tanks, and the post flight visual inspection confirmed the tube had in fact been deployed/ The presumed explanation is the inflation solenoid didn’t open when commanded, but opened during the 300 seconds between the last inflation pressure transducer reading and the post deployment census.

This condition had been observed prior to flight during the system level thermal vacuum testing. During the test, solenoid activation current was detected when the tube 1 inflation solenoid was commanded open, but the valve did not open. This was discovered after the hardware was removed from the chamber, and it was noted the inflation gas reservoir was still pressurized to local ambient. The valve was then tested outside the chamber and functioned properly. Troubleshooting consisted of multiple additional valve operations at various tank pressures ($0 - 15\text{psi}$) and disassembling the tube from the valve to search for evidence of debris or water vapor, but none was found.

The solution decided upon was to subject the pressure tank and tube system to vacuum and hold for several hours, after which purging the system with nitrogen. This was done at least twice. The condition could not be repeated, and it was assumed that either a small piece of debris or moisture had caused the malfunction during system level thermal vacuum testing. It was believed either problem would have been remedied by vacuum and purging.

Though the exact root problem is unknown, it is hypothesized the extreme cold ambient temperatures caused the inflation valve to “stick” at first when commanded open, but the valve opened soon after the pressure transducer stopped recording values. Discussed further in Section 4.3.4, tube 1 has the largest deployed shape deviation from true (exactly straight) – but the deviation is only 1.14 inches from true. In addition, Section 4.1.4 shows images of tube 1 unfolding from the oven box followed by an image of the deployed tube. These results suggest that residual strain energy in the composite matrix pushed the tube out of the oven, and the inflation valve opened before the tube cooled below T_g . Using Moeller’s [28] cooling profiles, if the temperature of the tube was 138°C (averaged between thermocouple A and B), it would take between 125-175 seconds for the tube to cool below the glass transition temperature (125°C). Based on the marginal deployment deviation, it is believed the tube inflated less than 50 seconds after the commanded inflation.

Another detail in the pressure data that complements this theory is the delay in tube 2 inflation pressure increase. The inflation pressure transducer in tube 2 detects the first increase in pressure 0.068 seconds into the data recording timeline, which suggests the inflation valve did not immediately open when commanded. The flight code commands the solenoid to open the valve just prior to opening the data file to record the pressure data, so it is possible the solenoid took even longer to open than the data suggests. Tube 3 inflation pressure data indicates pressure increase at 0.001 seconds into the data recording timeline.

Figure 4.6 presents the individual tubes’ inflation pressure data. The transducers measured absolute pressure (psi), but it is assumed in the space environment there was zero ambient pressure. Tube 1 plots a flat line at 0psi, indicating it did not inflate while

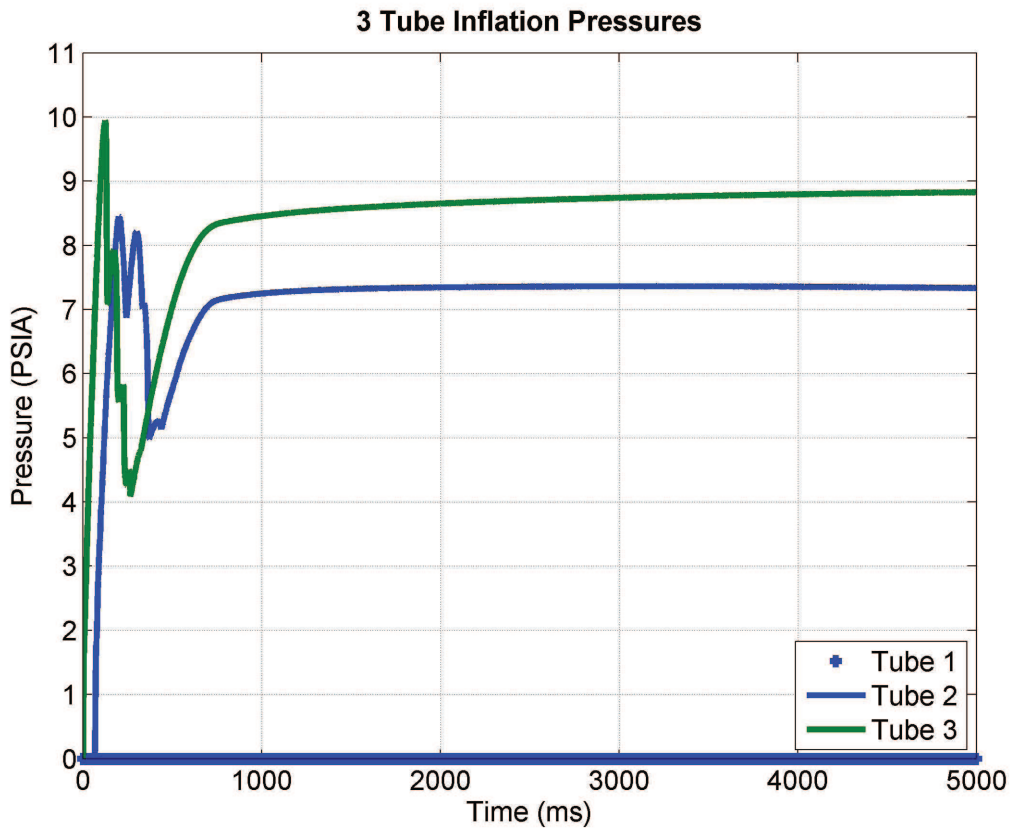


Figure 4.6: Tube inflation pressure over time

the pressure transducer readings were being recorded. Tubes 2 and 3 both inflated while pressure was being recorded, and they both had reached approximate steady state inflation pressure in approximately 0.75 seconds. The inflation pressure profiles follow the same basic shape, but tube 3 exhibited one sharp primary peak and lesser secondary, tertiary, and quaternary peak, whereas tube 2 exhibited equivalent primary and secondary peaks, with lesser tertiary and quaternary peaks.

Again, the most likely explanation hearkens back to the way the tubes were folded (Figure 3.3). Consider tubes 2 and 3 slightly straightened by the residual strain. As the pressurized gas traveled through tube 3 (plot with the single high peak), it hit the first short length of tube and the first 180° degree corner, resulting in a pressure spike. As the gas seeped through this first sharp corner, it immediately hit another short leg and sharp corner. The lower pressure air seeped through these corners as well, and as the

tube straightened through the first two major corners, gas was beginning to reach the end of the tube. This is an attempt to explain why there was only one major spike.

Conversely, tube 2 had a double spike. The second spike is most likely attributable to the pressure slug meeting a short leg followed by a long leg (instead of a short followed by a short as in tube 3). This long second leg allowed pressure to build up again before the gas could seep through the second corner, resulting in a double spike. Unfortunately, with the failure of tube 1 to deploy while pressure was being recorded, an inflation pressure profile comparison with tube 3 cannot be conducted. If the two inflation profiles had been similar, it would lend merit to the proposed explanation.

4.1.2.2 On-Orbit Instantaneous Pressure Census. There were also ten instantaneous pressure censuses of all three tubes and tanks – one during experiment initialization and three for each tube deployment. These values are presented in Table 4.1.

The first relevant observation is reservoir tank 2 started with $\sim 15\%$ less pressure than reservoir tanks 1 and 3. This difference explains the difference in steady state pressure between tubes 2 and 3 in Figure 4.6 – the internal pressures of both tube 2 and 3 equalized with their respective tank pressures, but tube 2 started with less pressure. After 5 seconds, tube 2 indicates approximately 7.25psi, but 300 seconds later, the tank and tube pressures are 1.24 and 1.17psi, respectively. This rapid pressure loss, coupled with the reduced initial reservoir tank pressure, provide strong evidence for a leak in tube 2’s inflation system. The exact location of the leak is unknown, but it was probably a combination of leaks. The leak was exacerbated when the inflation solenoid was opened, thus is probably downstream from the solenoid; however, the solenoid is most likely part of the problem as well, otherwise the reservoir would not have leaked pressure while on-orbit. Despite the leak, the system design was robust enough to successfully deploy and rigidize – again proving the inflatable/rigidizable structure design methodology’s definite advantage over purely inflatable space structures.

Table 4.1: On-Orbit pressure values recorded during the ten instantaneous pressure censuses. Pressures are presented in psi.

	Tank 1 Pressure	Tube 1 Pressure	Tank 2 Pressure	Tube 2 Pressure	Tank 3 Pressure	Tube 3 Pressure
Experiment Initialization	14.85	0.00	12.38	0.00	14.48	0.00
Tube 1 Initialization	14.83	0.00	12.37	0.00	14.46	0.00
Tube 1 Deploy + 300s	5.26	5.12	12.38	0.00	14.48	0.00
Tube 1 Post Vent	5.26	0.10	12.38	0.00	14.48	0.00
Tube 2 Initialization	5.26	0.00	12.39	0.00	14.49	0.00
Tube 2 Deploy + 300s	5.28	0.00	1.24	1.17	14.53	0.00
Tube 2 Post Vent	5.28	0.00	1.23	0.00	14.53	0.00
Tube 3 Initialization	5.28	0.00	1.23	0.00	14.55	0.00
Tube 3 Deploy + 300s	5.30	0.00	1.23	0.00	8.26	8.18
Tube 3 Post Vent	5.29	0.00	1.23	0.00	8.26	0.13

Also, note the trend of slightly increasing reservoir tank pressures. This is probably attributable to the tanks warming with the RIGEX structure and thus subtle pressure increases – the natural gas law relation between pressure and temperature.

4.1.3 Accelerometer Results. On-orbit accelerometer data consists of the majority of recorded data. Accelerations for each tube were monitored for five seconds during the tube deployment, another five seconds during a lull for ambient measurements, and during the 25 repetitions of one second vibration testing. The accelerometers functioned properly during all of the tests and good data was collected for the deployment and ambient tests. However, as alluded to in the introduction, an anomaly (probably a failure in the Butterworth filter) occurred during the vibration testing.

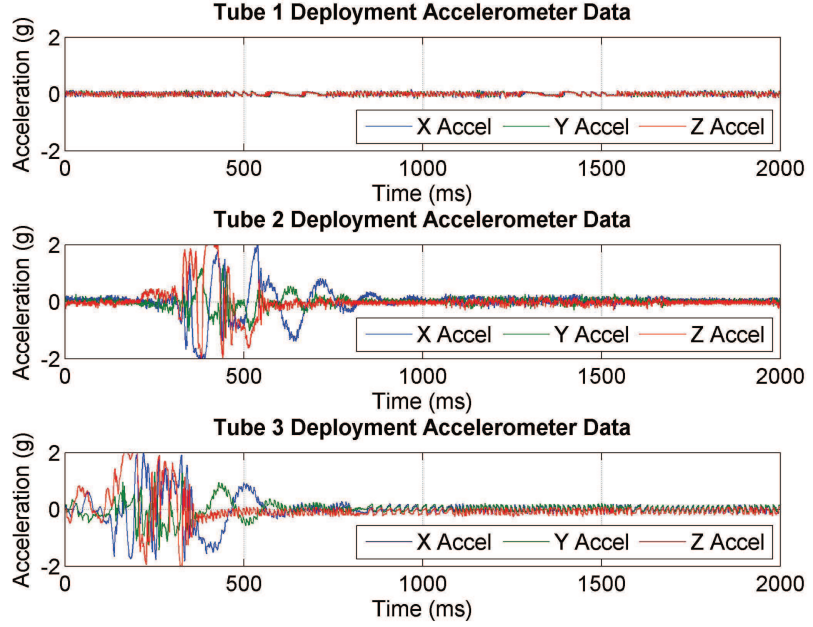


Figure 4.7: Tube tip inflation acceleration (X,Y,Z) over time

4.1.3.1 Deployment. Five seconds of acceleration data was recorded during the deployment process. Accelerations were recorded to determine how violently the tube deployed, critical data for satellites using inflatable structures. A forceful, uncontrolled deployment process could overwhelm a satellite’s attitude control system, perhaps leading to an uncontrollable tumble state ending in mission failure or could even dislodge the structure from the satellite; this effect has been seen when conducting strain based truss deployment for the first time in a laboratory – trusses have ripped themselves free from the wall.

Figure 4.7 plots the three axis accelerations, one plot for each flight tube. The time scale has been shortened to two seconds for clarity, as all of the deployment activity was completed in one second.

Tube 1 accelerometers did not record any accelerations during the 5 second window, which corresponds with the delayed inflation. This seems to indicate the deployment motivated by residual strain energy had exhausted itself in the approximately one second between the pin pull actuation and the inflation command. It is unlikely that this motion

occurred during acceleration monitoring. Tube 1 deployment acceleration measurements are similar to the ambient noise measurements.

Tube 2 and 3 accelerometers successfully recorded deployment accelerations coincidental to the pressure measurements. Unfortunately, both tubes exhibit several accelerometer X and Z-axis saturations (readings of $\geq 2g$); some of the Z-axis saturations last up to 0.04 seconds. These $> 2g$ sustained Z-axis accelerations highlight the need to have detailed understanding of the deployment process. Inflatable structure design engineers will have to balance the inertia of the structure to be deployed against the regulated pressure required (or available) and the need to deploy before the structure cools below sub- T_g and rigidizes.

The delay in pressure increase for tube 2 discussed in Section 4.1.2.1 is again present in the accelerometer data, although the accelerations do not begin at the same instant the pressure rise occurs. It appears as though acceleration, and thus deployment, begins with the second pressure peak (Figure 4.6. Tube 3 accelerations begin immediately with the pressure rise).

Care must be taken when attributing deployment accelerations to particular coordinate frames. The triaxial accelerometers record acceleration in relation to their own coordinate frame, which is fixed to the tube endcap. The tendency is to read accelerations from a deploying tube and relate them to the stowed or deployed tube's coordinate frame, which would be incorrect. The accelerometer coordinate frame rotates and translates quite a bit during deployment, as is portrayed in Figure 4.8.

Acceleration measurements taken during the deployment process therefore cannot be treated as relative to a stowed or deployed tube. Thus, X and Z maximum accelerations quoted above are relative to the tube endcap, but they are still real accelerations that must be accounted for when designing a deployment system. If the direction cosine matrix that related the endcap with the inertial (deployed tube) frame for every measurement was known, the accelerations could be integrated twice and the exact path the tube endcap took as the tube deployed could be determined. Moody [29] tried to do this when deploying the cloth tubes (used to test the inflation system) but ran into the same problem as with the space flight data – he did not have enough information to

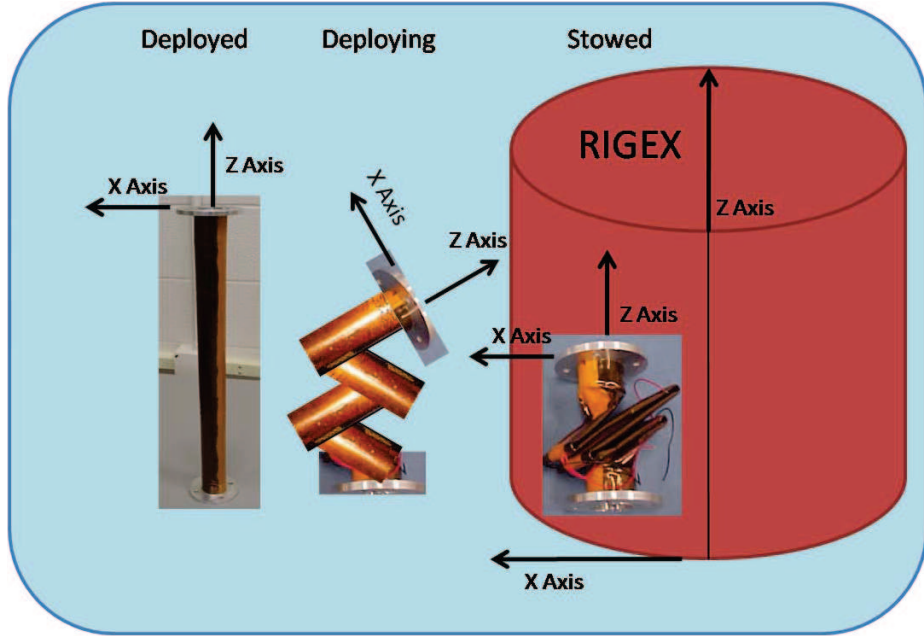
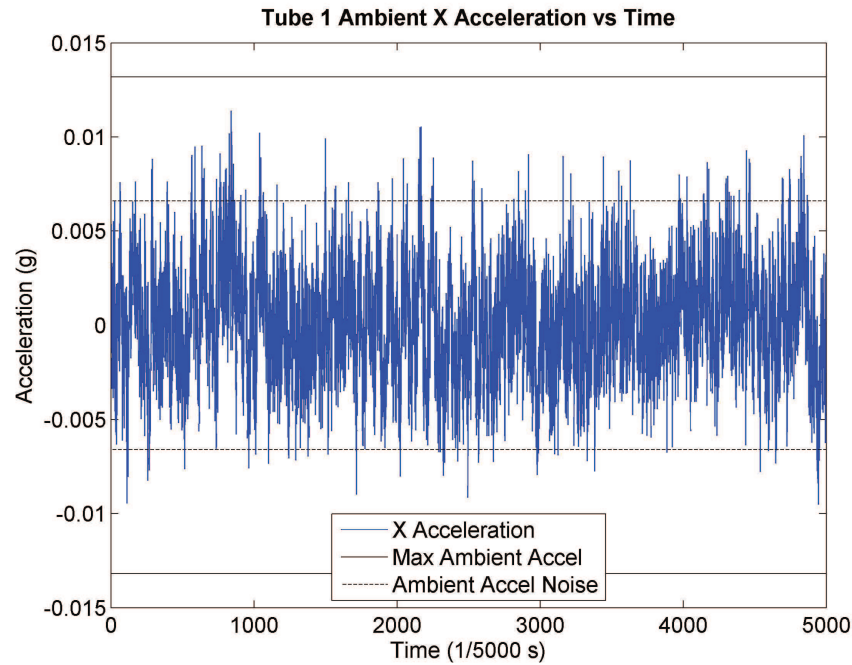


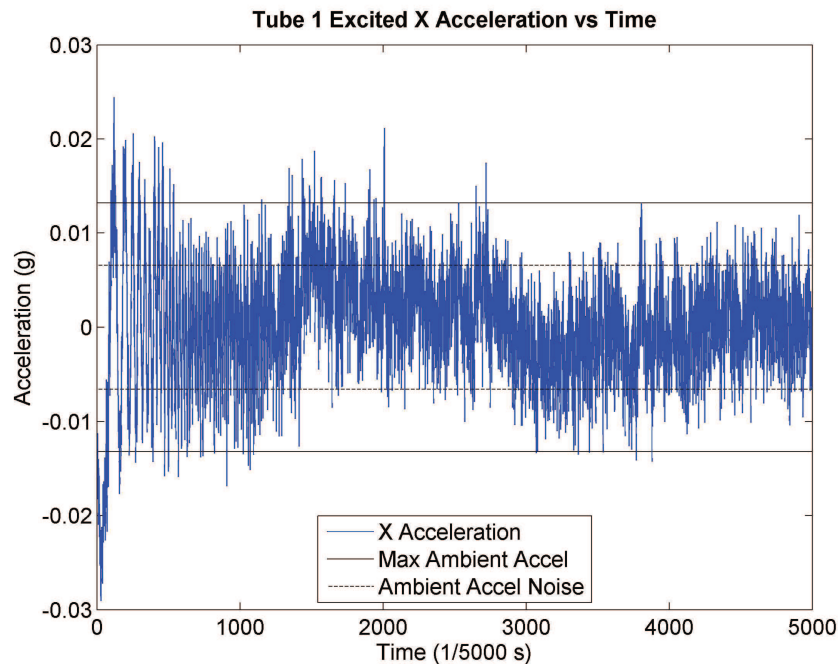
Figure 4.8: The accelerometer coordinate frame is fixed to the tube endcap. As the tube deploys, the endcap rotates and translates quite a bit, thus deployment accelerations measurements cannot be treated as inertial type accelerations.

solve the direction cosine matrix. He then assumed the endcap only translated vertically and did not rotate, which was acceptable for the cloth tubes as they deployed rather quickly. The translation assumption is not appropriate for the on-orbit deployments, however – the images taken by the camera during deployment clearly show the tube endcaps substantially rotated.

4.1.3.2 Ambient Accelerometer Measurements. The three axis ambient acceleration environment was recorded five times for each tube. This data was meant to form a noise level estimate (the vibration testing analysis would have to account for the noise level to develop accurate FRFs), and as a check to ensure the accelerometers were working properly. The ambient acceleration levels in all tubes were bounded between 2.48 and 2.52V ($\pm 0.0132g$), and data analysis indicated the noise level for all three tubes in each axis was less than 0.01V, or 0.0066g (two standard deviations). Figure 4.9 (a) presents an example ambient X acceleration time history, with lines showing maximum ambient noise readings and the accepted noise minimum.



(a)



(b)

Figure 4.9: (a) X-axis ambient accelerations time history. The ambient data is well within the accepted noise level of $0.0066g$ (dotted line) and there are no maximums exceeding the maximum accelerations (solid line).
 (b) X-axis acceleration time history from a vibration test. Note the slight sinusoidal response which corresponds to the beginning of the chirp input signal.

4.1.3.3 Vibration Testing . The space flight vibration testing yielded mixed results. The flight computer successfully recorded acceleration time histories for the 25 iterations of vibration testing for each tube. These time histories show low frequency actuation, as if the tube is responding to the low frequency input, but little discernable response to the rest of the chirp signal. The acceleration values associated with resonances are only slightly higher than the ambient noise levels (low signal-to-noise ratio), making the job of determining resonances very difficult. For example, Figure 4.9 (b) is a X-axis acceleration time history from one of the 25 tube 1 time histories. The maximum acceleration value recorded is nearly four times the noise level (measured in the ambient acceleration measurements), but only twice the maximum ambient accelerations observed. It had been hoped the resonances would be more obvious in the time history. Standard practice dictates a 10:1 signal to noise ratio for acceptable test data; accelerations 10 times the noise level were not seen.

The next step was to calculate FRFs from the accelerometer measurements and the recorded input signal. It was at this point trouble began. The exact input signal received by the PZTs were not recorded due to design (power, available ports, and memory) constraints, so the input chirp signal (given by Equation 3.1 and again in 4.1) was used as a surrogate (see Appendix C). The resultant averaged FRFs did not meet expectations – there were no clear natural frequency resonance spikes, although the averaging process had successfully washed out most of the noise up through 1000Hz (at which point the data became quite noisy). Given the accelerometers performed well during the tube deployments and ambient collections, attention turned to the input signal.

$$y(t) = \cos(2\pi(5 + (1000 - 5)t)t) \quad (4.1)$$

Moody [29] originally directed the use of a 1000Hz chirp input signal one second in duration, and presented a Power Spectral Density of such a signal. Equation 4.1, the input programmed on the flight computer, is actually a 2000Hz signal (as shown by the Power Spectral Density in Figure 4.10). Moody put the lowpass eighth order Butterworth with a cutoff frequency of 1000Hz after the input signal DAC to help prevent aliasing.

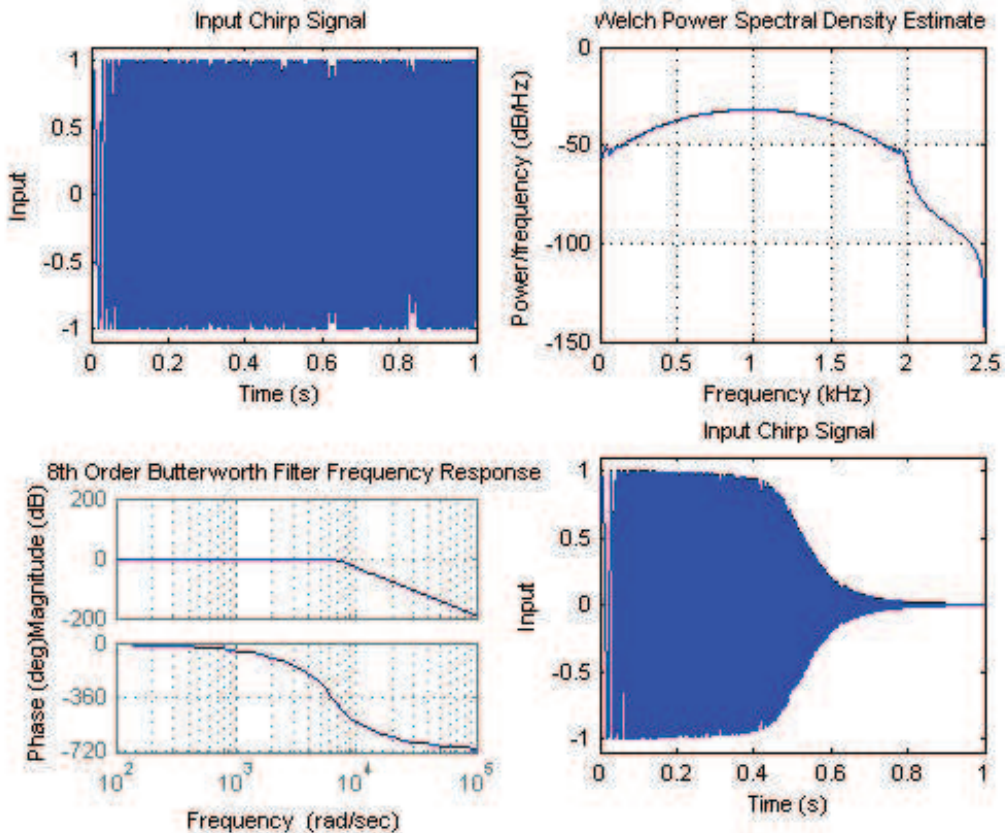


Figure 4.10: A quad plot presenting the time history of Equation 4.1, the Power Spectral Density of Equation 4.1, the Bode plot of the lowpass eighth order Butterworth filter with a cutoff frequency of 1000Hz, and the ideal filtered input as seen by the PZT.

The actual 2000Hz chirp signal was filtered after it crossed 1000Hz, attenuating the voltage seen by the PZT after ~ 0.5 seconds in each vibration test iteration. The filtered chirp input signal and frequency response of the eighth order Butterworth filter are also presented in Figure 4.10.

With the input signal trimmed by the filter, the next topic is the weak acceleration values. The most obvious conclusion to limited response is limited input, and it is believed the transformer voltage output was inadequate to drive the PZT input for the 0–1000Hz range. This would result in low signal-to-noise readouts by the accelerometers, increasing the difficulty in distinguishing the true acceleration response signals above the noise.

The initial modal analysis utilized MATLAB's `tfestimate` command. The 25 iterations of the one-second vibration response tests created 25 accelerometer data sets,

each containing 5000 X, Y, and Z-axis recordings. At first, the data was read in as 25 3 X 5000 matrices, which were then stacked into 1 3 X 125000 matrices and passed (along with the unfiltered signal) to `tfestimate`. The resulting FRFs were fairly smooth, but did not contain any real peaks, and the 1000 – 2000Hz data was very noisy. These unexpected results led to the belief that the flight computer had “choked” and did not maintain its 5000Hz sampling frequency, thus failing to obtain 5000 continuous accelerometer readings, which would have thus resulted in erroneous FRFs after the processing. This theory could not be verified on the ground until the flight computer power supplies were repaired (Appendix A), and the inability to conduct the vibration test on the ground during post flight testing (Section 4.2.2) meant the test could not be reproduced. When the flight computer was repaired, a test sample rate test was conducted which verified the flight computer was indeed sampling at the advertised 5000Hz rate. The data was reprocessed using the filtered input frequency and the resulting averaged FRFs were less noisy, but still did not exhibit any resonance peaks.

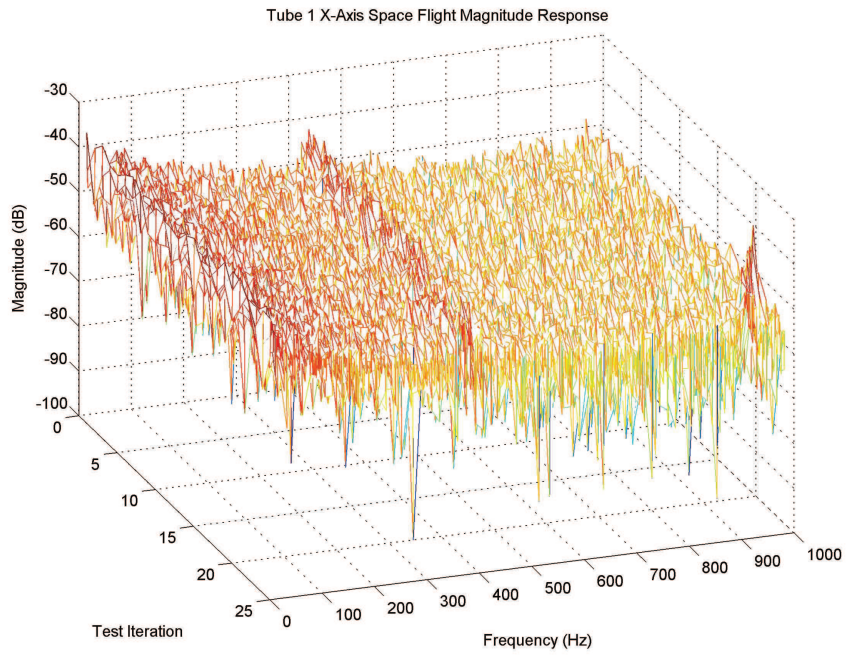
At this point, analysis of the individual vibration tests (with the filtered signal) revealed peaks in each test-specific FRF that were not present in the averaged FRFs. To further investigate this finding, the 25 individual single-axis FRF vectors were stacked in a matrix and plotted using MATLAB’s `mesh` command, which plots matrices in three dimensions and colors the plots based on amplitude rather than column or row.

The results immediately explained why the averaged FRFs did not contain any peaks – the natural frequency resonance peaks were drifting from test to test. The averaging process washed out the peaks in the same fashion as it washes out the noise; statistically uncorrelated data will average to some median value across a given frequency range, the resonant peaks frequencies drifting peak to peak essentially averaged themselves to the median value. Examples of this effect are shown in Figure 4.11 through 4.13. These figures present three dimensional plots of the stacked transfer functions and a two dimensional top view. The resonant peak drift is easily observed in the two dimensional top view for flight tubes 1 and 2. It appears as though tube 3 maintained relatively constant resonant frequencies, but the peaks are not very large (manifestation of the low

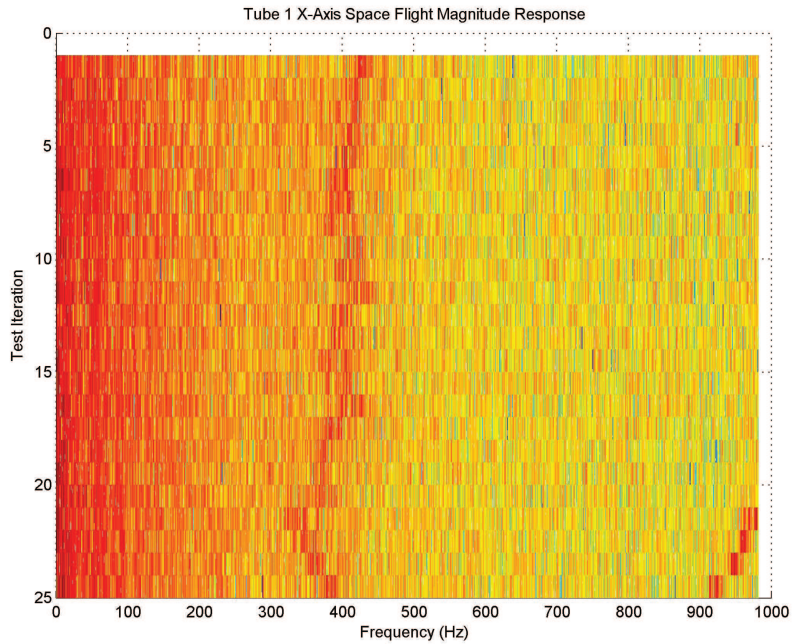
signal-to-noise ratio), and the slight drift causes the tube 3 peaks to be all but averaged out.

With the answer to the lack of peaks in the averaged space flight FRFs, the next question was simple: why do the peaks drift? The analysis efforts up this point had been based on the assumption of a linear and time invariant system, but Figures 4.11, 4.12, and 4.13 suggest the tubes were indeed demonstrating time dependence, which had not been seen before. No definite answer can be given as to why the tubes exhibit time dependency, but there are two potential solutions which center on the rigidity and temperature of the tube at the time of testing.

The first solution focuses on the overall temperature and rigidity of the tube itself. If the tube had not cooled enough to sufficiently rigidize during the five minutes prior to the vibration tests, the structural characteristics would still be changing while the tests were being conducted, yielding different structural natural frequencies. Although this theory cannot be proven (the temperature of the tubes at the start of the vibration response testing is not known), there is contrary evidence which suggests this should not have happened. Figure 5.4 plots the temperature profile of a cooling tube in a vacuum chamber with an ambient temperature of 25°C. The tube in this preflight ground test was heated to approximately 165°C and cooled to 100°C (well below T_g) in 150 seconds; the flight tubes maximum relative ambient structural temperature was approximately 0°C, and the tubes were only heated to 145°C, so the flight tubes' temperature should have been significantly below T_g by five minutes. The only unknown is whether the tube which was tested in Figure 5.4 was covered in Kapton tape; if it wasn't, it is possible the flight tubes could have cooled at a slightly slower rate.

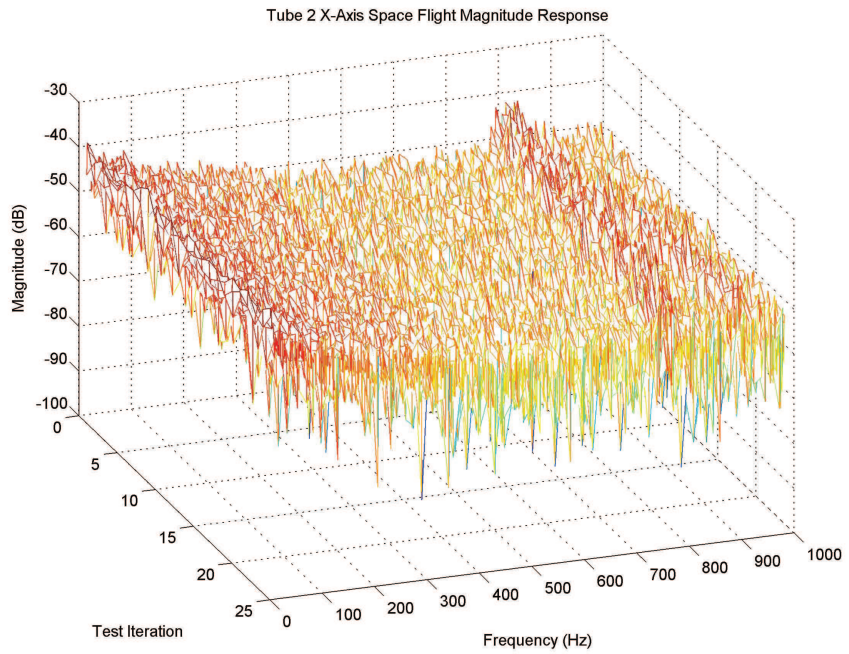


(a)

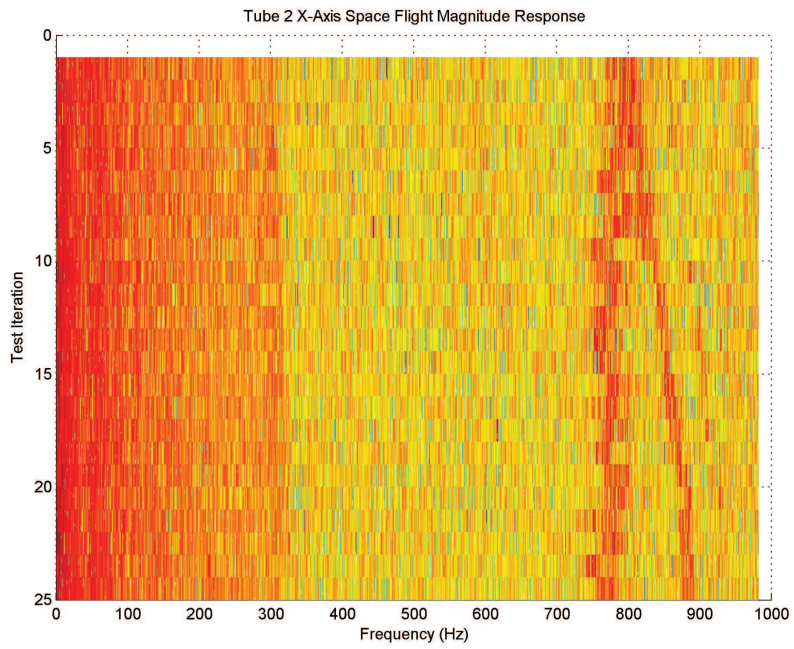


(b)

Figure 4.11: (a) Three dimensional view of the 25 space flight FRFs for tube 1. The plot is colored by amplitude rather than test iteration. (b) Two dimension top view of the three dimensional plot. The resonant frequency drift is easily observed in this view – the 425Hz peak in test one drifts to the left as far as 338Hz, before settling at 386Hz in test 25. Also, a resonant frequency is introduced in the last three test iterations, with an aggressive left drift. This peak settles at 925Hz in test 25.

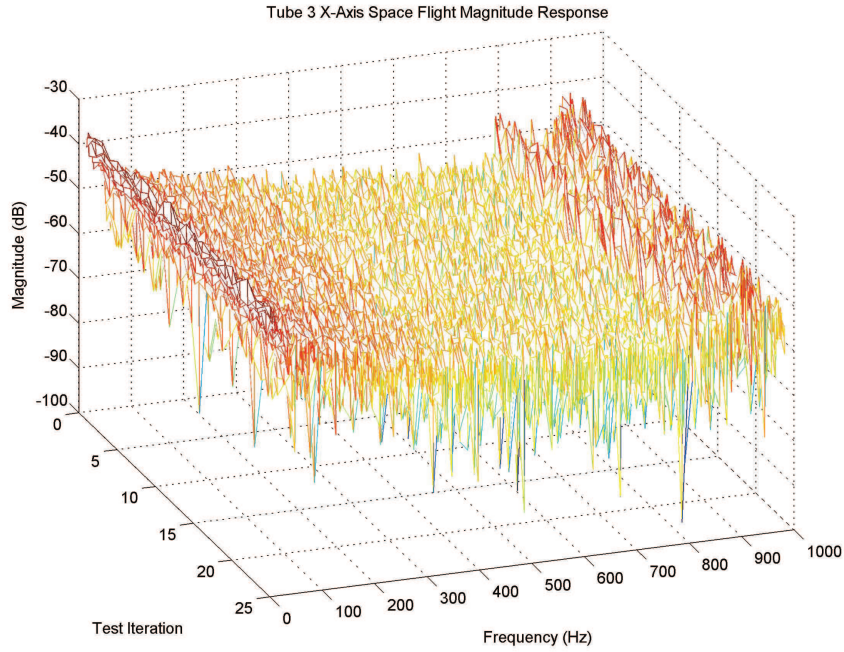


(a)

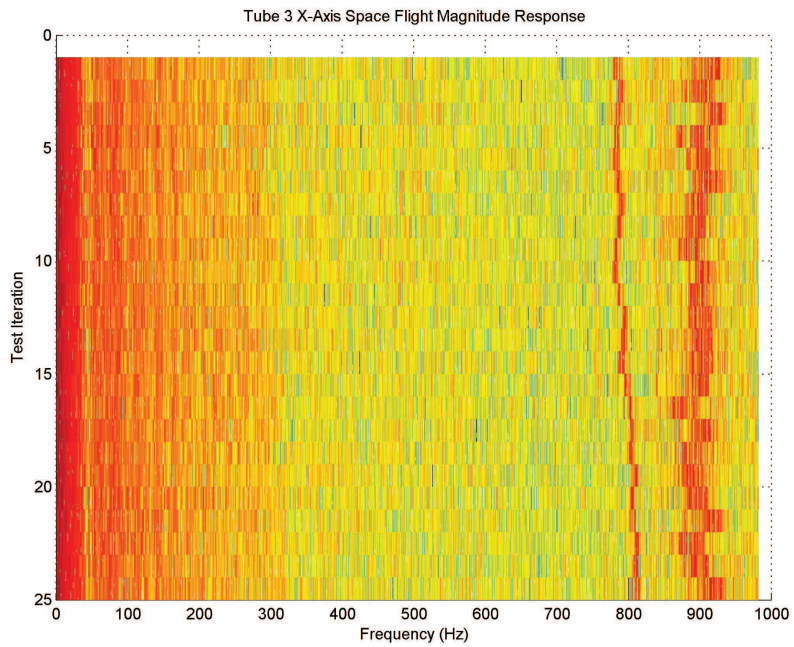


(b)

Figure 4.12: (a) Three dimensional view of the 25 space flight FRFs for tube 2. The plot is colored by amplitude rather than test iteration. (b) Two dimension top view of the three dimensional plot. The resonant frequency drift is easily observed in this view – the 800Hz peak in test one splits and the resultant peaks drift left and right, settling at 765Hz and 914Hz in test 25.



(a)



(b)

Figure 4.13: (a) Three dimensional view of the 25 space flight FRFs for tube 3. The plot is colored by amplitude rather than test iteration. (b) Two dimension top view of the three dimensional plot. The peaks at 786Hz and 928Hz in test one appear to drift less than the peaks in tubes 1 and 2, and end up at 828Hz and 918Hz, respectively.

The second solution suggests the PZTs changed the flight tubes' structural characteristics by slightly deforming the tube bases via the application of the input bending moment on a still warm (and perhaps pliable) tube surface. The PZTs are epoxied to the tube near the basecap, and remain inside of the oven box after the tube has deployed. It is possible the oven insulation prevented the lower portion of the tube from cooling as rapidly as the cooling profiles suggest, which would leave the base slightly flexible in the run-up to vibration testing. The PZTs could conceivably warp the semi-rigid tubes, causing the tubes' structural properties to change over time. Again, the temperature of the base of the tube was not known at the start of the vibration response testing, but the post-deployment image of flight tube 3 indicates the oven doors had closed after deployment (flight tubes 1 and 2 oven doors remained open). The closed oven doors would trap more heat and thus flight tube 3 should then exhibit the greatest peak drift – which it doesn't.

Each tubes' space flight test 25 X-axis FRF is presented in Figures 4.14, 4.15, and 4.16. The peaks are highlighted by red circles and the results are tabulated in Table 4.2. Though the FRFs appear relatively noisy, tube 1's 386Hz peak and tube 2's 765Hz peak line up perfectly with post flight and ground test results for tube 1's second bending mode and tube 2's fifth mode, respectively – very encouraging results. Unfortunately, the peaks seen in the space flight FRF for tube 3 are not seen in the post flight or ground test results. Note the flight tubes all present a ~ 920 Hz peak, an interesting correlation.

For completeness, the averaged three axis FRFs for all three flight tubes (and corresponding coherence data) are presented in Figures 4.17, 4.18, and 4.19.

Table 4.2: Natural frequencies observed during space flight vibration testing.

Space Flight Natural Frequencies	
Tube	Frequency (Hz)
Tube 1	386
	927
Tube 2	768
	914
Tube 3	828
	920

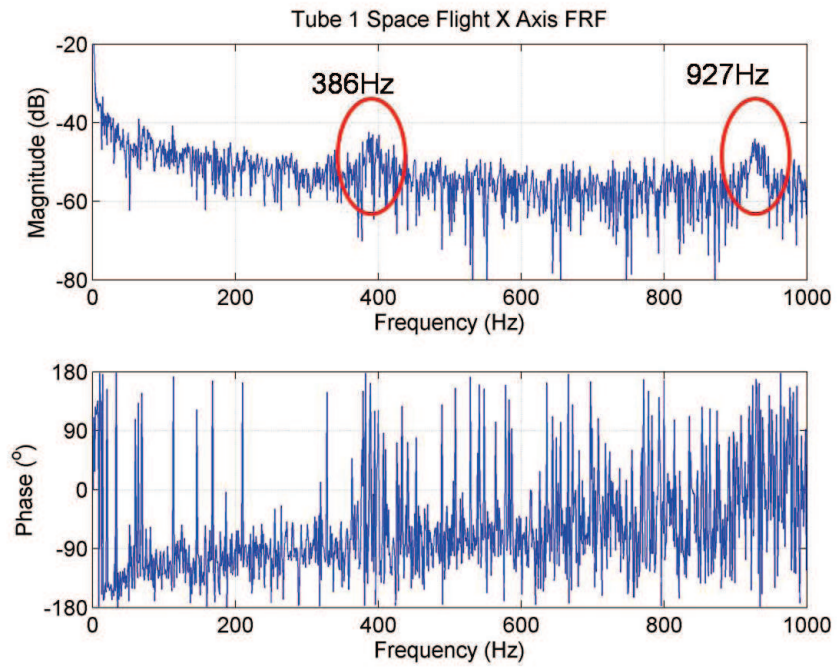


Figure 4.14: Tube 1 X-Axis FRF resulting from the space flight vibration response test. Note the red circles around the resonant frequency peaks at 386Hz and 927Hz.

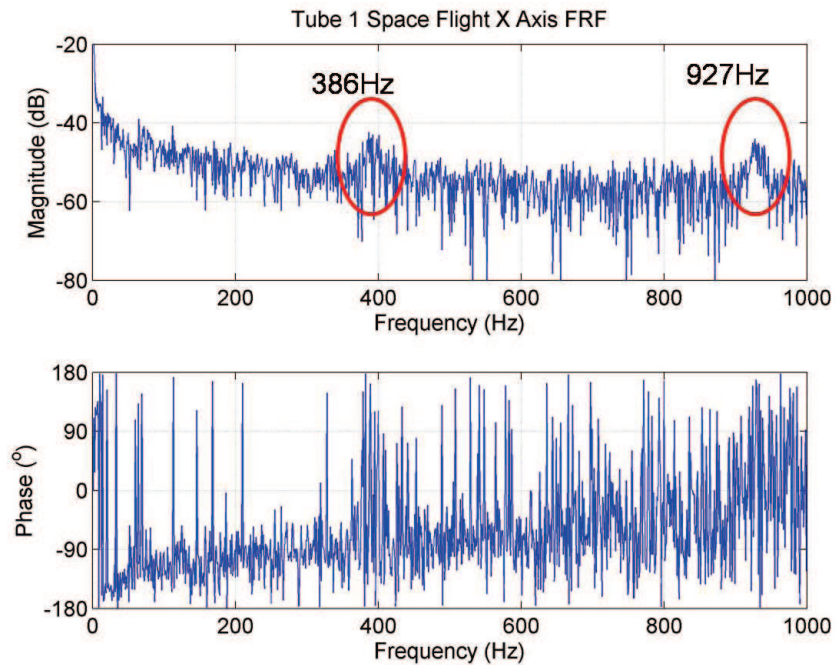


Figure 4.15: Tube 2 X-Axis FRF resulting from the space flight vibration response test. Note the red circles around the resonant frequency peaks at 768Hz and 914Hz.

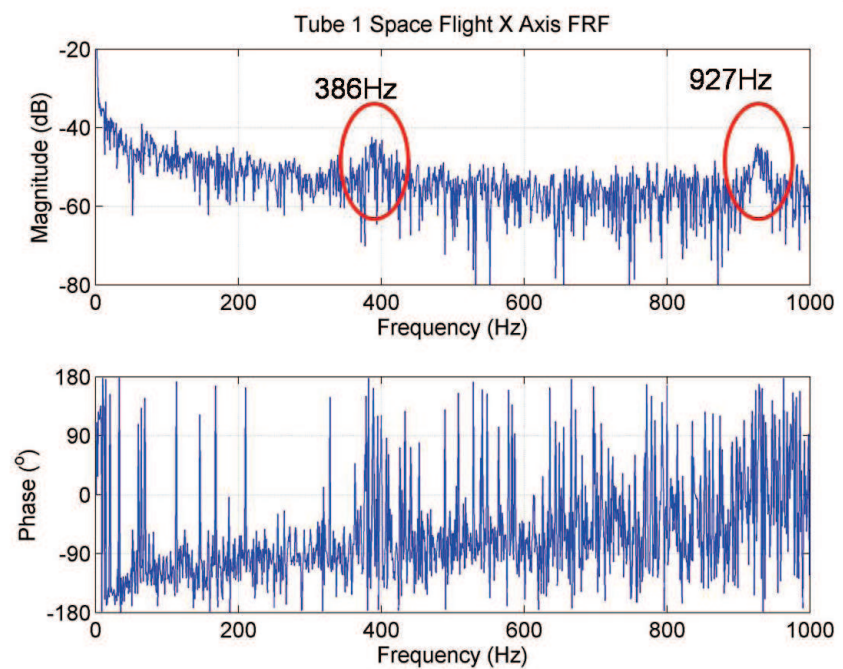
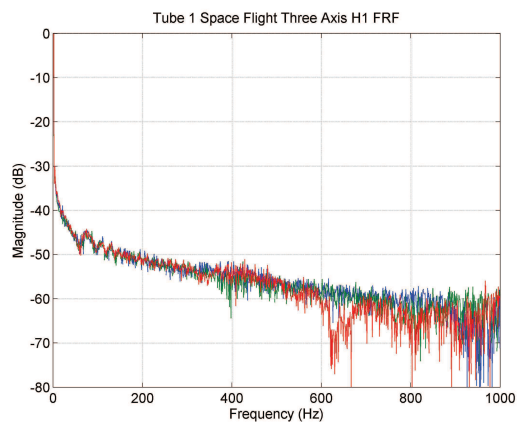
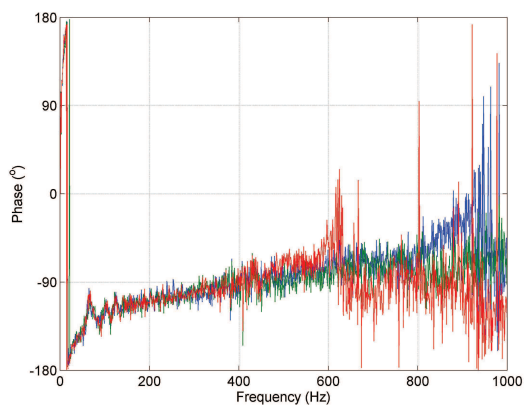


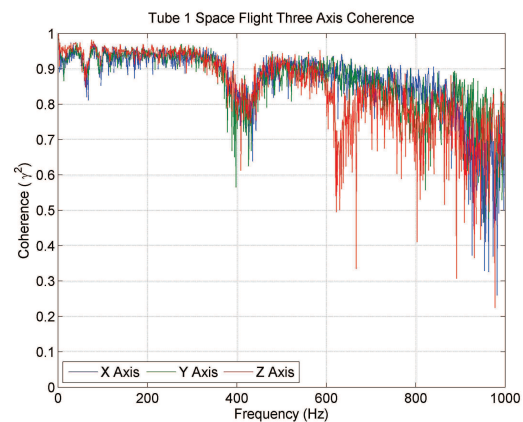
Figure 4.16: Tube 3 X-Axis FRF resulting from the space flight vibration response test. Note the red circles around the resonant frequency peaks at 828Hz and 920Hz.



(a)

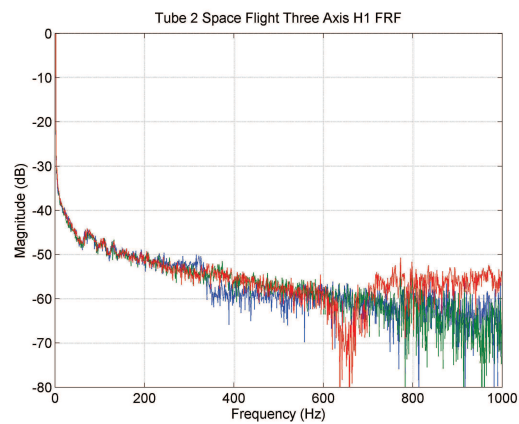


(b)

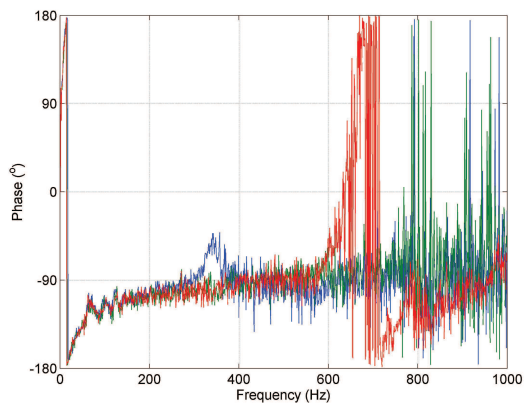


(c)

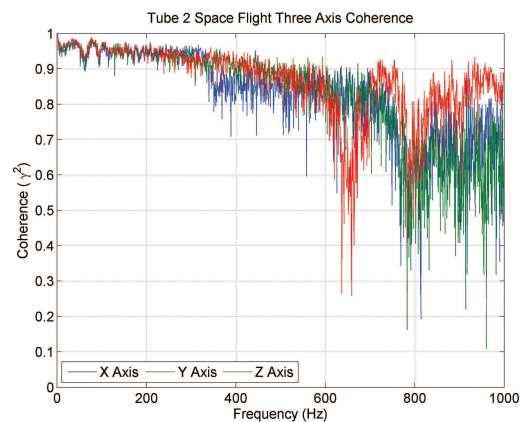
Figure 4.17: (a,b) Space flight three axis FRF for tube 1. (c) Coherence plot corresponding with the tube 1 space flight three axis FRF.



(a)

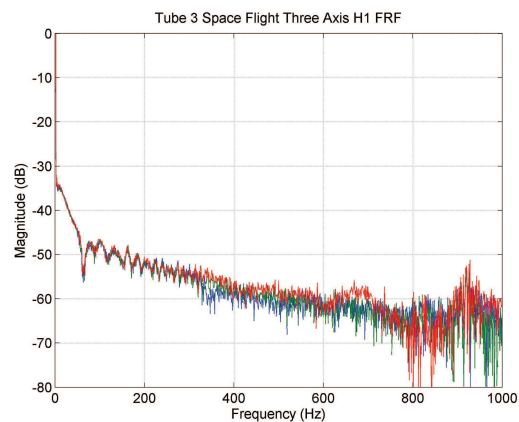


(b)

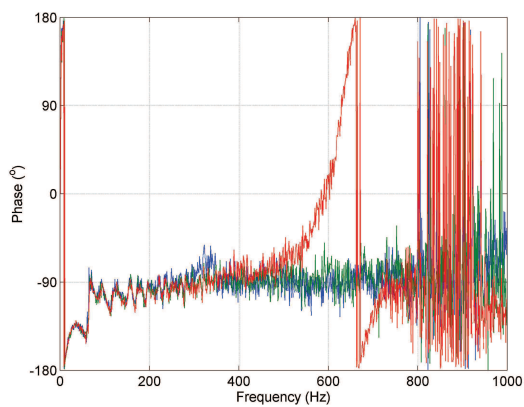


(c)

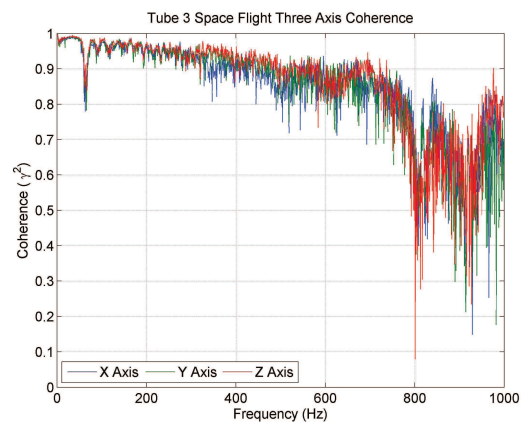
Figure 4.18: (a,b) Space flight three axis FRF for tube 2. (c) Coherence plot corresponding with the tube 2 space flight three axis FRF.



(a)



(b)



(c)

Figure 4.19: (a,b) Space flight three axis FRF for tube 3. (c) Coherence plot corresponding with the tube 3 space flight three axis FRF.

4.1.4 Image Results. The camera system performed flawlessly while on-orbit. The images of the deploying and deployed tubes were downloaded, and post flight images were taken when RIGEX was powered on after returning to AFIT, at which time three sets of LEDs and camera 2 did not function initially. It was thought changing the flight computer power supplies would solve the problem, but camera 2 and the LEDs were still not functional. Thus, the change detection analysis was only conducted for tubes 1 and 3.

4.1.4.1 On-orbit images. Each tube has on-orbit “action photos” of the deployment process. Taken every 0.9 seconds, these images give visual history of the manner in which the tubes deployed in the microgravity environment. There are several images of tube 1 slightly deployed after the pin puller had been activated, each image suggesting the tube had moved slightly further out of the oven. Figure 4.20 is a collage of three images. The first is an image of the stowed tube prior to the pin being pulled. The pin is the long, narrow object crossing the top of the oven in the long direction. The second image is the slightly deployed tube – this is a result of the internal strain energy resulting from the folding process. The final image is the fully deployed tube. The LEDs provided ample light, and their reflections are readily apparent in all three photos.

Tubes 2 and 3 have only one interim deployment photo due to the photo rate and the time the tubes took to deploy. The 0.9 second frame rate only allowed for one image in the < 1 second deployment process. Figures 4.21 and 4.22 show these images in collage format. Vertical is the Y-axis and horizontal is the X-axis in these images.

4.1.4.2 Change Detection Analysis. Change detection analysis is a technique of overlaying two independent samples of same data separated by time and observing any changes. If the data overlays do not align, it is an indication of environmental effects or time dependance. The overlays of space flight and post space flight images of tubes 1 and 3 did not precisely align, which warranted further investigation. It is possible for either the tubes or the cameras to have changed position through the course of reentry/reintroduction to gravity, the shuttle landing, or shipping. The camera positions can be checked by overlapping space flight images over post space flight images

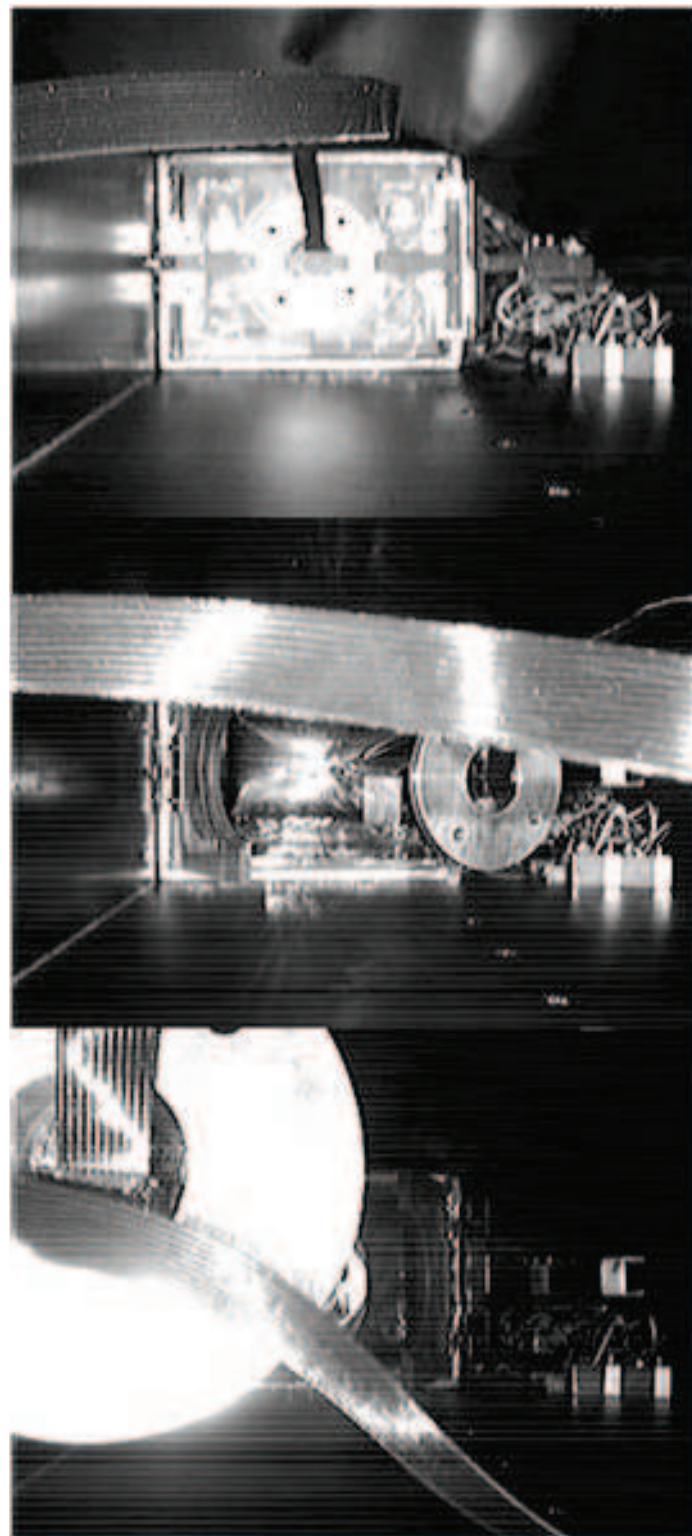


Figure 4.20: A collage of images taken during the deployment of tube 1. The top image is a stowed tube, prior to pin puller activation. The second is the result of the strain energy deployment, and the third is the fully deployed tube.

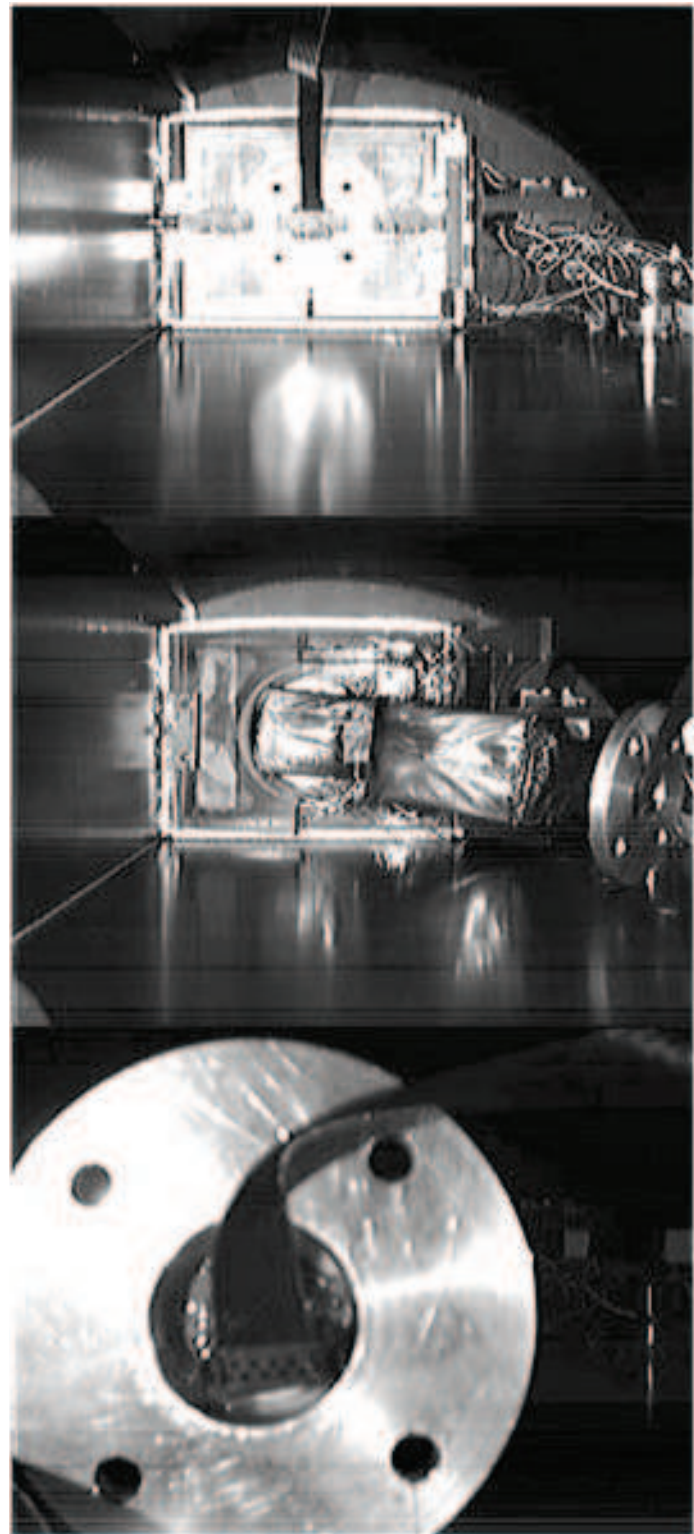


Figure 4.21: A collage of images taken during the deployment of tube 2. The top image is a stowed tube, prior to pin puller activation. The second image is partial inflation, and the third is the fully deployed tube.

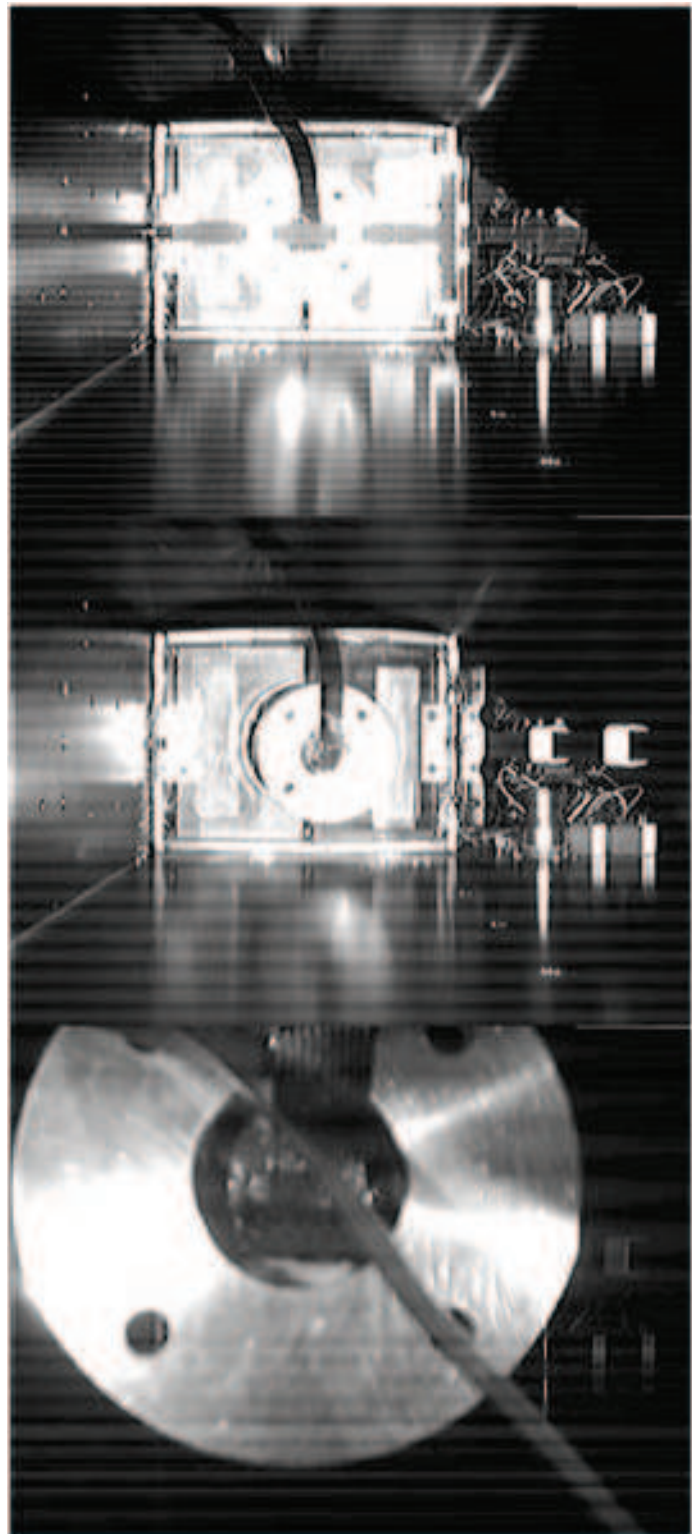


Figure 4.22: A collage of images taken during the deployment of tube 3. The top image is a stowed tube, prior to pin puller activation. The second image is immediately following the pin puller activation, and the third is the fully deployed tube.

and checking the overlay of hard mounted components and structural landmarks, such as the ovens and the rim of the bottom plate. If the landmarks align within one pixel it is assumed the camera position remained static. The next step is to determine the number of pixels required to span an object of known distance, such as the bolt holes in the tube endcap. This gives a $\frac{\text{inch}}{\text{pixel}}$ ratio, which is applicable for distances in the same X-Y plane (same distance from the focal plane) – hence the choice of the endcap bolt holes. The final step is to determine the X and Y-axis changes from the space images to the post space flight images.

For tubes 1 and 3, a space flight image of a deployed tube was loaded into MATLAB as an array (using MATLAB's Image Processing Toolbox) of intensity per pixel. A post flight image was then loaded in as another array, and the intensities from the two images were simply subtracted (Equation 4.2), resulting in a hybrid image.

$$\text{Space Flight Image} - \text{Post Space Flight Image} = \text{Hybrid Image} \quad (4.2)$$

Though the ambient light conditions changed, the shapes were still discernable. The next step was to check for collocation of the landmarks. The resulting array was opened with the `imtool` command, and the alignment of the oven borders (within one pixel picture to picture) confirmed cameras 1 and 3 had not moved. Figure 4.23 shows the hybrid image of tube 1 with the endcap bolt hole pixels measured and the X and Y-axis pixel deviations measured. In this image there are actually 2 Y-axis deviations measured, with the 35 pixel measurement assumed correct. The final step was to apply the number of pixels to the known diameter of the bolt hole. Equation 4.3 is the Tube 1 calculation:

$$0.2945 \text{ inches} \div 26.00 \text{ pixels} = 0.0113 \frac{\text{inch}}{\text{pixel}} \quad (4.3)$$

Table 4.3: Change detection analysis results for X and Y measured deviations for all three tubes.

Tube	X Deviation (inches)	Y Deviation (inches)
1	0.0339	-0.3618
2	not measured	not measured
3	w/in error	0.2836

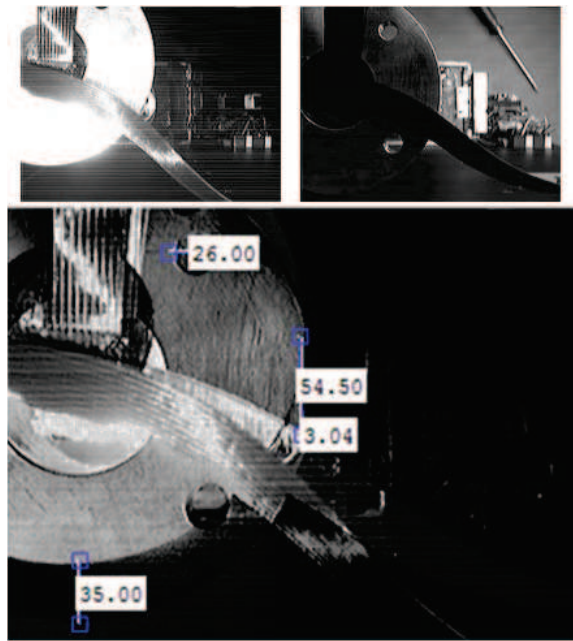


Figure 4.23: A collage of the space flight image (upper left), the post space flight image (upper right), and the hybrid image. The pixel measurements are shown for the X and Y-axis deviations and the endcap bolt hole.

The $\frac{\text{inch}}{\text{pixel}}$ solution for tube 3 was $0.0122 = \frac{\text{inch}}{\text{pixel}}$. The measurement error is assumed to be two averaged pixels (0.0235 inches). The results of the change detection analysis are shown in Table 4.3, and indicate both tube 1 and 3 moved in the $\pm Y$ direction during the transition from microgravity to gravity, and tube 1 barely moved in the X direction. These results will be combined with the FaroArm results (Section 4.3.4.1) to determine exact on-orbit position.

4.2 Post Space Flight Test Results

Post space flight testing consisted predominantly of vibration testing, and used the flight computer, dSpace, and SignalCalc. The first post space flight test was to be an end-to-end (minus heating and deployment) vibrations test using the flight computer and flight code. The failure of the flight computer to adequately power the PZT, combined with the other anomalies led to the work discussed in Appendix A. Vibration testing continued, moving to utilize dSpace as a surrogate flight computer and using SignalCalc concurrently as an immediate check for data quality (see the test setup in Figure 3.5). An additional SignalCalc test using a substantially increased number of frequency lines

and averages was conducted to generate high fidelity accelerometer data, suitable for comparison with the laser vibrometer testing.

4.2.1 Changes from Space Flight Configuration.

Anomaly resolution efforts led to changing out two power supplies in the flight computer stack and attaching new accelerometers to the tube endcaps. The flight accelerometers (which were no longer functional) were epoxied into the cavity in the endcap and could not be removed. This meant the new accelerometers added more tip mass to the tube. Adding tip mass to a cantilevered beam often reduces the first bending natural frequency, and can replace the standard cantilever beam second bending mode with the standard first bending mode of a pinned pinned beam. Section 5.3 compares the ground vibration testing vibration results (conducted without the second accelerometer) with the post space flight vibration tests to determine if the second accelerometer changed the modal properties of the RIGEX tubes.

4.2.2 Flight Computer Test Results.

A post space flight repeat of the space flight vibration response test was never successfully conducted. The first potential problem was a bad power supply not providing power to the PZTs. The flight power supplies were replaced, and after the new power supplies were verified, the test was run again, but was still unsuccessful. After checking the wiring connections, it was decided that the problem could lay in the components between the computer stack and all three PZTs (though unlikely). The dSpace testing with the specially-created cables disproved this theory (Section 4.2.3). After more troubleshooting and observing the weak space flight accelerometer data (in response to the vibration test data), the current theory of a bad Butterworth filter board was reached. The eight order Butterworth filter board worked correctly in the last system level thermal vacuum test (audible confirmation of PZT actuation), but the flight computer configuration was broken after that test and an end-to-end test could not be rescheduled before RIGEX was shipped to Cape Canaveral. It is believed this preflight configuration change may have impacted the input voltage, limiting the PZT actuation. Alternatively, the presumed on-orbit power surge (Appendix A) could have caused damage to the eighth order Butterworth filter board.

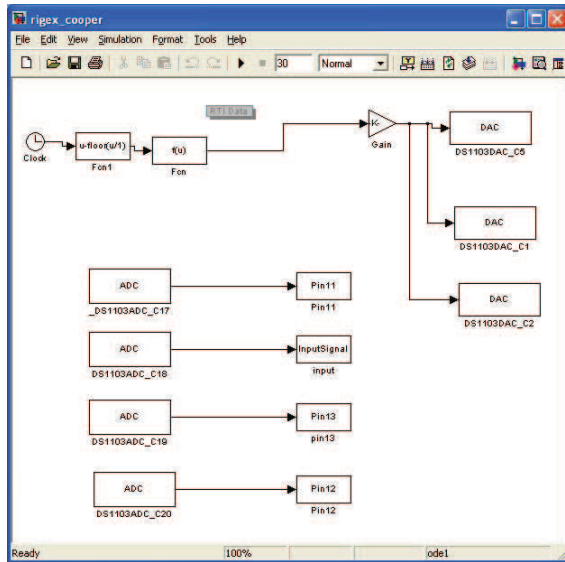


Figure 4.24: The SimuLink simulation used to drive the dSpace vibration response testing. DAC channels 1, 2, and 5 provided the input chirp signal to the Butterworth filter, the oscilloscope, and SignalCalc (when necessary). ADC channels 17, 18, 19, and 20 collected the filtered input signal and the three axis accelerometer voltages.

4.2.3 dSpace Test Results. Without a functioning flight computer, vibration testing turned to using dSpace as a surrogate flight computer. These tests were performed as proscribed for the flight computer with one exception – a fourth order Butterworth filter was used in place of an eighth order filter. Moody [29] had originally tried a fourth order Butterworth filter, but moved to the eighth order filter to further eliminate aliasing. The SimuLink *.mdl used to drive the input signal is shown in Figure 4.24, which shows the output and input channel relations. The SignalCalc settings are provided in Table 4.4. Given a 2000Hz input signal (though filtered over 1000Hz) over one second, the SignalCalc Frequency Span setting was selected to match the input signal and the Frequency Lines setting was selected to closely match the 1 second test duration. 25 Stable averages matched the 25 iterations of the vibration response test.

The results from the tests are acceptable and thus validate this method as a substitute for the flight computer-based vibration testing. Two axis FRFs and coherence plots are presented in Figures 4.25, 4.26, and 4.27. As a side note, the accelerometer responses were analyzed in conjunction with a idealized fourth order Butterworth filtered signal,

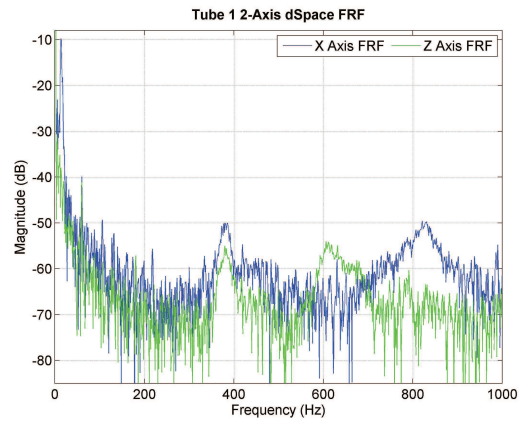
Table 4.4: SignalCalc settings for the dSpace-driven vibration response test.

Setting	Values	Comments
Frequency Span δF	2000Hz 1.250Hz	Set to 2000Hz to observe filter cutoff effects
Frequency Lines	1600	Set to match 1 second chirp
Time Span δT	0.8s 195 μ s	Resulted from Frequency Inputs
Block Size	4096	
Averages	25 Stable Averages	Average the 25 test iterations

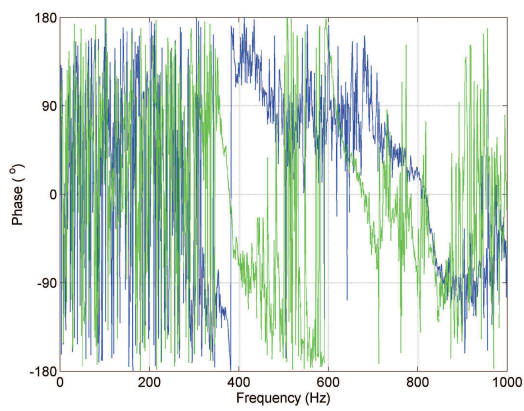
similar to that used in Section 4.1.3.3, with no discernable changes from the following FRFs – thus verifying the validity of the idealized filtered signal.

Only X and Z-axis data is presented here, as the Y data was relatively noisy and distracting. Given the relative symmetry of the cantilevered tube and the X-axis input, the X-axis FRF is assumed to reflect a Y-axis FRF given a Y-axis input. The phase wrapping phenomena is present in these plots as well, and the Butterworth filter introduced a 60Hz peak that is not seen in any of the other vibration testing results (except the concurrent SignalCalc results), which is believed to be associated with the 60Hz alternating current from the wall outlet power supply.

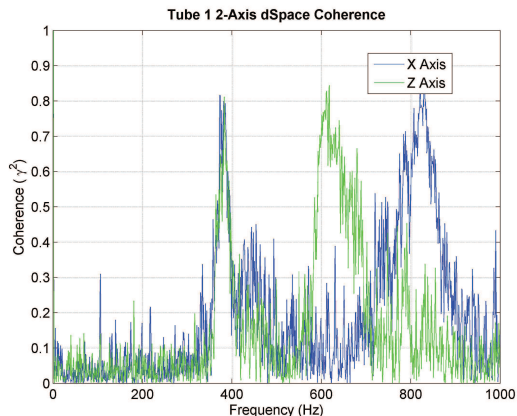
The poor coherence data is readily evident. Upon review of the dSpace sampled time history accelerometer data, it was observed the responses (given in voltages) were nearly all within one bit up or down from the median \pm bit value, recorded at four significant digits. The resonant frequencies were the exception – these values jumped two or three bits. Review of the concurrent SignalCalc data (discussed in Section 4.2.3.1) showed much more lively time histories, recorded at five significant digits. This suggests most of the response data is contained within the fifth significant digit, beyond the precision at which dSpace could measure. Thus, the noisy FRF and poor coherence data is explained: the recorded accelerometer data was typically within the noise distinguishable by dSpace, save the resonant responses, which were a few bits greater than the noise. In turn, the increased response (beyond the noise floor) explains why the coherence values increase at the peaks, instead of decrease – the natural frequencies are the only region in which dSpace developed adequate signal-to-noise ratios.



(a)

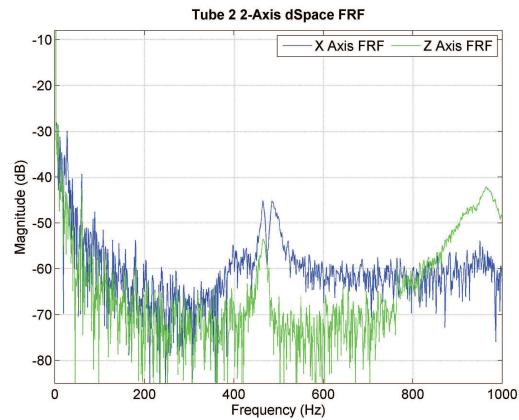


(b)

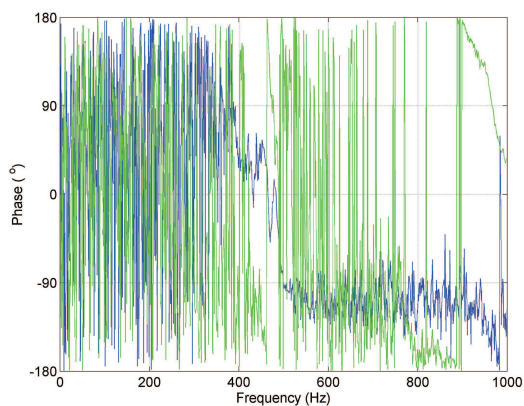


(c)

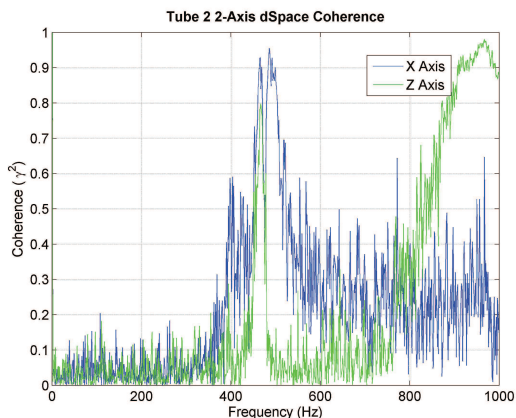
Figure 4.25: (a,b) Resultant two axis FRF from tube 1 post space flight dSpace vibration testing. (c) Two axis coherence plot from tube 1 post space flight dSpace vibration testing.



(a)

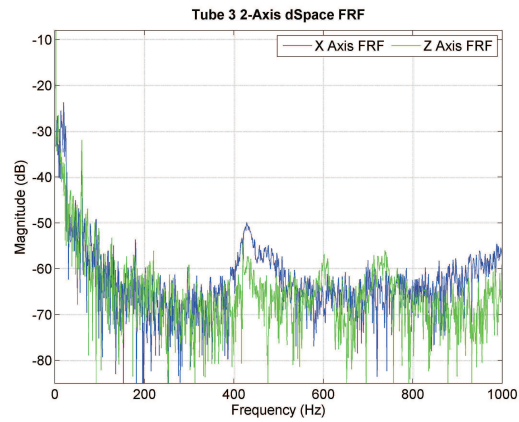


(b)

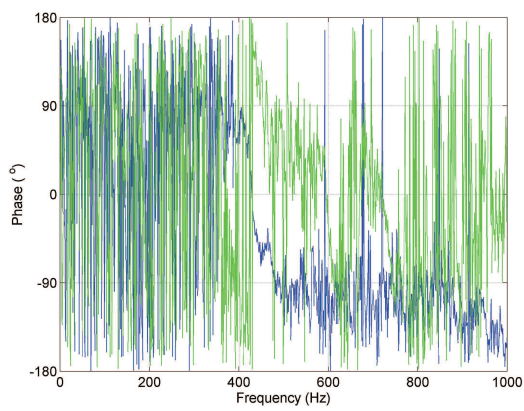


(c)

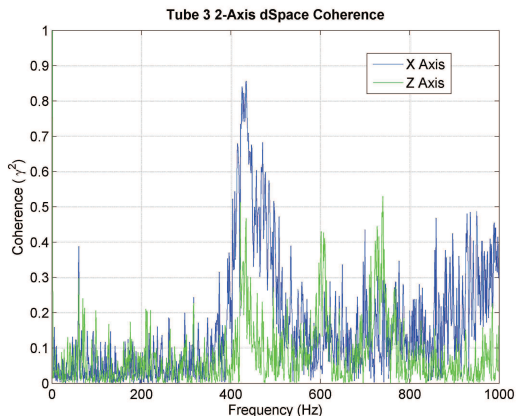
Figure 4.26: (a,b) Resultant two axis FRF from tube 2 post space flight dSpace vibration testing. (c) Two axis coherence plot from tube 2 post space flight dSpace vibration testing.



(a)



(b)



(c)

Figure 4.27: (a,b) Resultant two axis FRF from tube 3 post space flight dSpace vibration testing. (c) Two axis coherence plot from tube 3 post space flight dSpace vibration testing.

A cursory validation of the idealized filtered input signal was conducted as part of this test. The dSpace sampled accelerometer data was analyzed in conjunction with the idealized filtered input data used in Section 4.1.3.3; these FRFs were compared to the FRFs generated with real sampled input data (Figures 4.25, 4.26, and 4.27). The FRFs lined up with no appreciable changes.

The tube natural frequencies pulled from dSpace post space flight test results are presented in Table 4.5. The table includes comments on confidence, occurrence, and coherence, and do not include the 60Hz peak. The increasing noise level beyond 1000Hz made it challenging to pull out higher level peaks, and thus only clear peaks were selected. One feature of these FRFs are peaks that have split, and are probably a result of asymmetry in the deployed tube.

4.2.3.1 Signal Calc Test Results. SignalCalc was used twice during the post space flight testing: first, it was used to provide the “truth” data for dSpace vibration test, and second it was used for an increased resolution (increased sample rate, increased averaging, and additional frequency lines) accelerometer-based vibration test. The coherence data is much better and the plots considerably cleaner. SignalCalc has a better ADC than dSpace and recorded accelerometer voltage data to five significant digits, which resulted in an increased signal to noise ratio – improving the coherence and reducing the noise on the FRFs markedly. The “truth” FRFs from the dSpace test are presented in Figures 4.28, 4.29, and 4.30; the peaks line up with the previous dSpace FRFs, but the coherence is significantly better. The X, Y, and Z-axis ”truth” vibration test results for each tube are presented in Figures 4.31, 4.32, and 4.33. These figures dramatically demonstrate the effects of significant increase in Frequency lines. Table 4.6 provides the settings

A problem with the SignalCalc and dSpace driven tests is present in the last 6 plots – the low frequency data is quite noisy. As discussed earlier, it is believed the flight computer could not drive enough voltage through the transformers to adequately excite the PZTs and distinguish vibration response from the noise. In particular, this impacts the low frequency range, where more voltage is required to actuate the PZTs. This is an

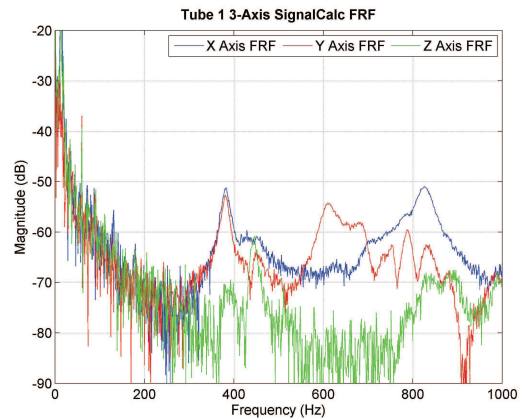
Table 4.5: X and Z-axis natural frequencies picked from Figure 4.25 - 4.27.

Tube	X-Axis Peak	Z-Axis Peak	Comment
	Frequency (Hz)	Frequency (Hz)	
1	13		Good Peak
	381	381	Good Peak, Good Coherence
		681	Good Coherence, Phase Change
	829		Good Peak, Good Coherence
2	27		Good Peak
	398	395	Good Peak, Marginal Coherence
	465	465	Very Good Peak, Good Coherence
	485		Split Peak, Very Good Coherence
		965	Very Good Peak, Good Coherence
3	19, 24		Split Peak
	431	431	Very Good Peak, Good Coherence
		602	Marginal Peak and Coherence

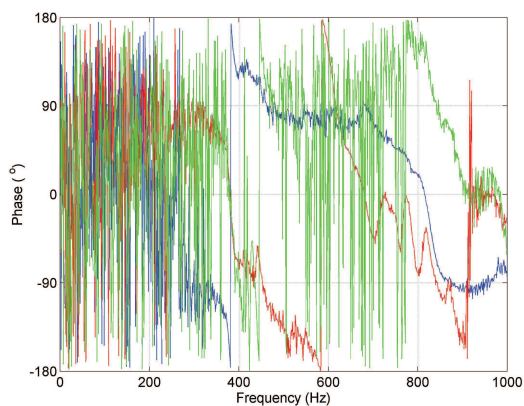
Table 4.6: Settings for the increased resolution SignalCalc vibration response test.

Setting	Values	Comments
Frequency Span	2000Hz	
δF	0.156Hz	
Frequency Lines	12800	Set maximize resolution
Time Span	6.4s	Resulted from Frequency Inputs
δT	195 μ s	
Block Size	32768	
Averages	25 Stable Averages	Average the 25 test iterations

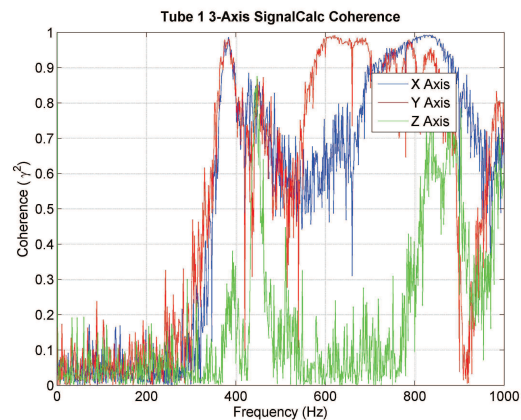
important result: all of the accelerometer based testing had noisy low frequency data, suggesting the $\pm 5V$ input voltage and flight transformers were not adequate to stimulate the low frequency modes. This was a preflight concern, but design limitations prevented any increase in voltage amplification.



(a)

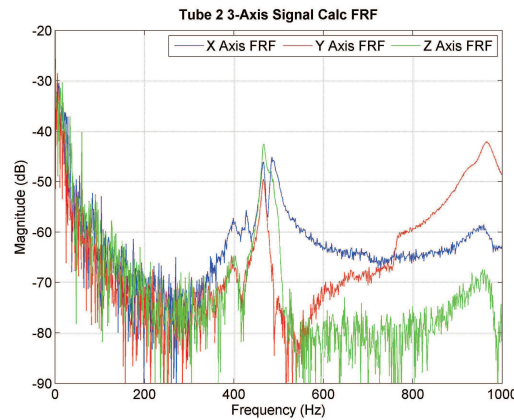


(b)

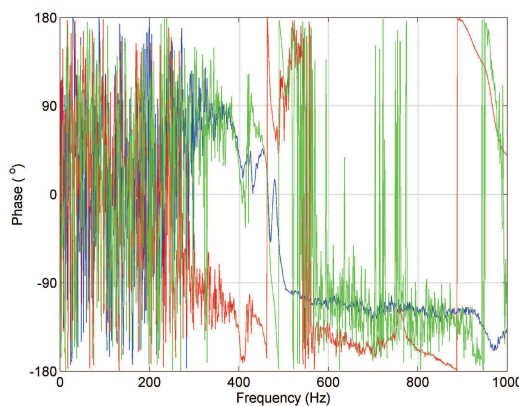


(c)

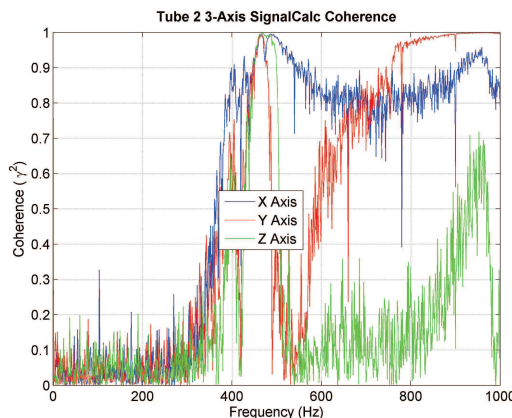
Figure 4.28: (a,b) Three axis SignalCalc FRF resulting from the tube 1 post space flight dSpace vibration testing. (c) Three axis SignalCalc coherence plot from the tube 1 post space flight dSpace vibration testing.



(a)

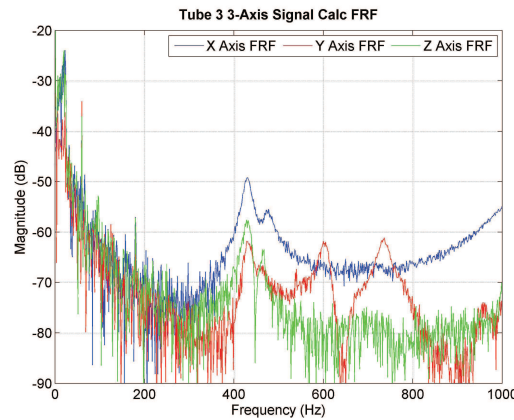


(b)

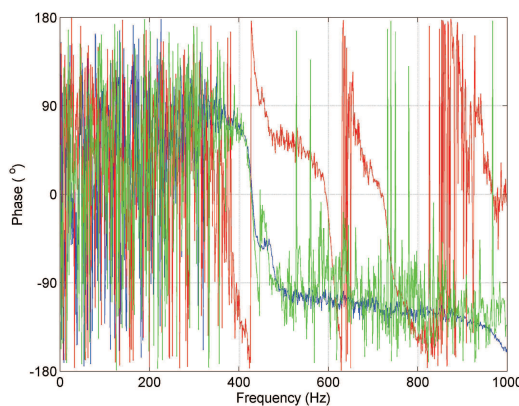


(c)

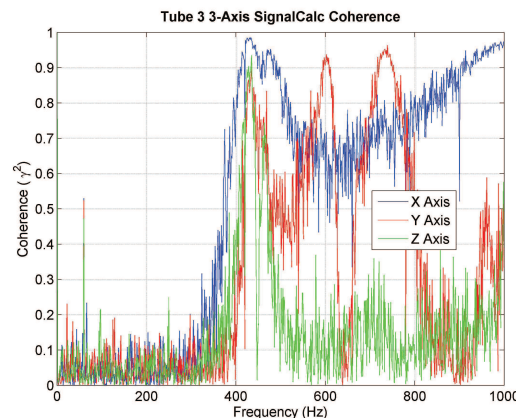
Figure 4.29: (a,b) Three axis SignalCalc FRF resulting from the tube 2 post space flight dSpace vibration testing. (c) Three axis SignalCalc coherence plot from the tube 2 post space flight dSpace vibration testing.



(a)

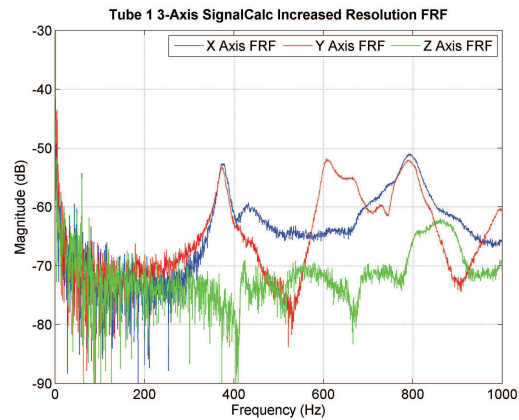


(b)

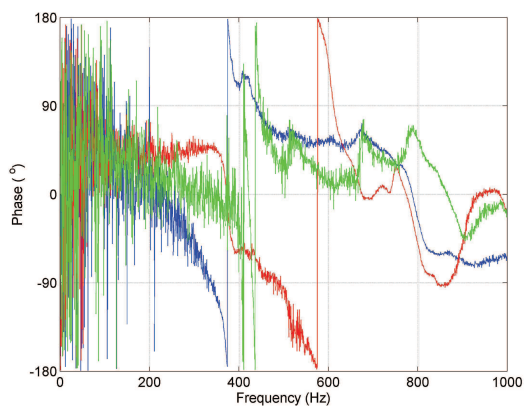


(c)

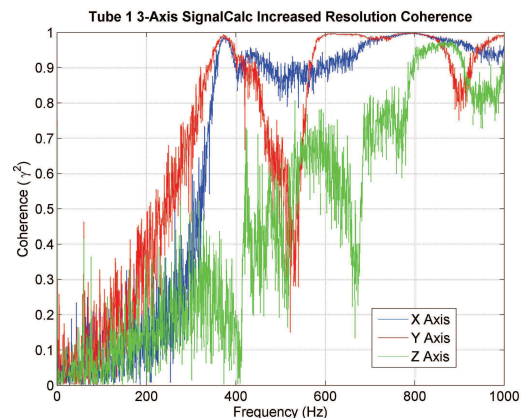
Figure 4.30: (a,b) Three axis SignalCalc FRF resulting from the tube 3 post space flight dSpace vibration testing. (c) Three axis SignalCalc coherence plot from the tube 3 post space flight dSpace vibration testing.



(a)

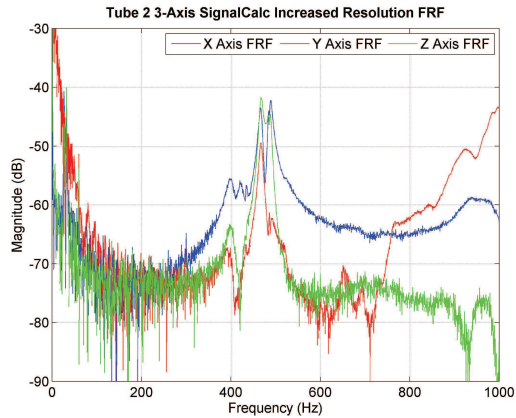


(b)

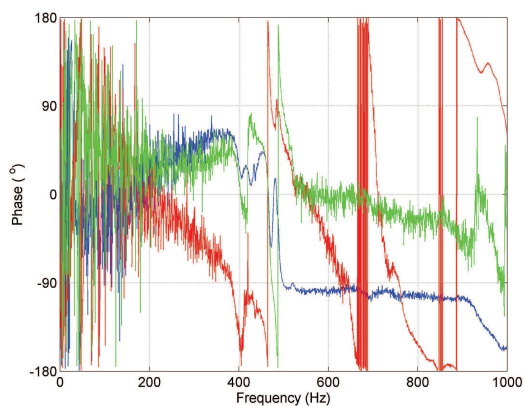


(c)

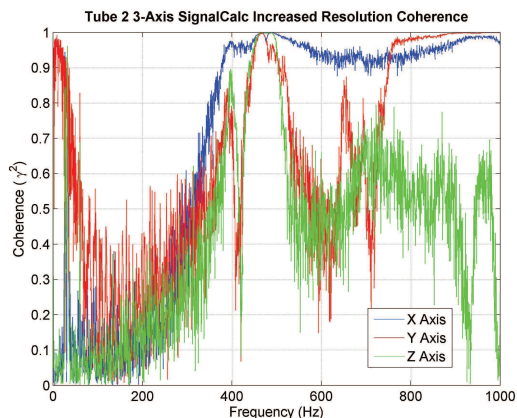
Figure 4.31: (a,b) Three axis SignalCalc FRF resulting from the tube 1 post space flight high resolution vibration testing. (c) Three axis SignalCalc coherence plot from the tube 1 post space flight high resolution vibration testing.



(a)

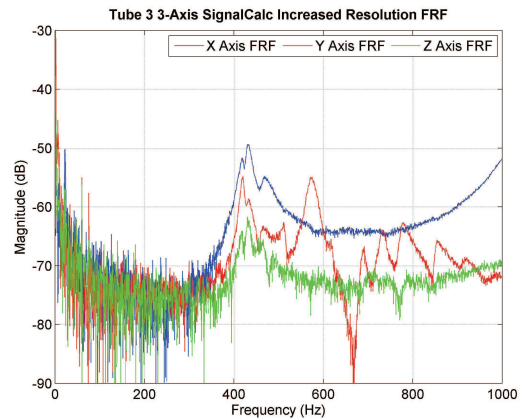


(b)

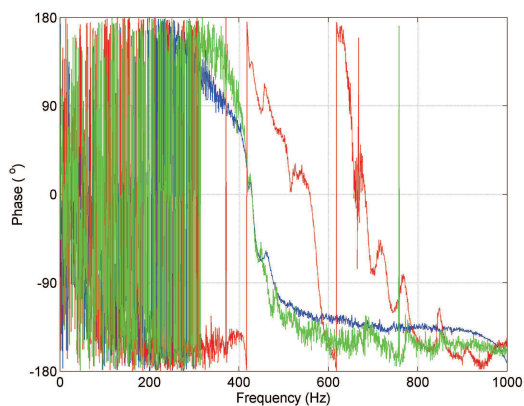


(c)

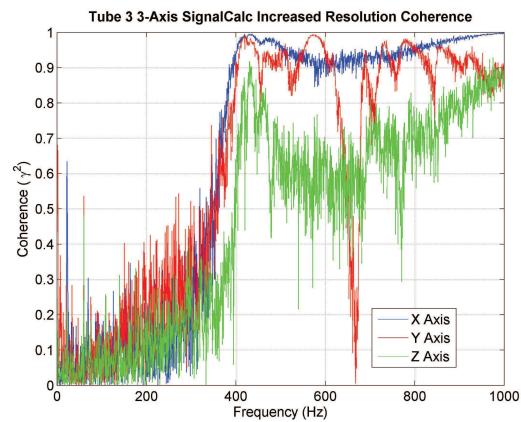
Figure 4.32: (a,b) Three axis SignalCalc FRF resulting from the tube 2 post space flight high resolution vibration testing. (c) Three axis SignalCalc coherence plot from the tube 2 post space flight high resolution vibration testing.



(a)



(b)



(c)

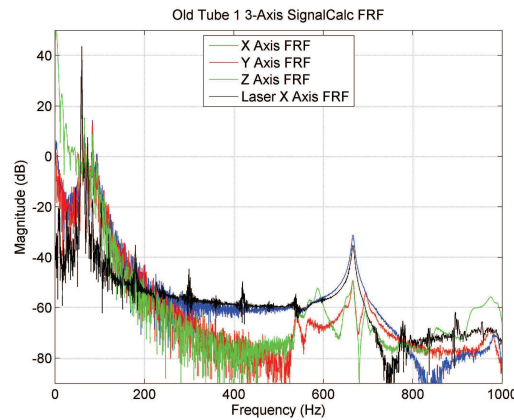
Figure 4.33: (a,b) Three axis SignalCalc FRF resulting from the tube 3 post space flight high resolution vibration testing. (c) Three axis SignalCalc coherence plot from the tube 3 post space flight high resolution vibration testing.

4.3 Ground Test Results

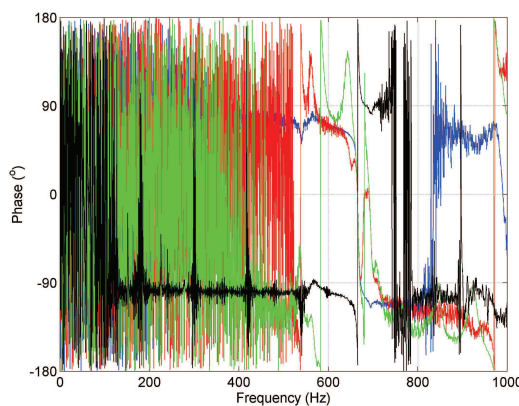
Ground testing includes validation of the previous student's preflight vibration testing results, conducting additional vibration testing on the ground with higher fidelity equipment, and using the FaroArm for a deviation analysis. All of the testing in this section was successful – the vibration testing of the old tubes validated the previous students findings, the Polytec triaxial laser provided excellent visualization of the mode shapes, and the Faro data is combined with the space flight images for a final on-orbit deviation analysis.

4.3.1 Validation of Previous Ground Testing Results. The validation of the previous ground testing was conducted using SignalCalc, tubes used during preflight testing, the triaxial accelerometers, and the 1-D Laser vibrometer. These tests were successful in both validating the previous student's results and verifying the specially-created interface cables did not alter the PZT input signal or the accelerometer output signals. These tubes were tested using the same input signal as the flight tubes, but without the fourth order butterworth filter. Three tubes were tested: two tubes similar in nature to Single and Moody's photos of the test setup (pristinely deployed tube, no Kapton), and a third Kapton covered tube, which was not pristinely deployed. In the analysis, old tubes 1 and 2 are the non-Kapton pristine tubes, and old tube 3 is the Kapton tube. The SignalCalc settings were identical to the increased resolution SignalCalc test discussed in Section 4.2.3.1.

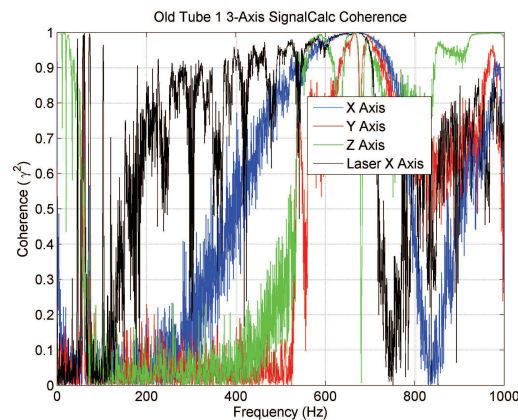
Old tubes 1 and 2 FRFs line up with Goodwin's [11] lightweight accelerometer vibration testing results, with corresponding natural frequencies of ~ 60 and ~ 660 Hz, but it appears both of these peaks are split, which is not observed in Goodwin's results. Old tube 3 had results similar to the flight tubes, with natural frequencies of ~ 47 and ~ 456 Hz. The results are shown in Figures 4.34, 4.35, and 4.36. Note the laser vibrometer's poor coherence data for old tubes two and three – it is believed the laser vibrometer's coaxial cable was having intermittent shorts, introducing noise to the signal. This effect was not noticed until after the test configuration was broken. The test was not re-conducted because the accelerometers provided sufficient high quality data. Also,



(a)

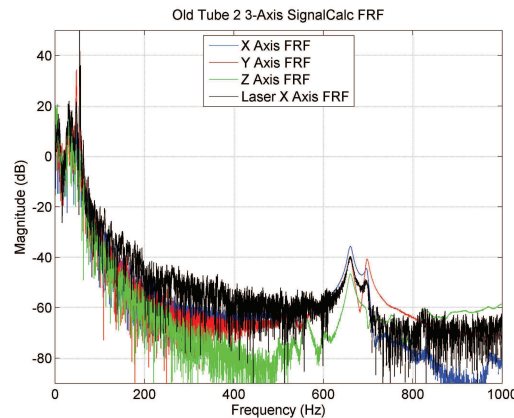


(b)

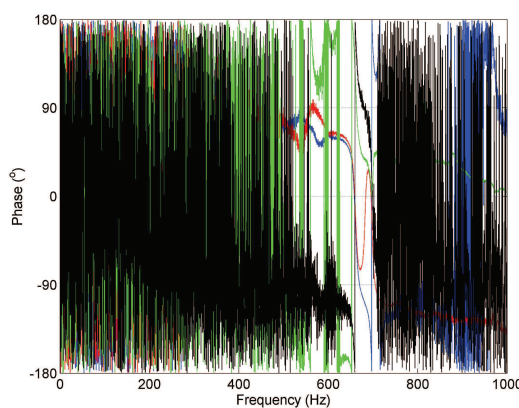


(c)

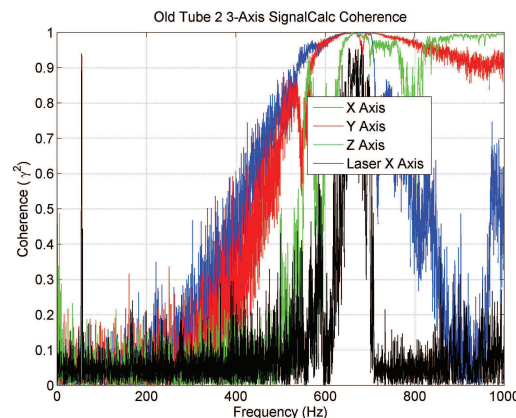
Figure 4.34: (a,b) Three axis SignalCalc FRF resulting from old tube 1. The data was collected with the triaxial accelerometers and the 1-d laser vibrometer. (c) Coherence plot from the old tube 1 vibration test.



(a)

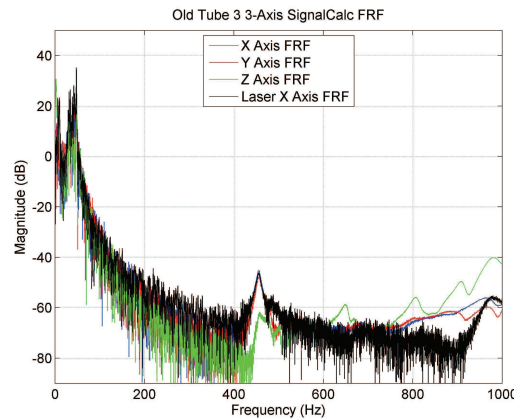


(b)

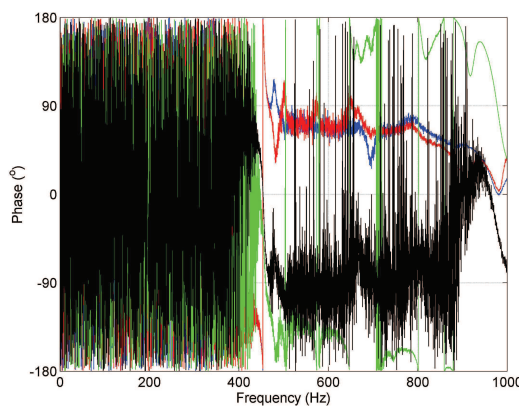


(c)

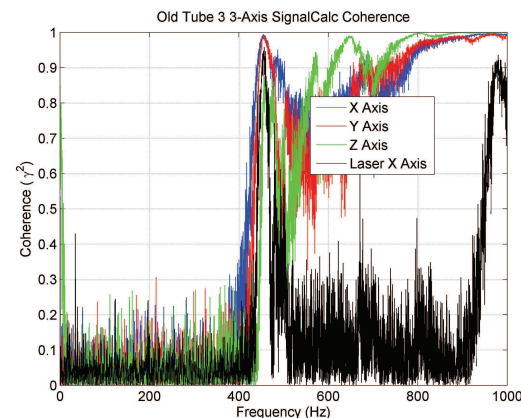
Figure 4.35: (a,b) Three axis SignalCalc FRF resulting from old tube 2. The data was collected with the triaxial accelerometers and the 1-d laser vibrometer. (c) Coherence plot from the old tube 2 vibration test.



(a)



(b)



(c)

Figure 4.36: (a,b) Three axis SignalCalc FRF resulting from old tube 3. The data was collected with the triaxial accelerometers and the 1-d laser vibrometer. (c) Coherence plot from the old tube 3 vibration test.

the low frequency data is again noisy, a result of the limited voltage input. This further implicates the theory of insufficient voltage amplification by the flight hardware, as these tests were conducted using a spare flight voltage transformer.

The successful match-up of these FRFs with Goodwin's FRFs validates the accelerometer and laser vibrometer-based vibration response test procedures conducted in post space flight testing, and verifies the test configuration (specifically, the use of the specially-manufactured interface cables) did not influence the test results.

4.3.2 Single Axis Laser Vibrometer Testing. The single axis (1-D) laser vibrometer SignalCalc flight tube vibration testing went as planned. The results are superfluous, however, as the X and Y-axis vibration response data is very similar to the high resolution accelerometer data shown above in Figures 4.31, 4.32, and 4.33. As previously mentioned, the 1-D laser was used in the testing of the old tubes as well.

4.3.3 Triaxial Laser Vibrometer Test Results. The PSV-400-3D flight tube vibration response tests went phenomenally. Very high quality FRFs were produced and the operating deflection shapes were captured from the visualization software and are presented here. These FRFs are considered "truth" data for each tube, against which the previous discussed results will be compared in Chapter 5. Each tube had four successful tests: two 0 – 500Hz and two 0 – 5000Hz tests, each range tested with and without the accelerometer cable attached. It was quickly determined the accelerometer cable had a negligible effect on the tube's vibration response. For the 0 – 500Hz testing, a low voltage amplifier was added inline with the input signal to boost the low frequency input voltage and thus increase excitation and the lower frequency response. The voltage amplification dramatically increased the signal-to-noise ratio of the low frequency responses, providing clear frequency response data below 500Hz and very clean coherence data. Another benefit of the Polytec software was the 3-D mapping of the scanned surface, yielding a representation of the surface of the deployed tubes. Table 4.7 presents the settings used for this set of tests.

Table 4.7: SignalCalc settings for the increased resolution SignalCalc vibration response test.

Setting	Values	Comments
Frequency Span	500, 5000Hz	500Hz test utilized voltage amplifier
Frequency Lines	6400, 12800	6400 lines for 500Hz test
Averages	25 Stable Averages	Average the 25 test iterations

4.3.3.1 Tube 1 Results. Figure 4.37 shows the grid of scan points which exhibit a slight tilt in the X-axis, confirmed by the Faro results in Section 4.3.4. The 0 – 500Hz X and 0 – 5000Hz Y-axis FRFs and coherence plots (developed from the red scan points shown in Figure 4.37) are shown in Figure 4.38 and Figure 4.39, respectively.

During the initial testing with the triaxial laser vibrometer, the low frequency noise seen in the accelerometer based testing was again present. To combat the noise and increase the signal-to-noise ratio, a voltage amplifier was added inline with the input signal. The voltage amplifier provided significant improvement in a 0 – 500Hz test, so the decision was made to include this test for the other two flight tubes. For the 0 – 5000Hz test, the voltage amplifier was removed.

The scan points behave similarly in the 0 – 500Hz FRF, exhibiting similar peaks and similar phase. After $\sim 500\text{Hz}$ in the 0 – 5000Hz FRF, the peaks begin to occur at different frequencies and phase shit becomes more obvious. As frequency increases, the operating deflection shapes become more complex, and the different scan points will not move in unison – the lead/lag of different scan points explains the diverging phase values. The coherence plots for these FRFs are considerably better than the previous accelerometer and 1-D laser vibrometer. The input voltage amplifier improved the low frequency data remarkably in the 0 – 500Hz FRF; the 0 – 5000Hz FRF experiences the same low frequency problems the post-flight vibration response testing suffered from (Section 4.2.3 and 4.2.3.1), but at the higher frequencies the coherence data and noise level smooth very nicely. Table 4.8 presents select natural frequencies and accompanying operating deflection shape descriptions.

Figure 4.40 presents snapshots of select operating deflection shapes for tube 1. The 0 – 5000Hz data is challenging to analyze with respect to a typical cantilevered beam

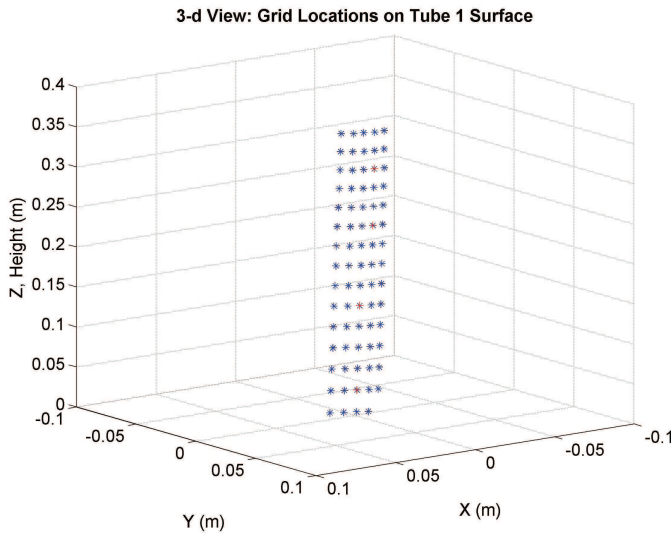


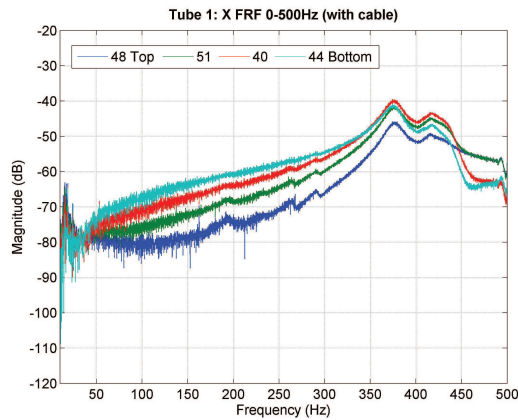
Figure 4.37: 3-D representation of the scanned points. Note the general tilt to the right of the plot - this is the genesis of the deployment errors.

Table 4.8: Tube 1 natural frequencies and operating deflection shape descriptions.

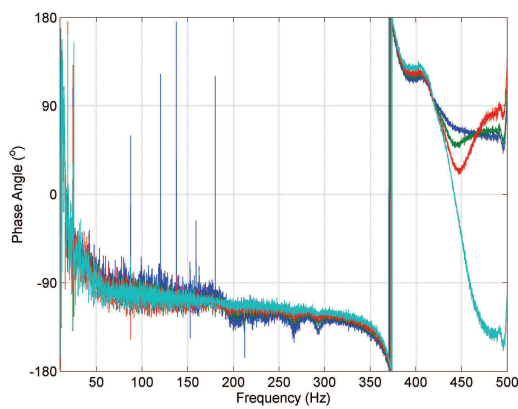
Resonance	Natural Frequency (Hz)	Operating Deflection Shape Comments
1	13, 15	First Cantilevered Bending
2	373	Second Cantilevered Bending with Tip Mass
3	787	Second Cantilevered Bending with Tip Mass and Breathing
6	1792	Fourth Cantilevered Bending, or Third Pinned-Pinned Bending

with a tip mass, probably a result of structural nonlinearities manifesting themselves within the vibration response testing. The first bending shape (A) for tube one is a double peak of 13 and 15Hz, representing first bending X-axis and first bending Y-axis, respectively. (A) shows first cantilevered bending X-axis at 15Hz. The second bending shape (B) occurs at 373Hz, and this operating deflection shape appears similar to the second bending mode of a beam with a tip mass. The mass of the endcap is $\sim 17\%$ of the beam mass, which limits the tip motion fairly effectively at the higher frequencies (as though the beam were pinned, or fixed, at the endcap). The operating deflection shapes (C) - (E) are less comparable to true mode shapes. Section 4.4.2 discusses the breathing eigenvectors (modes); these breathing motions are interspersed with bending motions. (C) is a good example – it appears as though it is a second pinned-pinned bending mode combined with first breathing (the grid lines are wider and the middle

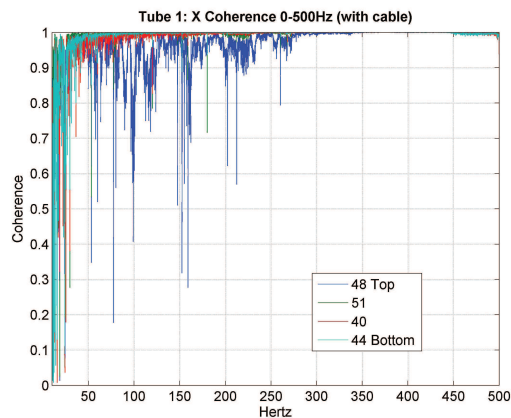
section appears bowl shaped). (E) appears as though it is a fourth cantilevered bending or a third pinned-pinned mode, with marginal breathing. There are additional operating deflection shapes that are not shown here, but they are all combinations of bending breathing similar to (C) - (E). It is important to note that these operating deflection shapes are *not* eigenvector mode shapes.



(a)

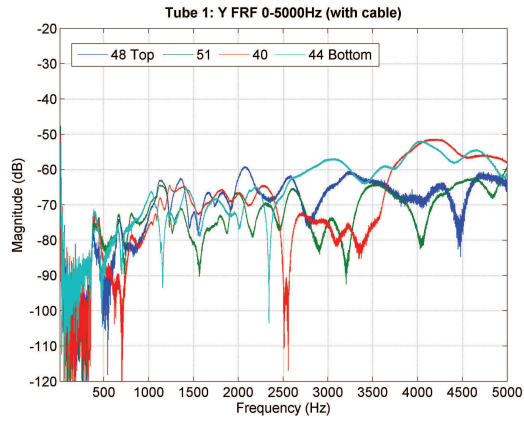


(b)

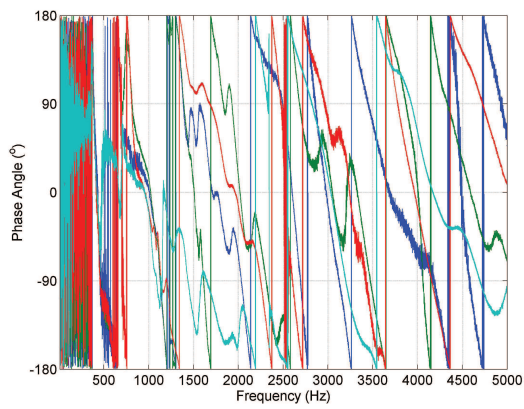


(c)

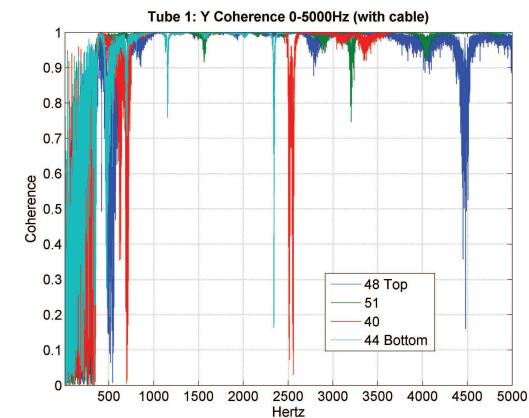
Figure 4.38: (a,b) 0 – 500Hz X-axis Polytec FRF resulting from tube 1. (c) X-axis coherence plot for the 0 – 500Hz Polytec tube 1 FRF. Note the legend corresponds to scan points highlighted in Figure 4.37.



(a)



(b)



(c)

Figure 4.39: (a,b) 0 – 5000Hz Y-axis Polytec FRF resulting from tube 1. (c) Y-axis coherence plot for the 0 – 5000Hz Polytec tube 1 FRF. Note the legend corresponds to scan points highlighted in Figure 4.37.

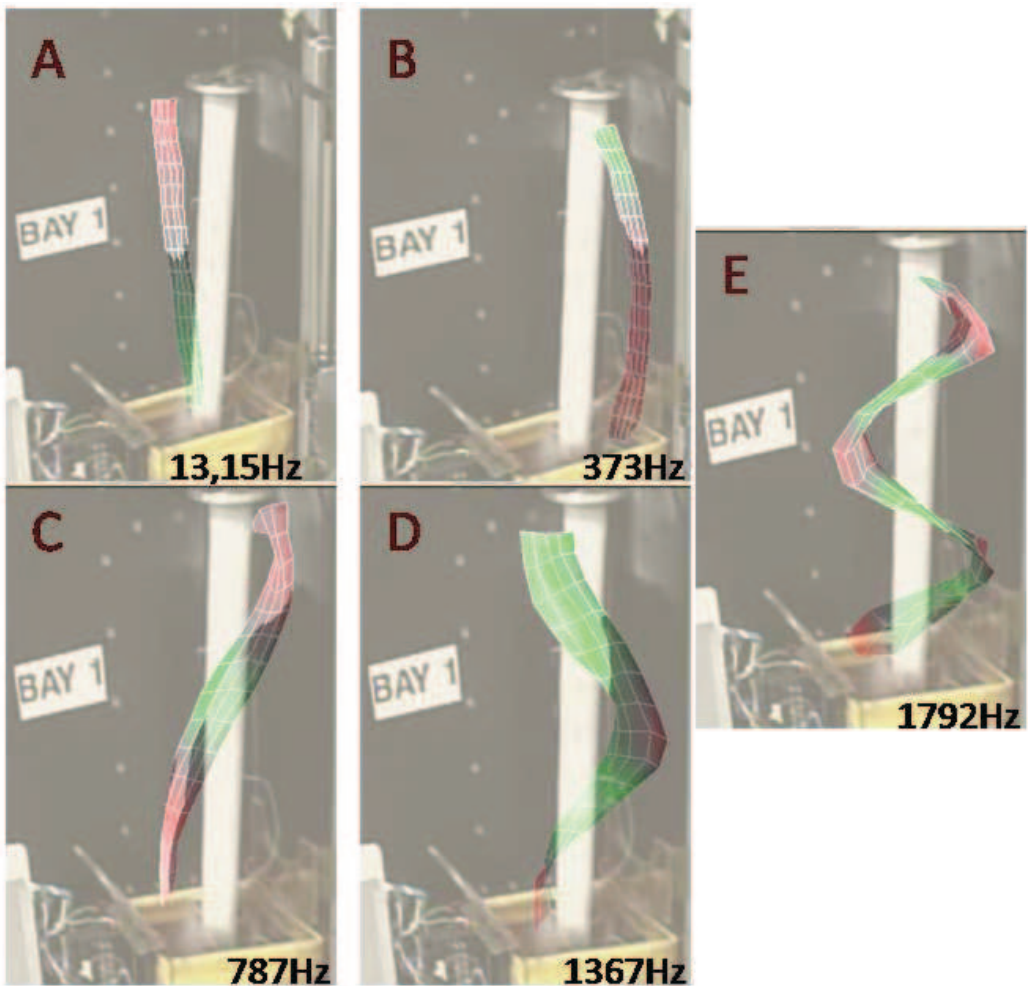


Figure 4.40: Tube 1 Operating Deflection Shapes and Natural Frequencies

4.3.3.2 Tube 2 Results. Figure 4.41 shows the scan points exhibiting a large “crank” in the Y-axis, which is not confirmed by the Faro results in Section 4.3.4 (because of limited Faro points along the tube), but the Faro results do show large Y-axis deviations. The 0–500Hz X and 0–5000Hz Y-axis FRFs and coherence plots (developed from the red scan points shown in Figure 4.41) are shown in Figures 4.42 and 4.43.

Again, the 0 – 500Hz low frequency data is very clean – nice coherence plots with little noise in the FRF. The scan points behave similarly in the 0 – 500Hz FRF, exhibiting similar peaks and similar phase. Phase and peak divergence are again present at the higher natural frequencies, which exhibit increasingly complex operating deflection shapes (as before with tube 1). Also as before, the 0–5000Hz data suffers from the lack of the input voltage amplifier in the lower frequencies, but the coherence data is acceptable after $\sim 700\text{Hz}$. Table 4.9 presents select natural frequencies and accompanying operating deflection shape descriptions. Note the inclusion of a cantilevered torsion deflection shape at 214Hz.

Figure 4.44 presents snapshots of select operating deflection shapes for tube 2. Tube 2’s first and second bending deflection shapes (resonance 1 and 3, (A/B) and (C)) are similar in nature to tube 1 but the corresponding natural frequencies are much higher. First cantilevered bending occurs at 28.4 and 34.3Hz; first pinned-pinned bending occurs at 400Hz. The first cantilevered torsion deflection shape is not shown due to difficulties in translating the shape into a suitable picture. Resonance 4, shown in (D) and (E), was similar to resonance 3 but incorporated breathing deflections. Resonances 5 and 9, (F)

Table 4.9: Tube 2 natural frequencies and operating deflection shape descriptions.

Resonance	Natural Frequency (Hz)	Operational Deflection Shape Comments
1	28.4,34.3	First Cantilevered Bending
2	214	First Cantilevered Torsion
3	400	Second Cantilevered Bending with Tip Mass
4	468,493	Second Cantilevered Bending with Tip Mass and Breathing
5	765	Second Pinned-Pinned with Breathing
9	1690	Fourth Cantilevered Bending, or Third Pinned-Pinned Bending

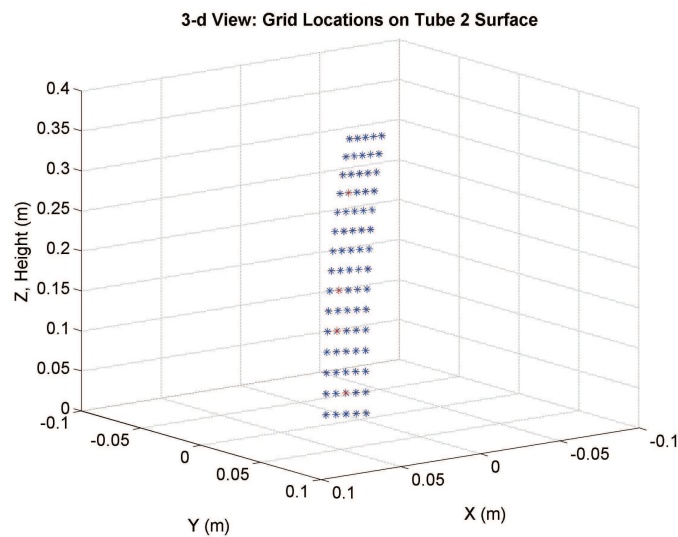
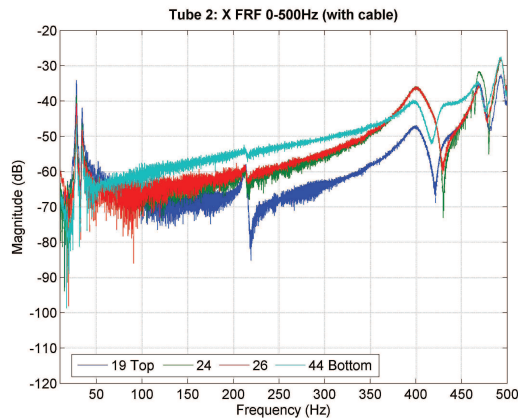
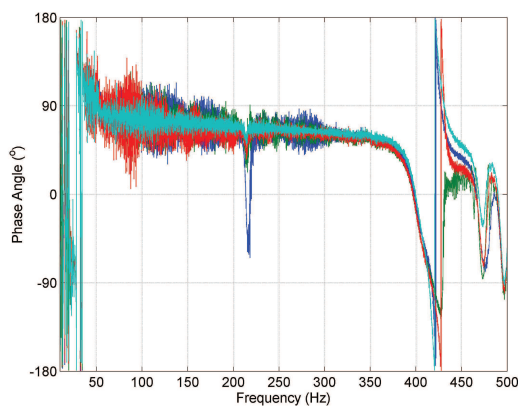


Figure 4.41: 3-D representation of the scanned points. Note the “crank”, or change in direction, halfway up the tube.

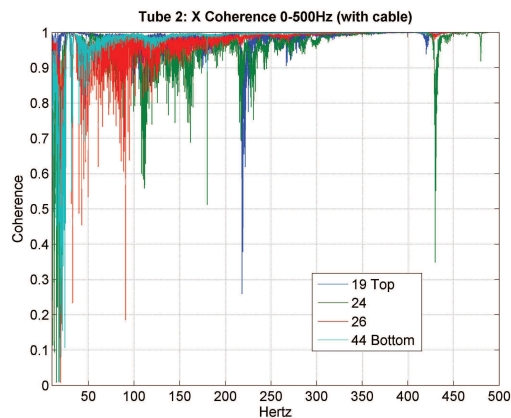
and (G), are the second pinned-pinned bending/breathing shape and fourth cantilevered bending or third pinned-pinned bending shape, similar to tube 1.



(a)

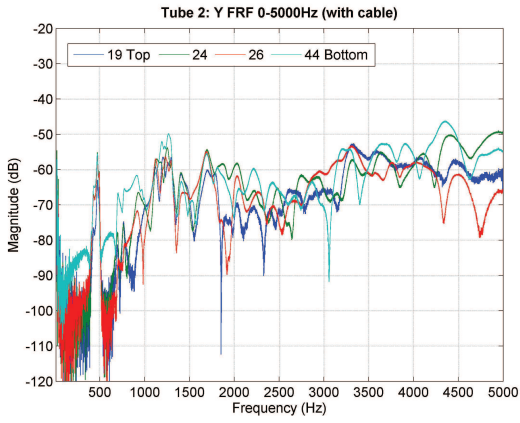


(b)

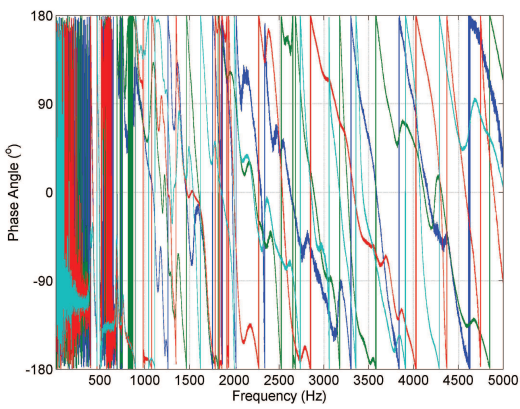


(c)

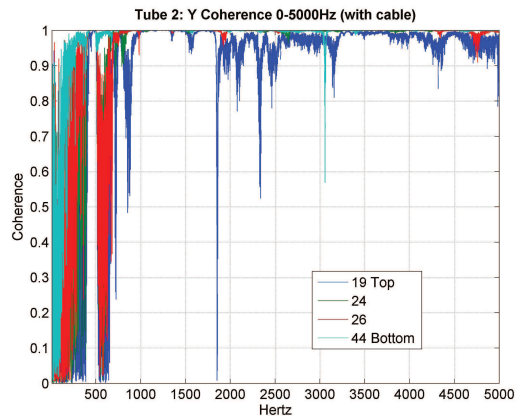
Figure 4.42: (a,b) 0 – 500Hz X-axis Polytec FRF resulting from tube 2. (c) X-axis coherence plot for the 0 – 500Hz Polytec tube 2 FRF. Note the legend corresponds to scan points highlighted in Figure 4.41.



(a)



(b)



(c)

Figure 4.43: (a,b) 0 – 5000Hz Y-axis Polytec FRF resulting from tube 2. (c) Y-axis coherence plot for the 0 – 5000Hz Polytec tube 2 FRF. Note the legend corresponds to scan points highlighted in Figure 4.41.

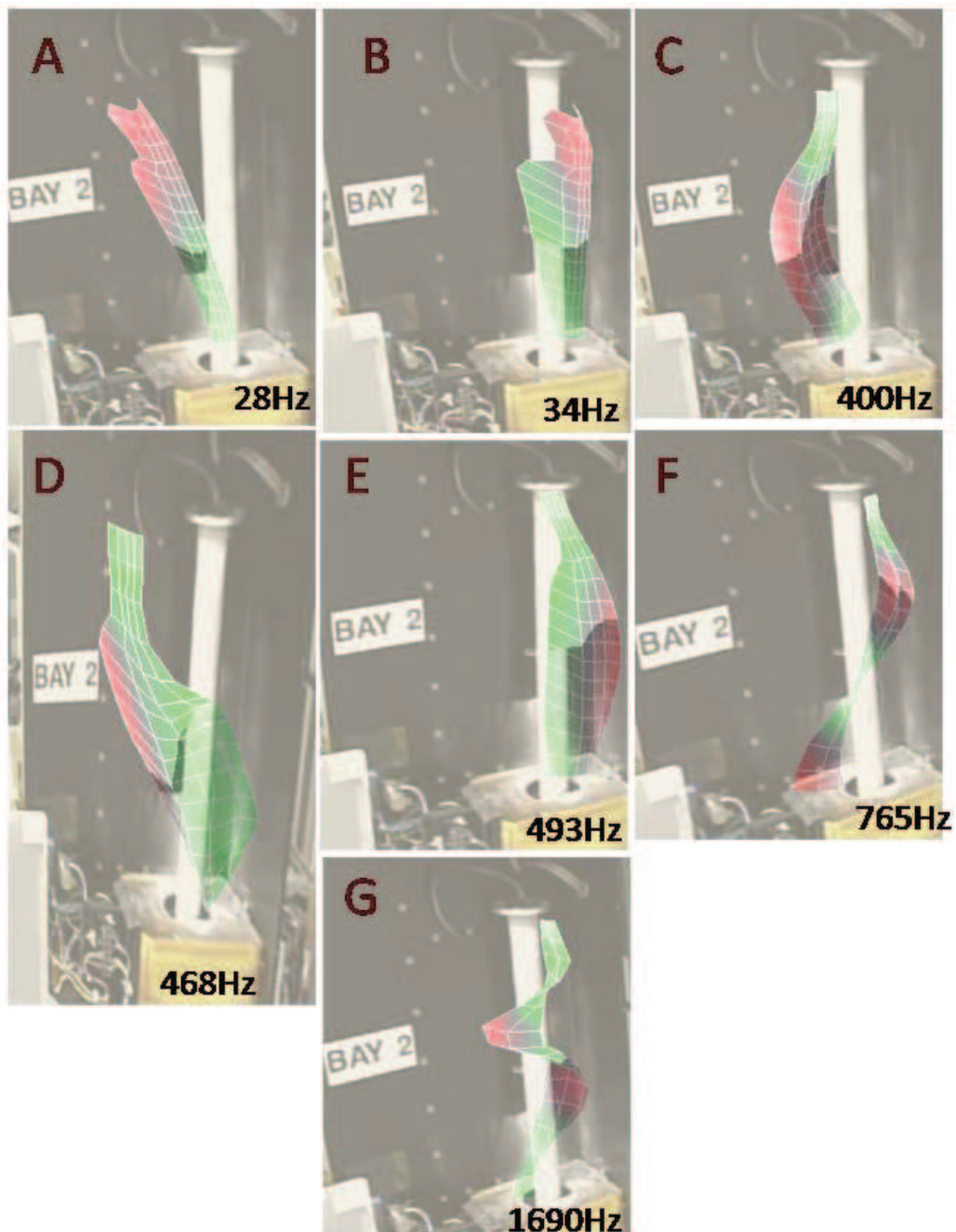


Figure 4.44: Tube 2 Operating Deflection Shapes and Natural Frequencies

4.3.3.3 Tube 3 Results. Figure 4.45 shows the scan points which exhibit very little deviation from true, confirmed by the Faro results in Section 4.3.4. The red points are the scan points used in for the FRFs. The 0 – 500Hz X and 0 – 5000Hz Y-axis FRFs and coherence plots are shown in Figure 4.46 and Figure 4.47, respectively.

Once again, the input voltage amplifier significantly improved the low frequency data for the 0 – 500Hz data. With the exception of ~ 200 Hz range, the 0 – 500Hz coherence is quite clean. There does appear to be a slight resonance at ~ 200 Hz for the top point, but the coherence for the top point is comparatively low, and the other points show little to zero resonance. The overall averaged 0 – 500Hz FRF does not show any resonance at the 200Hz range; thus it is believed the torsional resonance was not adequately stimulated by the axial PZT. The 0 – 5000Hz suffers through the low frequency data (as did tubes 1 and 2) until ~ 1000 Hz. Tube 3 is unique in that neither of the first two bending shapes exhibited doubled peaks, probably a result of the almost perfectly symmetrical deployment – tube 3 has the least X and Y-axis deviations. Table 4.10 presents select natural frequencies and accompanying operating deflection shape descriptions.

Figure 4.48 presents select operating deflection shapes for tube 3. Tube 3's first bending frequency is lower than tube 1's, but the second bending frequency is higher – first cantilevered bending occurs at 23.9 and first pinned-pinned bending occurs at 426Hz. Resonance 3, shown in (C), appears as though it is a pinned-pinned torsion deflection shape. Resonances 4 and 6, shown in (D) and (E), are further complications

Table 4.10: Tube 3 natural frequencies and operating deflection shape descriptions.

Resonance	Natural Frequency (Hz)	Operational Deflection Shape Comments
1	23.9	First Cantilevered Bending
2	426	Second Cantilevered Bending with Tip Mass
3	731	Second Cantilevered Bending with Tip Mass and Torsion
4	1202	Third Cantilevered Bending with Tip Mass and Torsion
6	1441	Fourth Cantilevered Bending with Tip Mass and Torsion

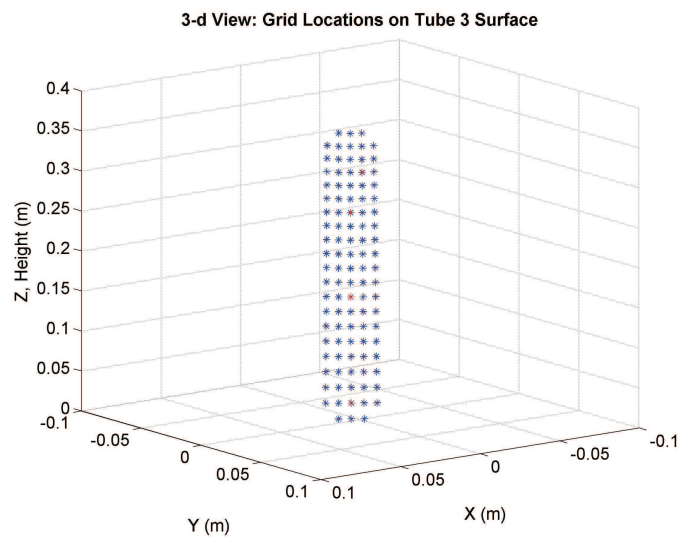
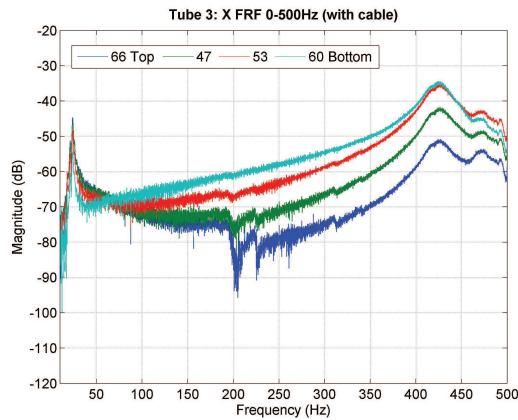
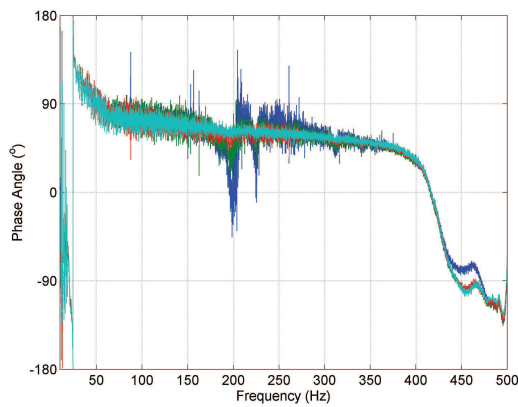


Figure 4.45: 3-D representation of the scanned points. Note how straight tube 3 is in comparison to tubes 1 and 2.

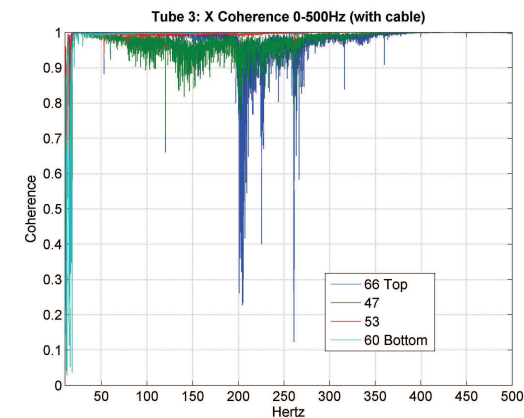
of resonance 3. These pinned-pinned torsion deflection shapes are not seen in tubes 1 and 2.



(a)

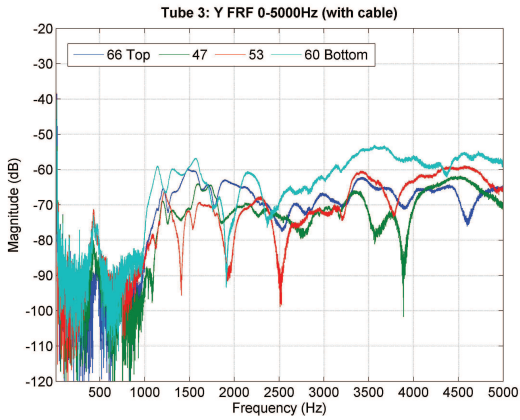


(b)

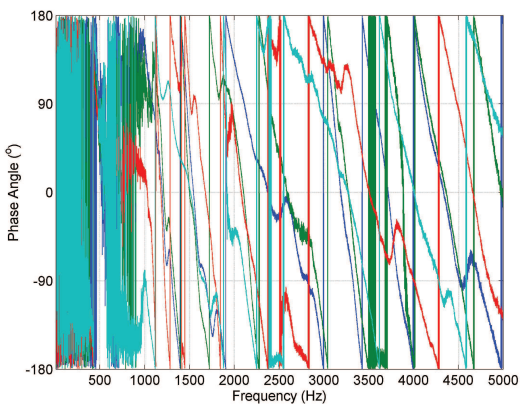


(c)

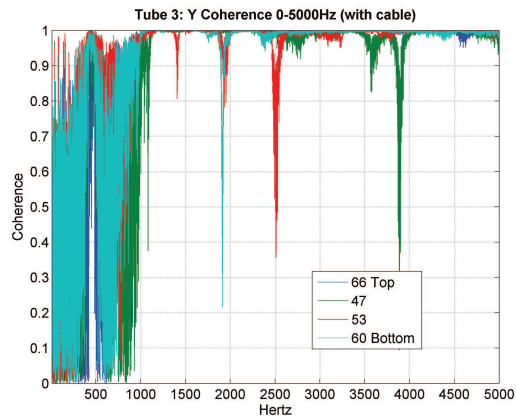
Figure 4.46: (a,b) 0 – 500Hz X-axis Polytec FRF resulting from tube 3. (c) X-axis coherence plot for the 0 – 500Hz Polytec tube 3 FRF. Note the legend corresponds to scan points highlighted in Figure 4.45.



(a)



(b)



(c)

Figure 4.47: (a,b) 0 – 5000Hz Y-axis Polytec FRF resulting from tube 3. (c) Y-axis coherence plot for the 0 – 5000Hz Polytec tube 3 FRF. Note the legend corresponds to scan points highlighted in Figure 4.45.

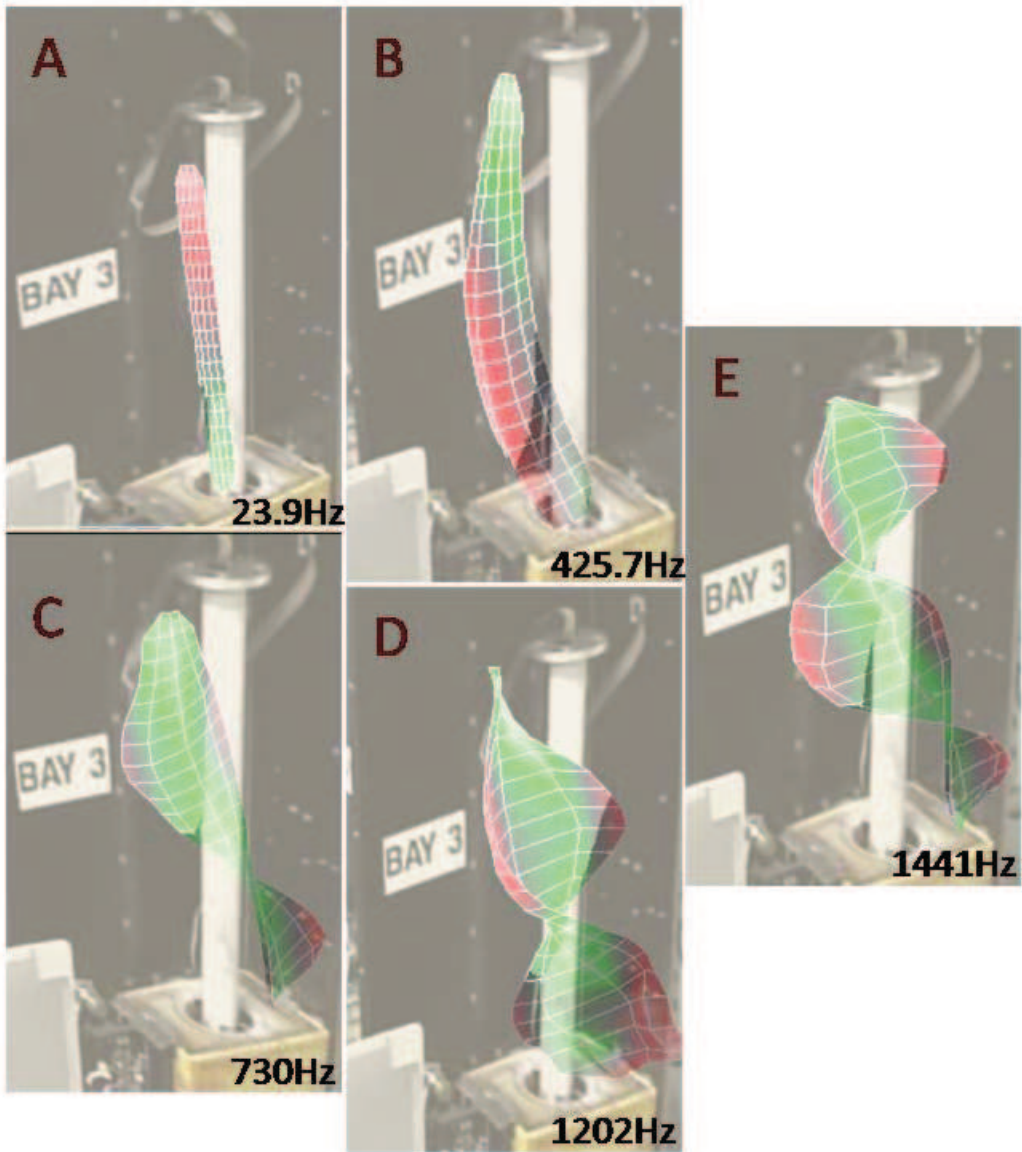


Figure 4.48: Tube 3 Operating Deflection Shapes and Natural Frequencies

4.3.4 Displacement Measurement Results. The Platinum FaroArm worked as prescribed in 3.3.4. Point clouds were taken the camera, bay walls, tube top endcap and the tube itself for all three bays. The carbon fiber tube could only be modeled from the tube tip through the top of the oven, as the oven prevented the probe from going any lower. While measuring along the length of the tube, care was taken to not move the tube with the hard probe – doing so would lower the accuracy of the hard probe measurements. The bay wall and camera point clouds were fit through planes and the tubes and top endcaps fit through cylinders, with the top of the endcap fit through another plane.

The three geometry files (one per bay) were imported into FEMAP (which contains a functional CAD package) for further processing. A linear expansion of the carbon fiber tube cylinder was extended to the floor of the bay to complete the model of the deployed tubes. Using the as-built drawings provided by Owens [31], a perfectly deployed tube was then modeled, centered on the exact location of the tube mount for comparison purposes. First, the horizontal planar X and Y-axis differences between the perfect and actual deployed tube were measured; this, in essence, is the deviation from true, or perfectly straight. Only the horizontal plane deviation calculations were conducted. The vertical differences were not measured due to the influence of potential manufacturing defects and the creases remaining from the major folds would increase the order of uncertainty beyond the error measurements themselves. The intersection of the perfect and actual deployed tubes with the floor of the bay lines up very well for all three bays; the deviation at the bottom between true and deployed is the genesis of the order of error in the horizontal plane deviation measurements.

Figure 4.49 shows the finished geometry models. The perfectly deployed tubes are represented with blue cylinders, and the actual deployed tubes are shown with representative black tubes a silver top flange (similar to the carbon fiber and aluminum endcap). Table 4.11 provides the digitally determined deviation dimensions.

As Table 4.11 indicates, tube 1 (the tube which did not inflate properly, discussed in 4.1.2) has the largest ΔX , or in-fold, deviation. The tube tip is approximately -1.1 inches from true in the in fold direction, or approximately 5.7% from true over the its 20 inch

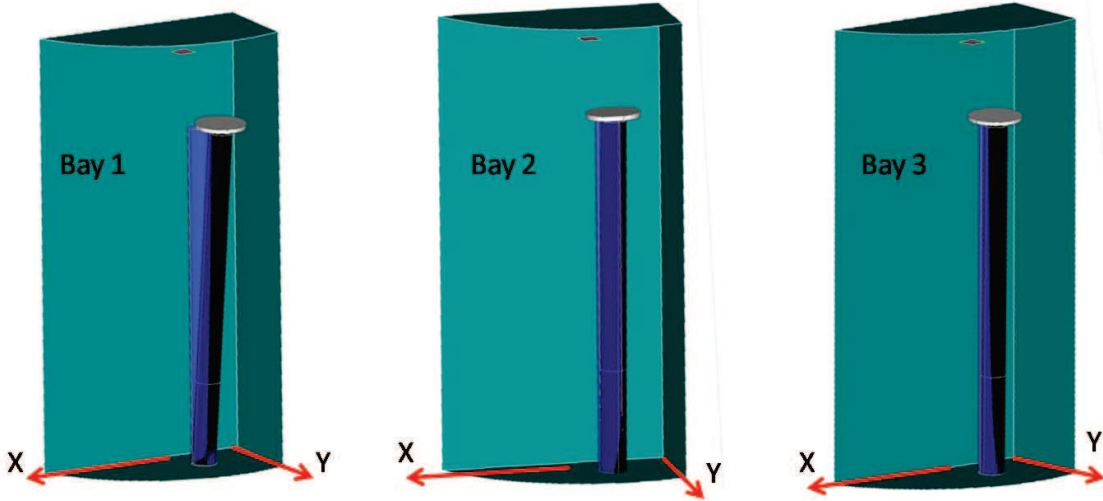


Figure 4.49: Measured deployment of each tube overlayed on a true deployment.

Table 4.11: X and Y measured deviations for all three tubes.

Tube	ΔX (inches) (% of 20" length)	ΔY (inches) (% of 20" length)	Measurement Error (inches)
1	-1.14 (5.7%)	0.33 (1.7%)	0.1
2	-0.389 (1.9%)	-0.490 (2.5%)	0.05
3	0.059 (0.3%)	.210 (1.1%)	0.04

length. The negative sign indicates the deviation is in the -X direction. Surprisingly, tube 2 has the largest ΔY , or out of fold, deviation. Tube 2 is almost 0.5 inches from true in the -Y direction. It had been thought that the out of fold direction would have relatively insignificant deviations, as the creases would increase the Y-axis Principle Moment of Inertia and in turn increase bending resistance in the Y direction. Referencing the point grid layout in 4.3.3.2 (Figure 4.41), it appears tube 2 has a slight Y direction “crank” half way up the tube which would contribute to the measured deviations. This negative Y-axis deviation causes tube 2 to hide behind the perfectly deployed shadow in Figure 4.49.

Table 4.12: Calculated on-orbit X and Y deployment deviations.

Tube	X Deviation (inches)	Y Deviation (inches)	Measurement error (inches)
1	$-1.14 - .034 = -1.17$	$0.33 - (-.3955) = 0.73$	0.1
2	not measured	not measured	not applicable
3	w/in error	$0.210 - .28 = 0.07$	0.04

Tube 3 was by far the straightest; this seems to indicate the heat from preceding tube deployments helps warm the following tubes more thoroughly. Also, as the experiment warmed to near equilibrium temperature, the pressure solenoids may have opened faster, and tube 3 had more reserve pressure, which postulates the tradeoff between inflation pressure, controlled deployment, and deployment accuracy.

4.3.4.1 In Flight Deployment Deviations. By collating the change detection analysis and Faro results, in Section 4.1.4.2 and 4.3.4, yields the on-orbit X and Y-axis deviations for tubes 1 and 3. The deviations cannot be simply added or subtracted, however; care was taken to add or subtract appropriately. For instance, the X-axis Faro results from tube 1 suggest the tube is -1.14 inches from true, in tube 1's current state. Assuming no change in position between the post flight image and the FaroArm data, the X-axis deviation on-orbit would have thus been -1.17 inches. The error from Table 4.3 was 0.0235 inches and the error from 4.11 was a 0.1 and 0.04 inches for tubes 1 and 3, respectively, therefore the error from the Faro results was used in this analysis. Table 4.12 presents the on-orbit deployment deviations. Note that Tube 3 is nearly within the 0.04 inch error bounds for both X and Y-axis – a remarkable result. This is excellent evidence that precision on-orbit deployment is feasible with these sub- T_g inflatable/rigidizable tubes.

4.4 Finite Element Modeling Results

The update to Holstien's FE model and the development of a simple coarse mesh model were both successful. The results of the fine mesh and the coarse mesh were very close to the measured data from tube 3. The mission oriented structure models were constructed of the coarse mesh model, which allowed a model reduction and faster run time, given the acceptable coarse mesh model results. The model development process focused first on tuning the fine mesh model, then tuning a coarse mesh to reduce the model size, followed by creation of large structures with the coarse mesh model. Two structures were analyzed – a triangular cross section boom and a flat panel similar to the L'Garde, Inc. solar array design mentioned in 2.1.1.1.

Table 4.13: Fundamental frequencies of the three flight tubes.

Flight Tube	Fundamental Frequency (Hz)
Tube 1	13.52
Tube 2	28.04
Tube 3	23.98

4.4.1 Fundamental Frequency and Young's Modulus. In preparation for his FE model efforts, Holstein [15] provided theory that utilized the fundamental frequency (first natural frequency [25]) for determination of Young's modulus. This Appendix begins by providing the fundamental frequency of the three flight tubes and continues by using the product of Holstein's theory review, the fundamental frequency formula, to determine an estimate for Young's modulus for each flight tube. This estimate is used as a starting point for updating Holstein's tube FE model (3.4). Using data from the Polytec PSV-400 Laser Vibrometer tests (4.3.3), Table 4.13 presents the first natural frequency for each of the flight tubes.

The lateral vibration fundamental frequency formula is used to determine the Young's modulus for the Kapton covered carbon fiber and resin composite material used in the flight tube configuration. The fundamental frequency formula is given as [15]:

$$f = .159 \sqrt{\frac{3EI}{L^3(m + \alpha m_b)}} \quad (4.4)$$

where

Lumped mass (Endcap), $m = 0.0746 \text{ kg}$

Beam Mass, $m_b = 0.24 \text{ kg}$

Young's modulus, E

Moment of Inertia, $I = 8.030 \times 10^{-9} \text{ m}^4$

Beam Length, $L = 20 \text{ inches}, 0.508 \text{ m}$

Material Thickness, $0.015 \text{ inches}, 0.000381 \text{ m}$

Outer Diameter, $d_o = 1.5 \text{ inches}, 0.0381 \text{ m}$

Inner Diameter, $d_i = 1.47 \text{ inches}, 0.03734 \text{ m}$

Lateral Vibration Constant, $\alpha = \frac{1}{4}$

fundamental frequency, f

The endcap and beam mass were provided by L'Garde, Inc. and quoted by Single [37], the diameter and beam length are approximations, and the cross section moment of inertia is given by as:

$$I = \frac{\pi(d_o^4 - d_i^4)}{64} \quad (4.5)$$

Backsolving for E using the fundamental frequency, we arrive at the initial Young's modulus estimates displayed in Table 4.14.

Table 4.14: Initial Young's modulus estimate for the Finite Element Model, derived from the fundamental frequency formula.

Flight Tube	Young's modulus (Pa)	Young's modulus (psi)
Tube 1	5.30×10^9	7.68×10^5
Tube 2	2.28×10^{10}	3.30×10^6
Tube 3	1.67×10^{10}	2.42×10^6

4.4.2 Individual Tube Model Results. The first step in building large structures in FEMAP was to model individual tubes and then tune the model modal properties to match the experimental results. Young's modulus was the primary tuning property, and tuning started with the approximation developed in Section 4.4.1. The goal for the fine mesh model was to match the first two natural frequencies; the coarse mesh to match the first natural frequency. These goals were met and even exceeded – the coarse mesh matched up closely to both the first *and* second natural frequency. The individual tube models yielded an important result: the first two operating deflection shapes visualized by the triaxial laser vibrometer correspond very closely to the first two eigenvectors (mode shapes).

The FE models also yielded another important result: there are several mode shapes which do not have corresponding observed (via triaxial laser vibrometer) operating deflection shapes. Either these mode shapes are rolled into one or more operating deflection shapes, the limitations of the model shift these modes into the range to lower frequencies, or the mode shapes were not excited by the axial input provided by the PZTs (which is most likely). The breathing modes were not seen as an independent operat-

ing deflection shape, but breathing was observed in several of the operation deflection shapes in Section 4.3.3. Additional breathing components of the operation deflection shapes may not have been observed in particular resonances due to the viewing geometry, and the breathing modes resulting from the FE model may result from the isotropic material properties discussed in below.

The carbon fiber material was assigned the manufacturer's quoted density of $8.64 \times 10^2 \frac{\text{kg}}{\text{m}^3}$, listed by Single [37] and presented in Table 2.4. Curiously, when the carbon fiber and endcap were weighed within the model, the result came back as 0.0944kg; adding the basecap weight yields 0.17kg, far short of the 0.24kg listed in Table 2.4. The early tubes tested by Single (which did not have the Kapton tape covering all external surfaces or a PZT attached) averaged $\sim 0.19\text{kg}$, a difference of about 10%. Therefore, it is concluded the Kapton tape and PZT add anywhere from $\sim 0.4 - 0.7\text{kg}$, and the material density provided by the manufacturer is a general quantity – each tube will have a specific carbon fiber (and corresponding matrix material) density. The 10% weight difference between a measured flight-like tube and the modeled tube is thus deemed acceptable.

4.4.2.1 Update to Holstein's Tube Fine Mesh Model. The first procedural step to updating Holstien's model was to import the model into FEMAP, but the fine model mesh was instead recreated from scratch. The geometry of the carbon fiber tube (1.5 inches in diameter, 0.015 inches thickness, 20 inches long) was geometrically modeled as a solid by extruding a surface cross section. Plate elements were selected and given the Young's modulus estimate derived in Section 4.4.1, at which point the model was then auto-meshed by FEMAP, which resulted in 9406 elements. The tube was modeled as a homogeneous and isotropic hollow beam rather than a three layer carbon fiber weave. This was done for two reasons, the first of which is simplicity, and the second of which is the unknown material makeup of the carbon fibers and composite. A point mass representing the weight of the aluminum endcap was used rather than modeling the endcap itself. The mass element was fixed to the tube elements using multiple symmetric rigid links. The base nodes were fixed (no translation or rotation) to approximate the tube clamped to RIGEX's base plate, which negated the need to model the basecap.

Table 4.15: Fine model natural frequencies matched with Tube 3 triaxial laser vibrometer results.

Mode	FE model Results (Hz)	Tube 3 Results (Hz)	Error (%)
1	23.9	23.9	0.0%
2	409.6	425.8	3.8%

After some effort to arrive at an consistent units within material properties card, the eigenvalue analysis iteration process began. The initial Young's modulus estimate proved to be much to high as was expected – the fundamental frequency equation was derived using homogeneous and isotropic beam theory, which in this instance prevents accounting for the composite makeup of the beam, as well as the multiple creases in the beam which result in a predisposition for increased buckling susceptibility. Therefore, multiple iterations were required until the appropriate Young's modulus was reached. The first natural frequency was eventually matched, with close results for the second. The accompanying mode shapes matched the experimental deflection shapes, as mentioned above. The third and fourth model natural frequencies were breathing mode shapes which were not distinctly seen in the operating deflection shapes, but where perhaps combined with additional bending modes in the operating deflection shapes. Therefore, the model is only experimentally confirmed through the first two modes.

The final isotropic Young's modulus value which matched the first two modes to experimental data appeared fairly low when compared to the original L'Garde, Inc. estimate and 6061 Aluminum. This stiffness value was accepted, however, as it is an isotropic representation which yields a tuned model which accurately depicts experimentally observed operating deflection shapes of a tube/endcap system. In addition, the fundamental frequency is related to mass and stiffness through Equation 4.4; thus, because the model mass is lower than the actual flight tubes (discussed above), the isotropic stiffness value is reduced as well – in the model. If the carbon fiber density were increased to yield a 0.24kg tube, a tuning process would probably yield a Young's modulus approximately 30% greater than the current model. The end result would be the same, however – a model that was tuned to match the first two natural frequencies of tube 3. Note that

Single listed a “reasonable value” Young’s modulus estimate, provided by L’Garde, Inc., of $9.5 \times 10^6 \frac{\text{lb}_f}{\text{in}^2}$, a value very close to aluminum.

Ultimately, the model reflects the behavior of the system, and thus the tuned Young’s modulus was simply a means to match behavior in a simple model. Section 5.4 elaborates further on the comparison of aluminum and the flight tubes’ Young’s modulus.

Table 4.15 presents the fine model natural frequency results, the tube 3 experimental (triaxial laser vibrometer) natural frequency results, and the percent difference. The model was tuned to tube 3 results because tube 3 was the straightest and had the cleanest first and second natural frequency peaks. The finely-meshed model exactly matched the first experimental natural frequency, and narrowly misses (3.8%) the second. Figure 4.50 presents the first two mode shapes of the coarse model, which compare favorably to Figure 4.48 (A) and (B).

4.4.2.2 Simple Coarse Mesh Model. Starting from a clean slate, a 20-inch flight tube was modeled as ten circular hollow beam elements with a point mass representing the endcap collocated with the final beam node. The base was again fixed (no translation or rotation) which again negated the need to model the basecap as a mass element, further simplifying the model. The elements were given the Young’s modulus values from the fine mesh elements, and the resulting analysis yielded very favorable results – the model was within 2% of the first natural frequency, and within $\sim 5\%$ of the second mode. Having exceeded the expectations, no further changes were necessary. Table 4.16 presents the natural frequency results from the coarse model, the tube 3 experimental (triaxial laser vibrometer) results, and the percent difference. Figure 4.51 presents the first two mode shapes of the coarse model. These shapes correlate very well to the fine mesh mode shapes and tube 3’s first two operating deflection shapes. With

Table 4.16: Coarse model natural frequencies matched with Tube 3 triaxial laser vibrometer results.

Mode	FE model Results (Hz)	Tube 3 Results (Hz)	Percent Difference
1	23.6	23.9	1.3%
2	406.3	425.8	4.5%

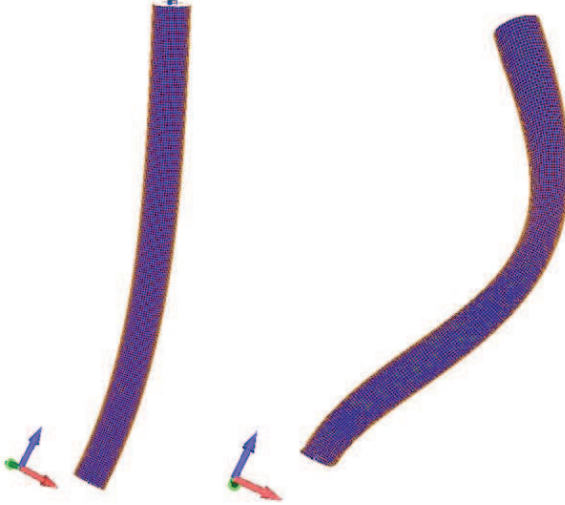


Figure 4.50: Finely meshed FE model mode shapes for first and second bending.

the simple, yet accurate, coarse mesh model, larger structures can be modeled without immediate concern over model size and computation time.

4.4.3 Mission Oriented Structures Model Results. Using the coarse mesh model developed above in 3.4.1.2, two versatile mission-oriented structures were developed and analyzed for trade study purposes. Each structure is 20 inches on a side and consists of multiples of the coarse tube FE model. The structures are fixed (no rotations, no translations) on one end as though attached to a spacecraft. The endcap connections between tubes where modeled every 10 elements (20 inches). Two assumptions were made regarding the connection of these endcaps: first, the mass element at the connection point

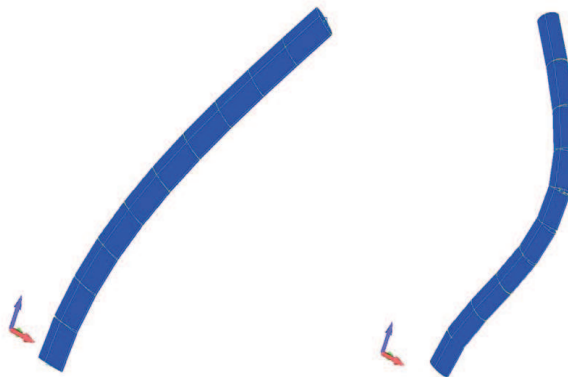


Figure 4.51: Coarsely meshed FE model mode shapes for first and second bending.

would equal one RIGEX endcap, regardless of the number of endcaps at that location (taking advantage of presumed design efficiency), and second, the connections could be rigidly linked between endcaps – essentially assuming the endcaps/basecaps are fixed together. These structural geometries were chosen because they could conceivably be rolled up or z-folded inside of a single oven box and inflated with a single pressure system (the all-in-one deployment system discussed in Section 5.5). The undeformed triangular cross section truss and the undeformed flat panel model are shown in Figure 4.52 (a) and (b), respectively. The resulting natural frequencies and mode shape descriptions are presented in Table 4.17.

4.4.3.1 Triangular Cross Section Truss Model. The triangular cross section truss model could feasibly be used for a boom, sunshade, SAR antenna, telescope, and many other potential applications. Consisting of simple 20 inch isometric triangle cross section with 20 inch longerons, this structure stretches 100 inches and is constructed of 33 coarse tube elements.

Twenty natural frequencies and corresponding eigenvector mode shapes were requested from the FEA. The resulting mode shapes would be the mode shapes no matter the material property used (an aluminum truss produces the same modes), but only the first three mode shapes are discussed here. The individual tube models were tuned to match the first two natural frequencies, which have simple bending mode shapes that consist of tension and compression in the outer and inner radius of the beam, respec-

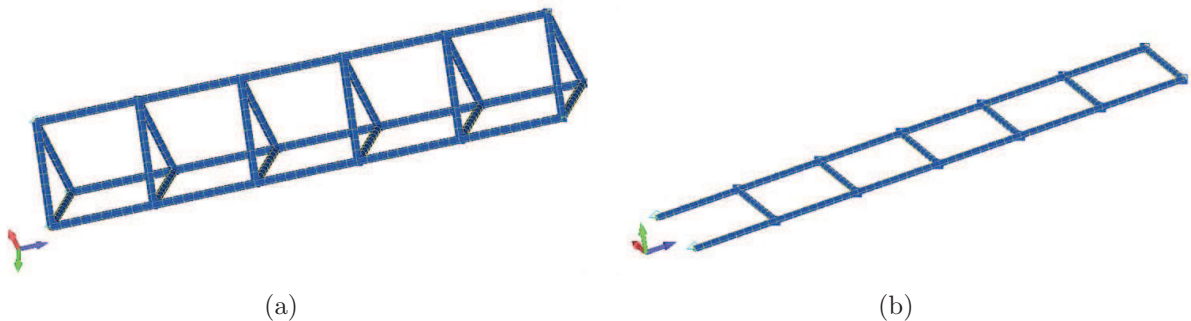


Figure 4.52: (a) 100 inch long triangle cross section truss consisting of 20 inch coarsely meshed tubes in isometric triangles and 20 inch longerons. (b) 120 inch long flat panel structure consisting of 20 inch coarsely meshed tubes in panels.

Table 4.17: Natural frequencies and corresponding mode shape descriptions of the mission oriented structures models.

Model	Natural Frequency (Hz)	Mode Shape Description
Triangular	8.2	+X -Y first bending mode
Cross Section	8.6	+X +Y second bending mode
Truss	10.5	First torsion mode
Flat Panel	1.1	+Y first bending mode
	6.9	First torsion mode
	7.1	+Y second bending mode

tively, and the only moment is transferred to the cantilevered beam constraint. FEMAP was used to post-process the resulting mode shapes and display the deformed shapes; this showed the first three modes exhibited simple bending, but the fourth mode had individual tubes exhibiting complex bending behavior, and were thus carrying a moment load. As a result, only the first three modes are accepted on the premise of only exhibiting motion tuned within the individual tube model itself. The first three mode shapes and accompanying descriptions are shown in Figure 4.53.

4.4.3.2 Flat Panel Model. The flat panel model could feasibly be used for a solar array, sunshade, SAR antenna, or many other potential applications. Consisting of simple 20 inch panel sections with 20 inch longerons, this structure measures 120 inches long by 20 inches wide, and is constructed of 18 coarse element tubes. The discussion pertaining to the first three modes for the triangular cross section truss model holds true for this model as well. The first three mode shapes and accompanying descriptions are shown in Figure 4.54.

4.5 Conclusions

In preparation for the detailed comparison analysis conducted in the next chapter, this section revisits the space flight, post space flight, and ground test results at a high level.

4.5.1 Space Flight Test Results. RIGEX successfully ran end-to-end while on-orbit. The thermocouples placed on the tubes, the structure, and internal to the

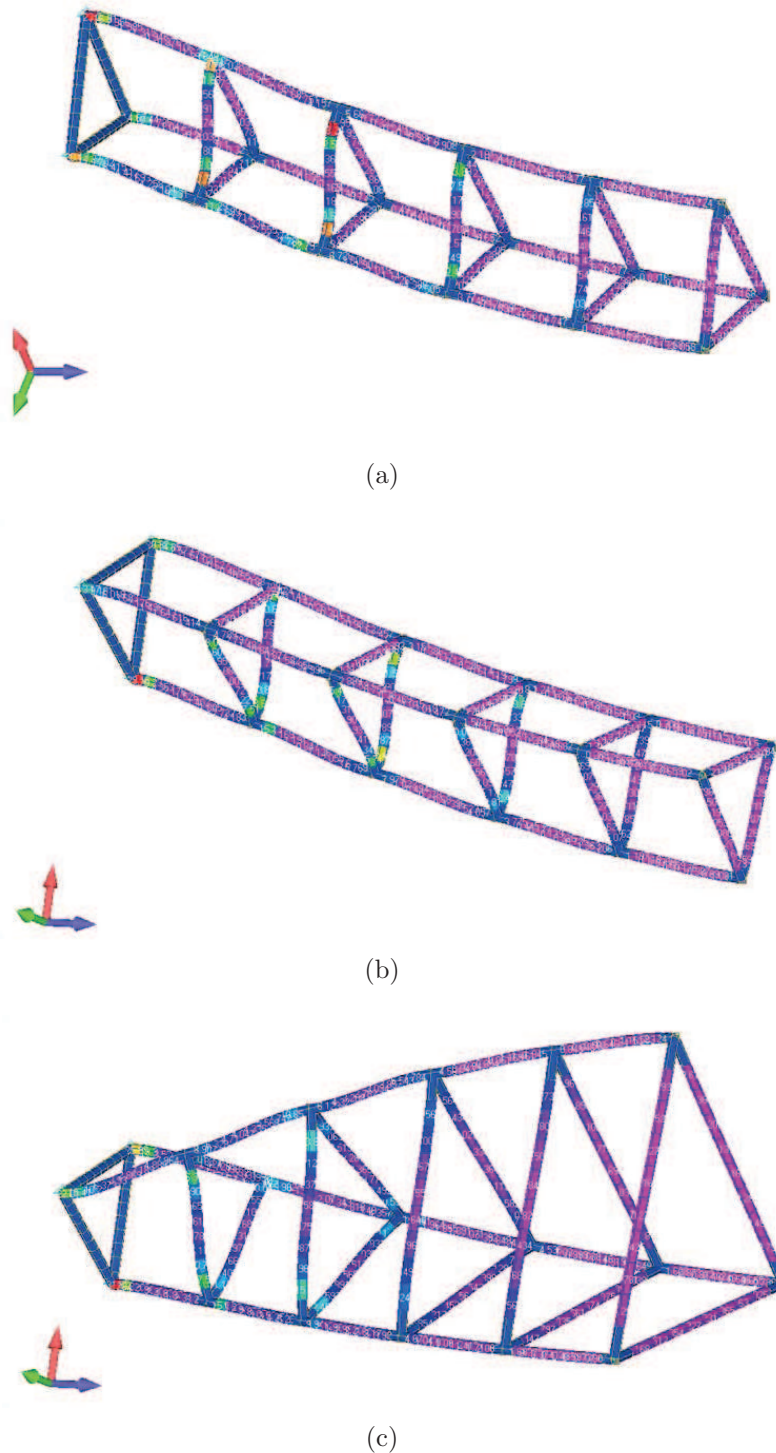


Figure 4.53: (a) 8.2Hz +X -Y first bending mode.
(b) 8.6Hz +X +Y second bending mode.
(c) 10.5Hz first torsion mode.

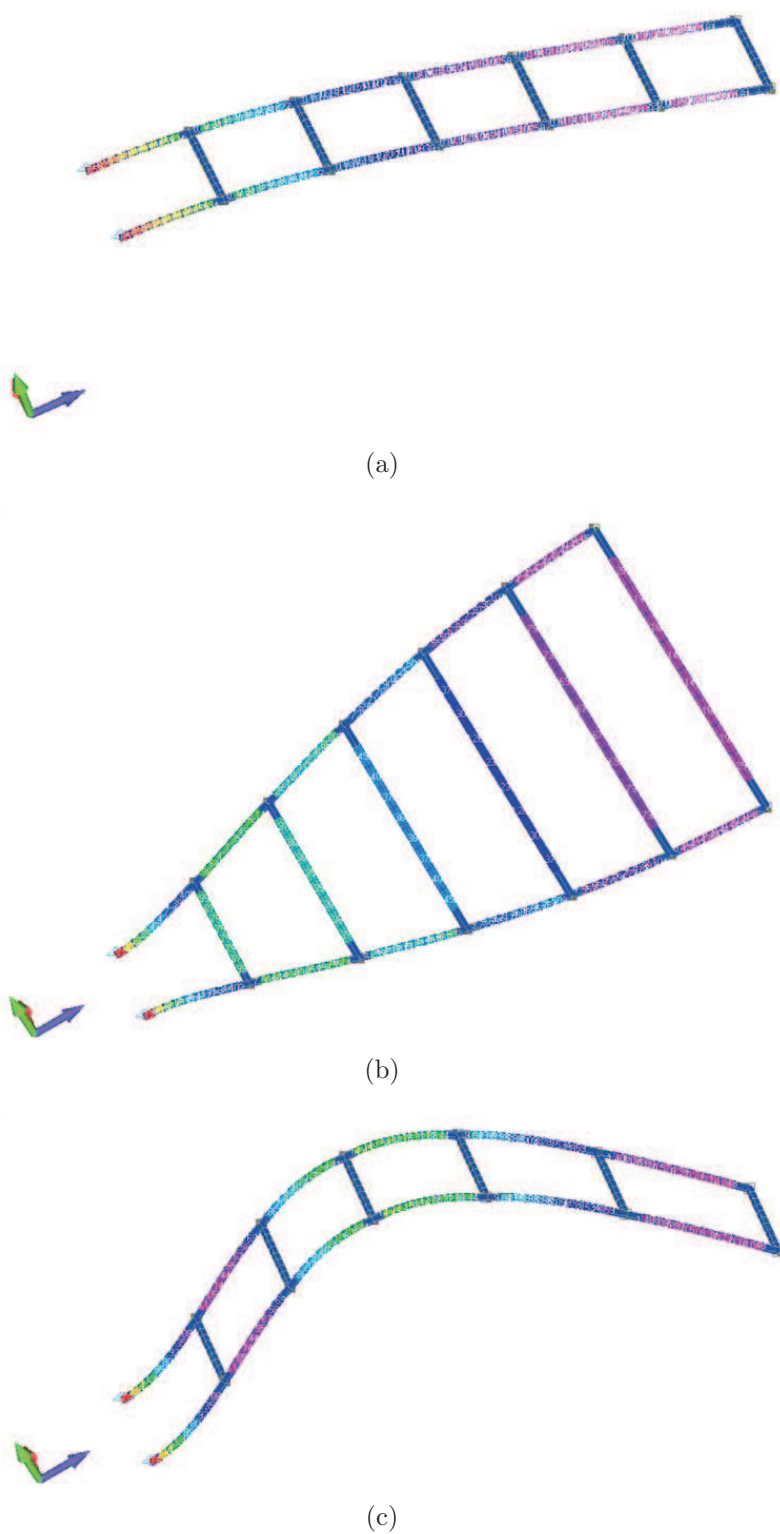


Figure 4.54: (a) 1.1Hz +Y first bending mode.
(b) 6.9Hz first torsion mode.
(c) 7.1Hz +Y second bending mode.

computer bay recorded good temperature data. Tube 2 took slightly longer to reach the glass transition temperature, which was attributed to thermocouple placement. At the conclusion of the heating process for tube 3, it appeared as though the structure and the computer stack were reaching an equilibrium temperature, which must be considered in future experiments. The cargo bay sill temperature data indicated RIGEX enjoyed a constant boundary condition temperature during operation, indicating all of the temperature data was a result from RIGEX operation and not external influence.

The pressure data showed a few surprises, namely tube 1 did not inflate when commanded, and tube 2 took ~ 0.1 seconds to inflate after commanded. The pressure spikes from tubes 2 and 3 were analyzed and attributed to the folds in the stowed tubes. The pressure data also suggests there is a leak in bay 2's inflation system.

The accelerometers functioned properly during the deployment and ambient/vibration response testing. The deployment acceleration data could not be integrated due to changes in the accelerometers orientation with respect to RIGEX. The ambient acceleration data provided an understanding of the noise level of the accelerometers. The vibration response testing was successfully accomplished, but the limited input voltage produced a low signal-to-noise ratio. While conducting the vibration response analysis, it was discovered the structural natural frequencies were drifting from test to test, which in effect caused the peaks to be averaged out along with the noise. This time varying behavior was not expected. Peaks from the last test iteration for tubes 1 and 2 correlated with data from the ground testing discussed later.

Image data of the tube deployments was also successfully collected on-orbit and presented. The on-orbit images where contrasted with post flight images for tubes 1 and 3, yielding changes in position due to the transition from space flight to AFIT. This data would be further analyzed with the Faro data to produce on-orbit deployment deviations.

4.5.2 Post Space Flight Test Results. Post space flight testing attempted to mimic the on-orbit vibration response as closely as possible. Changes from the on-orbit configuration to the post space flight test configurations were reviewed. The most notable of these changes were the new accelerometers and replacement of power supplies

internal to the flight computer. The flight computer based testing was not accomplished, as a suspected filter board anomaly prevented the flight computer from providing the input signal to the PZTs. dSpace was used as a surrogate flight computer for additional vibration response testing, while SignalCalc was used to monitor the data for immediate data quality analysis. The resulting data suggested the fifth significant digit that dSpace didn't capture (but SignalCalc did) was important for collecting the necessary acceleration data for the frequency response analysis. The sensitivity of SignalCalc was increased in an additional vibration response test, which yielded the relative "truth" accelerometer based FRF.

An important conclusion from the post space flight testing was the need to amplify the input voltage in the low frequency regime. The ± 5 volts pushed through the flight transformers did not appear adequate to properly stimulate the tubes' low frequency modes, and the low frequency FRFs were noisy and exhibited poor coherence.

4.5.3 Ground Test Results. Ground testing began by validating the previous students' vibration response findings. This tests used tubes that were tested throughout the preflight workup. By matching the FRFs created by Goodwin, the post space flight vibration test procedures were validated, and it was determined the specially-created tube connector interface cables were not influencing the test results.

Testing continued on to utilizing the triaxial laser vibrometer, which produced excellent FRFs with coherence data consistently approaching 1.0. A voltage amplifier was added inline with the input, which significantly improved the frequency response data collected in the 0 – 500Hz tests. These high fidelity FRFs will be used as the standard which the other vibration tests were measured against in Chapter 5, and tube 3's 0 – 500Hz FRF provided the target for the tuning conducted on the individual tube Finite Element Models.

The last ground test discusses was the precision contact measurement of all three tubes via the FaroArm. This data was combined with the on-orbit and post flight images, which indicates tube 3 was deployed almost perfectly true on-orbit, which suggests precision deployment is feasible for future space flight applications.

4.5.4 Finite Element Models. Two finite elements of tube 3 were created: a high fidelity, finely meshed model, and a simple coarsely meshed model. The finely meshed model was tuned to exactly match the first mode of tube 3 and was 3.8% from the second mode; the coarsely meshed model was 1.3% and 5.3% from the first and second mode, respectively. The coarsely meshed tube model was used to create two mission-oriented structures, which were created for comparison purposes with similar aluminum based structures in Chapter V. The first three modes of the mission-oriented structures were deemed acceptable, as these modes exhibited behavior similar to that which the individual tube models were tuned to.

V. Correlation with Previous Testing

THIS chapter attempts to satisfy the RIGEX mission statement by validating the preflight ground testing through correlation with the space flight test results to preflight (and post space flight ground) test results. The Mission Statement and first Primary Objective are reiterated here:

Mission Statement:

To verify and validate ground testing of inflation and rigidization methods for inflatable space structures against a zero gravity space environment.

Primary Objective:

- Design a GAS canister experiment to collect data on space-rigidized structures for validation of ground testing methods.

Prior to shipping RIGEX to Cape Canaveral, RIGEX was tested end-to-end inside of AFIT's thermal vacuum chamber. This chapter correlates temperature and pressure space flight test results with the preflight thermal vacuum chamber temperature and pressure results. Space flight vibration test results are cross correlated with preflight and post space flight testing. The mission oriented structures FE models, constructed of tuned FE models of RIGEX tube 3, are compared against aluminum based structures. Truss deployment processes are discussed, and a cursory Technology Readiness Level (TRL) review concludes the chapter.

RIGEX successfully satisfied its mission statement and completed all of its experimental objectives by validating the ground testing of inflation and rigidization methods. The space flight results validate the preflight temperature and inflation test procedures and results, and are correlated with the preflight vibration results. RIGEX also successfully validated and space qualified the inflation system and the tube heating method. The mission oriented truss structures weighed considerably less than the aluminum based structures, though the aluminum structures did prove to be stiffer. Finally, the Technology Readiness Level review suggests that RIGEX is now TRL 7.

Table 5.1: Correlation of the tube heating rates from the space flight and preflight thermal vacuum test results.

Tube	Rate of Change: $\frac{^{\circ}\text{C}}{\text{s}}$				
	Thermocouple A			Thermocouple B	
	Space Flight	Thermal Vacuum	Space Flight	Thermal Vacuum	
T1	0.21	0.12	0.17	0.13	
T2	0.15	0.12	0.13	0.12	
T3	0.19	0.11	0.14	0.11	

5.1 Comparison of Temperature Data

The preflight thermal vacuum testing used three Kapton-covered sub- T_g tubes that had been previously used for deployment testing. The tubes were outfitted with an accelerometer and two thermocouples each (but no PZT). The test conditions were as flight like as was practical – under vacuum, cycling through $\pm 45^{\circ}\text{C}$, and using the shuttle emulator power supply to supply current to the experiment. With respect to the actual space flight, there were four primary differences in configuration: RIGEX was not bolted into the CAPE canister, the containment shroud was not mated to the structure, the tubes involved had all been previously deployed and re-stowed (the flight tubes were pristine), and the initial tube temperatures were higher than those recorded on-orbit.

The space flight test results successfully validate the preflight temperature thermal vacuum test results. Figures 5.1 and 5.2 present the comparison of space flight (Space T1-T3) and thermal vacuum (TVac T1-T3) test results for thermocouple A and B, respectively. The difference in slope (rate of change in temperature with respect to time – $\frac{^{\circ}\text{C}}{\text{seconds}}$) between space flight and thermal vacuum results is apparent in both figures, but more so in Figure 5.1. This difference may be attributable to thermocouple locations (as discussed in Sections 3.1.1.1 and 4.1.1.1), but pictures are not available of the stowed tubes prior to the thermal vacuum test. The difference is more likely explained by the lack of the containment shroud and CAPE canister. The containment shield and canister would have both acted as additional layers of insulation surrounding the oven box, decreasing waste heat loss and increasing the oven efficiency and thus causing the tubes to heat faster on-orbit. Table 5.1 provides a side by side comparison

of the thermocouple temperature linear curve fit slope ($\frac{^{\circ}\text{C}}{\text{seconds}}$) for the space flight and thermal vacuum test results.

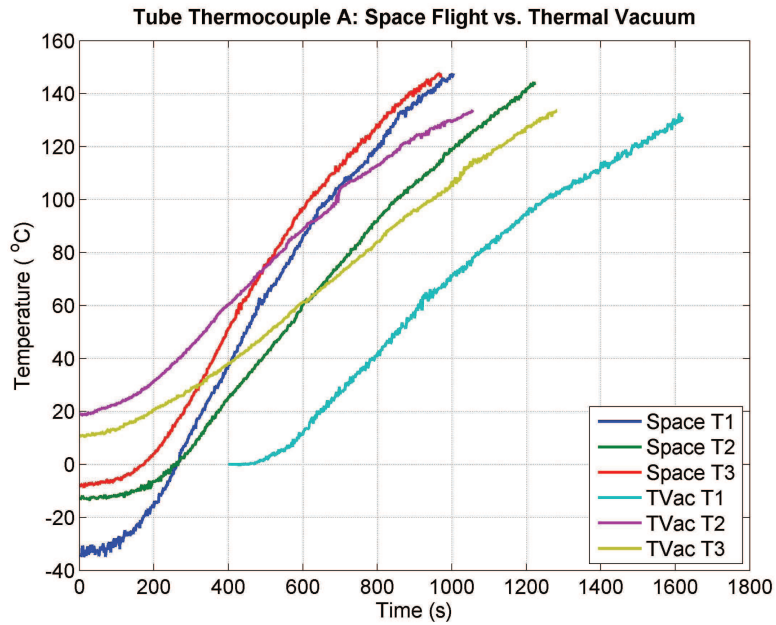


Figure 5.1: Correlation of tube thermocouple A from the space flight and preflight thermal vacuum test results.

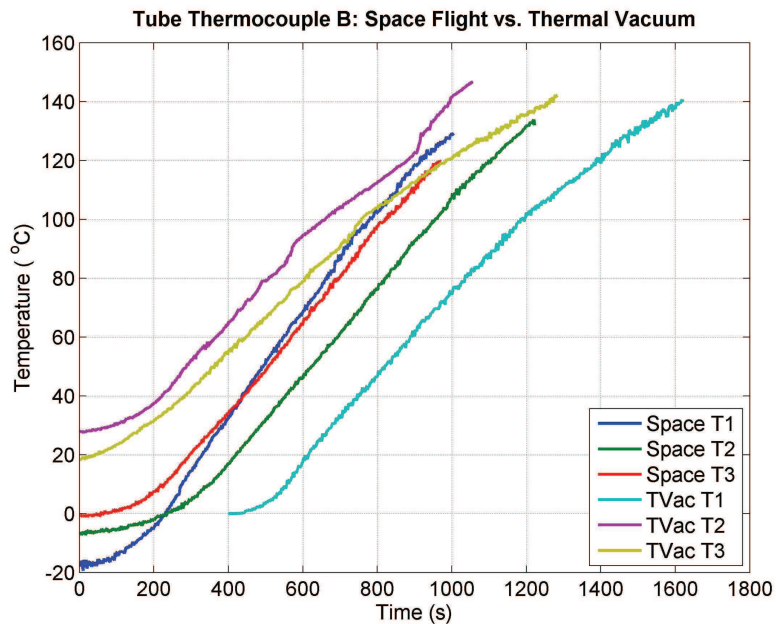


Figure 5.2: Correlation of tube thermocouple B from the space flight and preflight thermal vacuum test results.

5.2 Comparison of Pressure Data

The preflight thermal vacuum test was as flight realistic as was practical. Microgravity is a difficult condition to implement during ground thermal vacuum testing, so there are only three options for deploying a tube on the ground: against gravity (up), with gravity (down), or latterly (side to side). A lateral deployment is the best method to negate gravitational effects, but the cylindrical design of RIGEX prevented choosing this option. As such, the tubes were deployed in a gravity assist fashion – when the oven doors opened, the tubes “fell” out of the oven box prior to inflation. During the preflight thermal vacuum test, one tube failed to deploy (discussed in Section 4.1.2).

In addition to the preflight thermal vacuum tests, Moeller conducted deployment testing during the inflation system redesign process [28]. Using the vacuum chamber, he used an early version of the ovens to heat a tube and recorded the pressure inside the tube and the reservoir during the deployment process, as well as the temperature of tube post-deployment. The direction of deployment is assumed to be lateral (gravity offload).

The on-orbit pressure data successfully validates multiple preflight pressure test results and correlates successfully with external research concerning zero gravity inflatable tube deployments. The space flight pressure and thermal vacuum pressure test results are shown in comparatively in Figure 5.3, and Moeller’s vacuum chamber testing is shown in Figure 5.4. The gravity assisted deployments do not exhibit pressure spikes on the same scale as the space flight and Moeller’s gravity offload tests indicate, and they inflated approximately 100ms faster than the space flight tubes, while Moeller’s gravity offload test took approximately six times longer to reach inflation. This suggests gravity interacts with the fold corners of a stowed tube, introducing friction which acts as a seal, which in turn requires increased pressure to open, allowing the next section of tube to be inflated under gravity offload or microgravity conditions. This is consistent with the analysis presented in Section 4.1.2.

These results correlate well with results from testing conducted by researchers at the University of Kentucky, who repeatedly deployed a single-fold tube on a gravity offload mechanism both on the ground (1-g case) and onboard NASA’s modified KC-

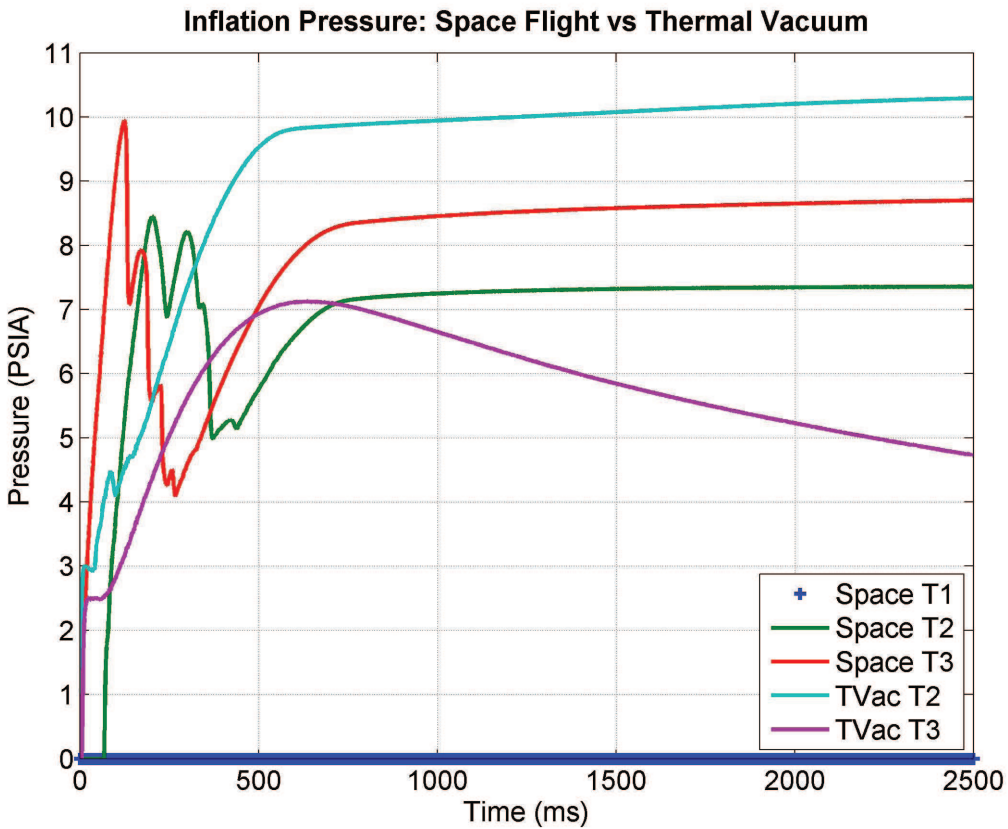


Figure 5.3: Correlation of space flight pressure and the preflight thermal vacuum pressure test results. Note the gravity assisted thermal vacuum deployments do not have pressure spikes.

135 Stratotanker (0-g case). The 1-g gravity offload tests suggest the single fold acts as a seal and introduces a “pressurization delay”, which was not observed during the 0-g testing. The 1-g gravity offload deployments for this particular test setup usually took longer than 25 seconds, whereas the 0-g deployments were typically complete within 20 seconds. This data is consistent the RIGEX test results and observations [38].

5.3 Comparison of Vibration Testing Results

The previous students have accomplished a significant amount of vibration response testing on the RIGEX preflight tubes. This work provides the basis with which to correlate the space flight vibration response test results. The space flight vibration response test results are then compared to the post space flight and ground test results, and a comparison of the preflight and post space flight results completes the section.

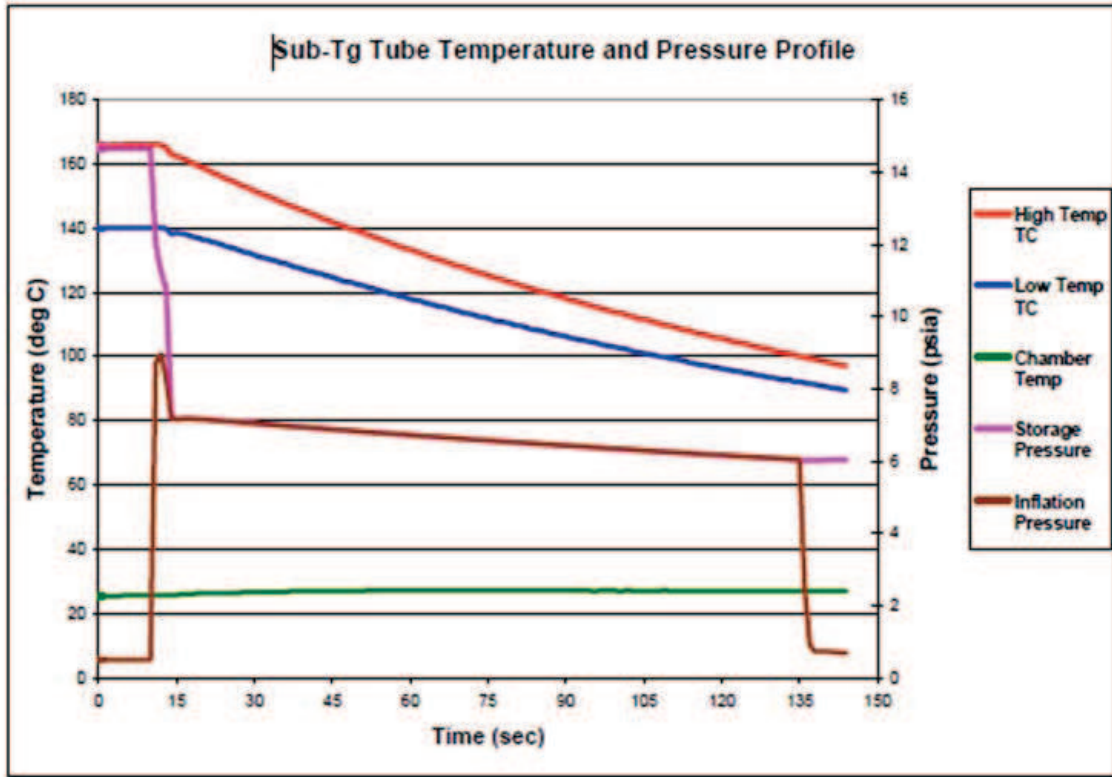


Figure 5.4: Pressure system and temperature results from a vacuum tank tube deployment test. Note the spike in the tube pressure and the temperature profile of the cooling tube.

5.3.1 Space Flight and Preflight Results. Single, Philley, Holstein, Moody, and Goodwin all completed some form of vibration response testing over a wide sample of inflatable/rigidizable tubes and test conditions during their research. Predominantly, the previous students located the first and second bending modes at 60 and 660Hz, respectively, which was confirmed in Section 4.3.1. Using a Polytec PSV-300 (a single axis predecessor to the triaxial Polytec PSV-400) Philly also located a torsional mode at 236Hz (Table 2.3).

As discussed in Section 4.1.3.3, the space flight vibration response testing suffered from a low signal to noise ratio, and the FRFs exhibited time dependant behavior. The FRFs from the last test iteration were presented and the results tabulated. All three tubes had a ~ 900 Hz peak, but the only natural frequencies comparable to the preflight data was the 386Hz second bending mode for tube 1 – considerably lower than the previously established second bending modes. Tube 1 possesses the largest deployment

deviations of the three space deployed tubes, and the fold creases are still evident in the deployed tube, both of which would weaken the tube and reduce resistance to bending. The reasons for the decrease in natural frequency are speculated upon in greater detail in Section 5.4. The other natural frequencies seen in the space flight FRFs were not seen in the preflight testing.

5.3.2 Space Flight and Post Space Flight Testing. A direct comparison to the space flight vibration response test results by using the flight computer cannot be accomplished. Section 4.2.2 details the failed attempt to repeat the flight computer driven vibration response testing. Follow-on testing was conducted, however, using dSpace as a surrogate flight computer coupled with an external fourth order Butterworth filter; the results from this testing are believed to be similar in nature to the flight computer results.

The tube 1 space flight 386Hz resonant frequency has excellent correlation with the dSpace vibration test results. The dSpace resonant frequency was 381Hz, only 1% off, almost an exact match. The tube 2 space flight 768Hz peak lines up with a slight bump in the dSpace results, but not enough to suggest a match. The remaining natural frequencies tabulated for the three tubes were not observed in the dSpace vibration test results.

The triaxial laser vibration response results again closely match the 386Hz peak for tube 1, but are almost exactly on the 768Hz peak for tube 2. The bottom scan point for tube 2 also has a slight peak at 910Hz, another very close match with the 914Hz resonance seen in the space flight FRF for tube 2. Unfortunately, neither of the tube 3 peaks selected in the space flight FRF closely correspond to any post flight vibration test results. It is possible these peaks were shifted to significantly higher frequencies on-orbit in the absence of air damping, but this is doubtful. It is much more likely these peaks are not true natural frequencies.

5.3.3 Preflight and Post Space Flight Testing. The space flight vibration test results provided only limited correlation with the preflight tests. Comparing the preflight

tests with the higher fidelity post space flight ground testing produces some interesting results, however.

First, all three flight tubes demonstrate a considerably lower first and second bending natural frequency than the preflight tests predicted. This is probably a result of the pristinely deployed test articles used in the preflight tests. All three flight tubes exhibit some deployment error, with flight tube 1 exhibiting the largest error and correspondingly the lowest first and second bending natural frequencies. Curiously, tube 3 is the straightest flight tube, but it has a lower first bending natural frequency (but higher second bending) than that of tube 2.

Another interesting result is the 214Hz first torsion mode of flight tube 2, which closely matches with Philley's 236Hz first torsion (about 9%). Flight tubes 1 and 3 exhibit very little response in this frequency range; tube 1 has a slight bump on the top scan point, and the top two scan points for tube 3 have an anti-resonance, but no peak in comparison to tube 2.

As a side note, it does not appear as though the added weight of the second accelerometer mounted to the top tip of the flight tubes for the dSpace and SignalCalc testing (the flight accelerometers were inoperable and could not be removed) appreciably impacted the vibration response in comparison to the triaxial laser data taken without the second accelerometer and accompanying accelerometer ribbon cable.

5.4 Comparison of Finite Element Models

A comparison analysis was conducted on RIGEX-based and aluminum-based mission oriented FE models of the structures presented in Section 4.4.3. Weights and natural frequencies were collated and the results are presented Table 5.2. As expected, the RIGEX-based structures weighed approximately 50% of the aluminum structures. The aluminum structures natural frequencies were approximately double the RIGEX-based structures for each corresponding mode, although the carbon fiber tubes should have been about as stiff (roughly equivalent Young's modulus) as aluminum tubes, according to L'Garde, Inc. [37]. This is a surprising result, and warrants additional testing in the future.

Table 5.2: A comparison of weight and natural frequencies for the coarse tube model and the two mission structures consisting of RIGEX and aluminum based tubes.

Comparison of RIGEX with Aluminum				
	Weight (kg)		Natural Frequencies (Hz)	
Structure	RIGEX	Aluminum	RIGEX	Aluminum
Coarse Tube	.0944	0.137	23.6	59
			406	635
Triangular	1.93	3.65	8.2	16.5
Cross Section			8.6	17.1
Truss			10.5	22.6
Flat Panel	1.25	2.02	1.1	2.4
			6.9	15.14
			7.1	16.58

Any relative stiffness to weight comparison provided by these models is somewhat suspect, however. The modeled behavior of the tube 3 is based on the system behavior exhibited by tube 3 during vibration response testing, but the model does not take into account the exact geometry of tube 3 (slight tilt, creases from the folds, etc). Furthermore, the comparison discussed above and presented in Table 5.2 are for trusses with the same beam thickness, which in retrospect was a less than optimal way to compare the structures. Finally, the aluminum based models do not have any deployment mechanisms modeled which would impact stiffness in a similar fashion as the creases created in the folding/stowing process.

As an aside, an alternative analysis was conducted using quoted L’Garde, Inc. values for the carbon fiber Young’s modulus. This analysis compares the same geometric model (thickness is equal) but the flight tubes’ deployment mechanism (creases) are no longer modeled – perhaps yielding a more “apples-to-apples” comparison. The results were not surprising: the increase in stiffness resulted in the flight tubes exhibiting a greater fundamental frequency than the aluminum tubes, while the flight tubes still approximately half the weight of the aluminum tubes.

Within the simplified model, a couple of possible explanations of this relative stiffness to weight divergence exist, both of which center on the creases created in the folding/stowing process. The first focusses on the potential of time varying structural properties. The flight tubes had been folded for several years prior to their on-orbit

deployment, and the fold creases in the deployed tubes are still quite evident (although less so for tube 3, the tube which the models were tuned to). The original tubes tested by Single and Philly were much stiffer (on the order of the aluminum tubes), and do not exhibit creases. Presumably these tubes were deployed at the factory immediately after they had been folded. It could be the carbon fiber “learns” these folds over time, much like the warping effect of wood. If this warping effect does occur in the tubes, then the best solution would be launching and deploying relatively recently folded tubes, or using additional inflation pressure to help push the folds out.

The second possible explanation is based on the weakened state of the carbon fiber and matrix at the fold locations. If the carbon fibers were broken at the folds or the matrix is inconsistent, the folds would become a major weak spot. Combine either of these explanations with the location of the first fold (immediately above the top of the basecap) and the result is a cantilevered beam with a significant weak spot near its base, through which all load induced moments must travel. This is readily observable with a flight representative tube that was deployed in the preflight thermal vacuum test – a seemingly insignificant moment applied in the in fold (X-axis) direction results in instantaneous buckling near the basecap.

The restoring force for the first cantilevered bending mode is the tension force on the outside bend. Given the creases from the folds, the carbon fiber matrix would tend to correct the creases before the full tension restoring force could work to resist the induced bending. On account of the creases, it is believed the flight tubes’ first bending restoring force is actually the compression resistance of the composite matrix, rather than the carbon fiber tension. Without these creases, resistance to bending would be greatly enhanced, resulting in an increase in relative stiffness to weight. The small sample size of space flight deployed tubes combined with the lack of physical inspection of the interior of the tubes prevents an assertion of the exact reason behind the relative differences in stiffness to weight.

5.5 Deployment Processes

The heating and inflation method of deploying sub- T_g inflatable tubes on-orbit has been validated and is now a proven, space qualified system. Given the success of deploying individual tubes, the next hurdle to surpass is deploying inflatable/rigidizable subsystems or mission structures. This will require changes to the heating system at a minimum, and perhaps the inflation system as well. Three types of processes are given a brief review: assembly line, all-in-one, and internal heating/inflation.

The most promising of these processes for very large structures is the assembly line process. Essentially an oven with doors on the top and the bottom, interconnected segments of the given structure are loaded into oven, which heats them beyond their respective T_g temperature, at which point they are inflated through one of two options: either connect to the heated segment and inflate only it, or attach the inflation system to the first deployed segment and use the deployed sections as the plumbing which transports the inflation pressure. The small oven size required and single inflation system are the benefits of this method, but the complexity is a definite limitation.

The second option is an all-in-one system, which is essentially an expanded version of RIGEX. The entire sub- T_g structure is stowed inside of the oven, which heats the structure, and a single inflation port and solenoid actuation is all that is required for deployment. The simplest of all three methods, it is also the only on-orbit proven method. This method has demonstrated ground based deployment of large trusses. L’Garde, Inc. has produced a video of deploying a large triangular cross section truss with this method [19]. Unfortunately, this method requires the bulkiest oven and the longest heating time – the entire structure would have to be thoroughly warmed; incomplete deployment would be the result of insufficient heating. This could be solved by adding a second layer of heaters within the cross section of the structure, which would allow outside-in and inside-out heating, limiting the risk of insufficiently heating the structure.

The final option discussed is an internal heating/inflation mechanism. Essentially, a resistive type heater and inflation mechanism would be placed inside of the structure during the manufacturing process, after which the structure would then be stowed. This

method would prevent insufficient heating, and a variety of inflation systems (tanked gas, phased change, or chemical gas generation) could be chosen, increasing design flexibility, both definite benefits. Unfortunately, this option would ultimately increase the stowed volume of the structure and would probably have the largest weight penalty.

5.6 Technology Readiness Level Review

A TRL is a measure of the maturity of a given technology, with readiness levels spanning from basic technology research to launch and operations. Developed by NASA and widely used within the DoD and the larger space community, TRLs are often used to provide decision makers a general level of understanding on the ability of the given system to enter operations. The scale is generally broken into four categories: basic technology research typically rated TRL 1-4, technology development and demonstration rated TRL 5-6, system level development and demonstration rated TRL 7-8, and system operations rated TRL 9. Jumping from one category to the next category is typically regarded as a major step. This scale is presented in Figure 5.5.

Several “flavors” of TRL calculators are available, but this analysis uses AFRL Transition Readiness Calculator, version 2.2. Exclusion of software, manufacturing and programmatic elements were key assumptions which narrowed the scope of the analysis. A TRL 7 rating results from completing the overall demonstration environment view (a top level perspective) assessment by virtue of RIGEX’s successful on-orbit demonstration – a prototype unit had been demonstrated in an operational environment.

Moving from the top level down to the individual TRL assessments, the inflatable/rigidizable sub- T_g tubes and RIGEX deployment system meet all requirements for TRL 1-6. Table 5.3 addresses the TRL 7 assessment. The TRL 8 assessment clearly indicated the RIGEX system was not a TRL 8, and not a single assessment for TRL 9 has been met. This results in a TRL 7 rating, which supports the top level rating for the given analysis set and assumptions.

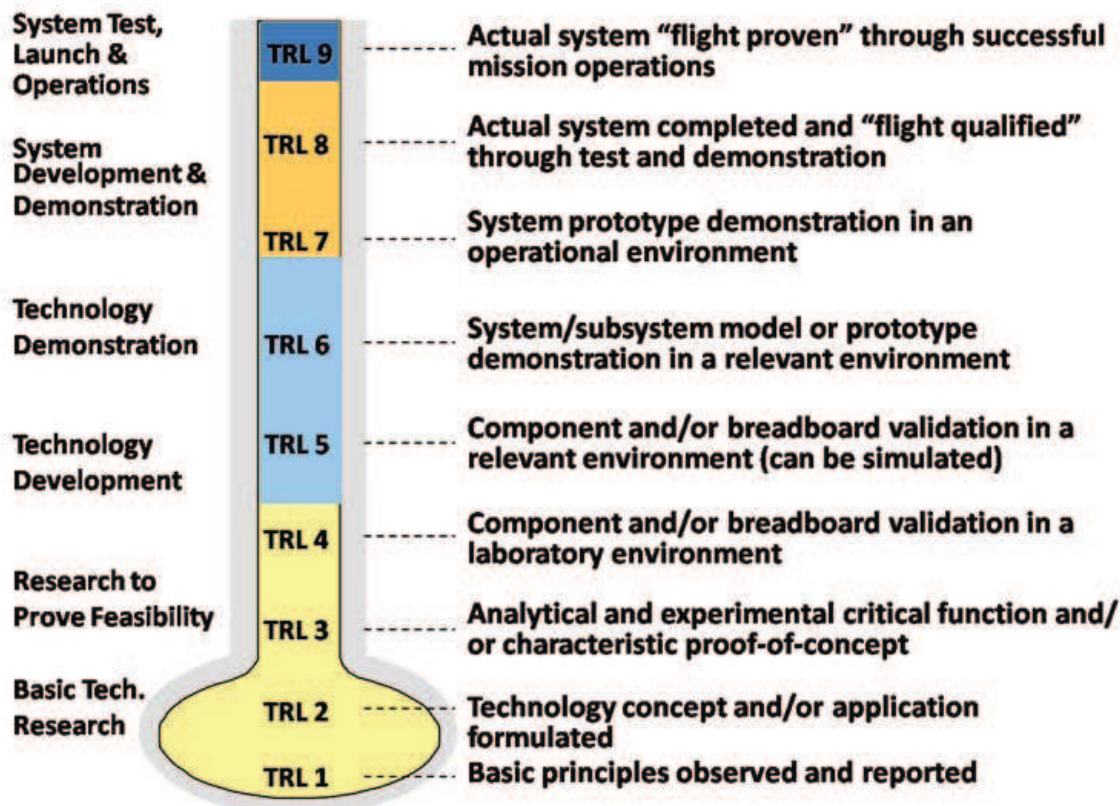


Figure 5.5: Technology readiness scale developed by NASA.

5.7 Conclusions

With respect to the test result correlations, the most obvious conclusion is RIGEX satisfied the mission statement and all of the experimental objectives by validating the ground testing of the inflation and rigidization methods. The space flight results validate the preflight temperature and inflation test procedures and results, and are correlated with the preflight vibration results. RIGEX also successfully validated and space qualified the inflation system and the tube heating method. In addition, RIGEX and aluminum-based mission oriented truss structures were compared; the RIGEX-based structures weighed considerably less than the aluminum based structures, though the aluminum structures did prove to be stiffer.

Beyond result correlation, this chapter reviewed deployment processes and the RIGEX Technology Readiness Level. Given the next challenge of deploying complete inflatable/rigidizable structures, the most promising deployment process reviewed was

Table 5.3: Overview of RIGEX deployment system TRL 7 assessment.
Technology Readiness Level 7 Assessment

% Complete	Assessment Question
100	Models and Simulations used to simulate some unavailable elements of system, but these instances are rare.
80	Each system/software interface tested individually under stressed and anomalous conditions.
100	Operational environment, but not the eventual platform.
100	Components are representative of production components.
100	Most functionality available for demonstration in simulated operational environment.
100	Operational/flight testing of laboratory system in representational environment.
100	Fully integrated prototype demonstrated in actual or simulated operational environment.
100	System prototype successfully tested in a field environment.

the assembly line process. The TRL assessment used the AFRL Transition Readiness Calculator version 2.2, and the results suggest the RIGEX deployment system rates a TRL 7.

VI. Conclusions and Recommendations

THIS chapter presents the capstone conclusions associated with the work presented in previous chapters and provides recommendations for the way forward, leveraging the experience and lessons learned courtesy of the RIGEX experience.

6.1 Conclusions

RIGEX successfully completed all of its experimental objectives by successfully validating the ground testing of inflation and rigidization methods. RIGEX also successfully validated and space qualified both the inflation system and the tube heating method.

While onboard STS-123, RIGEX successfully deployed all three inflatable/rigidizable tubes. Temperature, pressure, image, and accelerometer data were all successfully collected on-orbit and retrieved for processing. All of the data was successfully processed and presented in Chapter 4 and correlated with preflight and post space flight test results along with external research in Chapter 5.

The ovens performed flawlessly and appear as though they could be reused, important information for consideration in deploying multiple tubes on-orbit. The ovens increased the experiment structure temperature significantly and the structure appeared to be headed for a thermal equilibrium, but in the future thermal balance will need to be a more integral part of the design process, particularly for the flight computer.

Flight tube 3 inflated immediately after the inflation solenoid was commanded open, flight tube 2 had a 0.068 second delay, and flight tube 1 did not inflate while the inflation pressure was being monitored (first five seconds), but is believed to have inflated within 50 seconds of the commanded inflation. Inflation pressure profiles of various gravity conditions when compared with the on-orbit inflation pressure profiles, resulting in the determination that microgravity deployments occur almost as fast as gravity assist deployments, but much faster than gravity offload deployments. Also, inflation pressure spikes were correlated with opening pressure seals created by folds in the stowing process.

The imaging system worked as advertised on-orbit, and through a combination of image change detection analysis and high resolution contact measurement, the exact

on-orbit deployment error of flight tube 1 was determined to be -1.17 and 0.73 inches in the respective X and Y-axis, and flight tube 3 achieving an almost perfectly true deployment on-orbit (within error and 0.07 inches for X and Y-axis, respectively) – critical information for precision inflatable deployment necessary for joining large structures on-orbit.

The flight tubes exhibited lower natural frequencies than were predicted in the preflight tests, which was hypothesized to be attributable to the fold induced creases in the deployed flight tubes which where not smoothed during the inflation process. The filtered input signal and reduced voltage input to the PZT resulted in a limited input during the space flight vibration response tests. During the space flight vibration testing, the resonant frequencies drifted, showing time dependent behavior which was not expected. The flight vibration response test results consist of a few peaks which mostly correlated to post flight vibration response tests. Overall, the first and second bending mode shape of all three flight tubes and the first torsional mode shape of flight tube 2 were comparable (but typically significantly lower) to the preflight testing mode shapes.

Two finite element models were constructed and tuned to match the first and second bending modes of tube 3. The ten beam element coarse mesh FE model nearly matched the 9,406 plate element fine mesh FE model for the first and second bending mode. This confirmed the first two tube bending operational deflection shapes were in fact eigenvector mode shapes. Two mission oriented space structures were constructed out of the course mesh tube FE model, and their respective weight and modal properties were compared with the same structure made from aluminum. The RIGEX-based structures were typically half the weight of the aluminum structures but the natural frequencies of the aluminum structures were approximately double the RIGEX-based structures for each corresponding mode. However, comparisons of relative stiffness to weight of the two materials within the simplified models is somewhat suspect.

6.2 Recommendations

AFIT now has more experience deploying inflatable/rigidizable space structures on-orbit than any other DoD entity, and arguably more than any other commercial entity. There are broad opportunities with which to leverage this experience and expand the inflatable/rigidizable envelope, all of which could benefit from several key lessons learned from the on-orbit experience.

6.2.1 Lessons Learned. There were several lessons learned from the RIGEX experience in its entirety, but this section will focus on the work done during the preflight thermal vacuum test through the end of the post space flight testing.

System Architecture

- Increase the flight computer data storage capacity to allow for recording of complete thermocouple, pressure transducer, and accelerometer time histories.
- Increase the image storage capacity and increase the imaging frequency.
- Internal experiments should not share common hardware paths – if a linkage breaks it affects all of the experiments rather than just one.

Preflight Testing

- A complete end-to-end system test should be accomplished after any changes in configurations prior to shipment.
- Conduct a root cause analysis for test anomalies and obtain positive proof of anomaly resolution.

Shipping Environment

- Space flight experiments should have dedicated shipments rather than being shipped commercially.
- Maximum acceptable shock detection levels should be established. If these levels are breached an end-to-end system test should be conducted.

6.2.2 The Future and Legacy of RIGEX. There could be further structural information learned from destructive structural testing and inspection on the flight tubes. These tests could check for manufacturing quality, matrix consistency, and time varying material properties within the tubes themselves. Strain, creep, and buckling tests on the flight tubes would yield further information. Also, a increased fidelity FE model could be developed by modeling the composite weave and matching the deployed geometry of the flight tubes.

The next step for this technology is to create an inflatable/rigidizable subsystem (communications array, inflatable truss or panel, or inflatable solar array) to be flown on a small satellite. The RIGEX process of an overall system engineering review followed by subcomponent development and testing is an excellent model to follow, and the maturity of the deployment technology will help shorten the design to flight timeline. In addition, the on-orbit vibration response performed by RIGEX tests which occupied so much of the previous students time and energy would not be necessary for a satellite subsystem. Given this, it is conceivable a subsystem could be fielded for use within the next three student cycles. The operationally responsive space program, academy satellites, or even an AFIT built satellite would be perfect for this opportunity.

Appendix A. RIGEX Post Flight Examination and Condition

From the return of RIGEX from Cape Caneveral through the end of analysis for this thesis, the physical condition and appearance of RIGEX was observed. The construction process, shipping environment, shuttle interface and the space environment all impacted the performance of RIGEX, on-orbit and in ground testing. This Appendix describes the condition in which RIGEX arrived at AFIT.

A.1 Inoperable Components

The successful on-orbit data collection discussed in 4.1 is testament to the quality and skill used in creating the experiment. In the space environment, the experiment functioned end-to-end. However, when RIGEX returned to AFIT, the first post flight end-to-end test (minus heaters) did not execute properly, which led to an investigation into what had changed from orbit to AFIT.

A.1.1 Initial Anomalies. The post flight end-to-end test was started from the failsafe point set after tube 1 was vented. The first indication the test was not proceeding correctly was the failure of the Light Emitting Diodes (LEDs) to turn on during the deployed tube imaging process. This failure was followed by a lack of auditory confirmation of piezo patch operation during the modal response testing, suggesting the chirp input function was not being sent to the piezo patches. The 1-D laser vibrometer confirmed lack of piezo patch operation by measuring zero response during the modal test phase. The LED and piezo patch anomalies led to the decision to end the test and begin an investigation into potential problems.

A.1.2 Anomaly Determination. The computer had booted up properly and believed that the tests were running according to their proper timelines; this suggested the fault was between the computer and the LEDs and piezo patches. A multimeter was used to check the resistance in all of the fuses in search of a blown fuse, but none were found. Next, 12 volts were applied to the LEDs and Cameras which led to the determination that one camera and three LEDs were no longer functional.

The cameras and LEDs used the 12 volt power supply, so the next step was to check the power supply to see if it was still functional. The RIGEX Shuttle power emulator was powered up and plugged into RIGEX and the 12 volt power supply output was connected to an oscilloscope. The 12 volt power supply did not supply any voltage to the oscilloscope, indicating the power supply was bad.

At this point the 5 volt power supply output was connected to the oscilloscope, which displayed a wave pattern alternating between +3 and +5 volts, indicating that the 5 volt power supply was also bad. The 5 volt power supply provides +5 volts to the accelerometers mounted to the tips of the tubes and the piezo patches at the base of the tube; accelerometer functionality was checked and all three accelerometers were inoperable. Table A.1 summarizes the tested components operability.

A.1.3 Anomaly Resolution. With the accelerometers not functioning, post flight testing could not be accomplished, thus new accelerometers were purchased. Because the flight accelerometers could not be removed, the new ones were attached to the top flange of each tube. This mildly increased the tip weight, the effects of which are detailed in 4.2.1. The 5 and 12 volt power supplies were both removed and a new 5 volt power supply was inserted into computer stack, attaching to the low pass Butterworth filter. The filter provides power to the DAC and the transformers, which drive the piezo patches. A new 12 volt power supply was unnecessary because components powered by the 12 volt power supply (LEDs, pin pullers, solenoids) were no longer needed for post flight testing. The renewed attempt at post flight testing (using the new accelerometers and power supply) with the flight computer is discussed in 4.2.2. The cameras were powered via external power to produce the post flight images necessary for the analysis work done in 4.1.4, but camera 2 still failed to function.

A.1.4 Probable Cause. The last task the astronauts completed before going to sleep was to turn on power to the experiment. It took approximately 2 hours to run completely through the experiment, and RIGEX continued to receive power until the astronauts awoke the next morning and turned the power off. It is hypothesized that while the experiment remained in extended post experiment standby, a power surge

Table A.1: Overview of multimeter and oscilloscope tested RIGEX Components.

Location	Component	Functional Test Results
Computer Bay	+5V Power Supply +12V Power Supply	Erratic Inoperable
Bay 1	Camera	Operable
	Inboard LED	Inoperable
	Outboard LED	Operable
	Accelerometer	Inoperable
Bay 2	Camera	Inoperable
	Inboard LED	Inoperable
	Outboard LED	Operable
	Accelerometer	Inoperable
Bay 3	Camera	Operable
	Inboard LED	Operable
	Outboard LED	Inoperable
	Accelerometer	Inoperable

affected the power supplies such that they no longer functioned properly. Unfortunately, there is no means to confirm this explanation; the telemetry data for amperage drawn by RIGEX does not contain the resolution necessary to spot such a spike.

A.2 Contaminant in Connections

As part of the final construction process prior to shipment of RIGEX to Cape Canaveral, the computer stack and all wiring connections were epoxied together to prevent wires from coming loose and connections from backing out as discussed in Owens [31]. To conduct ground testing, the flight computer and flight accelerometer cables were disconnected. When the flight computer connections were removed, the connections were clean. When the accelerometer connections were removed, however, it appeared epoxy had worked into the inner contacts, which could have increased impedance across the connection, lessening the data quality. Figure A.1 illustrates the stake contaminate on one of the accelerometer connections.



Figure A.1: Stake contaminant on the accelerometer connections.

A.3 Oven Conditions

The ovens played a critical role in the successful on-orbit deployment of the RIGEX tubes. Working as advertised, the ovens successfully heated all three tubes well beyond their 125° transition temperature, setting the correct preconditions for inflation. Visual post flight inspection of the ovens shows zero contaminant or configuration changes. In fact, Figure A.2 the ovens appear very similar to their preflight condition. This indicates the ovens could be reused, probably many times over, an important result which lends credit to the assembly line, or “pizza oven” concept of using a single oven to heat tubes in an assembly line fashion. Indeed, the ovens developed by Maddux [24] and iterated on by Owens can now be considered space qualified, having been vibration tested, thermal vacuum tested, and operated in space, on-orbit.

A.4 Shipping Environment

When RIGEX was packaged for shipment from AFIT to Cape Canaveral, a Drop-N-Tell 5g shock damage detector strip was applied on three sides of the shipping container, representing the container’s X, Y, and Z-axis. Upon arrival at the Vehicle Assembly Building, the 3 shock damage detectors had been tripped, indicating the shipping container had experienced at least a 5g event in all three directions. This prompted an upgrade to 10, 15, and 25g shock damage detector strips for the shipment back to AFIT after flight. The negative vertical axis received at least a 25g event on the return, which

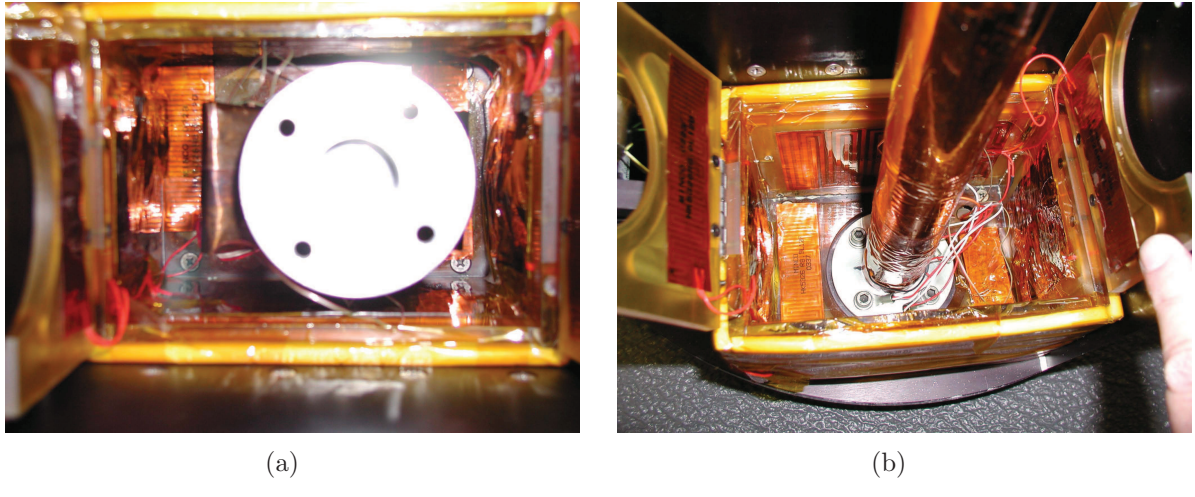


Figure A.2: (a) Closeout photo of an oven, with stowed flight tube shown.
(b) Post flight photo of an oven with deployed tube. Note how clean the post flight oven appears; with the tubes removed the ovens would be indistinguishable.

tripped all three detectors. One of the horizontal axis tripped a 10g detector, the other did not trip any detectors. The tripped shock detectors are shown in Figure A.3. This harsh shipping environment almost certainly played a role in the RIGEX component functionality upon return to AFIT.



Figure A.3: Shock damage detectors tripped during RIGEX return shipment to AFIT

Appendix B. Matlab Scripts

The primary tool used for data analysis for this thesis was MATLAB®. Several scripts were written to analyze the experimental data; the most pertinent of which analyzes the space flight data retrieved from the flight computer after RIGEX returned to AFIT.

Listing B.1: Appendix3/Space_Flight_Analysis_final.m

```
1 % RIGEX Post Test Evaluation
% This file imports all flight test data, analyzes as necessary and presents ...
in
% plot format, then saves the plots to the figures for thesis file.
% ...created by Capt Brett Cooper
% -----
6 tic;clc; close all; clear all;
%% Temperature
% Importing Temperatures....
temp1 = importdata('R1TEMP1.DAT'); %tempX(:,5) is time vector
temp2 = importdata('R1TEMP2.DAT'); %tempX(:,1) is tube thermocouple A, (:,2) ...
is thermocouple B
11 temp3 = importdata('R1TEMP3.DAT'); %tempX(:,3) is structural temp, (:,4) is ...
computer bay temp

%Plotting Quad Plot; each plot is a different thermocouple, but different ...
bays
%Structural thermocouple readings from all runs on same plot, etc
figure; set(gcf,'defaultaxesfontsize',14)
16 subplot(2,2,1); plot(temp1(:,5),temp1(:,1),temp2(:,5),temp2(:,1),...
temp3(:,5),temp3(:,1))
title('Tube Thermocouple A - All Bays','FontWeight','...
bold')
xlabel('Time (s)'); grid on;
ylabel('Temperature ( ^{o}C)');
subplot(2,2,2); plot(temp1(:,5),temp1(:,2),temp2(:,5),temp2(:,2),...
temp3(:,5),temp3(:,2))
title('Tube Thermocouple B - All Bays','FontWeight','...
bold')
```

```

        legend('Tube 1','Tube 2','Tube 3','Location','Best');
        xlabel('Time (s)'); grid on;
        ylabel('Temperature ( ^{o}C)');

subplot(2,2,3); plot(temp1(:,5),temp1(:,3),temp2(:,5),temp2(:,3),...
temp3(:,5),temp3(:,3))

26          title('Structural Temp','FontWeight','bold')
            xlabel('Time (s)'); grid on;
            ylabel('Temperature ( ^{o}C)');

subplot(2,2,4); plot(temp1(:,5),temp1(:,4),temp2(:,5),temp2(:,4),...
temp3(:,5),temp3(:,4))

            title('Computer Board Temp','FontWeight','bold')
31          xlabel('Time (s)'); grid on;
            ylabel('Temperature ( ^{o}C)');

print -dpng -r300 L:\everyone\Cooper_RIGEX\Figures_for_Thesis\...
Quad_Plot_Inflight_Temp.eps
print -dpng -r300 L:\everyone\Cooper_RIGEX\Figures_for_Thesis\png\...
Quad_Plot_Inflight_Temp.png

36 %Plot Structure Temperature in line, similar to cobb's pressure plot below
%Create Time Vectors
t1 = temp1(:,5); %While Temp being monitored
t12 = max(t1)+500; %~500 seconds derived from flight code (not monitored)
t2 = temp2(:,5) + max(t12); %while temp being monitored
41 t23 = max(t2) + 500; %~500 seconds derived from flight code (not monitored)
t3 = temp3(:,5) + max(t23); %While temp being monitored
%Acutal Plot
figure; set(gcf,'defaultaxesfontsize',14)
plot(t1,temp1(:,3),'b-',t2,temp2(:,3),'g-',t3,temp3(:,3),'r-'); grid ...
on; hold on;
46 plot(t1,temp1(:,4),'b*',t2,temp2(:,4),'g*',t3,temp3(:,4),'r*');
legend('Tube 1 Structure','Tube 2 Structure','Tube 3 Structure','Tube...
1 Computer','Tube 2 Computer','Tube 3 Computer','Location','Best',...
);
title('Experiment Structural Temperature vs. Time','FontWeight','bold...
');
xlabel('Time (s)'); ylabel('Temperature ( ^{o}C)');

```

```

print -dpng -r300 L:\everyone\Cooper_RIGEX\Figures_for_Thesis\Structural_Temp...
    .eps
51 print -dpng -r300 L:\everyone\Cooper_RIGEX\Figures_for_Thesis\png\...
    Structural_Temp.png

%% Pressure
t_p = zeros(5000,1);
% create a time matrix for prssure .dat files (no counter data in file)
% pressure and accel data measured for 5 secs at ~1000hz,
56
for ctr = 1:5000
    t_p(ctr) = ctr-1;
end
%plot tube data individually with scaled pressure calibration *3.0084
61 %Change from Counts to volts to Pressure
p1 = 5*((importdata('R1IT1I1.DAT')+32768)/2^16);
pressure1 = [p1(:,1), p1(:,2), p1(:,3), 3.0084*p1(:,4)];

p2 = 5*((importdata('R1IT2I1.DAT')+32768)/2^16);
66 pressure2 = [p2(:,1), p2(:,2), p2(:,3), 3.0084*p2(:,4)];

p3 = 5*((importdata('R1IT3I1.DAT')+32768)/2^16);
pressure3 = [p3(:,1), p3(:,2), p3(:,3), 3.0084*p3(:,4)];

71
%!!!!!!NOTE - Name includes volts, but it is changed to psia by 3.0084
%using FVT 8 data - FVT file that corresponds to orbit test
FVTvolts = 3.0084*importdata('FVTGAS8.DAT');
%Pull 3 Tube/Tank Deploy Data
76 T1_Deploy_volts = 3.0084*importdata('T1GAS1.DAT');
T2_Deploy_volts = 3.0084*importdata('T2GAS1.DAT');
T3_Deploy_volts = 3.0084*importdata('T3GAS1.DAT');
%Pull 3 Tube/Tank Cooling Data
T1_Cooling_volts = 3.0084*importdata('T1GCL1.DAT');
81 T2_Cooling_volts = 3.0084*importdata('T2GCL1.DAT');
T3_Cooling_volts = 3.0084*importdata('T3GCL1.DAT');
%Pull 3 Tube/Tank "After" Data

```

```

T1_After_volts = 3.0084*importdata('T1GVN1.DAT');
T2_After_volts = 3.0084*importdata('T2GVN1.DAT');
86 T3_After_volts = 3.0084*importdata('T3GVN1.DAT');

%Re Order Data into Specific Tubes and Tank Values: Tube 1/2/3 Tank 1/2/3
tube1p = [FVTvolts(1); T1_Deploy_volts(1); T1_Cooling_volts(1); ...
    T1_After_volts(1);
    T2_Deploy_volts(1); T2_Cooling_volts(1); T2_After_volts(1);
91     T3_Deploy_volts(1); T3_Cooling_volts(1); T3_After_volts(1)];
tube2p = [FVTvolts(2); T1_Deploy_volts(2); T1_Cooling_volts(2); ...
    T1_After_volts(2);
    T2_Deploy_volts(2); T2_Cooling_volts(2); T2_After_volts(2);
    T3_Deploy_volts(2); T3_Cooling_volts(2); T3_After_volts(2)];
tube3p = [FVTvolts(3); T1_Deploy_volts(3); T1_Cooling_volts(3); ...
    T1_After_volts(3);
    T2_Deploy_volts(3); T2_Cooling_volts(3); T2_After_volts(3);
    T3_Deploy_volts(3); T3_Cooling_volts(3); T3_After_volts(3)];
96 tank1p = [FVTvolts(4); T1_Deploy_volts(4); T1_Cooling_volts(4); ...
    T1_After_volts(4);
    T2_Deploy_volts(4); T2_Cooling_volts(4); T2_After_volts(4);
    T3_Deploy_volts(4); T3_Cooling_volts(4); T3_After_volts(4)];
101 tank2p = [FVTvolts(5); T1_Deploy_volts(5); T1_Cooling_volts(5); ...
    T1_After_volts(5);
    T2_Deploy_volts(5); T2_Cooling_volts(5); T2_After_volts(5);
    T3_Deploy_volts(5); T3_Cooling_volts(5); T3_After_volts(5)];
tank3p = [FVTvolts(6); T1_Deploy_volts(6); T1_Cooling_volts(6); ...
    T1_After_volts(6);
    T2_Deploy_volts(6); T2_Cooling_volts(6); T2_After_volts(6);
    T3_Deploy_volts(6); T3_Cooling_volts(6); T3_After_volts(6)];
106

%Plot three tube pressures and accel data on quad plot
figure; set(gcf,'defaultaxesfontsize',14);
h = plot(t_p,pressure1(:,4),'b+',t_p,pressure2(:,4),t_p,pressure3...
(:,4)); grid on; set(h,'linewidth',3)
111 title('3 Tube Inflation Pressures','FontWeight','bold');
xlabel('Time (ms)');

```

```

    ylabel('Pressure (PSIA)');
    legend('Tube 1','Tube 2','Tube 3','Location','SouthEast');
    axis([0 5000 0 11])

116 print -dpng -r300 L:\everyone\Cooper_RIGEX\Figures_for_Thesis\...
    Inflate_Pressures.eps
print -dpng -r300 L:\everyone\Cooper_RIGEX\Figures_for_Thesis\png\...
    Inflate_Pressures.png

121
figure; set(gcf,'defaultaxesfontsize',14)
    subplot(2,2,1); plot(t_p,pressure1(:,4),'b+',t_p,pressure2(:,4),t_p, ...
    pressure3(:,4)); grid on;
    title('3 Tube Inflation Pressures','FontWeight','bold',...
        );
    xlabel('Time (ms)');
    ylabel('Pressure (PSIA)');
    legend('Tube 1','Tube 2','Tube 3','Location',...
        'SouthEast');
    axis([0 5000 0 11])

126 %load Accel data from inflation (X,Y,Z are first three columns)
    subplot(2,2,2); plot((pressure1(:,1:3))); grid on;
    xlabel('Time (ms)');
    ylabel('Volts');
    legend('X Accel','Y Accel','Z Accel','Location',...
        'SouthEast');
    title('Tube 1 Inflation Accelerometer Data',...
        'FontWeight','bold')
    axis([0 5000 -.5 5.5])

    subplot(2,2,3); plot((pressure2(:,1:3))); grid on;
    xlabel('Time (ms)');
    ylabel('Volts');
    legend('X Accel','Y Accel','Z Accel','Location',...
        'SouthEast');
    title('Tube 2 Inflation Accelerometer Data',...
        'FontWeight','bold')
    axis([0 5000 -.5 5.5])

131
    subplot(2,2,4); plot((pressure3(:,1:3))); grid on;

```

```

    xlabel('Time (ms)');
141
    ylabel('Volts');
    legend('X Accel','Y Accel','Z Accel','Location',...
        'SouthEast');
    title('Tube 3 Inflation Accelerometer Data',...
        'FontWeight','bold')
    axis([0 5000 -0.5 5.5])

print -dpng -r300 L:\everyone\Cooper_RIGEX\Figures_for_Thesis\...
Quad_Plot_Inflate_Pressures_and_Accels.eps
146 print -dpng -r300 L:\everyone\Cooper_RIGEX\Figures_for_Thesis\png\...
Quad_Plot_Inflate_Pressures_and_Accels.png

%Accelerations only on triplot
figure; set(gcf,'defaultaxesfontsize',14)
    subplot(3,1,1); plot(detrend(pressure1(:,1:3),'constant')); grid on;
151
    xlabel('Time (ms)');
    ylabel('Acceleration (g)');
    legend('X Accel','Y Accel','Z Accel','Location',...
        'SouthEast','Orientation','Horizontal');
    title('Tube 1 Deployment Accelerometer Data',...
        'FontWeight','bold')
    axis([0 2000 -2 2])

156    subplot(3,1,2); plot((2/2.351)*detrend(pressure2(:,1:3),0)); grid on;
    xlabel('Time (ms)');
    ylabel('Acceleration (g)');
    legend('X Accel','Y Accel','Z Accel','Location',...
        'SouthEast','Orientation','Horizontal');
    title('Tube 2 Deployment Accelerometer Data',...
        'FontWeight','bold')
    axis([0 2000 -2 2])

161    subplot(3,1,3); plot((2/2.174)*detrend(pressure3(:,1:3),0)); grid on;
    xlabel('Time (ms)');
    ylabel('Acceleration (g)');
    legend('X Accel','Y Accel','Z Accel','Location',...
        'SouthEast','Orientation','Horizontal');

```

```

166          title('Tube 3 Deployment Accelerometer Data',...
           FontWeight','bold')
           axis([0 2000 -2 2])

print -dpng -r300 L:\everyone\Cooper_RIGEX\Figures_for_Thesis\...
    Tri_Plot_Inflate_Accels.eps
print -dpng -r300 L:\everyone\Cooper_RIGEX\Figures_for_Thesis\png\...
    Tri_Plot_Inflate_Accels.png
%% Ambient Accelerometer Data
171 %Load Ambient Data from Accelerometer in loop... in counts
%change from counts to volts... 5*(TXiXamb+32768)/2^16 within plot
%command ...

figure; set(gcf,'defaultaxesfontsize',14)

176 for i = 1:3
    ctr = i;
    for j = 1:5
        filename = sprintf('R1AT%ii%i.DAT',i,j);
        eval(sprintf('T%ii%iamb = detrend(importdata(filename))', i,j));
        eval(sprintf('T%ii%imean = mean(importdata(filename))',i,j));
        eval(sprintf('T%ii%istd = std(detrend(importdata(filename),0))',i,j))...
        ;
        subplot(5,3,ctr); plot(5*(eval(sprintf('T%ii%iamb',i,j))+32768)...
        /2^16); axis([0 5000 2.48 2.52]); hold on;
        title(['Tube ',num2str(i),' Amb Accel vs Time'],'FontWeight','bold');
        xlabel('Time'); ylabel('Volts'); grid on;
    ctr = ctr+3;
    end
end
print -dpng -r300 L:\everyone\Cooper_RIGEX\Figures_for_Thesis\15...
    _Ambient_Accel_measurements.eps
print -dpng -r300 L:\everyone\Cooper_RIGEX\Figures_for_Thesis\png\15...
    _Ambient_Accel_measurements.png
191 clc % clear up the command window after all of the eval commands

%one time history with bounds for nominal noise level (plotted in G's)
figure;set(gcf,'defaultaxesfontsize',14)

```

```

plot (.66*5*(T1i1amb(1:5000,1))/2^16); hold on;
196 plot (2*.66*.01*ones(5000,1), 'k'); plot (-.66*.01*ones(5000,1), 'k--')
plot (.66*.01*ones(5000,1), 'k--'); plot (-2*.66*.01*ones(5000,1), 'k')
title ('Tube 1 Ambient X Acceleration vs Time', 'FontSize', 'bold');
xlabel ('Time (1/5000 s)'); ylabel ('Acceleration (g)');
legend ('X Acceleration', 'Max Ambient Accel', 'Ambient Accel Noise', 'Location',...
'South')

201 print -dpng -r300 L:\everyone\Cooper_RIGEX\Figures_for_Thesis\png\...
Ambient_Accel_TimeHist.png

%determine the mean of the mean for each tube in each direction;
%T1mean = mean (.66*detrend(5*([T1I1mean; T1I2mean; T1I3mean; T1I4mean; ...
T1I5mean])+32768)/2^16);
206 T1mean = mean (.66*detrend([5*(T1I1mean+32768)/2^16; 5*(T1I2mean+32768)/2^16; ...
5*(T1I3mean+32768)/2^16; 5*(T1I4mean+32768)/2^16; 5*(T1I5mean+32768)...
/2^16]))
%T2mean = .66*mean ((5*([T2I1mean; T2I2mean; T2I3mean; T2I4mean; T2I5mean])...
+32768)/2^16);
T2mean = mean (.66*detrend([5*(T2I1mean+32768)/2^16; 5*(T2I2mean+32768)/2^16; ...
5*(T2I3mean+32768)/2^16; 5*(T2I4mean+32768)/2^16; 5*(T2I5mean+32768)...
/2^16]))
%T3mean = .66*mean ((5*([T3I1mean; T3I2mean; T3I3mean; T3I4mean; T3I5mean])...
+32768)/2^16);
T3mean = mean (.66*detrend([5*(T3I1mean+32768)/2^16; 5*(T3I2mean+32768)/2^16; ...
5*(T3I3mean+32768)/2^16; 5*(T3I4mean+32768)/2^16; 5*(T3I5mean+32768)...
/2^16]))

211 disp(' '); disp('Mean Ambient Acceleration for Table in Thesis');
Mean_Ambient_Acceleration = [T1mean; T2mean; T3mean]
figure; subplot(2,1,1); bar3([T1mean; T2mean; T3mean]);
title ('Mean 3 Directional Ambient Acceleration', '...
FontSize', 'bold')
legend ('Tube 1', 'Tube 2', 'Tube 3');
ylabel ('X Axis = 1; Y Axis = 2; Z Axis = 3');

216

%determine the mean standard deviation for each tube

```

```

T1std = 5*(var([T1I1std; T1I2std; T1I3std; T1I4std; T1I5std])+32768)/2^16;
T2std = 5*(var([T2I1std; T2I2std; T2I3std; T2I4std; T2I5std])+32768)/2^16;
221 T3std = 5*(var([T3I1std; T3I2std; T3I3std; T3I4std; T3I5std])+32768)/2^16;
      disp(' '); disp('Mean Standard Deviation Ambient Acceleration for Table in ...
      Thesis');
      Mean_Standard_Deviation_Ambient_Acceleration = [T1std; T2std; T3std]
      subplot(2,1,2); bar3([T1std; T2std; T3std]);
      title('Mean Standard Deviation of 3 Directional ...
      Ambient Acceleration','FontWeight','bold');
      legend('Tube 1','Tube 2','Tube 3');
      ylabel('X Axis = 1; Y Axis = 2; Z Axis = 3');
226
print -dpng -r300 L:\everyone\Cooper_RIGEX\Figures_for_Thesis\...
      Ambient_Accel_mean_&_std.eps
%% Excitation Accelerometer Data - Non Mesh try
n = 5000; window = hanning(5000);
231
%create SuperU with filtered input

t = 1/5000:1/5000:1;
y = 5*cos(2*pi*(5+(1000-5)*t).*t);

236
[a,b,c,d] = butter(8,1000*2*pi,'s');
sys = ss(a,b,c,d);
filtered_input = lsim(sys,y,t);

241 % Load Accelerometer Data
for i = 1:3
  ctr = 1;
  SuperX = zeros(25*5000,1);
  SuperY = zeros(25*5000,1);
246  SuperZ = zeros(25*5000,1);
  for j = 1:25
    filename = sprintf('R1VT%ii%ii.DAT',i,j); %sorts through all the file ...
    names
    vibe_data = detrend(importdata(filename),'constant'); %remove ...
    constant bias

```

```

Xvibe = ( vibe_data(:,1) + 32768 * ones( size( vibe_data(:,1) ) ) ) *5...
/ 65536;

251 Yvibe = ( vibe_data(:,2) + 32768 * ones( size( vibe_data(:,1) ) ) )* 5...
/ 65536;

Zvibe = ( vibe_data(:,3) + 32768 * ones( size( vibe_data(:,1) ) ) )* 5...
/ 65536;

%above changes from counts to volts

SuperX(ctr:ctr+4999) = Xvibe;
SuperY(ctr:ctr+4999) = Yvibe; %Stack Y Data into Super Column
256 SuperZ(ctr:ctr+4999) = Zvibe;
SuperU(ctr:ctr+4999) = filtered_input;
ctr = ctr + 5000;

end

%Working TFestimate for potential graph?

261 [Tx,F1] = tfestimate(SuperU,SuperX,window,0,2^14,5000);
[Ty,F2] = tfestimate(SuperU,SuperY,window,0,2^14,5000);
[Tz,F3] = tfestimate(SuperU,SuperZ,window,0,2^14,5000);
[Cx,F1] = mscohere(SuperU,SuperX,window,0,2^14,5000);
[Cy,F1] = mscohere(SuperU,SuperY,window,0,2^14,5000);
266 [Cz,F1] = mscohere(SuperU,SuperZ,window,0,2^14,5000);

eval(sprintf('T%iSuper = [SuperX, SuperY, SuperZ, transpose(SuperU)]',...
,i));
eval(sprintf('T%iFC = [F1,Tx,Ty,Tz,Cx,Cy,Cz]',i));

end

271

% Plot & Save Each Tube with respective X, Y, Z Transfer Function
% Tube 1
tf_sf_plotter(T1FC(:,1),T1FC(:,2),T1FC(:,1),T1FC(:,3),T1FC(:,1),T1FC(:,4),...
Tube ', 1, ' 3-Axis Space Flight FRF', 'X Axis FRF', 'Y Axis FRF', 'Z Axis ...
FRF');

print -dpng -r300 L:\everyone\Cooper_RIGEX\Figures_for_Thesis\FC_T1_3axisTF....
eps

276 print -dpng -r300 L:\everyone\Cooper_RIGEX\Figures_for_Thesis\png\...
FC_T1_3axisTF.png

% Tube 2

```

```

tf_sf_plotter(T2FC(:,1),T2FC(:,2),T2FC(:,1),T2FC(:,3),T2FC(:,1),T2FC(:,4),'...
Tube ', 2, ' 3-Axis Space Flight FRF','X Axis FRF','Y Axis FRF','Z Axis ...
FRF');

print -dpng -r300 L:\everyone\Cooper_RIGEX\Figures_for_Thesis\FC_T2_3axisTF....
eps
print -dpng -r300 L:\everyone\Cooper_RIGEX\Figures_for_Thesis\png\...
FC_T2_3axisTF.png

281 % Tube 3

tf_sf_plotter(T3FC(:,1),T3FC(:,2),T3FC(:,1),T3FC(:,3),T3FC(:,1),T3FC(:,4),'...
Tube ', 3, ' 3-Axis Space Flight FRF','X Axis FRF','Y Axis FRF','Z Axis ...
FRF');

print -dpng -r300 L:\everyone\Cooper_RIGEX\Figures_for_Thesis\FC_T3_3axisTF....
eps
print -dpng -r300 L:\everyone\Cooper_RIGEX\Figures_for_Thesis\png\...
FC_T3_3axisTF.png

286 % Coherence Plot Each Tube with respective X, Y, Z

% Tube 1

coh_sf_plotter(T1FC(:,1),T1FC(:,5),T1FC(:,1),T1FC(:,6),T1FC(:,1),T1FC(:,7),'...
Tube ', 1, ' 3-Axis Space Flight Coherence','X Axis','Y Axis','Z Axis');

print -dpng -r300 L:\everyone\Cooper_RIGEX\Figures_for_Thesis\FC_T1_3axisCoh....
eps
print -dpng -r300 L:\everyone\Cooper_RIGEX\Figures_for_Thesis\png\...
FC_T1_3axisCoh.png

291 % Tube 2

coh_sf_plotter(T2FC(:,1),T2FC(:,5),T2FC(:,1),T2FC(:,6),T2FC(:,1),T2FC(:,7),'...
Tube ', 2, ' 3-Axis Space Flight Coherence','X Axis','Y Axis','Z Axis');

print -dpng -r300 L:\everyone\Cooper_RIGEX\Figures_for_Thesis\FC_T2_3axisCoh....
eps
print -dpng -r300 L:\everyone\Cooper_RIGEX\Figures_for_Thesis\png\...
FC_T2_3axisCoh.png

%Tube 3

296 coh_sf_plotter(T3FC(:,1),T3FC(:,5),T3FC(:,1),T3FC(:,6),T3FC(:,1),T3FC(:,7),'...
Tube ', 3, ' 3-Axis Space Flight Coherence','X Axis','Y Axis','Z Axis');

print -dpng -r300 L:\everyone\Cooper_RIGEX\Figures_for_Thesis\FC_T3_3axisCoh....
eps

```

```

print -dpng -r300 L:\everyone\Cooper_RIGEX\Figures_for_Thesis\png\...
FC_T3_3axisCoh.png
%% Generate Input Data Plot

301 t = 1/5000:1/5000:1;
y = cos(2 * pi*(5+(1000-5)*t).*t);

[a,b,c,d] = butter(8,1000*2*pi,'s');
sys = ss(a,b,c,d);
306 filtered_input = lsim(sys,y,t);

figure; set(gcf,'defaultaxesfontsize',8)
subplot(2,2,1); plot(t,y); axis([0 1 -1.1 1.1]); set(gca,'YTick',[-1 -0.5...
0 0.5 1]);
title('Input Chirp Signal')
ylabel('Input'); xlabel('Time (s)');
311 subplot(2,2,2); pwelch(y,5000,0,5000,5000);
subplot(2,2,3); bode(sys); grid on; title('8th Order Butterworth Filter ...
Frequency Response','FontSize',8);
subplot(2,2,4); plot(t,filtered_input); axis([0 1 -1.1 1.1]); set(gca,'...
YTick',[-1 -0.5 0 0.5 1]);
title('Input Chirp Signal')
ylabel('Input'); xlabel('Time (s)');
316 print -dpng -r300 L:\everyone\Cooper_RIGEX\Figures_for_Thesis\png\...
quad_input_plot.png

%% Plot Accel Time History to search for resonances

321 figure;set(gcf,'defaultaxesfontsize',14)
plot(.66*detrend(T1Super(1:5000,1))); hold on;
plot(2*.66*.01*ones(5000,1),'k'); plot(-.66*.01*ones(5000,1),'k--')
plot(.66*.01*ones(5000,1),'k--'); plot(-2*.66*.01*ones(5000,1),'k')
title('Tube 1 Excited X Acceleration vs Time','FontWeight','bold');
326 xlabel('Time (1/5000 s)'); ylabel('Acceleration (g)');
legend('X Acceleration','Max Ambient Accel','Ambient Accel Noise','Location',...
'South')

```

```

print -dpng -r300 L:\everyone\Cooper_RIGEX\Figures_for_Thesis\png\...
Vibe_Accel_TH.png

%% Final Space Flight FRF data Analysis
331 clear all; clc; close all;

%n = 5000; window = hanning(5000);

%create SuperU with filtered input
336
t = 1/5000:1/5000:1;
y = 5*cos(2*pi*(5+(1000-5)*t).*t);

[a,b,c,d] = butter(8,1000*2*pi,'s');
341 sys = ss(a,b,c,d);
filtered_input = lsim(sys,y,t);

for i = 1:3 % should be 1:3

346     for j = 1:25 % should be 25
        filename = sprintf('R1VT%ii%ii.DAT',i,j); %sorts through all the file ...
        names
        vibe_data = detrend(importdata(filename),'constant'); %remove ...
        constant bias
        Xvibe = ( vibe_data(:,1) + 32768 * ones( size( vibe_data(:,1) ) ) ) *5...
        / 65536;
        Yvibe = ( vibe_data(:,2) + 32768 * ones( size( vibe_data(:,2) ) ) ) * 5...
        / 65536;
        Zvibe = ( vibe_data(:,3) + 32768 * ones( size( vibe_data(:,1) ) ) ) * 5...
        / 65536;
        u1 = fft(filtered_input);% U(:,j) = u1;
        x1 = fft(Xvibe); %X1(:,j) = x1;
        y1 = fft(Yvibe); %Y1(:,j) = y1;
        z1 = fft(Zvibe); %Z1(:,j) = z1;
351     H1(:,j) = 20*log10(abs(conj(u1).*x1./conj(u1).*u1)));
        H2(:,j) = 20*log10(abs(conj(x1).*x1./conj(u1).*x1)));

```

```

H1Y(:,j) = 20*log10(abs(conj(u1).*y1./(conj(u1).*u1)));
H2Y(:,j) = 20*log10(abs(conj(y1).*y1./(conj(u1).*y1)));
H1Z(:,j) = 20*log10(abs(conj(u1).*z1./(conj(u1).*u1)));
361 H2Z(:,j) = 20*log10(abs(conj(z1).*z1./(conj(u1).*z1)));
Suu(:,j) = u1.*conj(u1);
Sxx(:,j) = x1.*conj(x1);
Syy(:,j) = y1.*conj(y1);
Szz(:,j) = z1.*conj(z1);
366 Sux(:,j) = u1.*conj(x1);
Suy(:,j) = u1.*conj(y1);
Suz(:,j) = u1.*conj(z1);clear u1 x1 y1 z1
end
clear Xvibe Yvibe Zvibe vibe_data
371 eval(sprintf('H1Y_T%i = H1Y',i));
eval(sprintf('H1Z_T%i = H1Z',i));

376 SuuT1 = Suu;clc; clear Suu
eval(sprintf('SxxT%i = Sxx',i));clc; clear Sxx
eval(sprintf('SyyT%i = Syy',i));clc; clear Syy
eval(sprintf('SzzT%i = Szz',i));clc; clear Szz
eval(sprintf('SuxT%i = Sux',i));clc; clear Sux
eval(sprintf('SuyT%i = Suy',i));clc; clear Suy
eval(sprintf('SuzT%i = Suz',i));clc; clear Suz
381 end
Suu1_mean = mean(SuuT1,2);Sxx1_mean = mean(SxxT1,2);Syy1_mean = mean(SyyT1,2)...
;Szz1_mean = mean(SzzT1,2);
Sux1_mean = mean(SuxT1,2);Suy1_mean = mean(SuyT1,2);Suz1_mean = mean(SuzT1,2)...
;

%clear SuuT1 SxxT1 SyyT1 SzzT1 SuxT1 SuyT1 SuzT1
386 H1X_avg_T1 = 20*log10(abs(Sux1_mean./Suu1_mean));
H2X_avg_T1 = 20*log10(abs(Sxx1_mean./Sux1_mean));
% figure; subplot(3,1,1); plot(1:1:1000,H1X_avg_T1(1:1000)); title('...
Tube 1 H1 X');
% subplot(3,1,2); plot(1:1:1000,H2X_avg_T1(1:1000)); title('...
Tube 1 H2 X');

```

```

%
% subplot(3,1,3); plot(1:1:1000,H2X_avg_T1(1:1000)./...
% H1X_avg_T1(1:1000)); title('Tube 1 X Coherence');
391    H1Y_avg_T1 = 20*log10(abs(Suy1_mean./Suu1_mean));
    H2Y_avg_T1 = 20*log10(abs(Syy1_mean./Suy1_mean));
%
% figure; subplot(3,1,1); plot(1:1:1000,H1Y_avg_T1(1:1000)); title('...
% Tube 1 H1Y');
%
% subplot(3,1,2); plot(1:1:1000,H2Y_avg_T1(1:1000)); title('...
% Tube 1 H2Y');
%
% subplot(3,1,3); plot(1:1:1000,H2Y_avg_T1(1:1000)./...
% H1Y_avg_T1(1:1000)); title('Tube 1 Y Coherence');

396    H1Z_avg_T1 = 20*log10(abs(Suz1_mean./Suu1_mean));
    H2Z_avg_T1 = 20*log10(abs(Szz1_mean./Suz1_mean));
%
% figure; subplot(3,1,1); plot(1:1:1000,H1Z_avg_T1(1:1000)); title('...
% Tube 1 H1Z');
%
% subplot(3,1,2); plot(1:1:1000,H2Z_avg_T1(1:1000)); title('...
% Tube 1 H2Z');
%
% subplot(3,1,3); plot(1:1:1000,H2Z_avg_T1(1:1000)./...
% H1Z_avg_T1(1:1000)); title('Tube 1 Z Coherence');

401

%clear Sxx1_mean Syy1_mean Szz1_mean Sux1_mean Suy1_mean Suz1_mean
Sxx2_mean = mean(SxxT2,2); Syy2_mean = mean(SyyT2,2); Szz2_mean = mean(SzzT2,2)...
;
Sxx3_mean = mean(SxxT3,2); Syy3_mean = mean(SyyT3,2); Szz3_mean = mean(SzzT3,2)...
;
%clear SuuT1 SuuT2 SuuT3 SxxT1 SxxT2 SxxT3 SyyT1 SyyT2 SyyT3 SzzT1 SzzT2 ...
SzzT3

406 Sux2_mean = mean(SuxT2,2); Suy2_mean = mean(SuyT2,2); Suz2_mean = mean(SuzT2,2)...
;
Sux3_mean = mean(SuxT3,2); Suy3_mean = mean(SuyT3,2); Suz3_mean = mean(SuzT3,2)...
;
%clear SuxT1 SuyT1 SuzT1 SuxT2 SuyT2 SuzT2 SuxT3 SuyT3 SuzT3

411    H1X_avg_T2 = 20*log10(abs(Sux2_mean./Suu1_mean));
    H2X_avg_T2 = 20*log10(abs(Sxx2_mean./Sux2_mean));

```

```

% figure; subplot(3,1,1); plot(1:1:1000,H1X_avg_T2(1:1000)); title('...
Tube 2 H1 X');
%
% subplot(3,1,2); plot(1:1:1000,H2X_avg_T2(1:1000)); title('...
Tube 2 H2 X');
%
% subplot(3,1,3); plot(1:1:1000,H2X_avg_T2(1:1000)./...
H1X_avg_T2(1:1000)); title('Tube 2 X Coherence');

416

    H1X_avg_T3 = 20*log10(abs(Sux3_mean./Suu1_mean));
    H2X_avg_T3 = 20*log10(abs(Sxx3_mean./Sux3_mean));
%
figure; subplot(3,1,1); plot(1:1:1000,H1X_avg_T3(1:1000)); title('...
Tube 3 H1 X');
%
subplot(3,1,2); plot(1:1:1000,H2X_avg_T3(1:1000)); title('...
Tube 3 H2 X');
%
subplot(3,1,3); plot(1:1:1000,H2X_avg_T3(1:1000)./...
H1X_avg_T3(1:1000)); title('Tube 3 X Coherence');

421 %

    H1Y_avg_T2 = 20*log10(abs(Suy2_mean./Suu1_mean));
    H2Y_avg_T2 = 20*log10(abs(Syy2_mean./Suy2_mean));
%
figure; subplot(3,1,1); plot(1:1:1000,H1Y_avg_T2(1:1000)); title('...
Tube 2 H1Y');
%
subplot(3,1,2); plot(1:1:1000,H2Y_avg_T2(1:1000)); title('...
Tube 2 H2Y');
%
subplot(3,1,3); plot(1:1:1000,H2Y_avg_T2(1:1000)./H1Y_avg_T2...
(1:1000)); title('Tube 2 Y Coherence');

426 %

    H1Y_avg_T3 = 20*log10(abs(Suy3_mean./Suu1_mean));
    H2Y_avg_T3 = 20*log10(abs(Syy3_mean./Suy3_mean));
%
figure; subplot(3,1,1); plot(1:1:1000,H1Y_avg_T3(1:1000)); title('...
Tube 3 H1Y');
%
subplot(3,1,2); plot(1:1:1000,H2Y_avg_T3(1:1000)); title('...
Tube 3 H2Y');
%
subplot(3,1,3); plot(1:1:1000,H2Y_avg_T3(1:1000)./H1Y_avg_T3...
(1:1000)); title('Tube 3 Y Coherence');

431 %

    H1Z_avg_T2 = 20*log10(abs(Suz2_mean./Suu1_mean));
    H2Z_avg_T2 = 20*log10(abs(Szz2_mean./Suz2_mean));

```

```

% figure; subplot(3,1,1); plot(1:1:1000,H1Z_avg_T2(1:1000)); title('...
Tube 2 H1Z');
%
% subplot(3,1,2); plot(1:1:1000,H2Z_avg_T2(1:1000)); title('...
Tube 2 H2Z');
%
% subplot(3,1,3); plot(1:1:1000,H2Z_avg_T2(1:1000)./H1Z_avg_T2...
(1:1000)); title('Tube 2 Z Coherence');

441 H1Z_avg_T3 = 20*log10(abs(Suz3_mean./Suu1_mean));
H2Z_avg_T3 = 20*log10(abs(Szz3_mean./Suz3_mean));
%
figure; subplot(3,1,1); plot(1:1:1000,H1Z_avg_T3(1:1000)); title('...
Tube 3 H1Z');
%
subplot(3,1,2); plot(1:1:1000,H2Z_avg_T3(1:1000)); title('...
Tube 3 H2Z');
%
subplot(3,1,3); plot(1:1:1000,H2Z_avg_T3(1:1000)./H1Z_avg_T3...
(1:1000)); title('Tube 3 Z Coherence');

446
hz = 1:1:1000;
%%
*****  

figure; set(gcf,'defaultaxesfontsize',14)
451 subplot(3,1,1); plot(hz,H1X_avg_T1(1:1000),hz,H1Y_avg_T1(1:1000),hz,...
H1Z_avg_T1(1:1000));
title('Tube 1 Space Flight Three Axis H1 FRF'); axis([0 1000 -80 0]);
subplot(3,1,2); plot(hz,H2X_avg_T1(1:1000),hz,H2Y_avg_T1(1:1000),hz,...
H2Z_avg_T1(1:1000));
title('Tube 1 Space Flight Three Axis H2 FRF'); axis([0 1000 -80 0]);
subplot(3,1,3); plot(hz,H2X_avg_T1(1:1000)./H1X_avg_T1(1:1000),hz,...
H2Y_avg_T1(1:1000)./H1Y_avg_T1(1:1000),hz,H2Z_avg_T1(1:1000)./...
H1Z_avg_T1(1:1000))
title('Tube 1 Space Flight Three Axis Coherence'); axis([0 1000 0 1])...
;legend('X Axis','Y Axis','Z Axis','Location','SouthWest',...
Orientation','Horizontal');

print -dpng -r300 L:\everyone\Cooper_RIGEX\Figures_for_Thesis\S\Tube1FRFs.png
figure; set(gcf,'defaultaxesfontsize',14)
subplot(2,1,1); plot(hz, 180/pi*angle(Sux1_mean(1:1000)./Suu1_mean...
(1:1000))); title('Tube 1: 3-Axis H1 Phase'); hold all;

```

```

        plot(hz, 180/pi*angle(Suy1_mean(1:1000)./Suu1_mean...
(1:1000)));
461      plot(hz, 180/pi*angle(Suz1_mean(1:1000)./Suu1_mean...
(1:1000)); hold off;
subplot(2,1,2); plot(hz, 180/pi*angle(Sxx1_mean(1:1000)./Sux1_mean...
(1:1000))); title('Tube 1: 3-Axis H2 Phase'); hold all;
plot(hz, 180/pi*angle(Syy1_mean(1:1000)./Suy1_mean...
(1:1000)));
plot(hz, 180/pi*angle(Szz1_mean(1:1000)./Suz1_mean...
(1:1000)); legend('X Axis','Y Axis','Z Axis','Location',...
,'SouthWest','Orientation','Horizontal');
hold off;
466 print -dpng -r300 L:\everyone\Cooper_RIGEX\Figures_for_Thesis\S\Tube1Phase.....
png
%...
*****
figure; set(gcf,'defaultaxesfontsize',14)
470 subplot(3,1,1); plot(hz,H1X_avg_T2(1:1000),hz,H1Y_avg_T2(1:1000),hz,...
H1Z_avg_T2(1:1000));
title('Tube 2 Space Flight Three Axis H1 FRF'); axis([0 1000 -80 0]);
471 subplot(3,1,2); plot(hz,H2X_avg_T2(1:1000),hz,H2Y_avg_T2(1:1000),hz,...
H2Z_avg_T2(1:1000));
title('Tube 2 Space Flight Three Axis H2 FRF'); axis([0 1000 -80 0]);
subplot(3,1,3); plot(hz,H2X_avg_T2(1:1000)./H1X_avg_T2(1:1000),hz,H2Z_avg_T2(1:1000)./...
H1Z_avg_T2(1:1000))
title('Tube 2 Space Flight Three Axis Coherence'); axis([0 1000 0 1])...
;legend('X Axis','Y Axis','Z Axis','Location','SouthWest',...
Orientation,'Horizontal');
print -dpng -r300 L:\everyone\Cooper_RIGEX\Figures_for_Thesis\S\Tube2FRFs.png
476 figure; set(gcf,'defaultaxesfontsize',14)
subplot(2,1,1); plot(hz, 180/pi*angle(Sux2_mean(1:1000)./Suu1_mean...
(1:1000))); title('Tube 2: 3-Axis H1 Phase'); hold all;
plot(hz, 180/pi*angle(Suy2_mean(1:1000)./Suu1_mean...
(1:1000)));

```

```

        plot(hz, 180/pi*angle(Suz2_mean(1:1000)./Suu1_mean...
(1:1000))); hold off;
subplot(2,1,2); plot(hz, 180/pi*angle(Sxx2_mean(1:1000)./Sux2_mean...
(1:1000))); title('Tube 2: 3-Axis H2 Phase'); hold all;
481         plot(hz, 180/pi*angle(Syy2_mean(1:1000)./Suy2_mean...
(1:1000)));
        plot(hz, 180/pi*angle(Szz2_mean(1:1000)./Suz2_mean...
(1:1000))); legend('X Axis','Y Axis','Z Axis','Location',...
,'SouthWest','Orientation','Horizontal');
        hold off;
print -dpng -r300 L:\everyone\Cooper_RIGEX\Figures_for_Thesis\S\Tube2Phase....
png
%...
*****
```



```

486 figure; set(gcf,'defaultaxesfontsize',14)
subplot(3,1,1); plot(hz,H1X_avg_T3(1:1000),hz,H1Y_avg_T3(1:1000),hz, ...
H1Z_avg_T3(1:1000));
title('Tube 3 Space Flight Three Axis H1 FRF'); axis([0 1000 -80 0]);
subplot(3,1,2); plot(hz,H2X_avg_T3(1:1000),hz,H2Y_avg_T3(1:1000),hz, ...
H2Z_avg_T3(1:1000));
title('Tube 3 Space Flight Three Axis H2 FRF'); axis([0 1000 -80 0]);
491 subplot(3,1,3); plot(hz,H2X_avg_T3(1:1000)./H1X_avg_T3(1:1000),hz, ...
H2Y_avg_T3(1:1000)./H1Y_avg_T3(1:1000),hz,H2Z_avg_T3(1:1000)./...
H1Z_avg_T3(1:1000))
title('Tube 3 Space Flight Three Axis Coherence'); axis([0 1000 0 1])...
;legend('X Axis','Y Axis','Z Axis','Location','SouthWest',...
Orientation','Horizontal');

print -dpng -r300 L:\everyone\Cooper_RIGEX\Figures_for_Thesis\S\Tube3FRFs.png
figure; set(gcf,'defaultaxesfontsize',14)
subplot(2,1,1); plot(hz, 180/pi*angle(Sux3_mean(1:1000)./Suu1_mean...
(1:1000))); title('Tube 3: 3-Axis H1 Phase'); hold all;
496         plot(hz, 180/pi*angle(Suy3_mean(1:1000)./Suu1_mean...
(1:1000)));
        plot(hz, 180/pi*angle(Suz3_mean(1:1000)./Suu1_mean...
(1:1000))); hold off;
```

```

    subplot(2,1,2); plot(hz, 180/pi*angle(Sxx3_mean(1:1000)./Sux3_mean...
(1:1000))); title('Tube 3: 3-Axis H2 Phase'); hold all;
    plot(hz, 180/pi*angle(Syy3_mean(1:1000)./Suy3_mean...
(1:1000)));
    plot(hz, 180/pi*angle(Szz3_mean(1:1000)./Suz3_mean...
(1:1000))); legend('X Axis','Y Axis','Z Axis',...
Location,'SouthWest','Orientation','Horizontal');
501        hold off;
print -dpng -r300 L:\everyone\Cooper_RIGEX\Figures_for_Thesis\S\Tube3Phase.....
png
%% Mesh Plots
close all;
figure; mesh(H1_T1(20:1000,:)); title('Tube 1 X-Axis Space Flight Magnitude ...
Response'); view([70 32]);
506        xlabel('Test Iteration'); ylabel('Frequency (Hz)'); zlabel('Magnitude...
(dB)');
print -dpng -r300 L:\everyone\Cooper_RIGEX\Figures_for_Thesis\4\T1_Mesh_Angle...
.png
figure; mesh(H1_T1(20:1000,:)); title('Tube 1 X-Axis Space Flight Magnitude ...
Response'); view([90 90]);
xlabel('Test Iteration'); ylabel('Frequency (Hz)'); zlabel('Magnitude...
(dB)');
print -dpng -r300 L:\everyone\Cooper_RIGEX\Figures_for_Thesis\4\T1_Mesh_Drift...
.png
511
figure; mesh(H1_T2(20:1000,:)); title('Tube 2 X-Axis Space Flight Magnitude ...
Response'); view([70 32]);
xlabel('Test Iteration'); ylabel('Frequency (Hz)'); zlabel('Magnitude...
(dB)');
print -dpng -r300 L:\everyone\Cooper_RIGEX\Figures_for_Thesis\4\T2_Mesh_Angle...
.png
figure; mesh(H1_T2(20:1000,:)); title('Tube 2 X-Axis Space Flight Magnitude ...
Response'); view([90 90]);
516        xlabel('Test Iteration'); ylabel('Frequency (Hz)'); zlabel('Magnitude...
(dB)');

```

```

print -dpng -r300 L:\everyone\Cooper_RIGEX\Figures_for_Thesis\4\T2_Mesh_Drift...
.png

figure; mesh(H1_T3(20:1000,:)); title('Tube 3 X-Axis Space Flight Magnitude ...
Response'); view([70 32]);
xlabel('Test Iteration'); ylabel('Frequency (Hz)'); zlabel('Magnitude...
(dB)');
521 print -dpng -r300 L:\everyone\Cooper_RIGEX\Figures_for_Thesis\4\T3_Mesh_Angle...
.png
figure; mesh(H1_T3(20:1000,:)); title('Tube 3 X-Axis Space Flight Magnitude ...
Response'); view([90 90]);
xlabel('Test Iteration'); ylabel('Frequency (Hz)'); zlabel('Magnitude...
(dB)');
print -dpng -r300 L:\everyone\Cooper_RIGEX\Figures_for_Thesis\4\T3_Mesh_Drift...
.png

526 figure; mesh(H1Y_T1(20:1000,:)); title('Tube 1 Y-Axis Space Flight Magnitude ...
Response'); view([70 32]);
xlabel('Test Iteration'); ylabel('Frequency (Hz)'); zlabel('Magnitude...
(dB)');
print -dpng -r300 L:\everyone\Cooper_RIGEX\Figures_for_Thesis\4\...
T1Y_Mesh_Angle.png
figure; mesh(H1Y_T1(20:1000,:)); title('Tube 1 Y-Axis Space Flight Magnitude ...
Response'); view([90 90]);
xlabel('Test Iteration'); ylabel('Frequency (Hz)'); zlabel('Magnitude...
(dB)');
531 print -dpng -r300 L:\everyone\Cooper_RIGEX\Figures_for_Thesis\4\...
T1Y_Mesh_Drift.png

figure; mesh(H1Y_T2(20:1000,:)); title('Tube 2 Y-Axis Space Flight Magnitude ...
Response'); view([70 32]);
xlabel('Test Iteration'); ylabel('Frequency (Hz)'); zlabel('Magnitude...
(dB)');
print -dpng -r300 L:\everyone\Cooper_RIGEX\Figures_for_Thesis\4\...
T2Y_Mesh_Angle.png

```

```

536 figure; mesh(H1Y_T2(20:1000,:)); title('Tube 2 Y-Axis Space Flight Magnitude ...  

    Response'); view([90 90]);  

    xlabel('Test Iteration'); ylabel('Frequency (Hz)'); zlabel('Magnitude...  

    (dB)');  

print -dpng -r300 L:\everyone\Cooper_RIGEX\Figures_for_Thesis\4\...  

T2Y_Mesh_Drift.png

figure; mesh(H1Y_T3(20:1000,:)); title('Tube 3 Y-Axis Space Flight Magnitude ...  

    Response'); view([70 32]);  

541 xlabel('Test Iteration'); ylabel('Frequency (Hz)'); zlabel('Magnitude...  

    (dB)');  

print -dpng -r300 L:\everyone\Cooper_RIGEX\Figures_for_Thesis\4\...  

T3Y_Mesh_Angle.png

figure; mesh(H1Y_T3(20:1000,:)); title('Tube 3 Y-Axis Space Flight Magnitude ...  

    Response'); view([90 90]);  

    xlabel('Test Iteration'); ylabel('Frequency (Hz)'); zlabel('Magnitude...  

    (dB)');  

print -dpng -r300 L:\everyone\Cooper_RIGEX\Figures_for_Thesis\4\...  

T3Y_Mesh_Drift.png

546  

figure; mesh(H1Z_T1(20:1000,:)); title('Tube 1 Z-Axis Space Flight Magnitude ...  

    Response'); view([70 32]);  

    xlabel('Test Iteration'); ylabel('Frequency (Hz)'); zlabel('Magnitude...  

    (dB)');  

print -dpng -r300 L:\everyone\Cooper_RIGEX\Figures_for_Thesis\4\...  

T1Z_Mesh_Angle.png

figure; mesh(H1Z_T1(20:1000,:)); title('Tube 1 Z-Axis Space Flight Magnitude ...  

    Response'); view([90 90]);  

551 xlabel('Test Iteration'); ylabel('Frequency (Hz)'); zlabel('Magnitude...  

    (dB)');  

print -dpng -r300 L:\everyone\Cooper_RIGEX\Figures_for_Thesis\4\...  

T1Z_Mesh_Drift.png

figure; mesh(H1Z_T2(20:1000,:)); title('Tube 2 Z-Axis Space Flight Magnitude ...  

    Response'); view([70 32]);

```

```

    xlabel('Test Iteration'); ylabel('Frequency (Hz)'); zlabel('Magnitude...
    (dB)');
556 print -dpng -r300 L:\everyone\Cooper_RIGEX\Figures_for_Thesis\4\...
    T2Z_Mesh_Angle.png
figure; mesh(H1Z_T2(20:1000,:)); title('Tube 2 Z-Axis Space Flight Magnitude ...
    Response'); view([90 90]);
    xlabel('Test Iteration'); ylabel('Frequency (Hz)'); zlabel('Magnitude...
    (dB)');
print -dpng -r300 L:\everyone\Cooper_RIGEX\Figures_for_Thesis\4\...
    T2Z_Mesh_Drift.png

561 figure; mesh(H1Z_T3(20:1000,:)); title('Tube 3 Z-Axis Space Flight Magnitude ...
    Response'); view([70 32]);
    xlabel('Test Iteration'); ylabel('Frequency (Hz)'); zlabel('Magnitude...
    (dB)');
print -dpng -r300 L:\everyone\Cooper_RIGEX\Figures_for_Thesis\4\...
    T3Z_Mesh_Angle.png
figure; mesh(H1Z_T3(20:1000,:)); title('Tube 3 Z-Axis Space Flight Magnitude ...
    Response'); view([90 90]);
    xlabel('Test Iteration'); ylabel('Frequency (Hz)'); zlabel('Magnitude...
    (dB)');
566 print -dpng -r300 L:\everyone\Cooper_RIGEX\Figures_for_Thesis\4\...
    T3Z_Mesh_Drift.png

%%

figure; set(gcf,'defaultaxesfontsize',14)
571 plot(hz,H1X_avg_T1(1:1000),hz,H1Y_avg_T1(1:1000),hz,H1Z_avg_T1(1:1000));
    title('Tube 1 Space Flight Three Axis H1 FRF'); axis([0 1000 -80 ...
    -20]);
    ylabel('Magnitude (dB)'); xlabel('Frequency (Hz)'); grid on;
print -dpng -r300 L:\everyone\Cooper_RIGEX\Figures_for_Thesis\S\...
    Tube1Mag.png

576 figure; set(gcf,'defaultaxesfontsize',14); grid on;

```

```

plot(hz, 180/pi*angle(Sux1_mean(1:1000)./Suu1_mean...
(1:1000))); hold all;
plot(hz, 180/pi*angle(Suy1_mean(1:1000)./Suu1_mean...
(1:1000)));
plot(hz, 180/pi*angle(Suz1_mean(1:1000)./Suu1_mean...
(1:1000))); hold off; grid on;
axis([0 1000 -180 180]); set(gca,'Ytick',[-180,-90,0,90,180]);
581 ylabel('Phase (^o)'), xlabel('Frequency (Hz)');
print -dpng -r300 L:\everyone\Cooper_RIGEX\Figures_for_Thesis\S\...
Tube1Phase.png

figure; set(gcf,'defaultaxesfontsize',14)
plot(hz,H2X_avg_T1(1:1000)./H1X_avg_T1(1:1000),hz,H2Y_avg_T1(1:1000)...
./H1Y_avg_T1(1:1000),hz,H2Z_avg_T1(1:1000)./H1Z_avg_T1(1:1000))
586 title('Tube 1 Space Flight Three Axis Coherence'); axis([0 1000 0 1])...
;
ylabel('Coherence (\gamma^2)'), xlabel('Frequency (Hz)'), grid on;
legend('X Axis','Y Axis','Z Axis','Location','SouthWest','Orientation...
','Horizontal');
print -dpng -r300 L:\everyone\Cooper_RIGEX\Figures_for_Thesis\S\...
Tube1Coh.png

591 %...
*****
figure; set(gcf,'defaultaxesfontsize',14)
plot(hz,H1X_avg_T2(1:1000),hz,H1Y_avg_T2(1:1000),hz,H1Z_avg_T2(1:1000));
title('Tube 2 Space Flight Three Axis H1 FRF'); axis([0 1000 -80 ...
-20]);
ylabel('Magnitude (dB)'), xlabel('Frequency (Hz)'), grid on;
596 print -dpng -r300 L:\everyone\Cooper_RIGEX\Figures_for_Thesis\S\...
Tube2Mag.png

figure; set(gcf,'defaultaxesfontsize',14); grid on;
plot(hz, 180/pi*angle(Sux2_mean(1:1000)./Suu1_mean...
(1:1000))); hold all;

```

```

plot(hz, 180/pi*angle(Suy2_mean(1:1000)./Suu1_mean...
(1:1000)));
601 plot(hz, 180/pi*angle(Suz2_mean(1:1000)./Suu1_mean...
(1:1000)); hold off; grid on;
axis([0 1000 -180 180]); set(gca,'Ytick',[-180,-90,0,90,180]);
ylabel('Phase (^o)'); xlabel('Frequency (Hz)');
print -dpng -r300 L:\everyone\Cooper_RIGEX\Figures_for_Thesis\S\...
Tube2Phase.png

606 figure; set(gcf,'defaultaxesfontsize',14)
plot(hz,H2X_avg_T2(1:1000)./H1X_avg_T2(1:1000),hz,H2Y_avg_T2(1:1000)...
./H1Y_avg_T2(1:1000),hz,H2Z_avg_T2(1:1000)./H1Z_avg_T2(1:1000))
title('Tube 2 Space Flight Three Axis Coherence'); axis([0 1000 0 1])...
;
ylabel('Coherence (\gamma^2)'); xlabel('Frequency (Hz)'); grid on;
legend('X Axis','Y Axis','Z Axis','Location','SouthWest','Orientation...
','Horizontal');
611 print -dpng -r300 L:\everyone\Cooper_RIGEX\Figures_for_Thesis\S\...
Tube2Coh.png
%...
*****
figure; set(gcf,'defaultaxesfontsize',14)
plot(hz,H1X_avg_T3(1:1000),hz,H1Y_avg_T3(1:1000),hz,H1Z_avg_T3(1:1000));
title('Tube 3 Space Flight Three Axis H1 FRF'); axis([0 1000 -80 ...
-20]);
ylabel('Magnitude (dB)'); xlabel('Frequency (Hz)'); grid on;
print -dpng -r300 L:\everyone\Cooper_RIGEX\Figures_for_Thesis\S\...
Tube3Mag.png

figure; set(gcf,'defaultaxesfontsize',14); grid on;
plot(hz, 180/pi*angle(Sux3_mean(1:1000)./Suu1_mean...
(1:1000))); hold all;
621 plot(hz, 180/pi*angle(Suy3_mean(1:1000)./Suu1_mean...
(1:1000)));

```

```

plot(hz, 180/pi*angle(Suz3_mean(1:1000)./Suu1_mean...
(1:1000))); hold off; grid on;
axis([0 1000 -180 180]); set(gca,'Ytick',[-180,-90,0,90,180]);
ylabel('Phase (^{o})'); xlabel('Frequency (Hz)');
print -dpng -r300 L:\everyone\Cooper_RIGEX\Figures_for_Thesis\S\...
Tube3Phase.png

```

626

```

figure; set(gcf,'defaultaxesfontsize',14)
plot(hz,H2X_avg_T3(1:1000)./H1X_avg_T3(1:1000),hz,H2Y_avg_T3(1:1000)...
./H1Y_avg_T3(1:1000),hz,H2Z_avg_T3(1:1000)./H1Z_avg_T3(1:1000))
title('Tube 3 Space Flight Three Axis Coherence'); axis([0 1000 0 1])...
;
ylabel('Coherence (\gamma^2)'); xlabel('Frequency (Hz)'); grid on;
legend('X Axis','Y Axis','Z Axis','Location','SouthWest','Orientation...
','Horizontal');
print -dpng -r300 L:\everyone\Cooper_RIGEX\Figures_for_Thesis\S\...
Tube3Coh.png

```

631

%% EOF

toc

Appendix C. RIGEX Flight Code

The as-flown C++ flight code is presented here.

Listing C.1: Appendix4/flight_ready.cpp

```
/* RIGEX: Flight Program Routine
Based on software written by D. Moody with mods by J. Goodwin and J. Owens
*****
Set constants for desired operation
5
Last modified on: 11 Oct 07 by: R. Cobb
Assistance provided by Sean Miller

10 */

#include <stdio.h>
#include <conio.h>

15 #define delay_count 20 // conversion complete delay for thermocouple board

// Global variables containing the addresses for the different boards
const short int AD_addr = 0x380;
const short int temp_addr = 0x300;
20 const short int relay_addr = 0x240;
//const short int timer_addr = 0x2C0;

// Constants (#)=flight values
const int pin_puller_pause = 1; // (1) # of seconds to keep ...
    energized (1? for flight)
25 const short int cool_down_pause = 300 ; // (300) Change to 300 ...
    Extend for flight
const short int vent_pause = 5 ; // (5) wait for tubes to vent before...
    reading pressure
const short int LED_display_pause = 60; // (60) for FVT
const short int camera12 = 5; // (5) allow enough time to boot and ...
    take at least 1 good image
const short int num_iterations = 25; // (25) Use 25 for flight
```

```

30      const short int FVT_completion_pause = 300; // (300) Change to 300 for...
           flight;

      const short int FVThold=10; // (10) pause between steps
      const short int TVAC = 1; // (0) Change to '1' for TVAC, else 0 ...
           for flight

      const short int TVAC_HOLD_BAYS=180; // not used if TVAC==0, turns ...
           ds13-dn on after each bay during TVAC

      const short int FVT = 1; // (1) Change to '0' bypass FVT
35      const long int MAX_HEAT_TIME = 18000000; // (18000000) Stop heating ...
           even if temp not reached

// Function declarations for the data collection subroutines
int check_temp(short int,short int);
int check_gas(short int, short int, short int);
40 int read_xls(short int, short int, short int Xdigi[],short int Ydigi[],short ...
               int Zdigi[]);
int r_xls_w_dac(short int, short int, short int Xdigi[],short int Ydigi[],...,
                short int Zdigi[],short int MMSB[],short int LLSB[]);
//
int write_dac(short int, short int MMSB[],short int LLSB[]);
int write_xls_inflate(short int, short int, short int, short int Xdigi[...],
                      short int Ydigi[],short int Zdigi[],short int press[]);
45 int write_xls_excite(short int, short int, short int, short int Xdigi[],short ...
                       int Ydigi[],short int Zdigi[],short int Xdac[]);
int write_xls_ambient(short int, short int, short int, short int Xdigi[...],
                      short int Ydigi[],short int Zdigi[]);
int read_press(short int, short int, short int press[]);
int enable_xformer(short int);
//
50 int HOLD(short int);

int main(void){
    short int *X_array = new short int[5000];
    short int *Y_array = new short int[5000];
55    short int *Z_array = new short int[5000];
    short int *press_array= new short int[5000];

```

```

short int *LLSB_array = new short int[5000];
short int *MMSB_array = new short int[5000];
short int *Dac_array = new short int[5000];

60
    // Needed variables
    FILE *failsafe_file;
    FILE *run_file;
    FILE *FVTrun_file;
    FILE *fidl;
    FILE *fidm;

65

    short int failsafe;
    short int run = 0;
70
    short int FVTrun;
    short int mdummy,ldummy;
    short int i = 0;
    short int k = 0;
    short int r = 0;
75
    short int j = 0, s = 0;
    short int indx=0;

// RESET all boards

80    //Ensure all relays are de-activated
    printf("Resetting Relay board...\n");
    outp(relay_addr+4,0x20); //Reset board and select bank 1
    outp(relay_addr+0,0);

85    // Initialize A/D Board
    printf("Reseting the A/D board...\n");
    outp(AD_addr+8,32);

    // Enable AD (internal timer controlled) and Timer 0
90    // interrupts occur on base+9 read
    printf("Initializing Timer 0\n");
    outp(AD_addr+9,0x21); // ,0x21);

```

```

// Configure timer 0 to use internal clock source
95    printf("Configure timer 0 to use internal clock source\n");
        outp(AD_addr+10,0xC2);

// set counter 0 to mode 2 operation (clk source)
        printf("%d\n",inp(AD_addr+10));
100   outp(AD_addr+15,0x14);
        outp(AD_addr+12,0x02);

//TEST FOR ...
ARRAYS-----
```

```

105  if(X_array==NULL){           // Memory Allocation Check
        printf("Error allocating memory for X-Axis!\n");
        return 0;
    }

110  if(Y_array==NULL){           // Memory Allocation Check
        printf("Error allocating memory for Y-Axis!\n");
        return 0;
    }
    if(Z_array==NULL){           // Memory Allocation Check
115    printf("Error allocating memory for Z-Axis!\n");
        return 0;
    }
    if(press_array==NULL){        // Memory Allocation Check
        printf("Error allocating memory for Tube Pressure Measurement!\n");
120    return 0;
    }
    if(MMSB_array==NULL){        // Memory Allocation Check
        printf("Error allocating memory for MMSB!\n");
        return 0;
    }
125    }
    if(LLSB_array==NULL){        // Memory Allocation Check
        printf("Error allocating memory for LLSB!\n");

```

```

        return 0;
    }

130   if(Dac_array==NULL){           // Memory Allocation Check
        printf("Error allocating memory for Dac!\n");
        return 0;
    }

135
    fidl = fopen("ex_LSB.dat","r");
    fidm = fopen("ex_MSB.dat","r");

    i = 0;
140   while(i<5000){
        fscanf(fidl,"%d",&ldummy);
        LLSB_array[i] = ldummy;
        fscanf(fidm,"%d",&mdummy);
        MMSB_array[i] = mdummy;
145     // Create a excitation data vector for storage check
        Dac_array[i] = ldummy + mdummy*256;
        i++;
    }

    printf("Register Loaded...\n");
150   fclose(fidl);
    fclose(fidm);

//END TEST FOR ...
ARRAYS-----

```

155 // Beginning of FVT

```

if(FVT){

    // Mark FVTrun file to continuously count # of times run
    // NEED to install "FVT_file.dat" file in same folder as program
    printf("\nMarking run # for FVT files...\n");

160   FVTrun_file = fopen("fvt_file.txt","r");
    fscanf(FVTrun_file,"%d",&FVTrun);
}

```

```

fclose(FVTrun_file);

FVTrun_file = fopen("fvt_file.txt","w");
fprintf(FVTrun_file,"%d",FVTrun+1);
165   fclose(FVTrun_file);
printf("Current run of FVT is %d...\n",FVTrun);

printf("Intializing Functional...\n");

170 // Turn DS13-Up On
printf("Turning DS13-Up On...\n");
outp(relay_addr+4,0x01);
outp(relay_addr+0,0x04);

175 // Hold
HOLD(3); // Adjust this number to force DS-13 off in 125s

//-----
printf("\n\nStarting Functional for tube experiment 1...\n");

180 // Activate Tube 1 Heaters and lights
printf("\n Activating Heaters and Lights.....BAY 1\n");
outp(relay_addr+4,0);           //Select Bank 0
outp(relay_addr+0,0x02);
outp(relay_addr+4,0x03);       //Select Bank 3
outp(relay_addr+0,0x01);

185 // Hold
HOLD(FVThold);

190 // Shut off heater
printf("\n Shutting off heaters\n");
outp(relay_addr+0,0);

195 // Hold
HOLD(FVThold);

```

```

    //Turn Camera on
    printf("\n Starting Camera for experiment bay #1...\n");
200    outp(relay_addr+4,0);           //Select Bank 0
    outp(relay_addr+0,0x03);         //Leave LED on and turn on Camera

    // Hold
    HOLD(FVThold);

205    // Stop Camera
    printf("\n Bay #1 Functional Complete...\n");
    outp(relay_addr+0,0);

210    // Hold
    HOLD(FVThold);

    //...
    -----
    printf("\n\nStarting Functional for tube experiment 2...\n");

215    // Activate Tube 2 Heaters and lights
    printf("\n Activating Heaters and Lights of experiment bay #2...\n");
    outp(relay_addr+4,0);           //Select Bank 0
    outp(relay_addr+0,0x08);         // Turn on LED 2
220    outp(relay_addr+4,0x03);       //Select Bank 3
    outp(relay_addr+0,0x04);         //Turn on Oven 2

    // Hold
    HOLD(FVThold);

225    // Shut off heater
    printf("\n Shutting off heaters\n");
    outp(relay_addr+0,0);

230    // Hold
    HOLD(FVThold);

```

```

//Turn Camera on
    printf("\n\tStarting Camera for experiment bay #2...\n");
235     outp(relay_addr+4,0);           //Select Bank 0
        outp(relay_addr+0,0x0C);       //Activate Camera

// Hold
HOLD(FVThold);

240
// Stop Camera
printf("\n Bay #2 Functional Complete...\n");
outp(relay_addr+0,0);

245
// Hold
HOLD(FVThold);

//...
-----  

printf("\n\nStarting Functional for tube experiment 3...\n");
250
// Activate Tube 3 Heaters and lights
printf("\n Activating Heaters and Lights of experiment bay #3...\n");
    outp(relay_addr+4,0);           //Select Bank 0
    outp(relay_addr+0,0x20);       // Turn on LEDs
255    outp(relay_addr+4,0x03);       //Select Bank 3
    outp(relay_addr+0,0x10);       //Turn on Oven 3

/// Hold
HOLD(FVThold);

260
// Shut off heater
printf("\n Shutting off heaters...\n");
    outp(relay_addr+0,0);

```

```

265      // Hold
        HOLD(FVThold);

        // Turn Camera on bay 3
        printf("\n Starting Camera for experiment bay #3...\n");
270      outp(relay_addr+4,0);           //Select Bank 0
        outp(relay_addr+0,0x30);       //Activate Camera
        // Hold
        HOLD(FVThold);

275      // Stop Camera
        printf("\n Bay #3 Functional Complete...\n");
        outp(relay_addr+0,0); ///
        // Hold
        HOLD(FVThold);

280      //...
-----  

        // Check Storage Tank Pressures
        printf("\tChecking Tank and vent pressures\n");
        check_gas(FVTrun+1,1,0);

285      // Turn DS13-Up Off
        printf("\n Turning DS13-Up Off...\n");
        outp(relay_addr+4,0x01);
        outp(relay_addr+0,0);

290      // HOLD
        HOLD(LED_display_pause);

        // Turn DS13-Down On
295      printf("\n Turning DS13-Down On...\n");
        outp(relay_addr+0,0x08);

        // HOLD

```

```

    HOLD(LED_display_pause);

300
    // Turn DS13-Down Off
    printf("\n Turning DS13-Down Off...\\n");
    outp(relay_addr+4,0x01);
    outp(relay_addr+0,0);

305
    // HOLD
    HOLD(FVT_completion_pause);

    // End of FVT

310 }

// -----
// Initialize Actual Experiment

315 // Mark run file to continuously count # of times run
    //NEED to add "run_file.dat" file to same directory as main program
    printf("\nMarking run # for run files...\\n");
    run_file = fopen("run_file.txt","r");
    fscanf(run_file,"%d",&run);

320
    run=run+1;
    fclose(run_file);
    run_file = fopen("run_file.txt","w");
    fprintf(run_file,"%d",run);
    fclose(run_file);

325
    printf("Current run of experiment is %d...\\n",run);

    printf("\n Starting Actual Experiment.\\n");

    // Turn DS13-Up On

330
    printf("Turning DS13-Up On...\\n");
    outp(relay_addr+4,0x01); // select bank
    outp(relay_addr+0,0x04); // switch DS-13 up

    // Check Failsafe File

```

```

335 //NEED to add "failsafe.txt" file to same directory

    printf("Checking failsafe file to determine if interrupted...");
    failsafe_file = fopen("failsafe.txt","r");
    fscanf(failsafe_file,"%d",&failsafe);
340    fclose(failsafe_file);

    printf("Current failsafe value: %d\n",failsafe);

if (failsafe !=0){ //failsafe file needs to be reset to 0 for flight
    if (failsafe == 10) // Heating and inflating of Tube #1
345        goto Tube10;
    if (failsafe == 15) // Excitation and data collection of Tube #1
        goto Tube15;
    if (failsafe == 20) // Heating and inflating of Tube #2
        goto Tube20;
350    if (failsafe == 25) // Excitation and data collection of Tube #2
        goto Tube25;
    if (failsafe == 30) // Heating and inflating of Tube #3
        goto Tube30;
    if (failsafe == 35) // Excitation and data collection of Tube #3
355        goto Tube35;
    else
        goto Data_collect;
}

360 //-----
// Tube 1 Process
// Mark failsafe point
failsafe_file = fopen("failsafe.txt","w");
fprintf(failsafe_file,"%d",10);
365    fclose(failsafe_file);

Tube10:      // Activate Tube 1 Heaters and lights
    printf("Activating Heaters and Lights for experiment bay #1...\n");
    outp(relay_addr+4,0);      //Select Bank 0
370    outp(relay_addr+0,0x02); //Turn on Bay LED

```

```

        outp(relay_addr+4,0x03);      //Select Bank 3
        outp(relay_addr+0,0x01);      //Turn on Oven 1

        // Sample Gas Storage Container
375    printf("Checking Gas Storage Pressure for experiment bay #1...\n");
        check_gas(run,0,1); // 

        // Collect temperature data and check versus threshold
        check_temp(1,run);

380    printf("Threshold Temperature Achieved for experiment bay #1...\n");

        //Turn Camera on
        printf("Starting Camera for experiment bay #1...");
        outp(relay_addr+4,0);          //Select Bank 0
385    outp(relay_addr+0,0x03);      //Leave LED on and turn on Camera

        // Hold for Camera boot up
        HOLD(3);

390    // Open Heater Box and Inflation Valve
        printf("\n Opening Heater Box for experiment bay #1...\n");
        outp(relay_addr+4,0x03);      //Select Bank 3
        outp(relay_addr+0,0x03);      //Turn on Pin puller and leave ovens on

395    //Hold
        HOLD(pin_puller_pause);

        printf("\n Opening Gas Valve for experiment bay #1...\n");
        outp(relay_addr+0,0x40);      //Turn off pinpuller and oven, but ...
        activate solenoid

400    // Sample Pressure and Vibration Upon Inflation
        printf("Inflation Data being collected for experiment bay #1...\n");
        read_xls(1,0,X_array,Y_array,Z_array);
        read_press(1,0,press_array);
405    s=1; idx=1;

```

```

        for (i=0;i<25000;i++){

            while(!(inp(AD_addr+9) & 0x20)); // wait for timing interrupt
            outp(AD_addr+8,0x08); // reset timing interrupt
            if (s>4){

                read_xls(1,indx,X_array,Y_array,Z_array);
                read_press(1,indx,press_array);
                s=0;
                indx++;
            }
            s++;

        }

        write_xls_inflate(1,run,run,X_array,Y_array,Z_array,press_array); // ...
        write inflation results

420    // Stop Camera
printf("Stopping Camera for experiment bay #1...\n");
outp(relay_addr+4,0); //Select Bank 0
outp(relay_addr+0,0x02); //Leave LEDS on

425    // Hold to cool the tube
printf(" Cooling tube ... \n");
HOLD(cool_down_pause);

check_gas(run,2,1); //check gas after cooling, but before vent

430
// Vent the gas from the tube
printf("\n Venting Gas for experiment bay #1...\n");
outp(relay_addr+4,0x03); //Select Bank 0
outp(relay_addr+0,0); //Turn off solenoid

435
HOLD(vent_pause);
check_gas(run,3,1); //check gas after venting

// Mark failsafe point
failsafe_file = fopen("failsafe.txt","w");

```

```

fprintf(failsafe_file,"%d",15);
fclose(failsafe_file);

445 Tube15:      // Take one picture
    printf("Take 1-2 pictures of deployed tube for bay #1...\n");
    outp(relay_addr+4,0);           //Select Bank 0
    outp(relay_addr+0,0x03);        //Activate Camera while leaving the LEDs ...
                                    on.

450          //Hold
HOLD(camera12);

printf("\n Stopping pictures for experiment bay #1...\n");
outp(relay_addr+0,0x02);        //Keep LEDs on for now

455          // Record ambient vibration levels before using PZTs
printf("Recording ambient vibe levels for experiment bay #1...\n");

460          for (j=0;j<5;j++){
    for (i=0;i<5000;i++){
        while(! (inp(AD_addr+9) & 0x20)); // wait for timing interrupt
        outp(AD_addr+8,0x08);           // reset timing interrupt
        r_xls_w_dac(1,i,X_array,Y_array,Z_array,MMSB_array,LLSB_array...
                    );
    }
    write_xls_ambient(1,run,j+1,X_array,Y_array,Z_array);
}
// Excite Tube and measure vibrations
470          printf("Exciting the tube and collecting data for experiment bay ...
#1...\n");
enable_xformer(1); // enable bay 1 transformer
for (j=0;j<num_iterations;j++){

```

```

    for (i=0;i<5000;i++){

        while(!(inp(AD_addr+9) & 0x20)); // wait for timing interrupt
        outp(AD_addr+8,0x08); // reset timing interrupt
        write_dac(i,MMSB_array,LLSB_array);} // excite but don't ...
        sample yet

    for (i=0;i<5000;i++){

        while(!(inp(AD_addr+9) & 0x20)); // wait for timing interrupt
475      outp(AD_addr+8,0x08); // reset timing interrupt
        write_dac(i,MMSB_array,LLSB_array);} // excite but don't ...
        sample yet

    for (i=0;i<5000;i++){

        while(!(inp(AD_addr+9) & 0x20)); // wait for timing interrupt
480      outp(AD_addr+8,0x08); // reset timing interrupt
        write_dac(i,MMSB_array,LLSB_array);} // excite but don't ...
        sample yet

    for (i=0;i<5000;i++){

        while(!(inp(AD_addr+9) & 0x20)); // wait for timing interrupt
485      outp(AD_addr+8,0x08); // reset timing interrupt
        r_xls_w_dac(1,i,X_array,Y_array,Z_array,MMSB_array,LLSB_array...
        );
    }

    write_xls_excite(1,run,j+1,X_array,Y_array,Z_array,Dac_array);
}

490      outp(relay_addr+0,0); //turn off transformer

// Take one picture
printf("Turn camera on to get 1-2 pictures of final state of tube for...
       experiment bay #1...\n");
outp(relay_addr+4,0); //Select Bank 0
495      outp(relay_addr+0,0x03); //Activate Cameras

//Hold
HOLD(camera12);

500      printf("\n END EXPERIMENT IN BAY #1...\n");
outp(relay_addr+0,0); //Turn off Cameras and LEDs
// Mark failsafe point

failsafe_file = fopen("failsafe.txt","w");
505      fprintf(failsafe_file,"%d",20);

```

```

fclose(failsafe_file);

if (TVAC){

    outp(relay_addr+4,0x01);

510    outp(relay_addr+0,0x08); // switch from green to red
    HOLD(TVAC_HOLD_BAYS); // power down during this period if desired
    outp(relay_addr+0,0x04); // switch back to green
}

//-----
515 // Tube 2 Process

Tube20: // Activate Tube 2 Heaters and lights
printf("Activating Heaters and Lights for experiment bay #2...\n");
520    outp(relay_addr+4,0); //Select Bank 0
    outp(relay_addr+0,0x08); //Turn on Bay LED
    outp(relay_addr+4,0x03); //Select Bank 3
    outp(relay_addr+0,0x04); //Turn on Oven 2

525    // Sample Gas Storage Container
printf("Checking Gas Storage Pressure for experiment bay #2...\n");
check_gas(run,0,2);

// Collect temperature data and check versus threshold
530    printf("Collecting Temperature Data...\n");
    check_temp(2,run);
printf("\n Threshold Temperature Achieved for experiment bay #2...\n"...
);

//Turn Camera on
535    printf("Starting Camera for experiment bay #2...");
    outp(relay_addr+4,0); //Select Bank 0
    outp(relay_addr+0,0x0C); //Leave LED on and turn on Camera

//Hold for Camera boot up
540    HOLD(3);

```

```

// Open Heater Box and Inflation Valve
printf("\n Opening Heater Box for experiment bay #2...\n");
outp(relay_addr+4,0x03);      //Select Bank 3
545   outp(relay_addr+0,0x0C);      //Turn on Pin puller and solenoid and ...
      leave ovens on

//Hold
HOLD(pin_puller_pause);

550   printf("\n Opening Gas Valve for experiment bay #2...\n");
      outp(relay_addr+0,0x80);    //Turn off pinpuller and oven, but ...
      activate solenoid

// Sample Pressure and Vibration Upon Inflation
printf("Inflation Data being collected for experiment bay #2...\n");
555   read_xls(2,0,X_array,Y_array,Z_array);
      read_press(2,0,press_array);
      s=1; idx=1;
      for (i=0;i<25000;i++){
          while(!inp(AD_addr+9) & 0x20)); // wait for timing interrupt
560   outp(AD_addr+8,0x08);    // reset timing interrupt
      if (s>4){
          read_xls(2,idx,X_array,Y_array,Z_array);
          read_press(2,idx,press_array);
          s=0;
565   idx++;
      }
      s++;
  }

570   write_xls_inflate(2,run,run,X_array,Y_array,Z_array,press_array); // ...
      write inflation results

// Stop Camera
printf("\n Stopping Camera for experiment bay #2...\n");

```

```

        outp(relay_addr+4,0);           //Select Bank 0
575      outp(relay_addr+0,0x08);     //Leave LEDs on

        // Hold to cool the tube
        printf(" Cooling tube ...\\n");
        HOLD(cool_down_pause);

580      check_gas(run,2,2);        //check gas after cooling, but before vent

        // Vent the gas from the tube
        printf("\\n Venting Gas for experiment bay #2...\\n");
585      outp(relay_addr+4,0x03);     //Select Bank 0
        outp(relay_addr+0,0);         //Turn off solenoid

        HOLD(vent_pause);
        check_gas(run,3,2);          //check gas after venting

590      // Mark failsafe point
        failsafe_file = fopen("failsafe.txt","w");
        fprintf(failsafe_file,"%d",25);
        fclose(failsafe_file);

595      Tube25: // Take one picture
        printf("Take 1-2 pictures of deployed tube for bay #2...\\n");
        outp(relay_addr+4,0);         //Select Bank 0
        outp(relay_addr+0,0x0C);       //Activate Camera while leaving the LEDs ...
        on.

600      //Hold
        HOLD(camera12);

        printf("\\n Stopping pictures for experiment bay #2...\\n");
605      outp(relay_addr+0,0x08);     //Keep LEDs on for now

        // Record ambient vibration levels before using PZTs
        printf("Recording ambient vibe levels for experiment bay #1...\\n");

```

```

610    for  (j=0;j<5;j++){
      for  (i=0;i<5000;i++){
        while(!inp(AD_addr+9) & 0x20)); // wait for timing interrupt
        outp(AD_addr+8,0x08);    // reset timing interrupt
        r_xls_w_dac(2,i,X_array,Y_array,Z_array,MMSB_array,LLSB_array...
      );
    }
615
    write_xls_ambient(2,run,j+1,X_array,Y_array,Z_array);
}
//
// Excite Tube and measure vibrations
620 printf("Exciting the tube and collecting data for experiment bay ...
          #2...\n");

enable_xformer(2); // enable bay 2 transformer
for  (j=0;j<num_iterations;j++){

625    for  (i=0;i<5000;i++){
      while(!inp(AD_addr+9) & 0x20)); // wait for timing interrupt
      outp(AD_addr+8,0x08);    // reset timing interrupt
      write_dac(i,MMSB_array,LLSB_array);} // excite but don't ...
      sample yet
    for  (i=0;i<5000;i++){
      while(!inp(AD_addr+9) & 0x20)); // wait for timing interrupt
      outp(AD_addr+8,0x08);    // reset timing interrupt
      write_dac(i,MMSB_array,LLSB_array);} // excite but don't ...
      sample yet
    for  (i=0;i<5000;i++){
      while(!inp(AD_addr+9) & 0x20)); // wait for timing interrupt
630      outp(AD_addr+8,0x08);    // reset timing interrupt
      r_xls_w_dac(2,i,X_array,Y_array,Z_array,MMSB_array,LLSB_array...
    );
}

635
write_xls_excite(2,run,j+1,X_array,Y_array,Z_array,Dac_array);

```

```

640    }

    outp(relay_addr+0,0); //turn off transformer

    // Take one picture
    printf("Turn camera on to get 1-2 pictures of final state of tube for...
           experiment bay #2...\n");
645    outp(relay_addr+4,0); //Select Bank 0
    outp(relay_addr+0,0x03); //Activate Cameras

    //Hold
    HOLD(camera12);

650

    printf("\n END EXPERIMENT IN BAY #2...\n");
    outp(relay_addr+0,0); //Turn off Cameras and LEDs

    // Mark failsafe point
655    failsafe_file = fopen("failsafe.txt","w");
    fprintf(failsafe_file,"%d",30);
    fclose(failsafe_file);

    if (TVAC){

660        outp(relay_addr+4,0x01);
        outp(relay_addr+0,0x08); // switch from green to red
        HOLD(TVAC_HOLD_BAYS); // power down during this period if desired
        outp(relay_addr+0,0x04); // switch back to green
    }

665

//-----
// Tube 3 Process

670
Tube30:      // Activate Tube 3 Heaters and lights
    printf("Activating Heaters and Lights for experiment bay #3...\n");
    outp(relay_addr+4,0); //Select Bank 0
    outp(relay_addr+0,0x20); //Turn on Bay LED

```

```

675      outp(relay_addr+4,0x03);      //Select Bank 3
        outp(relay_addr+0,0x10);      //Turn on Oven 3

        // Sample Gas Storage Container
printf("Checking Gas Storage Pressure for experiment bay #3...\n");
680      check_gas(run,0,3);

        // Collect temperature data and check versus threshold
printf("Collecting Temperature Data...\n");
check_temp(3,run);
685      printf("Threshold Temperature Achieved for experiment bay #3...\n");

        //Turn Camera on
printf("Starting Camera for experiment bay #3...");
outp(relay_addr+4,0);          //Select Bank 0
690      outp(relay_addr+0,0x30);      //Leave LED on and turn on Camera

        //Hold for Camera boot up
HOLD(3);

695      // Open Heater Box and Inflation Valve
printf("\n Opening Heater Box for experiment bay #3...\n");
outp(relay_addr+4,0x03);      //Select Bank 3
outp(relay_addr+0,0x30);      //Turn on Pin puller and leave ovens on

700      //Hold
HOLD(pin_puller_pause);

        outp(relay_addr+4,0x03);
        outp(relay_addr+0,0);      //Turn off pinpuller and oven, but leave ...
        solenoid active
outp(relay_addr+4,0x04);
outp(relay_addr+0,0x01);      // Activate Solenoid

        // Sample Pressure and Vibration Upon Inflation

```

```

710     printf("Inflation Data being collected for experiment bay #3...\n");
    read_xls(3,0,X_array,Y_array,Z_array);
        read_press(3,0,press_array);
        s=1; idx=1;
        for (i=0;i<25000;i++){
            while(!inp(AD_addr+9) & 0x20)); // wait for timing interrupt
            outp(AD_addr+8,0x08); // reset timing interrupt
            if (s>4){
                read_xls(3,idx,X_array,Y_array,Z_array);
                read_press(3,idx,press_array);
                s=0;
                idx++;
            }
            s++;
        }
    }

725     write_xls_inflate(3,run,run,X_array,Y_array,Z_array,press_array); // ...
        write inflation results

        // Stop Camera
        printf("Stopping Camera for experiment bay #3...\n");
730     outp(relay_addr+4,0); //Select Bank 0
        outp(relay_addr+0,0x20); //Leave LEDS on

        // Hold to cool the tube
        printf(" Cooling tube ... \n");
735     HOLD(cool_down_pause);

        check_gas(run,2,3); //check gas after cooling, but before vent

        // Vent the gas from the tube
        printf("\n Venting Gas for experiment bay #3...\n");
740     outp(relay_addr+4,0x04); //Select Bank 0
        outp(relay_addr+0,0); //Turn off solenoid

        HOLD(vent_pause);

```

```

745     check_gas(run,3,3);    //check gas after venting

        // Mark failsafe point
        failsafe_file = fopen("failsafe.txt","w");
        fprintf(failsafe_file,"%d",35);
750     fclose(failsafe_file);

Tube35:          // Take one picture
    printf("Take 1-2 pictures of deployed tube for bay #3...\n");
    outp(relay_addr+4,0);           //Select Bank 0
755    outp(relay_addr+0,0x30);      //Activate Camera while leaving the LEDs ...
        on.

        //Hold
        HOLD(camera12);

760    printf("\n Stopping pictures for experiment bay #3...\n");
        outp(relay_addr+0,0x20);      //Keep LEDs on for now

        // Record ambient vibration levels before using PZTs

765    printf("Recording ambient vibe levels for experiment bay #1...\n");

        for (j=0;j<5;j++){
            for (i=0;i<5000;i++){
                while(!(inp(AD_addr+9) & 0x20)); // wait for timing interrupt
770        outp(AD_addr+8,0x08);      // reset timing interrupt
                r_xls_w_dac(3,i,X_array,Y_array,Z_array,MMSB_array,LLSB_array...
                    );
            }
            write_xls_ambient(3,run,j+1,X_array,Y_array,Z_array);
        }
775    //

        // Excite Tube and measure vibrations

```

```

printf("Exciting the tube and collecting data for experiment bay ...
#3...\n");
enable_xformer(3); // enable bay 3 transformer
780 for (j=0;j<num_iterations;j++){

    for (i=0;i<5000;i++){
        while(!inp(AD_addr+9) & 0x20)); // wait for timing interrupt
        outp(AD_addr+8,0x08); // reset timing interrupt
        write_dac(i,MMSB_array,LLSB_array);} // excite but don't ...
        sample yet
    for (i=0;i<5000;i++){
        while(!inp(AD_addr+9) & 0x20)); // wait for timing interrupt
        outp(AD_addr+8,0x08); // reset timing interrupt
        write_dac(i,MMSB_array,LLSB_array);} // excite but don't ...
        sample yet
790 for (i=0;i<5000;i++){
        while(!inp(AD_addr+9) & 0x20)); // wait for timing interrupt
        outp(AD_addr+8,0x08); // reset timing interrupt
        r.xls_w_dac(3,i,X_array,Y_array,Z_array,MMSB_array,LLSB_array...
        );
    }

795
    write.xls_excite(3,run,j+1,X_array,Y_array,Z_array,Dac_array);
}
outp(relay_addr+0,0); //turn off transformer

800 // Take one picture
printf("Turn camera on to get 1-2 pictures of final state of tube for...
experiment bay #3...\n");
outp(relay_addr+4,0); //Select Bank 0
outp(relay_addr+0,0x30); //Activate Cameras

805 //Hold
HOLD(camera12);

printf("\n END EXPERIMENT IN BAY #3...\n");

```

```

        outp(relay_addr+0,0);           //Turn off Cameras and LEDs

810
        // Mark failsafe point
        failsafe_file = fopen("failsafe.txt","w");
        fprintf(failsafe_file,"%d",40);
        fclose(failsafe_file);

815
// END OF TUBE TESTS    ...

-----


// Turn on DS13-Down and clear memory

820 Data_collect:
        outp(relay_addr+4,0x01); //Reset Relay Board and Select Bank 1
        outp(relay_addr+0,0x08); //Turn DS-13 DN on.

        printf("The Ridizable Inflatable Get-A-Way-Special EXperiment is ...
               complete!...\n");
825     printf("The failsafe file will need to be manually opened and reset ...
               to 0...\\n");

// Clean up
delete []X_array; //deleted memory allocation after data was recorded to ...
               vibdat
delete []Y_array; //deleted memory allocation after data was recorded to ...
               vibdat
830 delete []Z_array; //deleted memory allocation after data was recorded to ...
               vibdat
delete []press_array; //deleted memory allocation after data was recorded to ...
               vibdat
delete []Dac_array; //deleted memory allocation after data was recorded ...
               to vibdat
delete []MMSB_array; //deleted memory allocation after data was recorded ...
               to vibdat
delete []LLSB_array; //deleted memory allocation after data was recorded ...
               to vibdat

```



```

        status = inp(AD_addr+9) & 0x20; // load status ...
        register
    } while(status != 32); // check for timing ...
        interrupt
870     outp(AD_addr+8,0x08); // Reset interrupts
        i++;
    }
    printf(".");
}
875 printf("\n");
return 0;
}

// BEGINNING OF SUBROUTINES
880
///////////
int check_temp(short int tube_num,short int run){

885     float temp_a;
     float temp_b;
     short int status;
     short int volt1;
     short int volt2;
890     short int j;
     long int k;
     long int i=1;
     int time_chk;
     int temp_ok = 0;
895     short int ch_a,ch_b;
     float temp_struc = 0.0;
     float temp_brd = 0.0;
     float temp_a_ave = 0.0,temp_b_ave = 0.0;
     float temp_brd_ave = 0.0,temp_struc_ave = 0.0;
900     FILE *temp_data;
     char filename[13];

```

```

// set channel number parameters

if (tube_num == 1)

905 {
    ch_a = 7;
    ch_b = 6;
}

if (tube_num == 2)

910 {
    ch_a = 5;
    ch_b = 4;
}

if (tube_num == 3)

915 {
    ch_a = 3;
    ch_b = 2;
}

920 sprintf(filename,"r%dtemp%d.dat",run,tube_num);
temp_data = fopen(filename,"w");
printf("Collecting temperature data for bay %d\n",tube_num);
printf("\tMonitoring temp_ave\n\t A temp   B temp Structure CPU  time...
sec) \n");

925 j=0;k=0;
while( (i < MAX_HEAT_TIME) && !temp_ok){           // Loop to count 5000 ...
cycles of clk per second
do {
    status = inp(AD_addr+9) & 0x20; // Loop to wait for timing ...
    interrupt
} while(status != 32);                  // check for timing interrupt
930 outp(AD_addr+8,0x08);              // Activate interrupts
i++;j++;k++;

//Take Board Temperature

```

```

935      outp(temp_addr,0x48+0);
time_chk = 0;
do{
    status = inp(temp_addr+8) & 1; time_chk++;
}while(status != 0 && time_chk < delay_count);

940
volt1=(inp(temp_addr+1) & 0x0F)*256;
volt2=inp(temp_addr+0);
temp_brd = 500.0*((volt1+volt2))/2048.0;

945 //conditions
if(temp_brd < -100.0 || temp_brd > 200.0){
    temp_brd=0.0;
}

950 //average
temp_brd_ave=temp_brd_ave*0.95+temp_brd*0.05; // 20 Averages

//Take OVEN Thermocouple Temperatures

955 // a Temp
outp(temp_addr+0,0x48+ch_a);
time_chk = 0;
do{
    status = inp(temp_addr+8) & 1; time_chk++;
}while(status != 0 && time_chk < delay_count);

960
volt1=(inp(temp_addr+1) & 0x0F)*256;
volt2=inp(temp_addr+0);
temp_a = 500.0*((volt1+volt2))/2048.0;

965 // b Temp
outp(temp_addr+0,0x48+ch_b);
time_chk = 0;
do{
    status = inp(temp_addr+8) & 1; time_chk++;
}

```

```

        }while(status != 0 && time_chk < delay_count);

        volt1=(inp(temp_addr+1) & 0x0F)*256;
        volt2=inp(temp_addr+0);
975      temp_b = 500.0*((volt1+volt2))/2048.0;

        //conditions
        if(temp_a < -100.0 || temp_a > 200.0){
            temp_a=0.0;
980    }
        if(temp_b < -100.0 || temp_b > 200.0){
            temp_b=0.0;
        }
        //average
985      temp_a_ave=temp_a_ave*0.95+temp_a*0.05;
        temp_b_ave=temp_b_ave*0.95+temp_b*0.05;

        // Temp struc
        outp(temp_addr+0,0x48+1);
990      time_chk = 0;
        do{
            status = inp(temp_addr+8) & 1; time_chk++;
            }while(status != 0 && time_chk < delay_count);
            volt1=(inp(temp_addr+1) & 0x0F)*256;
            volt2=inp(temp_addr+0);
            temp_struc = 500.0*((volt1+volt2))/2048.0;
995      //conditions
            if(temp_struc < -100.0 || temp_struc > 200.0){
                temp_struc=0.0;
1000    }

            //average
            temp_struc_ave=temp_struc_ave*0.95+temp_struc*0.05; // 20 Averages

1005      // print results to screen and file

```

```

        if(j==5000){ //print data every 1 second
            j=0;
            printf("\t%6.1f\t%6.1f\t%6.1f\t%6.1f\t%6i\n",temp_a_ave,temp_b_ave, ...
                temp_struc,temp_brd,i/5000);
1010        }
        if(k==10000){ //Print data to file every 2 seconds
            k=0;
            fprintf(temp_data,"%f %f %f %f %d\n",temp_a_ave,temp_b_ave, ...
                temp_struc,temp_brd,i/5000);
1015        }
    }

    if((temp_a_ave > 135.0) && (temp_b_ave > 135.0)){
        temp_ok=1;
1020    }
    if((temp_a_ave > 150.0 )|| (temp_b_ave > 150.0)){
        temp_ok=1;
    }
1025}

fclose(temp_data);
return 0;
} // end of check_temp

////////// CHECK PRESSURE for ALL XDUCERS //////////
1030 int check_gas(short int run_num, short int typ_str, short int tube_num){
    FILE *gas_str;
    short int MSBad,LSBad;
    float ad_result;
    short int i;
1035    char filename[13];

    // set filename, typ_str = 1 for FVT, 2 for after cooling
    // 3 after, else 0 for deploy
    if (typ_str==1){sprintf(filename,"FVTgas%d.dat",run_num);}
    if (typ_str==2){sprintf(filename,"T%dgcl%d.dat",tube_num,run_num);}


```

```

    if (typ_str==3){sprintf(filename , "T%dgvn%d.dat",tube_num,run_num);}
    if (typ_str==0){sprintf(filename , "T%dgas%d.dat",tube_num,run_num);}

    gas_str = fopen(filename,"w");
1045   printf("Pressure readings 1-6 tube1/2/3 tank1/2/3 (in volts) \n");

    //// the following lines sample, and discards...samples saved on 2nd ...
    run through
    /// this appears to give better results ???
    outp(AD_addr+7, 0x02); // FIFO reset (bit1)
1050   outp(AD_addr+2,0); // set channels scan 0-5
    outp(AD_addr+3,5); // ""
    outp(AD_addr+7,0x04); // enable scan (bit2)
    outp(AD_addr+11,13); // Configure channels to 0-5V range (for new ...
    pressure transducers)
    while(inp(AD_addr+11) & 0x80); // Wait for wait bit on register to ...
    settle)
1055   outp(AD_addr+0,0); // Activate A/D conversion
    while(inp(AD_addr+8) & 0x80); // Wait for A/D to settle)
    for (i=0;i<6;i++){
        LSBad = inp(AD_addr+0);
        MSBad = inp(AD_addr+1);
1060   }
    //// end of dummy sampling //////////////////////

    outp(AD_addr+7, 0x02); // FIFO reset (bit1)
    outp(AD_addr+2,0); // set channels scan 0-5
1065   outp(AD_addr+3,5); // ""
    outp(AD_addr+7,0x04); // enable scan (bit2)
    outp(AD_addr+11,13); // Configure channels to 0-5V range (for new ...
    pressure transducers)

    while(inp(AD_addr+11) & 0x80); // Wait for wait bit on register to ...
    settle)
1070   outp(AD_addr+0,0); // Activate A/D conversion
    while(inp(AD_addr+8) & 0x80); // Wait for A/D to settle)

```

```

// loop through all channels and store to file in volts
for (i=0;i<6;i++){
1075    LSBad = inp(AD_addr+0);
    MSBad = inp(AD_addr+1);
    ad_result = ((MSBad*256+LSBad+32768)/65536.0)*5.0;
    fprintf(gas_str,"%6.3f \n",ad_result);
    printf("%6.3f \n",ad_result);
1080}
}

fclose(gas_str);
return 0;
} // end of check_gas
1085
/////////// read 3 xls /////////////
int read_xls(short int tube_num,short int index,short int Xdigi[],short int ...
Ydigi[],short int Zdigi[]){
1090    short int MSBad,LSBad;
    short int ch_high, ch_low;

    if (tube_num == 1){ch_high = 12;ch_low = 10;}
    if (tube_num == 2){ch_high = 15;ch_low = 13;}
    if (tube_num == 3){ch_high = 26;ch_low = 24;}
1095
        //outp(AD_addr+9,0x80); //?? Diasble all interrupt
        outp(AD_addr+7, 0x02); // FIFO reset (bit1)
        outp(AD_addr+2,ch_low); // set channels to scan
        outp(AD_addr+3,ch_high); // ""
1100
        outp(AD_addr+7,0x04); // enable scan (bit2)
        outp(AD_addr+11,13); // Configure channels to 0-5V range (for new ...
            pressure transducers)

        while(inp(AD_addr+11) & 0x80); // Wait for wait bit on register to ...
            settle)
        outp(AD_addr+0,0);           // Activate A/D conversion

```

```

1105     while(inp(AD_addr+8) & 0x80); // Wait for A/D to settle

1110     // loop through all channels and store

1111     LSBad = inp(AD_addr+0);
1112     MSBad = inp(AD_addr+1);
1113     *(Xdigi+index) = (MSBad << 8) + LSBad;
1114     LSBad = inp(AD_addr+0);
1115     MSBad = inp(AD_addr+1);
1116     *(Ydigi+index) = (MSBad << 8) + LSBad;
1117     LSBad = inp(AD_addr+0);
1118     MSBad = inp(AD_addr+1);
1119     *(Zdigi+index) = (MSBad << 8) + LSBad;

1120     return 0;
}

/////////
////////// read pressure xducer (tube/vent) /////////////
int read_press(short int tube_num,short int index,short int press[]){

1125     short int MSBad,LSBad;
     short int ch_high, ch_low;

1130     if (tube_num == 1){ch_high = 0;ch_low = 0;}
     if (tube_num == 2){ch_high = 1;ch_low = 1;}
     if (tube_num == 3){ch_high = 2;ch_low = 2;}

     //outp(AD_addr+9,0x80); //?? Diasble all interrupt
     outp(AD_addr+7, 0x02); // FIFO reset (bit1)
1135     outp(AD_addr+2,ch_low); // set channels to scan
     outp(AD_addr+3,ch_high); // ""
     // outp(AD_addr+7,0x04); // enable scan (bit2)
     outp(AD_addr+11,13); // Configure channels to 0-5V range (for new ...
     pressure transducers)

```

```

1140     while(inp(AD_addr+11) & 0x80); // Wait for wait bit on register to ...
        settle)
        outp(AD_addr+0,0);           // Activate A/D conversion
        while(inp(AD_addr+8) & 0x80); // Wait for A/D to settle)

        // loop through all channels and store
1145
        LSBad = inp(AD_addr+0);
        MSBad = inp(AD_addr+1);
        *(press+index) = (MSBad << 8) + LSBad;

1150     return 0;
    }

////

int write_xls_inflate(short int tube_num,short int run,short int iter,short ...
    int Xdigi[],short int Ydigi[],short int Zdigi[], short int Xpress[]){

1155
    short int j;
    char filename[13];
    FILE *results;

1160     //write data to files//
    sprintf(filename,"R%dI%d%d.dat",run,tube_num,iter);
    printf("\t Filename is %s\n",filename);
    results = fopen(filename,"w");
    printf("writing to file...\n");

1165
    j=0;
    while(j<5000){
        fprintf(results,"%d %d %d %d \n",*(Xdigi+j),*(Ydigi+j),*(...
            Zdigi+j),*(Xpress+j));
        j++;
    }

1170
    fclose(results);

```

```

    printf("Inflation data file written...\n");
1175
    return(0);

}

////

1180 int write_xls_excite(short int tube_num,short int run,short int iter,short ...
    int Xdig[],short int Ydig[],short int Zdig[], short int Xdac[]){

    short int j;
    char filename[15];
    FILE *results;

1185
    //write data to files//
    sprintf(filename,"R%dVT%dI%d.dat",run,tube_num,iter);
    printf("\t Filename is %s\n",filename);
    results = fopen(filename,"w");
    printf("writing to file...\n");

1190

    j=0;
    while(j<5000){
        fprintf(results,"%d %d %d %d \n",*(Xdig+j),*(Ydig+j),*(...
            Zdig+j),*(Xdac+j));
        j++;
    }

    fclose(results);

1200    printf("Excitation data file written...\n");

    return(0);

}
1205
////
```

```

int write_xls_ambient(short int tube_num,short int run,short int iter,short ...
    int Xdigi[],short int Ydigi[], short int Zdigi[]){

    short int j;
1210    char filename[15];
    FILE *results;

        //write data to files//
        sprintf(filename,"R%dAT%dI%d.dat",run,tube_num,iter);
1215    printf("\t Filename is %s\n",filename);
    results = fopen(filename,"w");
    printf("writing to file...\n");

    j=0;
1220    while(j<5000){
        fprintf(results,"%d %d %d \n",*(Xdigi+j),*(Ydigi+j),*(Zdigi+...
            j));
        j++;
    }

1225    fclose(results);

    printf("Ambient data file written...\n");

    return(0);
1230}
}

/////////// read 3 xls write DAC /////////////
int r_xls_w_dac(short int tube_num, short int index, short int Xdigi[],short ...
    int Ydigi[],short int Zdigi[],short int MMSB[],short int LLSB[]){
1235
    short int MSBad,LSBad;
    short int ch_high, ch_low, updateDAC;

    if (tube_num == 1){ch_high = 12;ch_low = 10;}

```

```

1240     if (tube_num == 2){ch_high = 15;ch_low = 13;}
1241     if (tube_num == 3){ch_high = 26;ch_low = 24;}

1242         //outp(AD_addr+9,0x80); //?? Disable all interrupts
1243         outp(AD_addr+7, 0x02); // FIFO reset (bit1)
1244         outp(AD_addr+2,ch_low); // set channels to scan
1245         outp(AD_addr+3,ch_high); // ""
1246         outp(AD_addr+7,0x04); // enable scan (bit2)
1247         outp(AD_addr+11,13); // Configure channels to 0-5V range (for new ...
1248             pressure transducers)

1250     while(inp(AD_addr+11) & 0x80); // Wait for wait bit on register to ...
1251         settle)

1252         // set DAC (excitation signal)
1253         /* while((inp(AD_addr+4) & 0x80) == 0x80){} */ // wait if DAC not...
1254             ready
1255             outp(AD_addr+4,*(LLSB+index)); // load LSB to register
1256             outp(AD_addr+5,*(MMSB+index)); // load MSB to register
1257             updateDAC = inp(AD_addr+5); // Activate DAC
1258             // Sample
1259             outp(AD_addr+0,0); // Activate A/D conversion
1260             while(inp(AD_addr+8) & 0x80); // Wait for A/D to settle)

1261             // loop through all channels and store

1262             LSBAd = inp(AD_addr+0);
1263             MSBAd = inp(AD_addr+1);
1264             *(Xdigi+index) = (MSBAd << 8) + LSBAd;
1265             LSBAd = inp(AD_addr+0);
1266             MSBAd = inp(AD_addr+1);
1267             *(Ydigi+index) = (MSBAd << 8) + LSBAd;
1268             LSBAd = inp(AD_addr+0);
1269             MSBAd = inp(AD_addr+1);
1270             *(Zdigi+index) = (MSBAd << 8) + LSBAd;

```

```

        return 0;
    }

1275 //////////////

int enable_xformer( short int tube_num){

    outp(relay_addr+4,0x04);

1280
    if (tube_num == 1)
    {
        outp(relay_addr+0,0x02); //Turn on Transformer #1
    }

1285    if (tube_num == 2)
    {
        outp(relay_addr+0,0x04); //Turn on Transformer #2
    }

    if (tube_num == 3)
1290    {
        outp(relay_addr+0,0x08); //Turn on Transformer #3
    }

    return 0;
}

1295 ////////////// write DAC only /////////////
int write_dac( short int index, short int MMSB[], short int LLSB[]){

    short int updateDAC;

1300    // set DAC (excitation signal)
    /* while((inp(AD_addr+4) & 0x80) == 0x80){} */ // wait if DAC not...
    ready
    outp(AD_addr+4,*(LLSB+index));      // load LSB to register
    outp(AD_addr+5,*(MMSB+index));      // load MSB to register
    updateDAC = inp(AD_addr+5); // Activate DAC

1305
    return 0;
}

```

////////// END OF RIGEX CODE ...
///////////////////////////////

Bibliography

1. (2003), *Air Force Doctrine Document 1*, HQ AFDC/DR, Montgomery, AL.
2. Bigelow Aerospace (2009), Bigelow Aeropsace Website, <http://www.bigelowaerospace.com>.
3. Cassapakis, C., and M. Thomas (1995), Inflatable Structures Technology Development Overview, *AIAA 95-3738, April*.
4. Cobb, R. G. (2008), SENG 719 Vibration Damping and Control, Class Handouts.
5. Covault, C. (2007), Bigelow Reveals Business Plan, *Aviation Week and Space Technology*, 166(14).
6. D'Alto, N. (2007), The Inflatable Satellite, *Invention and Technology*, 23(1), 38–43.
7. DiSebastion III, J. D. (2001), *RIGEX: Preliminary Design of a Rigidized Inflatable Get-Away-Special Experiment*, MS Thesis, Air Force Institute of Technology (AU), Wright-Patterson AFB OH.
8. FARO Technologies, Inc. (2009), FARO Technologies, Inc. Website, <http://www.faro.com>.
9. Freeland, R., S. Bard, G. Veal, C. Cossapakis, T. Campbell, and M. Bailey (1996), Inflatable Antenna Technology with Preliminary Suttle Experiment Results and Potential Applications, <http://www.lgarde.com/papers/96-1367.pdf>.
10. Freeland, R. E., G. D. Bilyeu, G. R. Veal, and M. M. Mikulas (1998), Inflatable Deployable Space Strutures Technology Summary.
11. Goodwin, J. S. (2006), *Detailed Design of the Rigidizable Inflatable Get-Away-Special Experiment*, MS Thesis, Air Force Institute of Technology (AU), Wright-Patterson AFB OH.
12. Guidanean, K., and D. Lichodziejewski (2002), An Inflatable Rigidizable Truss Structure Based on New Sub-Tg Polyurethane Composites, *AIAA 02-1593*.
13. Gunn-Golkin, A. E. (2006), *Structural Analysis of the Rigidizable Inflatable Get-Away-Special Experiment*, MS Thesis, Air Force Institute of Technology (AU), Wright-Patterson AFB OH.
14. Helms, S. K. (2006), *Development and Testing of an Inflatable, Rigidizable Space Structure Experiment*, MS Thesis, Air Force Institute of Technology (AU), Wright-Patterson AFB OH.
15. III, R. G. H. (2004), *Structural Design and Analysis of a Rigidizable Space Shuttle Experiment*, MS Thesis, Air Force Institute of Technology (AU), Wright-Patterson AFB OH.
16. ILC Dover (2009), ILC Dover Website, <http://www.ilcdover.com>.
17. Inman, D. J. (2008), *Engineering Vibration*, 2nd ed., Pearson Education, Inc., Upper Saddle River, New Jersey.

18. Jenkins, C. H. M. (2001), *Gossamer Spacecraft: Membrane and Inflatable Structures Technology for Space Applications, Progress in Astronautics and Aeronautics*, vol. 191, American Institute of Aeronautics and Astronautics, Inc., Reston, Virginia.
19. L'Garde, Inc. (2009), L'Garde, Inc. Website, <http://www.lgarde.com>.
20. Lichodeziejewski, D., G. Veal, R. Helms, R. Freeland, and M. Kruer (2003), Inflatable Rigidizable Solar Array for Small Satellites, *AIAA 2003-1898*.
21. Lichodziejewski, D., R. Cravey, and G. Hopkins (2003), Inflatably Deployed Membrane Waveguide Antenna for Space, *AIAA 2003-1649*.
22. Lindemuth, S. N. (2004), *Characterization and Ground Test of an Inflatable Rigidizable Space Experiment*, MS Thesis, Air Force Institute of Technology (AU), Wright-Patterson AFB OH.
23. Little, G. (2008), Mr. B's Big Plan, *Air & Space Smithsonian*, 22(1).
24. Maddux, M. (2002), *RIGEX Heater/Storage Box Design and Testing*, Summer Internship Report, Air Force Institute of Technology (AU), Wright-Patterson AFB OH.
25. Meirovitch, L. (2001), *Fundamentals of Vibrations*, 1st ed., McGraw Hill, New York, New York.
26. Mikulas Jr, M. M. (1978), Structural Efficiency of Long Lightly Loaded Truss and Isogrid Columns for Space Applications, *NASA Technical Memorandum*, (78687).
27. Miller, Z. R. (2007), *Final Development, Testing, and Flight Preparation of the Rigidizable Inflatable Get-Away-Special Experiment (RIGEX)*, MS Thesis, Air Force Institute of Technology (AU), Wright-Patterson AFB OH.
28. Moeller, C. R. (2005), *Design and Ground-Testing of an Inflatable-Rigidizable Structure Experiment in Preparation for Space Flight*, MS Thesis, Air Force Institute of Technology (AU), Wright-Patterson AFB OH.
29. Moody, D. C. (2004), *Microprocessor-Based Systems Control for the Rigidized Inflatable Get-Away-Special Experiment*, MS Thesis, Air Force Institute of Technology (AU), Wright-Patterson AFB OH.
30. O'Neal, B. (2007), *Development and Testing of the Rigidizable Inflatable Get-Away Special Experiment*, MS Thesis, Air Force Institute of Technology (AU), Wright-Patterson AFB OH.
31. Owens, J. J. (2007), *Final Assembly, Testing and Processing of the Rigidizable Inflatable Get-Away-Special Experiment (RIGEX) for Spaceflight Qualification*, MS Thesis, Air Force Institute of Technology (AU), Wright-Patterson AFB OH.
32. Pappa, R. S., J. O. Lassiter, and B. P. Ross (2001), Structural Dynamics Experimental Activities in Ultra-Lightweight and Inflatable Structures, *AIAA 2001-1263*.
33. Philley Jr., T. L. (2003), *Development, Fabricatin, and Ground Test of an Inflatable Structure Space-Flight Experiment*, MS Thesis, Air Force Institute of Technology (AU), Wright-Patterson AFB OH.

34. Phipps, K. D. (2006), Beyond Ballons: Inflatable Modules Full of Potential, *Space Center Roundup*, 45(9), 8–9.
35. Satter, C. M., and R. E. Freeland (1995), Inflatable Structure Technology Applications and Requirements, *AIAA 95-3737*.
36. Shepard, M. J., R. G. Cobb, G. A. Peterson, and A. N. Palazotto (2007), Quasi-Static Optics-Based Surface control of an In-Plane Actuated Membrane Mirror, *Journal of Spacecraft and Rockets*, 44(4), 953–963.
37. Single (2002), *Experimental Vibration Analysis of Inflatable Beams for an AFIT Experiment*, MS Thesis, Air Force Institute of Technology (AU), Wright-Patterson AFB OH.
38. Smith, S., M. Elliott, J. A. Main, and A. L. Clem (2001), Post-Flight Testing and Analysis of Zero-Gravity Deployment of an Inflating Tube, *AIAA 2001-1265*.
39. Space Exploration Technologies Corp. (2009), Space Exploration Technologies Corp. Website, <http://www.spacex.com>.
40. Swenson, E. D. (2008), MECH 542 Introduction to Finite Element Analysis and Computer-Aided Design, Class Handouts.
41. Thomas, M. (1992), Inflatable Space Structures: Redefining aerospace design concepts keeps costs from ballooning, <http://www.1garde.com/people/papers/stuctures.pdf>.
42. Walker, C. (2005), *Atlas: The Ultimate Weapon by Those Who Built It*, Collector's Guild Publishing, Inc.
43. Wertz, J. R., and W. J. Larson (2003), *Space Mission Analysis and Design*, Microcosm Press.

Vita

Captain Brett J. Cooper graduated Valedictorian from Dawson-Verdon Consolidated High School, in Dawson, Nebraska. He entered undergraduate studies at Texas A&M University in College Station, Texas, where he graduated Magna Cum Laude with a Bachelor of Science Degree in Aerospace Engineering in May 2003. He was commissioned through Officer Training School in September 2003

His first assignment was at Los Angeles Air Force Base as a developmental engineer in the Space Based Infrared Systems Program Office, where he worked as a System Test Engineer, Program Manager, and Early Orbit Test Manager for DSP-23 and HEO-1. Capt Cooper earned the Air Force Commendation Medal for his efforts to integrate National Intelligence Community user requirements into the Space Based InfraRed Systems operational architecture. In Aug 2007, he reported to the Air Force Institute of Technology, and upon graduation in March 2009 he will be assigned to the National Reconnaissance Office in Chantilly, Virginia.

REPORT DOCUMENTATION PAGE
*Form Approved
OMB No. 0704-0188*

The public reporting burden for this collection of information is estimated to average 1 hour per response, including the time for reviewing instructions, searching existing data sources, gathering and maintaining the data needed, and completing and reviewing the collection of information. Send comments regarding this burden estimate or any other aspect of this collection of information, including suggestions for reducing this burden to Department of Defense, Washington Headquarters Services, Directorate for Information Operations and Reports (0704-0188), 1215 Jefferson Davis Highway, Suite 1204, Arlington, VA 22202-4302. Respondents should be aware that notwithstanding any other provision of law, no person shall be subject to any penalty for failing to comply with a collection of information if it does not display a currently valid OMB control number. PLEASE DO NOT RETURN YOUR FORM TO THE ABOVE ADDRESS.

1. REPORT DATE (DD-MM-YYYY) 26-03-2009			2. REPORT TYPE Master's Thesis	3. DATES COVERED (<i>From — To</i>) April 2008-March 2009
4. TITLE AND SUBTITLE Rigidizable Inflatable Get-Away-Special Experiment (RIGEX) Post Flight Analysis, Ground Testing, Modeling, and Future Applications			5a. CONTRACT NUMBER	
			5b. GRANT NUMBER	
			5c. PROGRAM ELEMENT NUMBER	
6. AUTHOR(S) Capt Brett J. Cooper			5d. PROJECT NUMBER	
			5e. TASK NUMBER	
			5f. WORK UNIT NUMBER	
7. PERFORMING ORGANIZATION NAME(S) AND ADDRESS(ES) Air Force Institute of Technology Graduate School of Engineering and Management (AFIT/ENY) 2950 Hobson Way WPAFB OH 45433-7765			8. PERFORMING ORGANIZATION REPORT NUMBER AFIT/GA/ENY/09-M02	
9. SPONSORING / MONITORING AGENCY NAME(S) AND ADDRESS(ES) AFIT/ENY			10. SPONSOR/MONITOR'S ACRONYM(S)	
			11. SPONSOR/MONITOR'S REPORT NUMBER(S)	
12. DISTRIBUTION / AVAILABILITY STATEMENT APPROVED FOR PUBLIC RELEASE; DISTRIBUTION UNLIMITED				
13. SUPPLEMENTARY NOTES				
14. ABSTRACT <p>The Rigidizable Inflatable Get-Away-Special EXperiment (RIGEX) Space Shuttle experiment was run successfully onboard STS-123 (<i>Endeavour</i>) in March 2008. The objective of this thesis is to analyze the space flight and post space flight test data, correlate the data to previous ground tests, and update finite element models. In turn, this research will help demonstrate the feasibility of using lightweight and low stowage volume (high packaging ratio) inflatable/rigidizable space structures in remote sensing applications.</p> <p>RIGEX was an Air Force Institute of Technology graduate-student-built Space Shuttle cargo bay experiment intended to heat and inflate three 20-inch long carbon fiber tubes in a microgravity environment. Designed to measure the individual tubes' structural characteristics and deployed configuration, pressure, temperature, vibration response, and physical alignment data were all collected successfully on-orbit and are presented in comparison to pre- and post flight ground test data. Using the space and ground test results, previously developed finite element models of the tubes are updated and models of mission oriented structures are created for trade study purposes.</p> <p>RIGEX successfully accomplished its mission statement by validating the heating and inflation methods of the inflatable/rigidizable tubes, and successfully met all other primary and secondary research objectives.</p>				
15. SUBJECT TERMS Inflatable Structures, Space Shuttle, Space Missions, Space Technology, Launch Vehicles, Vibration, Temperature, Pressure, Image, Test, Deployment				
16. SECURITY CLASSIFICATION OF:		17. LIMITATION OF ABSTRACT	18. NUMBER OF PAGES	19a. NAME OF RESPONSIBLE PERSON Dr. Jonathan Black, Assistant Professor
a. REPORT U	b. ABSTRACT U	c. THIS PAGE U	UU 244	19b. TELEPHONE NUMBER (Incld Area Code) Jonathan.Black@afit.edu 937.255.3636 x4578